UNIVERSITY OF OKLAHOMA
GRADUATE COLLEGE

CHARACTERIZING ROCK PROPERTIES AND THEIR IMPACT ON THE MECHANICAL BEHAVIOR OF CRYSTALLINE BASEMENT AND CAPROCKS

A DISSERTATION
SUBMITTED TO THE GRADUATE FACULTY
in partial fulfillment of the requirements for the
Degree of
DOCTOR OF PHILOSOPHY

By

WILLIAM M. KIBIKAS
Norman, Oklahoma
2021

CHARACTERIZING ROCK PROPERTIES AND THEIR IMPACT ON THE MECHANICAL BEHAVIOR OF CRYSTALLINE BASEMENT AND CAPROCKS

A DISSERTATION APPROVED FOR THE
SCHOOL OF GEOSCIENCES

BY THE COMMITTEE CONSISTING OF

Dr. Brett M. Carpenter, Chair

Dr. Ahmad Ghassemi, Co-chair

Dr. Ze'ev Reches

Dr. Doug Elmore

Dr. Xiaowei Chen

ACKNOWLEDGEMENTS

Foremost, I would like to thank my co-advisors, Dr. Brett Carpenter and Dr. Ahmad Ghassemi. Brett worked from the very beginning to make my PhD possible here at OU, even as he was just starting out as a new professor. For four years he guided me in my research, teaching me everything from laboratory techniques to field methods, all the while pushing me into new areas of research. It is no exaggeration to say that without his help, none of what follows would have been possible for me. Ahmad deserves particular thanks, as my work was only possible because he agreed to co-advise me and allow me to use of his Geomechanics lab for my research. Even more though, Ahmad introduced me to my advisor at Sandia National Laboratories back in 2019, and without his help I doubt I would have been able to secure my internship with their lab in 2020 and 2021. While many rocks deeply regret them helping me, Brett and Ahmad made a difference in one man's life, and I will never forget that.

Besides my advisors, I would like to thank my committee members: Dr. Ze'ev Reches, Dr. Xiaowei Chen, and Dr. Doug Elmore. Their contribution of time and knowledge to my work was greatly appreciated.

I also want to thank members of both my geoscience and petroleum engineering groups here at OU. Dr. Ze'ev Reches, who has been a passionate source of scientific knowledge and critique…even if he still has not walked as many steps as me. Folarin Kolawole, who was a wellspring of useful information and a personal inspiration during my PhD. Tanner Shadoan, Max Firkins, Xiaofeng Chen, Paul Gilbert, Brittany Stroud, Connor Mears deserve thanks for offering commentary and assisting me as I progressed through my PhD. I also owe much to the people I have worked with in the Geomechanics

Lab: Zhi Ye, Lianbo Hu, Alex Vachaparampil, Xue Jun Zhou, Yawei Li, and especially Steve Dwyer who keeps all from blowing up the lab with his efforts.

Thanks go out to my many collaborators during my PhD: Zonghu Liao, Mengni Wu, Xiaofeng Chen, Jacob Walter, and many others. My velocity research would not have been possible without assistance from John Brumley and the geomechanics team at Chesapeake Energy Corporation. I especially want to thank Steve Bauer over at Sandia National Laboratories, who has been an advisor, co-author, and mentor in my time as an intern.

I want to thank my brother and mother, Matt and Cindy, for being there to support me when I needed them. Matt, who I have always respected, has driven me to be better than I am. He helped me when I didn't know how to move forward, even took much of the burden that should have been mine. Cindy, what can I say that would ever be enough? She has always been on my side, no matter what. They are the most important people in my life, and I wouldn't be the same without them.

And finally, I want to thank my father Bill Kibikas, who passed away in May of 2020. He believed in me when I so rarely believed in myself. He encouraged me to pursue geology, to pursue my graduate degrees beyond. From helping me with Boy Scout merit badges to discussing geothermal energy balance in the Earth, he was the one who encouraged me to be a scientist. I promise Dad, I'll keep trying to get better at it.

TABLE OF CONTENTS

ACKNOWLEDGEMENTS iv

TABLE OF CONTENTS vi

LIST OF TABLES xi

LIST OF FIGURES xiv

ABSTRACT xxiii

CHAPTER I: INTRODUCTION 1

1.1 Motivations 1

1.2 Focus of Research 2

1.2.1 Crystalline Basement of Oklahoma/Kansas Region 2

1.2.2 Caprocks in the Northern Sichuan Basin 4

1.3 Organization of Dissertation 4

References 5

CHAPTER II: MECHANICAL AND PETROPHYSICAL PROPERTIES OF OKLAHOMA'S IGNEOUS BASEMENT 10

2.1 Introduction 10

2.1.1 Motivation 10

2.1.2 Geologic Setting 12

2.2 Experimental Methodology 14

2.2.1 Basement Rocks 14

2.2.3 Velocity and Axial Deformation Tests 15

2.3 Experimental Results 18

2.3.1 Ultrasonic Velocity Tests 18

2.3.2 Uniaxial and Triaxial Deformation Tests 19

2.4 Discussion 22

2.4.1 Basement Mechanical Strength 22
2.4.2 Elastic and Inelastic Basement Properties 25
2.4.3 Field and Laboratory Data Comparison 28
2.4.4 Implications for Igneous Basement in CEUS 30
2.5 Conclusions 32
Acknowledgements 33
References 33
CHAPTER II FIGURES 44
CHAPTER II TABLES 57
CHAPTER III: DEVELOPING A 1D VELOCITY MODEL OF THE CONTINENTAL BASEMENT UTILIZING ULTRASONIC VELOCITY MEASUREMENTS 60
3.1 Introduction 60
3.2 Methods 62
3.2.1 Basement Rocks 62
3.2.2 Vertical Velocity Testing 63
3.3 Experimental Results 65
3.4 Discussion 67
3.4.1 Comparing Laboratory and Field Data 67
3.4.2 Synthesizing a Cumulative 1D Model 70
3.5 Conclusions 70
Acknowledgements 71
References 72
CHAPTER III FIGURES 77
CHAPTER III TABLES 86
CHAPTER IV: ULTRASONIC VELOCITY ANISOTROPY IN THE CRYSTALLINE BASEMENT OF THE MIDCONTINENT 87
4.1 Introduction 87

4.2 Materials and Methodology 90
4.2.1 Basement Rocks 90
4.2.2 Velocity Tests 92
4.2.3 Microstructural Characterization 95
4.3 Experimental Results 96
4.3.1 Velocity Measurements 96
4.3.2 Dynamic Elastic Moduli 98
4.3.3 Microstructural Observations 98
4.4 Analysis and Discussion 100
4.4.1 Inherent Velocity Anisotropy 100
4.4.2 Microstructural Controls of Anisotropy 104
4.4.3 Comparing Laboratory and Field Data 107
4.5 Conclusions 110
Acknowledgements 110
References 111
CHAPTER IV FIGURES 118
CHAPTER IV TABLES 134
CHAPTER V: ANALYSIS OF MECHANICAL PROPERTIES OF CAPROCKS FROM THE NORTHEAST SICHUAN BASIN: IMPLICATIONS FOR SEALING EFFICIENCY OF LITHOLOGIES 137
5.1 Background 137
5.2 Geologic Setting 139
5.3 Experimental Methodology 141
5.3.1 Caprock Lithology and Petrophysics 141
5.3.2 Hardness Tests 143
5.3.3 Ultrasonic Velocity Tests 144
5.3.4 Deformation Tests 144

5.4 Experimental Results 146
5.4.1 Hardness 146
5.4.2 Ultrasonic Velocities 147
5.4.3 Deformation Tests 148
5.5 Discussion 151
5.5.1 Linking Caprock Lithology and Geomechanical Properties 151
5.5.2 Implications for Caprock Integrity 155
5.6 Summary and Conclusions 159
References 159
CHAPTER V FIGURES 171
CHAPTER V TABLES 183
CHAPTER VI: CONCLUDING REMARKS 186
6.1 Summary of Chapters 186
6.2 Future Work 188
APPENDIX A: MECHANICAL RESPONSE OF CASTLEGATE SANDSTONE UNDER HYDROSTATIC CYCLIC LOADING 191
A.1 Motivation and Methods 191
A.2 Stress Cycling Induced Deformation and Permeability Changes 193
A.3 Impact of Stress Path on Reservoir-Analogue Properties 195
A.4 Prescriptions for Cyclic Loading in Sandstone Reservoirs 199
Acknowledgements 201
References 201
APPENDIX A FIGURES 205
APPENDIX A TABLES 212
APPENDIX B: CAPROCK SUPPLEMENTARY MATERIALS 214
References 216

APPENDIX B FIGURES 217

APPENDIX B TABLES 220

LIST OF TABLES

Table 2.1: Bulk rock information for basement specimens evaluated in this study. All values are reported with ± 1 standard deviation. 57

Table 2.2: Strength and deformation properties of Granite A (TG), Granite B (CG), diabase (MCD) and rhyolite (CR). P_c and σ_f are the confining pressure and maximum differential stress during sample deformation. $E_{0.2}$, $E_{0.4}$, $\nu_{0.2}$, $\nu_{0.4}$ are the Young's moduli and Poisson's ratio measured at 0.2 and 0.4 of the failure stress. a – during TG_19 test, radial LVDT data above ~600 MPa was not valid as strain data experienced anomalous dilation behavior. b – value is the maximum strength recorded during deformation of CG_16, but higher differential stresses were not recorded, so value is not the peak strength. 58

Table 2.3: Numerically derived strength parameters for basement rock tests from Equations (4) and (5). 59

Table 3.1: List of sample dimensions for all rocks evaluated in this work. 86

Table 3.2: List of V_P and V_S values recorded at the maximum confining pressure 60 MPa in each test. 86

Table 4.1: XRD analysis of basement rocks examined in this study. *Chlorite group identified is Fe-Mg rich and most closely matches chamosite composition. 134

Table 4.2: List of sample dimensions for all cylindrical and octagonal samples evaluated in this work. Orientations indicate the primary axis the sample was cored parallel to, with X/Y being horizontal and Z being vertical. The average diameter of the octagonal samples is the average of the four diameters between parallel horizontal faces. 134

Table 4.3: Linear fracture density measured in the vertically oriented thin-sections ($P_{I/II}$) and horizontally oriented thin-sections (P_{II}) of five octagonal samples. Superscripts of V, 0-180º, 45-225º, 90-270º, and 135-315º were used to indicate the primary orientation of the measured fractures. S_V and Ω_{23} calculations are reported for the four different horizontal orientations and are labeled with the horizontal orientation utilized in each calculation. 135

Table 4.4: Mean horizontal anisotropy and dynamic moduli recorded with different observation methods for the KGS 1-32 Wellington well. *Only the horizontally polarized S-waves were reported for the KGS well log, and so were compared with S2-anisotropy measurements. 136

Table 5.1: Quantified X-ray Powder Diffraction (XPRD) analyses. Values are reported in wt. %. Measurements of LS2 show the high variability of the caprock layer, with LS2 (1) being highly dolomitized with large mica and phyllosilicate content and LS2 (2) being more homogenous and no clay content. 183

Table 5.2: Caprock petrophysical properties calculated from direct measurement of samples (1) and inference from XPRD data (2), noted by superscripts. Density and porosity values are reported in g/cm^3 and %, respectively. 183

Table 5.3: Key variables for all deformation tests conducted. σ_e = effective confining pressure; T = temperature; σ_f = failure stress; σ_y = yield stress; *E* = Young's modulus; υ = Poisson's ratio; *H* = hardening modulus. 184

Table 5.4: Angle of internal friction and cohesive strength derived from analysis of deformed samples post-deformation. Values were calculated using the fracture angle of each triaxially deformed caprock to find the shear and normal stresses, which were then linearized to find the overall angle of internal friction and cohesive strength. 185

Table 5.5: Range and mean value of properties determined from mechanical tests of caprocks and analogous lithologies in the existing literature. UCS = Unconfined Compressive Strength; *E* = Young's modulus; υ = Poisson's ratio. *Anomalously high UCS and Poisson's ratio observed in limestones and mudstones tested by Trujillo (2018), respectively. 185

Table A.1: Dimensions of Castlegate sandstone samples tested in this study. 212

Table A.2: Testing conditions for each hydrostatic loading test. Tests with multiple pressure conditions indicate maximum and minimum pressure of each cycle. P_c = confining pressure; P_p = pore pressure; P_{eff} = effective pressure during cycles; P_k = effective pressure during permeability tests. When two values of P_c, P_p, P_{eff}, or P_k are listed, this represents the maximum and minimum pressure of each cycle. 212

Table A.3: Values of the bulk modulus *B* measured during hydrostatic loading at test inception and unloading at test ending. Unloading ε_v is the volumetric strain calculated from a third-degree polynomial best-fit of the unloading curve. Test duration indicates the number of days each test lasted. Cycle loading rate represents the rate of effective stress change during cyclic loading. 213

Table B.1: Dynamic properties measured in EV1 samples up to confining pressures of 60 MPa. 220

Table B.2: Dynamic properties measured in LS1 samples up to confining pressures of 60 MPa. 221

Table B.3: Dynamic properties measured in EV2 samples up to confining pressures of 60 MPa. 222

Table B.4: Dynamic properties measured in LS2 samples up to confining pressures of 60 MPa. 223

Table B.5: Dynamic properties measured in DS1 samples up to confining pressures of 60 MPa. 224

Table B.6: Dynamic properties measured in DS2 samples up to confining pressures of 60 MPa. 225

Table B.7: List of sources for mechanical properties measured through deformation tests with major caprock lithologies. 226

LIST OF FIGURES

Figure 2.1: Lithologic map of surface geology in Oklahoma (a) (adapted from Northcutt and Campbell, 1998), with locations of Mill Creek Quarry (b) and Davis Quarry (c) where samples were procured. 44

Figure 2.2: Representative basement samples (top) and measured bulk characteristics (bottom). Effective porosity (measured through saturation method (ISRM 2007)) and bulk dry density of rock types are displayed beneath each rock sample. 45

Figure 2.3: Photomicrographs and SEM images of basement rocks tested here. Q = quartz; AFs = alkali feldspar; Pl = plagioclase; Bt = biotite; Mag = magnetite; Cpx = clinopyroxene; Fe = iron oxide; Cal = calcite. 46

Figure 2.4: MTS frames used and setup schematic for ultrasonic velocity and axial deformation tests. Examples of P- and S-waveforms generated in red and blue, respectively. 47

Figure 2.5: Variation in compressional (V_P) and shear wave (V_S) velocities loaded hydrostatically from 0 to 60 MPa. Points indicate average velocity measured at each condition. Curves are polynomial fits of average V_P and V_S for each rock type. Error bars show ± 1 standard deviation of the average velocity. 48

Figure 2.6: a) Schematic of axial and radial strain with data indicating key deformation characteristics such as the crack closure, initiation, yield and failure stresses, as well as the Young's modulus *E* (see Martin (1997) for more detail). Deformation data for uniaxial compressive tests of b) Granite A, c) Granite B, d) diabase, and e) rhyolite are displayed below. Colored lines represent tests under room dry conditions, while black lines represent tests of water-saturated samples. 49

Figure 2.7: Axial strain data for basement samples deformed under confined conditions. Deformation tests were conducted until steady state stress was reached or complete sample failure occurred. 50

Figure 2.8: Maximum and minimum stresses of basement rocks during failure. Linear regression of strength data shows the evolution of basement strength with increasing confining pressure. 51

Figure 2.9: Mohr-Coulomb failure envelopes extrapolated from maximum and minimum compressive stresses at failure in Figure 2.8. Envelopes derived from Equation (1) are plotted in each with dashed lines. Granitic samples have higher friction angles but lower cohesion than the finer-grained diabase or rhyolite. 52

Figure 2.10: UCS values for basement samples deformed in both dry and wet conditions. 53

Figure 2.11: Data for static Young's modulus (a), dynamic Young's modulus (b), static Poisson's ratio (c), and dynamic Poisson's ratio (d) against least principal stress (P_c). Only static moduli values measured at 0.4 of failure stress are plotted against dynamic measurements. 54

Figure 2.12: Deformation modulus of samples deformed uniaxially (left) and at 52.5 MPa confining pressure (right). Degradation of elastic moduli with increasing differential stress can give an approximation of the relative proportions of elastic and inelastic damage in each rock mass. 55

Figure 2.13: Dynamic Young's modulus and Poisson's ratio calculated from laboratory tests and sonic log data from Wah Zha Zhi and Wellington wells. Effective pressure and depth are approximated based on the assumed lithostatic and hydrostatic gradients of 27.5 and 10 MPa/km. Log data for Wah Zha Zhi and Wellington wells made available by Spyglass Energy Group LLC and the Kansas Geological Survey, respectively. 56

Figure 3.1: a) Regional tectonic provinces of Oklahoma and Kansas with the sampling and well locations marked by boxes (adapted from Selves (2017)) and b) regional schematic showing recent seismic activity (M3.0+) from the OGS catalogue. 77

Figure 3.2: Images of tested cylindrical (top row) and octagonal (bottom row) samples. 78

Figure 3.3: Schematic of samples and orientation of velocity measurements relative to sample axes. Z1 and Z2 of the cylindrical tests mark the plane parallel to the S-wave

piezoelectric crystal on the platens during the first and second loading of the cylindrical samples. Z1 and Z2 of the octagonal tests mark the P- and S-waves propagating vertically down and vertically up, respectively. 79

Figure 3.4: P- and S-wave velocities from a) octagonal basement rock tests, b) cylindrical basement rock tests, and c) basement rocks tested in Kibikas et al. (2020) and Yu (2017). Circles represent the first orientation utilized for velocity tests; X represents the second orientation used for velocity tests. 80

Figure 3.5: P- and S-wave velocities normalized by the values at 60 MPa for a) octagonal basement rock tests, b) cylindrical basement rock tests, and c) basement rocks tested in Kibikas et al. (2020) and Yu (2017). Circles represent the first orientation utilized for velocity tests; X represents the second orientation used for velocity tests. 81

Figure 3.6: V_P/V_S ratio, dynamic Young's moduli (E_d) and dynamic Poisson's ratios (ν_d) for a) the octagonal basement rock tests and b) the cylindrical specimen tests. Circles represent the first orientation (Z1) utilized for velocity tests; X represent the second orientation (Z2) used for velocity tests. 82

Figure 3.7: 1D models for P-wave velocity with depth and pressure extrapolated from ultrasonic velocity data, seismic inversions, and well logs. Velocity models listed are from a) the octagonal tests, b) the cylindrical tests, c) data from Kibikas et al. (2020) and Yu (2017), and d) seismic models developed by other researchers, while e) displays sonic log data from Oklahoma and Kansas. 83

Figure 3.8: 1D models for S-wave velocity with depth and pressure extrapolated from ultrasonic velocity data, seismic inversions, and well logs. Velocity models listed are from a) the octagonal tests, b) the cylindrical tests, c) data from Kibikas et al. (2020) and Yu (2017), and d) seismic models developed by other researchers, while e) displays sonic log data from Oklahoma and Kansas. 84

Figure 3.9: 1D models for velocity ratios with depth and pressure extrapolated from ultrasonic velocity data, seismic inversions, and well logs. Velocity models listed are from a) the octagonal tests, b) the cylindrical tests, c) data from Kibikas et al. (2020) and Yu

(2017), and d) seismic models developed by other researchers, while e) displays sonic log data from Oklahoma and Kansas. 85

Figure 4.1: Regional tectonic provinces of Oklahoma and Kansas with the rock sampling and well locations marked by boxes. Modified from Selves (2017). 118

Figure 4.2: Photomicrographs (left) and SEM images (right) of five basement rock samples: a) Frisco Railroad; b) KGS 1-32; c) Jones-46; d) Mill Creek; e) Spavinaw. The symbols used indicate: Q = quartz; AF = K-feldspar; Pl = plagioclase; Bt = biotite; Ca = calcite; Ti = titanite; Ap = apatite; Ch = chlorite; Rt = rutile; Ep = epidote; FeO = iron-oxide; My = myrmekite texture. 119

Figure 4.3: Images of tested cylindrical (top row) and octagonal (bottom row) samples. 120

Figure 4.4: Schematic of the velocity setup for the cylindrical sample tests. a) Photos of the MTS 810 apparatus used in this study; b) general setup of each sample before loading into apparatus for testing; c) general orientation of the samples and velocity measurements for the first (X1/Y1/Z1) and second (X2/Y2/Z2) measurements. 121

Figure 4.5: a) Schematic of apparatus used for octagonal velocity tests and b) orientation of velocity measurements in octagonal samples, with 0-360º being horizontal orientations and Front-Back being velocities measured being velocities traveling vertically up (Front) and down (Back). 122

Figure 4.6: a) Composite image of photomicrographs for vertically oriented thin-section and b) example of gridlines for calculating fracture density over sample, each set of lines parallel to one of the primary directions for each thin-section. 123

Figure 4.7: Velocity measured for cylindrical samples as a function of confining pressure. P-, S1-, and S2-wave velocities are given for the a) Y-orientation, b) X-orientation, and c) Z-orientations in each column. 124

Figure 4.8: Velocity of P-, S1-, and S2-waves for octagonal samples measured in horizontal and vertical directions. P-, S1-, and S2-wave velocities are shown for the horizontal orientations a) 0-180, b) 45-225, c) 90-270, and d) 135-315, as well as the

vertical orientation e) Front-Back. X indicate the 0/45/90/135/Back measurements while circles indicate 180/225/270/315/Front measurements. 125

Figure 4.9: Maximum velocity change in octagonal (a-f) and cylindrical (g-j) sample tests from 10 to 60 MPa. Left column shows the maximum change in the horizontal plane in each orientation and the vertical plane for a) KGS 1-32, b) Jones-46, c) Frisco Railroad, d) Mill Creek, e) Spavinaw 1, and f) Spavinaw 2 octagonal samples. Right column shows the maximum change in the horizontal plane in each orientation and the vertical plane for g) KGS 1-32, h) Jones-46, i) Mill Creek, and j) Spavinaw cylindrical samples..... 126

Figure 4.10: The relationship of the dynamic Young's moduli (a-e) and Poisson's ratio (f-j) with pressure is shown for both octagonal and cylindrical tests. Elastic moduli were calculated for samples KGS 1-32 (a and f), Jones-46 (b and g), Frisco Railroad (c and h), Mill Creek (d and i), and Spavinaw (e and j). Moduli were calculated for both the S1 and S2 velocity measurements from both the vertical measurements (solid lines) and horizontal measurements (dashed lines). 127

Figure 4.11: Linear fracture density measured in vertical and horizontal thin sections. 128

Figure 4.12: Ratios of V_P (top row) and V_S (bottom row) corresponding to the velocities measured in the horizontal directions (V_{PH} and V_{SH}) and vertical direction (V_{PV} and V_{SV}) as a function of confining pressure. 129

Figure 4.14: Horizontal velocity anisotropy (*An*) calculated for all basement samples as a function of both effective pressure and depth. Anisotropy of P-, S1-, and S2-waves is displayed for each basement rock. Values are reported for: a) KGS 1-32; b) Jones-46; c) Frisco Railroad; d) Mill Creek; e) Spavinaw (for both octagonal samples). 131

Figure 4.15: Circle diagrams showing the horizontal P-wave velocity measured at 60 MPa (left column) and linear fracture densities measured in the horizontal plane (right column). Measurements included are for: a) KGS 1-32; b) Jones-46; c) Frisco Railroad; d) Spavinaw #1; e) Mill Creek. Data for the Spavinaw #2 core is not shown since no thin section was prepared from the sample..... 132

Figure 5.1: Overview map of the greater Sichuan Basin: a) general map showing major basin boundaries, structural provinces and region caprocks were retrieved (blue box) and b) map showing location of Sichuan Basin in China (adapted from Lyu et al., 2017)… 171

Figure 5.2: Generalized stratigraphic column of Sichuan Basin, modified from Hao et al. (2006). Stratigraphic location of caprock formations sampled for this study are indicated in the right-side column. 172

Figure 5.3: Cylindrical specimens of six caprocks cored perpendicular to bedding (top) and photomicrographs of thin-sections for corresponding caprocks (bottom). a) EV1 a fine-grained anhydrite rock with weak lamination; b) LS1 is a fine-grained homogeneous limestone; c) EV2 is a heterogenous rock composed primarily of anhydrite and dolomite distinct even in hand samples; d) LS2 is a muddy limestone that is highly heterogenous from sample to sample; e) DS1 is a dolostone with a large grain-size heterogeneity indicating multiple generations of dolomotization; f) DS2 is a fine-grained dolostone with a texture similar to that of LS1 indicative of early dolomitization. 173

Figure 5.4: Photos of MTS 810 triaxial frame used for pressurizing samples (left) and setup of perpendicular (⊥) and parallel (∥) oriented samples for measuring elastic velocities (right). 174

Figure 5.5: Axial deformation frame (MTS 816) used to conduct deformation tests and the general setup of samples for tests conducted (right). Thermocouples were attached during 50 Cº experiments to monitor temperature change in the pressure vessel and along the caprock specimen. 175

Figure 5.6: Cross-plot of hardness versus specimen length from the different caprock bulk lithologies. Lithology has a strong control on hardness measurements, as carbonate hardness values are greater and more consistent than those of evaporites. R = correlation coefficient. 176

Figure 5.7: Velocity data for tests with direct and regional caprocks oriented parallel and perpendicular to bedding. Regional caprocks are primarily anhydrites, while the direct caprocks are limestones and dolostones. 177

Figure 5.8: The influence of effective pressure on the representative stress-strain behavior of limestone (a), dolostone (b), and evaporite (c) caprocks and the change in caprock failure stress (σ_f) with effective pressure (d). Deformation tests for LS1 (limestone), DS2 (dolostone) and EV1 (evaporite) caprocks are plotted to distinguish the effect lithology can play on mechanical behavior with pressure. While the uniaxial tests all display characteristic brittle mechanical behavior, at effective confining pressures of 45 MPa the difference between the regional caprocks (EV1) and the direct caprocks (LS1, DS2) becomes more apparent..... 178

Figure 5.9: Axial strain data for deformation tests at 22.5 MPa effective confining pressures at temperatures of 23 C° (solid lines) and 50 C° (dashed lines). Increasing temperature tends to reduce the elastic properties (ex. Young's moduli or slope of strain curves) and strength properties (ex. peak differential stress experienced), with the degree varying by lithology. The effect is particularly prominent in the anhydrite-rich EV1, which experiences a large reduction in strength and elastic moduli compared to the other caprock lithologies..... 179

Figure 5.10: Summary of UCS (unconfined compressive strength) and Young's moduli data collected from literature. Means are plotted as horizontal black lines, bottom and top of each box are the 25th and 75th percentiles, whiskers extend to maximum and minimum values observed. Red crosses represent outlier values that are unrepresentative of data. 180

Figure 5.11: Plot of individual geomechanical properties measured in experiments. The central points represent mean value of geomechanical properties for each lithology where measured, while error bars indicate ±1 standard deviation. Gradients indicate the brittle/ductile nature of each property relative to each other. 181

Figure 5.12: Representative data of caprock axial and volumetric strain in different lithologies are shown at each effective confining pressures. Yield and failure stresses are marked with circles and dots on each curve, respectively. Volumetric strain serves as a proxy for porosity change, as under the stress conditions tested the primary mechanisms for porosity change are pore closure and fracture nucleation. Rock permeability will evolve

depending upon whether the confining pressure applied and whether the bulk volumetric change is compacting or dilating. 182

Figure A.1: Model of stress-strain evolution over time during cyclic loading tests. a) Plot of confining pressure (P_c) and pore pressure (P_p) over test duration; b) Plot of axial (ε_{ax}), radial (ε_{rad}) and volumetric strains (ε_v) over test duration. 205

Figure A.2: Axial and radial strains for the duration of each test. 206

Figure A.3: Change in volumetric strain during unloading portion of each cycle plotted against number of cycles (a) and time elapsed (b). Volumetric strain change is calculated from the difference in the peak and valley of each cycle during the unloading portion. 207

Figure A.4: Permeability determinations: a) Permeability as a function of time during for 8-hour cycle tests; b) Permeability as a function of time during for 4-hour cycle tests (CG_006, CG_007), 2-hour cycle tests (CG_010), and tests without stress cycling (CG_009); c) Permeability measured at intervals of 0.69 MPa during the initial confining pressure loading of CG_005, CG_006, and CG_007, prior to stress cycling initiation. 208

Figure A.5: Average peak volumetric strain of every five cycles during the tests; tests conducted with 8-hour cycle rates are plotted against cycle number (a) and time elapsed (b), while samples hydrostatically loaded with 4-hour cycle rates, 2-hour cycle rates and no stress cycling are plotted against cycle number (c) and time elapsed (d). CG_010 in (c) only shows the strain during cycling, while CG_010 in (d) shows both the initial static period (~5 days) followed by the initiation of stress cycling. 209

Figure A.6: Evolution of unloading bulk moduli during hydrostatic stress cycling. Bulk moduli values are compared with the number of cycles (a) and the time elapsed (b). ... 210

Figure A.7: Comparison of permeability and volumetric strain measured during each permeability test. High P_k permeability measurements are compared with time (a) and number of cycles (c) elapsed, while low P_k permeability measurements are compared with time (b) and number of cycles (d) elapsed. Volumetric strain recorded at high P_k (e) and low P_k (f) permeability measurements are compared with time elapsed. 211

Figure B.1: Schematic of stress-strain curves and methodology for deriving elastic and inelastic properties from deformation test data. 217

Figure B.2: Example of properties such as failure strength (σ_f) and Young's moduli (E) measured in this research and others with different caprock lithologies. 218

Figure B.3: The predicted stress gradients in the northeastern Sichuan Basin in our area of study (a) and the effective principal stresses for each caprock lithology at depth (b). ... 219

ABSTRACT

Understanding our observations of the subsurface and its behavior over time requires quantifying both the in-situ conditions and the intrinsic material properties. Because of the difficulty in directly quantifying the relevant rock properties, in many cases the rock characteristics are often assumed while emphasis is put on determining the in-situ conditions. These assumptions are problematic, especially since the material properties are often used to model and predict subsurface response to short- and long-term perturbations in the in-situ conditions. Accurately modeling the subsurface structure and stability requires the relevant rock properties and their variability with in-situ conditions be quantified. This work utilizes a laboratory-based approach to analyze the rock properties of several lithologies in two areas of interest: 1) the crystalline basement rocks of Oklahoma and Kansas and 2) deeply buried caprocks from the northern Sichuan Basin.

The recent surge of seismicity in Oklahoma and Kansas has been attributed to wastewater injection in the subsurface reactivating previously dormant faults in the crystalline basement. Research has primarily focused on factors related to in-situ stress changes and basement structure, but little attention has been given to the basement rock properties that could affect seismicity. In the first study, several different basement rocks were characterized using a suite of mechanical and petrophysical laboratory tests. Laboratory experiments were conducted with granite, rhyolite and diabase samples collected from southern Oklahoma. Evolution of compressional and shear wave velocity with increasing confinement was measured through a series of ultrasonic velocity tests. A suite of uniaxial and triaxial tests were conducted to measure the elastic and inelastic deformation behavior of the basement rocks. Deformation data was evaluated using the

Mohr-Coulomb criterion and compared with additional preexisting deformation data of igneous basement rocks. Dynamic and static elastic properties compare favorably with available field measurements and demonstrate the role physical properties can play in varying mechanical behavior. Water-weakening in the basement rocks may indicate fluid-assisted processes such as stress corrosion cracking enhance deformation in the crystalline basement.

In the next study, work was focused on incorporating laboratory-based observations into modeling the geophysical behavior of the crystalline basement. The construction of accurate velocity models remains a key step in seismological studies and subsurface imaging. As the vertical or 1D velocity structure is often difficult to determine through field and well log observations, we measured the ultrasonic velocity in vertically oriented basement samples from Oklahoma and Kansas to synthesize 1D velocity models from different lithologies. The results were compared with well log measurements and 1D velocity models developed through seismologic observations. The agreement between the laboratory-based models and seismic models depends heavily upon the properties of the basement rocks in different locations and the assumptions used to develop each seismic velocity model. Changes in V_P/V_S ratios of basement samples with pressure suggest that the constant V_P/V_S assumed in many 1D velocity models for the crystalline basement is incorrect.

Following the previous work, the next study examined the 3D velocity anisotropy inherent in several basement rocks from Oklahoma and Kansas. Velocity anisotropy and particularly shear-wave splitting is a powerful tool for determining the in-situ stress orientations in the subsurface. Factors other than the stress field are capable of generating

velocity anisotropy, including fracture orientations and mineral alignment. For the crystalline basement, rocks are often assumed as isotropic and thus observed anisotropy is attributed solely to the stress orientations. Two sets of laboratory tests were used to measure the horizontal and vertical velocities of several basement rocks from Oklahoma and Kansas. Tests were conducted under hydrostatic stress conditions (i.e., $\sigma_1 = \sigma_2 = \sigma_3$) where any velocity anisotropy observed could not be attributed to the stress orientations. Microstructural observations were used to quantify the inherent anisotropy attributed to fractures in five basement rock sample in the vertical and horizontal orientations. All rocks were shown to exhibit velocity anisotropy both in the vertical and horizontal planes, though velocity anisotropy was found to be greatest in the horizontal plane (relative to surface). Sample anisotropy was highly variable between different regions and depths. The results were compared with well log and seismically measured anisotropy to show that the agreement between the velocity polarizations and stress orientations depends upon 1) whether the stresses are aligned with anisotropic structural features such as faults; 2) the degree of deformation in the basement that can induce velocity anisotropy; and 3) the scale at which velocity anisotropy is measured in the basement.

The last study focuses on characterizing several identified caprocks from the northern Sichuan Basin. Caprocks are a crucial component of petroleum systems as they act as impermeable barriers to upward migration of hydrocarbons. Their impermeability or integrity depends upon their lack of features such as fractures that enhance fluid flow. As a result, the geomechanical properties in determining whether a lithology may act as an efficient seal. Laboratory mechanical tests were conducted to measure various strength, elastic, and hardness properties of several evaporite and carbonate caprocks. The results

were compared with other laboratory caprock tests and used to develop a map of the ideal caprock characteristics. Strength data from the deformation tests was combined with stress magnitudes determined for the region to identify the stresses required to induce failure in each caprock and quantify the potential risk of caprock failure.

CHAPTER I: INTRODUCTION

1.1 Motivations

The behavior of rocks in the subsurface is a result of their inherent physical properties, which are both spatially and temporally heterogenous. Spatially the lithologies composing the subsurface vary both vertically and laterally and as a result the in-situ behavior will vary with changes in the local lithology. Furthermore, rock behavior is also a function of a given orientation. For example, many sedimentary and layered metamorphic rocks exhibit anisotropic properties, including sonic velocity (Rai and Hanson, 1988), electrical resistivity (Georgi et al., 2002), and permeability (Rasolofosaon and Zinszner, 2002), depending upon the orientation considered. This is complicated further by the temporal variation of subsurface conditions, as the hydro-thermo-chemo-mechanical conditions are known to vary over both short- and long-time scales. Hydrothermal conditions and the migration of pore fluids can substantially alter the physical properties of rocks over time (Watters and Delahaut, 1995; Mielke et al., 2015). At a regional scale the state of stress is anisotropic and variable over time, producing directional deformation such as faulting and fractures that can control subsurface behavior (Schoenball and Davatzes, 2017). Even under relatively static subsurface conditions, rock properties such as strength, elasticity, and permeability are expected to vary depending upon the lithology (Damjanac and Fairhurst, 2010; Ingebritson and Gleeson, 2014).

Human development is also known to alter rock behavior in-situ. Projects such as hydrocarbon production, geothermal energy, nuclear waste disposal, and wastewater injection all induce hydrological, chemical, thermal, and mechanical load changes to rocks in the subsurface (Segall, 1985; Schoenball et al., 2014; Keranen et al., 2014). Although

much attention is paid to the immediate effect of these changes to the in-situ conditions, ignorance of the physical properties and how they are altered by the changing conditions is often detrimental. Economically, insufficient understanding of rock properties and their alterations can lead to significant losses, as was observed in the enhanced-oil recovery project in the Ekofisk oil field and the enhanced geothermal energy project in Basel, Switzerland (Sylte, 1999; Giardini, 2009). Scientifically, our understanding of the subsurface is predicated upon assumptions about the intrinsic physical properties, which are in-turn used to model the subsurface structure, composition, and behavior (Prioul et al., 2004). Much research is focused on 1) the conditions that produced our modern geologic and geophysical observations and 2) predicting future subsurface behavior based on current conditions and subsurface behavior. Though often necessary due to both fiscal and technical limitations, it is self-evident that such assumptions about the nature of rock properties can produce errors in our characterization of the subsurface.

1.2 Focus of Research

My research is focused on the rock properties in two regions: 1) the crystalline basement rocks from Oklahoma and Kansas and 2) deeply buried direct and indirect caprocks in the northern Sichuan Basin. Characterization of these rocks is critical to interpreting and corroborating current day indirect observations, predicting future subsurface behavior, and mitigating risks induced by changing in-situ conditions induced by anthropogenic activity.

1.2.1 Crystalline Basement of Oklahoma/Kansas Region

The last decade in Oklahoma and Kansas saw a dramatic surge in seismic activity. Prior to 2009, the region had been considered tectonically stable, with earthquakes few and

far between. Such a rise was attributed primarily to wastewater injection in deep sedimentary formations and the concomitant changes to the in-situ stress field (Hincks et al., 2018). However, seismic events were sourced almost entirely from the crystalline basement, along previously inactive faults occurring from 2-12 km deep. In response to these observations, considerable effort has been made in the last few years to understand the basement structure and stability, particularly what factors contribute to seismicity and how they might be mitigated in the future. Research has primarily focused on factors that affect the in-situ conditions of the basement (e.g., fault locations and distribution, pressure changes, injection volume and rate, depth to basement, etc.) (Keranen et al., 2014; Langenbruch and Zoback, 2016; Hincks et al., 2018).

While it is known that the basement is composed primarily of igneous and metamorphic rocks, little attention has been paid to critical geomechanical and petrophysical properties of basement rocks that control the in-situ response to given conditions. Part of this is due to assumptions about the basement composition, lateral and vertical heterogeneity, and similarity to other regions in the intraplate United States. This lack of knowledge nevertheless hinders successful understanding of basement structure and stability, as many geophysical measurements and models rely on accurate calibration of rock properties to properly characterize the subsurface (Walsh and Zoback, 2016). The main objectives of researching the basement rocks are: 1) characterize the relevant physical properties of the basement rocks needed to understand seismicity in the region and 2) utilize experimental measurements to evaluate existing geophysical models, methods, and assumptions employed to describe the basement in the region.

1.2.2 Caprocks in the Northern Sichuan Basin

The Sichuan Basin in China is a prolific source for the production of hydrocarbons. Continued production in the basin since the initial discovery has necessitated further exploration for new prospective petroleum systems (Shen et al., 2015). A critical component of any petroleum system is a caprock or seal that acts as an impermeable barrier to fluid migration (England et al., 1987). Previous discoveries in the Sichuan Basin have all been associated primarily with evaporitic or mudstone caprocks (Liu et al., 2018). Recent discoveries at greater depths have shown that other lithologies are able to act as caprocks for petroleum systems in the region as well. A lithology's capability to act as a caprock is dependent upon its integrity, or the lack of features that increase permeability and reduce its ability to trap hydrocarbons. At crustal conditions, deformation features such as fractures and faults are the greatest risk to caprock integrity (Ingram and Urai, 1999; Cartwright et al., 2007). As a result, the long-term caprock efficiency in sealing hydrocarbons depends both upon its impermeability and its ability to withstand deformation, both of which are controlled by a caprocks properties and the in-situ conditions. Caprocks from the northern Sichuan Basin were studied in order to quantify individual geomechanical properties and use these observations to map the ideal characteristics of caprocks in the region.

1.3 Organization of Dissertation

The proceeding chapters of the dissertation are reformatted from manuscripts that are either published, in review, or in preparation for submission. Each chapter is summarized as follows:

- Chapter II provides new mechanical and petrophysical characterization of basement rocks in Oklahoma that are likely representative of the rocks in the seismically active basement. The results have been published in both an *ARMA* conference paper and the journal of *Tectonophysics*.
- Chapter III utilizes oriented laboratory measurements of vertically-propagating velocities in basement rocks to synthesize a new 1D velocity model and compare with existing models for the Oklahoma and Kansas regions.
- Chapter IV focuses on the inherent velocity anisotropy in the basement of Oklahoma and Kansas and how it may affect in-situ stress determinations for the region.
- Chapter V is a localized study of direct and indirect caprocks from the Sichuan Basin whereby different properties were used to map the characteristics of an effective caprock.
- Chapter VI is a summary of chapters and speculation on future areas of research based on the results discussed.

Additionally, a brief summary of work conducted on the impact of stress cycling in reservoir sandstones is provided in Appendix A. Supplementary material for the caprock research in Chapter V is provided in Appendix B.

References

Bjørlykke, Knut, and Jens Jahren. "Sandstones and sandstone reservoirs." In Petroleum Geoscience, pp. 113-140. Springer, Berlin, Heidelberg, 2010.

Cartwright, J., Huuse, M., & Aplin, A. (2007). Seal bypass systems. AAPG bulletin, 91(8), 1141-1166.

Damjanac, Branko, and Charles Fairhurst. "Evidence for a long-term strength threshold in crystalline rock." Rock Mechanics and Rock Engineering 43, no. 5 (2010): 513-531.

England, W. A., A. S. Mackenzie, D. M. Mann, and T. M. Quigley. "The movement and entrapment of petroleum fluids in the subsurface." Journal of the Geological Society 144, no. 2 (1987): 327-347.

Georgi, D., A. Bespalov, L. Tabarovsky, and Js Schoen. "On the relationship between resistivity and permeability anisotropy." In SPE Annual Technical Conference and Exhibition. Society of Petroleum Engineers, 2002.

Giardini, Domenico. "Geothermal quake risks must be faced." Nature 462, no. 7275 (2009): 848-849.

Hincks, Thea, Willy Aspinall, Roger Cooke, and Thomas Gernon. "Oklahoma's induced seismicity strongly linked to wastewater injection depth." Science 359, no. 6381 (2018): 1251-1255.

Ingebritson, S. E., and Tom Gleeson. "Crustal permeability: Introduction to the special issue." (2014).

Ingram, Gary M., and Janos L. Urai. "Top-seal leakage through faults and fractures: the role of mudrock properties." Geological Society, London, Special Publications 158, no. 1 (1999): 125-135.

Keranen, Katie M., Matthew Weingarten, Geoffrey A. Abers, Barbara A. Bekins, and Shemin Ge. "Sharp increase in central Oklahoma seismicity since 2008 induced by massive wastewater injection." Science 345, no. 6195 (2014): 448-451.

Langenbruch, Cornelius, and Mark D. Zoback. "How will induced seismicity in Oklahoma respond to decreased saltwater injection rates?." Science advances 2, no. 11 (2016): e1601542.

Liu, Hong, Xiucheng Tan, Yonghao Li, Jian Cao, and Bin Luo. "Occurrence and conceptual sedimentary model of Cambrian gypsum-bearing evaporites in the Sichuan Basin, SW China." Geoscience Frontiers 9, no. 4 (2018): 1179-1191.

Mielke, Philipp, Mathias Nehler, Greg Bignall, and Ingo Sass. "Thermo-physical rock properties and the impact of advancing hydrothermal alteration—A case study from the Tauhara geothermal field, New Zealand." Journal of Volcanology and Geothermal Research 301 (2015): 14-28.

Prioul, Romain, Andrey Bakulin, and Victor Bakulin. "Nonlinear rock physics model for estimation of 3D subsurface stress in anisotropic formations: Theory and laboratory verification." Geophysics 69, no. 2 (2004): 415-425.

Rai, Chandra S., and Kenneth E. Hanson. "Shear-wave velocity anisotropy in sedimentary rocks: A laboratory study." Geophysics 53, no. 6 (1988): 800-806.

Rasolofosaon, Patrick NJ, and Bernard E. Zinszner. "Comparison between permeability anisotropy and elasticity anisotropy of reservoir rocks." Geophysics 67, no. 1 (2002): 230-240.

Segall, Paul. "Stress and subsidence resulting from subsurface fluid withdrawal in the epicentral region of the 1983 Coalinga earthquake." Journal of Geophysical Research: Solid Earth 90, no. B8 (1985): 6801-6816.

Schoenball, Martin, and Nicholas C. Davatzes. "Quantifying the heterogeneity of the tectonic stress field using borehole data." Journal of Geophysical Research: Solid Earth 122, no. 8 (2017): 6737-6756.

Schoenball, Martin, Louis Dorbath, Emmanuel Gaucher, J. Florian Wellmann, and Thomas Kohl. "Change of stress regime during geothermal reservoir stimulation." Geophysical Research Letters 41, no. 4 (2014): 1163-1170.

Shen, Ping, Jian Zhang, Jiarong Song, Haitao Hong, Dahai Tang, Xiaojuan Wang, Hua Wang, and Wenjun Luo. "Significance of new breakthrough in and favorable targets of gas exploration in the Middle Permian system, Sichuan Basin." Natural Gas Industry B 2, no. 5 (2015): 391-398.

Sylte, J. E., L. K. Thomas, D. W. Rhett, D. D. Bruning, and N. B. Nagel. "Water induced compaction in the Ekofisk field." In SPE Annual Technical Conference and Exhibition. Society of Petroleum Engineers, 1999.

Walsh III, F. Rall, and Mark D. Zoback. "Probabilistic assessment of potential fault slip related to injection-induced earthquakes: Application to north-central Oklahoma, USA." Geology 44, no. 12 (2016): 991-994.

Watters, Robert J., and Warren D. Delahaut. "Eflect of argillic alteration on rock mass stability." Clay and shale slope instability 10 (1995): 139.

Zoback, Mary Lou. "First-and second-order patterns of stress in the lithosphere: The World Stress Map Project." Journal of Geophysical Research: Solid Earth 97, no. B8 (1992): 11703-11728.

CHAPTER II: MECHANICAL AND PETROPHYSICAL PROPERTIES OF OKLAHOMA'S IGNEOUS BASEMENT

2.1 Introduction

2.1.1 Motivation

The geomechanical properties of rocks characterize the in-situ response of different lithologies in the state of stress in the subsurface. Broadly speaking, the two types of geomechanical properties that describe deformation behavior are (1) the elastic deformation properties (i.e., Young's modulus, Poisson's ratio) and (2) the strength or failure properties (e.g., Paterson and Wong, 2005). These properties are in-turn dependent on a number of physical properties such as mineralogy (Dyke and Dobereiner, 1991), grain-size (Eberhardt et al., 1999), and fracture density (Baud et al., 2014), all of which are often spatially and temporally heterogeneous in the crust (Bruhn et al., 1994). Given that such characteristics are also correlated with other geophysical measurements (ex. elastic wave velocity), geomechanical properties and subsurface deformation are often determined through indirect methods (Wyllie et al., 1956; Gregory, 1976; Yun et al., 2005). However, such methods rely on numerous assumptions that may lead to incorrect predictions of the in situ mechanical response. Understanding the structure and stability of rocks in the subsurface, as well their corresponding response to changing in situ conditions, requires accurate characterization of their mechanical behavior and physical properties.

From 2009 to 2016, a dramatic surge in seismicity was observed in north-central Oklahoma and southern Kansas in the United States (e.g., Keranen et al., 2014). While seismic activity in the Central and Eastern United States (CEUS) has previously been observed in areas such as the Madrid Seismic Zone and Eastern Tennessee (Frankel, 1995),

the increase of seismic activity in Oklahoma was unprecedented. Though largely attributed to the disposal of wastewater in sedimentary formations (e.g., Ellsworth, 2013), the overwhelming majority of earthquakes occurred along previously unmapped faults in the crystalline basement. This has raised several questions, including why there was such significant rise in earthquakes focused in Oklahoma's crystalline basement as opposed to other regions where large-scale fluid disposal has occurred (ex. Western Canadian Sedimentary Basin, Illinois Basin, etc.) (Skoumal et al., 2018).

Wastewater injection is thought to facilitate earthquake nucleation on basement faults through pore fluid pressurization in fault zones and poroelastic stress effects (McGarr, 2014; Goebel et al., 2017). While the mechanisms of induced seismicity are fairly well understood, triggered events have been erratic and often occur over distances and durations that cannot be explained solely through fluid diffusion processes (Goebel et al., 2017). A number of factors have been shown to influence the observed seismicity (i.e., fault distribution and orientation, in situ stress state, preexisting pore pressure, injection rate and volume, depth to crystalline basement, etc.) (Ellsworth et al., 2015; Walsh and Zoback, 2016; Hincks et al., 2018; Kolawole et al., 2019). Previous investigations into the induced seismicity in Oklahoma has focused predominantly on the impact changing pore pressure has on subsurface behavior (McGarr, 2014; Segall and Lu, 2015; Walsh and Zoback, 2016; Hemami and Ghassemi, 2018).

There remains to date a notable lack of work characterizing the petrophysical and geomechanical properties of the crystalline basement (Katz et al., 2001; Katz and Reches, 2004; Carpenter et al., 2016; Kibikas et al., 2019). This is a significant oversight for several reasons. Firstly, the geomechanical properties of the basement strongly control the tectonic

evolution and structure of both the crystalline basement and the overlying sediment, which in turn influences the susceptibility of faults to reactivation in Oklahoma (Ferrill et al., 2017). Secondly, constraining the probability of injection-induced fault slip requires an understanding of the geomechanical properties and the role of different physical properties (Walsh and Zoback, 2016). Thirdly, Shah and Keller (2017) recently inferred that basement lithology in Oklahoma exerted a strong influence on seismicity regardless of injection distance or event depth. Pei et al. (2018) also observed that large magnitude events in Oklahoma tended to occur along boundaries of contrasting mechanical properties in the basement. Such observations imply a better characterization of the mechanical and petrophysical behavior is needed to understand both past and present deformation in the crystalline basement.

This paper details a compendium of laboratory tests measuring the mechanical and petrophysical properties of Cambrian and Precambrian basement samples collected from outcrops in Oklahoma. Velocity measurements conducted under hydrostatic conditions serve as an upper bound for in situ elastic wave measurements and corresponding dynamic moduli evolution. Deformation tests were conducted under various mechanical and chemical conditions to characterize rock behavior with increasing depth. This data was compared with existing direct and indirect measurements of rock properties in the crystalline basement. Taken together, this work provides new insight into the mechanical behavior and geomechanical parameters of the crystalline basement in the CEUS.

2.1.2 Geologic Setting

The crystalline basement rock in Oklahoma is the result of a series of separate magmatic events. The oldest Precambrian rocks are part of a larger granite-rhyolite

province in the southern United States (Denison et al., 1981, Van Schmus et al., 1993). These rocks are predominantly felsic igneous rocks and their metamorphic derivatives, along with a few mafic intrusions (Gilbert and Hughes, 1986; Bickford et al., 2015). Radiometric dating from surface outcrops and drill core samples constrains the date of formation for these terranes to 1.34 – 1.4 Ga (Bickford et al., 2015). The second magmatic event occurred as part of a failed rift forming in the Early and Middle Cambrian (referred to as the Southern Oklahoma Aulacogen or SOA). Several terranes of granite, rhyolite, gabbro and basalt formed overlying the older basement rock in south-central and southwestern Oklahoma (Hogan and Gilbert, 1998). This event led to significant uplift and alteration of preexisting basement rock and sediment.

Subsurface depth of the crystalline basement is highly variable throughout Oklahoma (Johnson et al., 1989; Shah and Keller, 2017; Crain and Chang, 2018), ranging from surface outcrops in the south and northeast to depths exceeding 10 km in the Anadarko Basin. In northern Oklahoma, where the majority of the recent seismicity has occurred, the basement depth ranges from 1-3 km. This topographic variation is the result of significant phases of tectonic deformation - including rifting events in the Precambrian and Cambrian and major orogenesis in the Pennsylvanian Period - creating both major subsidence and orogenesis in the south and gentler uplift in northern Oklahoma (Johnson, 2008). Uplift during this period led to the exposure of basement rock in the south and the creation of a broad arch of north-trending fault blocks referred to as the Nemaha Uplift in the north (Figure 2.1).

The basement rocks examined in this work originate from one of the exposures of uplifted basement rock in the eastern Arbuckle Mountains (Figure 2.1) (Denison, 1973).

Various igneous and metamorphic terranes are exposed here, including granites, granodiorites, rhyolites, and mafic intrusions (Lidiak and Denison, 1999). Rocks in this exposure formed as part of the same southern granite and rhyolite province as basement in the seismically active region of northern Oklahoma and have likely experienced a similar tectonic evolution (Bickford et al., 2015). The variability of exposed basement rocks in the Arbuckle Uplift is also similar to geologic interpretations of buried basement rock in northern Oklahoma (Shah and Keller, 2017).

2.2 Experimental Methodology

2.2.1 Basement Rocks

Four igneous rocks – two granites, one rhyolite and one diabase – from south-central Oklahoma were selected for testing. Samples were collected from fresh material in active railroad ballast quarries. One granite (labeled here as Granite A) and the diabase were quarried from Mill Creek, Oklahoma, while the other granite (labeled here as Granite B) and rhyolite were quarried from Davis, Oklahoma (Figure 2.1). Specimens of Granite A, Granite B, diabase, and rhyolite were referred to with the nomenclatures TG, CG, MCD and CR, respectively (Figure 2.2).

Granite A has been identified as Troy Granite (Lidiak et al., 2014), while Granite B is quarried from an area that has been mapped as part of the Colbert Rhyolite. Both granites are medium- to coarse-grained, dominantly composed of microcline feldspar, quartz and calcic-plagioclase. Grain-size of the granites was found to range from 0.1-4.6 mm, with a mean grain diameter of 1.3 and 1.0 mm for Granite A and B, respectively. Granite A displays prominent feldspar solid solution and microfracturing (Figure 2.3), as well as a greater biotite content than Granite B. Granite B by contrast shows evidence of

rock-fluid interaction, including biotite alteration to chlorite and magnetite and fracture sealing with calcite, and less preexisting damage. The greatest difference between the two materials appears to be the degree of fracturing, as suggested by the observations in Figure 2.2. Granite A has been previously dated at ~1.4 Ga (Bickford and Lewis, 1979) and given the similarity and proximity of the two granites, it is assumed both are Precambrian in origin.

The rhyolite is part of the Carlton Rhyolite Group, mapped as the Colbert rhyolite, one of numerous intrusive and extrusive igneous rock suites formed as part of the SOA. The rocks are uniformly porphyritic, with clasts of perthite, quartz and orthoclase amidst a groundmass of microcrystalline to cryptocrystalline feldspar and quartz (Denison, 2015). Grain-size of the matrix was found to be 0.2 ± 0.12 mm, though the diameter of larger clasts can be greater than 0.5 mm. Hydrothermal fluid flow has altered the original texture, producing calcite-filled vesicles and feldspar alteration. The diabase, part of numerous dikes crosscutting the Troy Granite, is very fine-grained with a mean grain size of 0.13 ± 0.07 mm. Samples consist mainly of plagioclase, clinopyroxene and iron-oxide, with a few alteration products such as chlorite and calcite along minor fractures (Figure 2.3). The majority of basement dikes have been dated as forming during the Cambrian, during the aforementioned rifting event (Lidiak et al., 2014).

2.2.3 Velocity and Axial Deformation Tests

Samples of each basement component were cored and polished into right cylinders with diameters of 25.4 mm and lengths of 48-54 mm. End faces of each specimen were ground flat and parallel to within ± 0.01 mm.

Prior to testing, density and effective porosity of each sample were measured (Table 2.1, Figure 2.2). Specimens were dried at 50 C^{o} for a minimum of 24 hours, with sample dry weight and volume measured after to calculate bulk densities. Dried samples were then vacuum-saturated in a bath of de-ionized water for 48 hours. Dry and wet weight of each rock mass was used to calculate the effective (or connected) porosities (Figure 2.2). Samples were vacuum-saturated for a period of ten days to determine accuracy of saturation measurements. Granites A and B, diabase and rhyolite were found to have effective porosities of 0.78%, 0.38%, 0.52% and 2.15% respectively, suggesting effective saturation is achieved within 48 hours.

Ultrasonic velocities of ten samples of each rock (except rhyolite where only nine samples were tested) were measured using the pulse transmission technique (Mattaboni and Schreiber, 1967) from ambient pressure up to hydrostatic pressures of 60 MPa. Samples were placed between two steel end caps with mounted P- and S-wave piezoelectric transducers (resonant frequency of 500 kHz) on each cap. A pulse generator was used to pass a signal through the rock cylinders, exciting each transducer. Resultant compressional and shear waveforms were recorded using a Tektronix MDO3022 oscilloscope and used to identify first arrivals. Delay time of each platen was subtracted from first arrival time to determine compressional and shear wave velocities of each sample. Initial measurements at room conditions were made through application of a small differential load with a benchtop vice. Once measured, samples were then jacketed with polyolefin tubing and secured in a triaxial loading frame (Figure 2.4, MTS 810). Samples were loaded hydrostatically in increments of 10 MPa, recording P- and S-wave velocity at each pressure step, up to pressures of 60 MPa.

Uniaxial and triaxial deformation tests were conducted to directly measure the strength and deformation properties of the basement samples. All tests were conducted using a triaxial loading frame (MTS 315) with a stiffness of 2.9 x 107 kN/m. Samples were either dried for 24 hours or saturated in a vacuum for 48 hours beforehand depending on the test. Each sample was situated between two steel caps and jacketed with heat-shrink tubing (Figure 2.4). Axial strain was measured by a set of vertically oriented linear variable displacement transformers (LVDT) and corrected for the elastic deformation of the steel caps as a function of differential load. Radial strain was measured through a circumferential extensometer with a mounted LVDT oriented perpendicular to the cylindrical axis. Depending on the test, rocks were either deformed under uniaxial ($\sigma_1 > \sigma_2 = \sigma_3 = 0$ MPa) or triaxial ($\sigma_1 > \sigma_2 = \sigma_3$) conditions. Confining pressure was increased at a rate of ~2 MPa/min until the desired pressured was achieved. Experiments were conducted with axial strain rates of 10-5 s-1 until sample failure occurred.

Post-deformation analysis of axial deformation was conducted to analyze the geomechanical properties of the basement rocks. The maximum and minimum compressive stresses at failure were used to identify the relation of basement strength with lithostatic stress. Since stress-strain curves are generally non-linear, each curve was fitted to a polynomial similar to the proposed method of Heap and Faulkner (2008) and then differentiated to find the tangent moduli at any point. With this the Young's modulus (E_S) could be calculated by:

$$E_S = \frac{\delta\sigma}{\delta\varepsilon_{axial}} \quad (1)$$

and the Poisson's ratio (υ_S) could be calculated by:

$$v_S = -\frac{\delta \varepsilon_{radial}}{\delta \varepsilon_{axial}} \quad (2)$$

where σ, ε_{axial}, and ε_{radial} are the applied differential stress, axial strain and radial strains, respectively. The crack initiation stress (or the stress at which inelastic crack propagation and nucleation begins) has been found to vary from 0.4 to 0.55 in rocks regardless of specific properties (Nicksiar and Martin, 2014). Since this point marks the onset of inelastic (or non-recoverable) strain, here the elastic moduli were determined at 0.2 and 0.4 of the failure stress.

2.3 Experimental Results

2.3.1 Ultrasonic Velocity Tests

Average values of axially-oriented P-wave (V_P) and S-wave (V_S) measurements for each basement rock are displayed in Figure 2.5. All basement samples exhibit increasing elastic wave velocities with pressure, though this effect is greatest in the two granites. Elastic wave velocities measured for different samples of each rock type can vary significantly, though this scatter decreases with increasing pressure.

P-wave velocities were generally greatest in the diabase samples, though at low pressures the rhyolite samples have comparable velocities to diabase. While the general trends are similar between the two granites, velocities measured for Granite B are consistently greater than Granite A measurements. Rhyolite samples exhibit the least change with pressure, with P-values on average increasing only 6% to 8% up to 60 MPa. This is in contrast to Granite A, which displays an increase in velocity from 24 to 27% up to 60 MPa. P-wave velocity data follows two distinct trends: the two granites show large increases in velocity with increased pressure, becoming linear only near ~50 MPa, while

the fine-grained diabase and rhyolite display comparably moderate increases in velocity with pressure.

S-wave velocities tend to be greatest in Granite B, with the other three rocks displaying comparable velocities as pressure increases. S-wave velocities increase with pressure less than P-waves, meaning that the V_P/V_S tends to grow with increasing pressure in each basement rock. Similar to P-wave measurements, S-wave velocities follow two distinct trends of large increases with pressure (e.g., granite samples) and moderate or incremental increases with pressure (e.g., diabase and rhyolite samples). Similar pressure-dependence of elastic velocities implies specific petrophysical characteristics are shared by rocks within each of these trends.

2.3.2 Uniaxial and Triaxial Deformation Tests

Dry and wet samples were deformed under unconfined conditions, with failure and significant strength loss occurring in all samples tested. Rock failure in all samples occurred through propagation of tensile fractures parallel to the direction of maximum compression (σ_1). Strength and deformation properties were relatively consistent between samples, with the largest variability in the two granites.

The two granites, despite slight density and porosity variations, display qualitatively similar deformation behavior. The range of unconfined compressive strength (UCS) for the two granites is fairly similar (Table 2.2). The larger variation in peak strength for Granite A could be a result of the more pervasive fracturing observed in the rock, though the effect is seemingly small. The Young's moduli (Figure 2.6a) differ noticeably between the two granites, with Granite A moduli generally 5-10 GPa lower than Granite B

tests. Granite samples generally exhibit stable strain-softening behavior with negative post-peak slopes (Labuz and Biolzi, 2007).

Diabase specimens are by far the strongest of the different basement rocks tested. This is expected given both the high average density of the samples and relative homogeneity of the rock compared to the more felsic basement rocks. UCS values for dry diabase samples range from 350 – 396 MPa, more than twice the UCS of either granite. The diabase is also the most rigid of the basement rocks tested here, with Young's moduli values predominantly between 70-85 GPa. Unlike Granites A and B, the diabase is able to accommodate very little inelastic deformation. Failure behavior is unstable or even critical (positive slope or complete strength loss post-peak) with samples generally exhibiting complete strength loss following the maximum stress achieved (Labuz and Biolzi, 2007).

Rhyolite samples are surprisingly strong - though the peak strength of dry samples is lower than that of diabase (Table 2.2), it is still quite high and greater than either granite tested. Behavior pre- and post-peak stress is akin to the failure behavior of the diabase samples, with fracture propagation in the samples resulting in near complete strength loss as mechanical loading continues. Unlike the diabase though, rhyolite samples are far less rigid, as their Young's moduli are comparable to that of the granite samples instead. Such a discrepancy implies the elastic and failure behaviors are controlled by different inherent properties in the basement samples.

Basement samples deformed in the presence of de-ionized water display similar mechanical behavior and failure mechanisms, though with a few key differences. Firstly, the presence of water lowers the peak strength noticeably in samples of Granite A, diabase and rhyolite, but has little effect on the strength of Granite B. Secondly, the presence of

water appears to affect the post-peak mechanical behavior (Figure 2.6b,c,d,e), particularly in the brittle diabase and rhyolite samples.

Data for confined tests of basement samples are displayed in Figure 2.7. Tests were conducted with confining pressures of 26.25, 52.5, 78.75 and 105 MPa. We assume lithostatic and hydrostatic gradients in Oklahoma of 27.5 and 10 MPa/km respectively, and that these confining pressures are equivalent to effective stresses at depths of approximately 1.5, 3.0, 4.5 and 6.0 km (Walsh and Zoback, 2016; Kolawole et al., 2019).

The maximum differential stress that the basement samples may accommodate increases with confining pressure at all conditions. To evaluate the change in basement strength with mechanical loading, the maximum and minimum compressive stresses at failure for each test is shown in Figure 2.8. To provide a more thorough analysis of the basement in Oklahoma, peak strength of the Mt. Scott granite (Katz et al., 2001), a fine- to medium-grained (0.9 ± 0.2 mm) Cambrian granite from southern Oklahoma, is plotted as well. Following peak strength, basement rocks experience a moderate to complete strength loss as microcracks coalesce along a plane of failure in each sample. Sample inelastic strain (e.g., non-linear portion of stress-strain curves) prior to failure tends to increase with increasing pressure, though this behavior varies between rock types tested.

Rhyolite samples displayed the greatest strength and generally the lowest elastic moduli (Table 2.2). As with the uniaxial tests, rhyolite samples tend to experience unstable or critical failure behavior, with near complete strength loss following peak strength. Mechanical behavior of the two granites is relatively similar as pressure is increased. Both granites exhibit greater changes in elastic parameters with increasing pressure than the diabase or rhyolite, and have comparable peak strengths. Notably though, Granite B lose

strength more spontaneously than Granite A, as Granite A samples generally exhibit more stable strain-softening behavior rather than the complete strength loss of Granite B (Figure 2.7). Diabase samples are the least impacted by the addition of confining pressure, as their tangent Young's moduli are relatively similar to those of the unconfined samples. Pressure change appears to have less impact on increasing diabase peak strength, especially at lower pressure conditions. However, Young's moduli of the diabase samples remain consistently greater than that of the other basement components.

2.4 Discussion

2.4.1 Basement Mechanical Strength

It is commonly assumed that earthquakes occur along natural faults that are inherently weaker than the intact host rock. However, the strength of intact rock is important for understanding basement deformation and earthquake propagation because: (1) it is not known what percentage of earthquakes nucleate on preexisting faults, as part of rupture in a new fault, or involve the breaking of near-intact rock at fault jogs or locked sections; (2) similar deformation micromechanisms, such as fracture and comminution of grains and asperities, may control the nucleation of earthquakes at fault zones (Lockner and Beeler, 2002). It is therefore necessary to analyze strength properties of the undamaged basement rock as well.

The cohesion C and the angle of internal friction φ characterize a rocks geomechanical response to an applied load. These properties can be used to extrapolate shear strength of rocks undergoing brittle deformation through the relation:

$$\tau = \sigma_n \tan\varphi + C \quad (3)$$

where σ_n and τ are the normal and shear stress along the principal plane of failure in the rock. While direct measurement of principal fracture angle is often used to calculate these properties, such measurements can be subject to human error and questionable. For basement rock strength, φ and *C* were determined using a linear regression of the peak strength values in σ_1-σ_3 space (e.g., Brady and Brown, 2013). Values for φ and *C* were found through equations:

$$C = \frac{\sigma_c(1-\sin\varphi)}{2sin\varphi} \quad (4)$$

$$sin\varphi = \frac{tan\psi-1}{tan\psi+1} \quad (5)$$

where σ_c and $\tan\psi$ are the intercept and slope of the linear regression lines for σ_1-σ_3 values (Figure 2.8). Values determined through Equations (4) and (5) were used to derive the Mohr-Coulomb envelope for each basement rock type, including the Mt. Scott granite (Figure 2.9).

Cohesion *C* is greatest in the diabase and rhyolite samples tested here and is nearly twice that of the three granites discussed. Between the three granites, the Mt. Scott granite has a greater cohesive strength as well, correlating with the greater strength observed by Katz et al. (2001). From petrographic observations of the rock types (Section 2.2), basement cohesion is seemingly related to grain-size. The finest-grained (and most homogenous) rock – diabase – has the greatest cohesion, while the coarse basement granites have the lowest. This would also fit with the observation that cohesion is greater in the fine-grained Mt. Scott granite than either of the granites tested here (~0.9 mm). The internal friction angle φ is similar between Granites A, B and rhyolite. The similar φ values, despite differences such as grain size, may reflect similar bulk mineralogic compositions,

as all are part of the larger Arbuckle Uplift (Figure 2.1). The fact that Mt. Scott granite, quarried from a different igneous province, has a noticeably greater φ (53.6º) may support this supposition as well. Diabase samples have the lowest friction angle, reflecting the previous observation that increasing confining pressure does little to change the mechanical behavior. This may be due to diabase having less capability to accommodate inelastic damage during deformation. Once the fracture propagation threshold is reached, diabase requires less work for fracture coalescence and failure to occur.

The interpreted Mohr-Coulomb failure envelopes can be taken as the upper bound for failure strength in the basement in Oklahoma. The stresses required for failure and earthquake nucleation to occur along preexisting fault zones are likely to be lower than is required for the fracture of intact basement. In Oklahoma, this has been demonstrated by: (1) focal mechanism inversions used by Walsh and Zoback (2016) to derive the in-situ conditions of fault slip in north-central Oklahoma; (2) laboratory friction tests, using similar basement lithologies and stress conditions to our own analysis, conducted by Kolawole et al. (2019). In both laboratory and field observations, the failure strength of preexisting faults in Oklahoma was shown to be much lower than that of the intact basement, with lower friction coefficients around 0.6-0.75. Combined with the shear envelopes for intact basement rock reported in Figure 2.9, this data places new constraint on the in-situ stress state under which failure and potential earthquake nucleation may occur in Oklahoma.

The impact of fluid interaction on basement strength bares further discussion. With the exception of Granite B, samples saturated for a period of two days with de-ionized water show a noticeable reduction in UCS values (Figure 2.11). The degradation of rock

strength with even partial fluid saturation is a well-known phenomenon in geomechanics, with other researchers having observed similar water-weakening in granite (e.g., Lajtai et al., 1987; Lau et al., 1995; Masuda, 2001), rhyolite (Chang and Haimson, 2007) and diabase (Simpson and Fergus, 1968).

In our tests, considering that water has limited impact on the elastic moduli (Table 2.2), the effect of partial- to complete-saturation is predominantly in reducing the failure strength (Figure 2.10). The presence of water appears to lower the stress required for inelastic crack processes to occur (Wong et al., 2016). If the saturating fluid is primarily occupying preexisting flaws or microcracks in the basement rocks, then the fluid at the crack tips may be reducing the threshold stress required for propagation either by reducing the surface free energy or stress-corrosion processes (Atkinson and Meredith, 1981; Hawkins and McConnell, 1992; Dunning et al., 1994; Brantut et al., 2013). If so, it is feasible that failure strength in the crystalline basement may not be solely due to embrittlement and weakening associated with pore fluid pressurization.

2.4.2 Elastic and Inelastic Basement Properties

Using ultrasonic velocity measurements and known sample bulk density, the dynamic elastic moduli of a rock may be derived (Mavko et al., 2009). In particular, the dynamic Young's modulus (E_D) and Poisson's ratio (ν_D) may be found using the empirical relations:

$$E_D = \frac{\rho * V_S^2 * (3V_P^2 - 4V_S^2)}{V_P^2 - V_S^2} \quad (6)$$

$$\nu_D = \frac{V_P^2 - 2V_S^2}{2(V_P^2 - V_S^2)} \quad (7)$$

where V_P, V_S and ρ are the P-wave velocity, S-wave velocity and dry bulk density, respectively. However, rocks often respond differently to dynamic loading compared to static loading or direct deformation tests such that the dynamic elastic moduli determined often deviate from those determined under static loading conditions (Simmons and Brace, 1965; Cheng and Johnston, 1981). In Figure 2.11 we compare the average dynamic moduli values derived from the basement velocity tests with the values determined from the direct deformation or static tests (E_S and ν_S).

Though dynamic measurements do tend to be greater than those measured under static loading conditions, the trends of behavior with increasing confining pressure are consistent with the static measurements made here. The discrepancy between the static and dynamic measurements is not consistent though, as the static moduli at lower differential loads (i.e., 0.2) tend to approach the dynamic moduli only at greater confining pressures, while the static parameters at higher differential loads (i.e., 0.4) are more consistent with the dynamic measurements (Figure 2.12).

Young's moduli measured using both static and dynamic methods generally increase with increasing confinement, though mainly this occurs at lower differential stresses. Elevated confining pressure closes preexisting fractures and further suppresses the opening of microcracks which would otherwise decrease the rigidity of the rocks (Walsh and Grosenbaugh, 1979). At low differential stresses, the Young's moduli measured increase correspondingly with the increased confining pressure among each rock type. However, as differential loading increases the Young's moduli approach a narrower range of values that is largely unaffected by increased confining pressure (Figure 2.11)

Similar observations can be seen with the Poisson's ratio. ν at low differential loads appears to increase with confining pressure as well, but with greater mechanical loading each rock approaches a constant value regardless of confining condition. The impact of confining pressure on both static and dynamic Poisson's ratio is greatest at the lower pressures for the basement rocks. Considering the low porosity of igneous rocks (Table 2.1), the dynamic measurements suggest that above confining pressures of 20-30 MPa a majority of the open pore spaces and microcracks are closed, though the "true" closure pressure is expected to be in the range of 100 - 250 MPa for igneous rocks such as these (Kern, 1978).

As shown in Figure 2.6a, the mechanical behavior of a rock under increasing differential load is not constant prior to failure, commonly undergoing different stages of mechanical behavior during compression (Wawersik and Brace, 1971). At low differential loads, the strain is non-linear as the closure of open cracks and pore spaces dominates rock behavior. As stress increases, rock strain becomes quasi-linear as mechanical behavior is primarily elastic or recoverable strain. With continued stress application, rock strain becomes non-linear again as slow inelastic or non-recoverable fracture nucleation and propagation begins to dominate, until failure or strength loss occurs through coalescence of fractures in each rock. During each stage, the elastic properties of a rock vary as the stress state changes the proportions of elastic and inelastic damage. The deformation modulus, or the incremental slope of the axial stress-strain curve during deformation, is often shown to demonstrate how the elastic-inelastic behavior of a rock changes as mechanical loading continues.

Deformation moduli data at 0 and 52.5 MPa in Figure 2.12 demonstrate how the elastic parameters change both with increasing differential load and with confining pressure. Initially elastic moduli increase markedly with loading as crack closure occurs. Following this the deformation moduli incrementally degrades in a quasi-linear manner with increased loading where deformation is primarily elastic. Finally, the deformation moduli begin to decay rapidly as inelastic fracture propagation becomes dominant. This continues until the peak stress occurs and failure occurs. When confining pressure rises, the change due to crack closure is reduced, but the linear-elastic behavior remains relatively consistent with lower stress-states. This can explain why the static moduli exhibit the trends they do (Table 2.2, Figure 2.11). At low differential loads, cracks and pores are likely still open and some inelastic strain is still occurring. As loading increases, the rock's elastic behavior is controlled by the intrinsic mineralogy, which does not vary with increasing confining pressure at the conditions of the upper crust.

2.4.3 Field and Laboratory Data Comparison

Here we compare laboratory properties of the basement rocks tested with field data sets and common analogues of basement rocks. Using the aforementioned lithostatic and hydrostatic gradients, the velocity data up to 60 MPa are extrapolated to represent measurements up to ~3.4 km in Oklahoma's subsurface. While the average depth of the recent seismic activity in the region is 5-6 km, top basement is normally 1-3 km or shallower in Oklahoma, except in the vicinity of the Anadarko Basin in the west, and substantial seismicity has occurred at depths as shallow as 1.5 km (Crain and Chang, 2018).

The utility of ultrasonic velocity measurements and corresponding elastic parameters may be validated by examining existing well log data from the Oklahoma-

Kansas region. Few wells intersect basement rock in the region, but one prominent example is the Wah Zha Zhi No.1 well in Osage County of northern Oklahoma (Liner, 2015). Basement rock was reached at depths of approximately ~1.35 km, and sonic logs provide compressional and shear wave velocities for basement granite in the region, to depths of ~2.5 km. Average V_P and V_S in the crystalline basement were found to be 5900-6100 m/s and 3300-3500 m/s, respectively. Other examples are the Wellington wells drilled by the Kansas Geologic Survey in southern Kansas, which intersected granitic basement rock from 1.2 to 1.6 km depths. Sonic logs from through the granitic basement exhibit V_P and V_S ranges of 4500-6200 m/s and 2500-3300 m/s, respectively. The in-situ stresses of the basement in these wells are expected to be comparable to the basement tests reported here. Laboratory V_P and V_S of the granite samples measured in this study ranged from 4400-5800 m/s and 2700-3400 m/s, respectively (Figure 2.5).

To compare the field and laboratory elastic behavior, sonic and density logs from the Wah Zha Zhi and Wellington wells were used to derive the elastic moduli in the basement (Figure 2.13). Laboratory-measured dynamic properties were plotted versus depth and effective pressure as well, assuming the effective pressures at depth based on lithostatic and hydrostatic gradients of 27.5 and 10 MPa/km. Overall, laboratory and field measurements compare favorably. Poisson's ratio calculated from both logs were found to average 0.22-0.24, consistent with the values measured for both Granite A and B at 20 and 30 MPa confining pressures (Figure 2.12d). Conversely, granites in the Wah Zha Zhi well exhibited much greater Young's moduli than Granite A or B. Young's moduli derived from the Wellington log exhibited significant variation, with an average value of 66 GPa. These measurements are consistent with both laboratory-tested granites, particularly Granite A,

which at 20 and 30 MPa confining pressures were found to have dynamic Young's moduli ranging from 56-66 GPa. Our measurements are certainly on par with those the sonic data, particularly the Wellington data. The slightly greater velocities in the Wah Zha Zhi well can be attributed to the observation that basement penetrated in this region was microgranite (i.e., very fine-grained granite), whereas the Wellington log data was for a much coarser and fractured granite.

2.4.4 Implications for Igneous Basement in CEUS

Basement-focused seismicity in the continental interior of regions such as the United States (Horton, 2012; Keranen et al., 2014), Canada (Bao and Eaton, 2016), and India (Gupta et al., 2017) has become increasingly prominent within the last few decades. While of significant utility, geophysical and geomechanical models necessitate proper calibration of geomechanical parameters such as elastic moduli and mechanical strength to accurately assess basement structure and seismicity (Walsh and Zoback, 2016; Hemami and Ghassemi, 2018). This work, along with a few other relevant works (e.g., Katz et al., 2001; Carpenter et al., 2016; Yu, 2017), provides new insight into many of the physical properties that control the mechanical behavior of crystalline basement in the CEUS.

The experimental data here highlights not only the disparity between properties of individual basement components, but also what intrinsic characteristics affect mechanical behavior in the crystalline basement. Rock behavior is a function of numerous factors including porosity, microcracking, density, grain-size and fabric or textural orientation (Lockner and Beeler, 2002; Schön, 2015). The strength of intact basement rock most strongly correlates with grain-size and to a lesser extent lithology, consistent with the observation that grain-size acts as a constraint on fracture initiation and propagation in

crystalline rocks (Eberhardt et al., 1999). Conversely, the dynamic and static moduli measured in the basement suggest that elastic behavior is better related to the porosity or preexisting fractures (Table 2.1). Even among the mineralogically similar granites tested here, small variations such as increased microfractures can produce noticeable differences in the elastic response under different loading conditions. Under the microscope, Granite B samples show less fracturing than Granite A, as well as pervasive fracture healing and secondary mineral precipitation (Figure 2.3, Magnetite) in most existing fractures. Examination of Granite A reveals little fracture healing or mineralization with most fractures and cleavage planes remaining open. However, mechanical behavior is complex and likely the result of numerous intrinsic properties. The experimental data demonstrates that assumptions of the physical properties of basement rocks will significantly affect attempts predict in situ deformation behavior and structure (Laubach et al., 2009; Goswami et al., 2017).

Identifying zones of seismic hazard in the basement is often difficult, as factors such as in situ stress orientation and magnitude, fault structure, and pore pressure are rarely known. However, the strong contrast between the geomechanical properties of different rock types (e.g., granites, rhyolites, diabase) in contact may indicate regions of probable seismic rupture (Pei et al., 2018). Lithologic contacts, such as those in the basement and suggested by Shah and Keller (2017), with differences in stiffness, strength, and cohesion, are areas of stress concentration (Langer et al., 2014). The asymmetry of mechanical properties may enhance deformation in the more compliant fault block and alter the dynamics of earthquake rupture both at and adjacent to the mechanical boundary (Brietzke et al., 2009). This is supported by observations that (1) contrasts of elastic properties of

adjacent minerals and weak grain boundaries act as stress concentrators (Peng and Johnson, 1972) and (2) bimaterial contact surfaces produce radically different frictional responses (Logan and Teufel, 1986; Shadoan, 2019), suggesting a lithology may play a larger role in basement seismic response than previously assumed.

The impact of fluids on failure behavior also raises questions regarding the mechanisms of injection-induced seismicity in Oklahoma. The supposition that pore pressure changes or poroelastic effects are the main factors is complicated by the impact that fluids may contribute through stress-corrosion processes, which have previously been linked to many time-dependent observations of seismicity in the crust (Das and Scholz, 1981). Injection of fluid will likely reduce the prior threshold strength of subsurface structures over moderate geologic time-scales (Hickman et al., 1995), and could lead to incorrect assumptions of the impact of fluid infiltration in the subsurface. This is of even greater significance given that natural seismicity in intraplate regions has also been attributed to fluid migration in deformation zones (Thomas and Powell, 2017).

2.5 Conclusions

We have measured the ultrasonic velocity, elastic parameters, and compressive strength through laboratory experiments on granite, diabase and rhyolite components of the igneous basement in Oklahoma. This data provides new constraints on the geomechanics of the CEUS basement.

Velocity measurements show that V_P and V_S values increase with lithostatic pressure in the crystalline basement. The granitic terranes are far more compressible, and thus show greater velocity change with increased pressure. Dynamic elastic moduli for the basement rocks are of variable utility in light of the true values measured from deformation

tests. While values predicted for mafic dike material or extrusive rhyolite are relatively similar to static measurements, granitic rocks are more anisotropic due to fracture density and grain size heterogeneity, and may thus overestimate geomechanical properties of the basement.

Uniaxial and triaxial tests provide a constraint of basement strength in the subsurface to a depth of 6 km. Rock strength increases quasi-linearly with pressure, such that the Mohr-Coulomb envelope of the basement components may be determined. Coarse-grained granites fail in a more stable manner with increasing mechanical load, while fine-grained rocks are far more brittle and can accommodate little inelastic damage prior to fracture propagation and failure. Water-weakening was observed in uniaxial tests of three basement rock types. This may indicate that fluid-interaction can enhance basement rock embrittlement beyond what occurs through pore fluid pressurization.

Acknowledgements

This work has been previously published in the journal *Tectonophysics*, https://doi.org/10.1016/j.tecto.2020.228336.

References

Atkinson, Barry Kean, and Philip George Meredith. "Stress corrosion cracking of quartz: a note on the influence of chemical environment." Tectonophysics 77.1-2 (1981): T1-T11.

Bao, Xuewei, and David W. Eaton. "Fault activation by hydraulic fracturing in western Canada." Science 354.6318 (2016): 1406-1409.

Baud, Patrick, Teng-fong Wong, and Wei Zhu. "Effects of porosity and crack density on the compressive strength of rocks." International Journal of Rock Mechanics and Mining Sciences 67 (2014): 202-211.

Bickford, M. E., W. R. Van Schmus, K. E. Karlstrom, P. A. Mueller, and G. D. Kamenov. "Mesoproterozoic-trans-Laurentian magmatism: A synthesis of continent-wide age distributions, new SIMS U–Pb ages, zircon saturation temperatures, and Hf and Nd isotopic compositions." Precambrian Research 265 (2015): 286-312.

Bickford, M. E., and Richard D. Lewis. "U-Pb geochronology of exposed basement rocks in Oklahoma." Geological Society of America Bulletin 90.6 (1979): 540-544.

Brady, Barry HG, and Edwin T. Brown. Rock mechanics: for underground mining. Springer Science & Business Media, 2013.

Brantut, Nicolas, M. J. Heap, P. G. Meredith, and Patrick Baud. "Time-dependent cracking and brittle creep in crustal rocks: A review." Journal of Structural Geology 52 (2013): 17-43.

Brietzke, Gilbert B., Alain Cochard, and Heiner Igel. "Importance of bimaterial interfaces for earthquake dynamics and strong ground motion." Geophysical Journal International 178.2 (2009): 921-938.

Bruhn, Ronald L., William T. Parry, William A. Yonkee, and Troy Thompson. "Fracturing and hydrothermal alteration in normal fault zones." Pure and applied geophysics 142, no. 3-4 (1994): 609-644.

Carpenter, Brett M., Chance Morgan, David A. Lockner, and Ze'ev Reches. "Strength and stability of Oklahoma basement rock: Preliminary observations from experiments

at in-situ conditions." In AGU Fall Meeting Abstracts, vol. 2016, pp. S44C-06. 2016.

Chang, Chandong, and Bezalel Haimson. "Effect of fluid pressure on rock compressive failure in a nearly impermeable crystalline rock: implication on mechanism of borehole breakouts." Engineering Geology 89.3-4 (2007): 230-242.

Cheng, CoH, and David H. Johnston. "Dynamic and static moduli." Geophysical Research Letters 8, no. 1 (1981): 39-42.

Crain, Kevin D., and Jefferson C. Chang. "Elevation map of the top of the crystalline basement in Oklahoma and surrounding states." Oklahoma Geological Survey Open-File Report (2018): 1-2018.

Das, Sh, and C. H. Scholz. "Theory of time-dependent rupture in the Earth." Journal of Geophysical Research: Solid Earth 86, no. B7 (1981): 6039-6051.

Denison, R. E. "Basement rocks in the Arbuckle Mountains." In Ham, WE, Regional Geology of the Arbuckle Mountains, Oklahoma: Geological Society of America Annual Meeting, pp. 73-3. 1973.

Denison, Rodger E. "Basement rocks in northeastern Oklahoma." (1981).

Denison, R. "Rhyolites of Oklahoma." In Proceedings of the Oklahoma Academy of Science, vol. 39, pp. 124-126. 2015.

Dunning, J., B. Douglas, M. Miller, and S. McDonald. "The role of the chemical environment in frictional deformation: stress corrosion cracking and comminution." Pure and Applied Geophysics 143, no. 1 (1994): 151-178.

Dyke, C. G., and L. Dobereiner. "Evaluating the strength and deformability of sandstones." (1991): 123-134.

Eberhardt, E., B. Stimpson, and D. Stead. "Effects of grain size on the initiation and propagation thresholds of stress-induced brittle fractures." Rock mechanics and rock engineering 32.2 (1999): 81-99.

Ellsworth, William L. "Injection-induced earthquakes." Science. 341, no. 6142 (2013): 1225942.

Ellsworth, William L., Andrea L. Llenos, Arthur F. McGarr, Andrew J. Michael, Justin L. Rubinstein, Charles S. Mueller, Mark D. Petersen, and Eric Calais. "Increasing seismicity in the US midcontinent: Implications for earthquake hazard." The Leading Edge 34, no. 6 (2015): 618-626.

Frankel, Arthur. "Mapping seismic hazard in the central and eastern United States." Seismological Research Letters 66, no. 4 (1995): 8-21.

Ferrill, David A., Alan P. Morris, Ronald N. McGinnis, Kevin J. Smart, Sarah S. Wigginton, and Nicola J. Hill. "Mechanical stratigraphy and normal faulting." Journal of Structural Geology 94 (2017): 275-302.

Gilbert, M. C., and S. S. Hughes. "Partial chemical characterization of Cambrian basaltic liquids of the Southern Oklahoma Aulacogen." Petrology of the Cambrian Wichita Mountains igneous suite: Oklahoma Geological Survey Guidebook 23 (1986): 73-79.

Goebel, T. H. W., M. Weingarten, X. Chen, J. Haffener, and E. E. Brodsky. "The 2016 Mw5.1 Fairview, Oklahoma earthquakes: Evidence for long-range poroelastic triggering at> 40 km from fluid disposal wells." Earth and Planetary Science Letters 472 (2017): 50-61.

Goswami, Deepjyoti, Vyasulu V. Akkiraju, Surajit Misra, Sukanta Roy, Santosh K. Singh, Amalendu Sinha, Harsh Gupta, B. K. Bansal, and Shailesh Nayak. "Rock strength measurements on Archaean basement granitoids recovered from scientific drilling in the active Koyna seismogenic zone, western India." Tectonophysics 712 (2017): 182-192.

Gregory, A. R. "Fluid saturation effects on dynamic elastic properties of sedimentary rocks." Geophysics 41.5 (1976): 895-921.

Gupta, Harsh K., Kusumita Arora, N. Purnachandra Rao, Sukanta Roy, V. M. Tiwari, Prasanta K. Patro, H. V. S. Satyanarayana et al. "Investigations of continued reservoir triggered seismicity at Koyna, India." Geological Society, London, Special Publications 445, no. 1 (2017): 151-188.

Hawkins, A. B., and B. J. McConnell. "Sensitivity of sandstone strength and deformability to changes in moisture content." Quarterly Journal of Engineering Geology and Hydrogeology 25.2 (1992): 115-130.

Heap, M. J., and D. R. Faulkner. "Quantifying the evolution of static elastic properties as crystalline rock approaches failure." International Journal of Rock Mechanics and Mining Sciences 45.4 (2008): 564-573.

Hemami, Behzad, and Ahmad Ghassemi. "A Study of Basement Structures in Central Oklahoma with Reference to Seismicity." 52nd US Rock Mechanics/Geomechanics Symposium. American Rock Mechanics Association, 2018.

Hincks, Thea, Willy Aspinall, Roger Cooke, and Thomas Gernon. "Oklahoma's induced seismicity strongly linked to wastewater injection depth." Science 359, no. 6381 (2018): 1251-1255.

Hickman, Stephen, Richard Sibson, and Ronald Bruhn. "Introduction to special section: Mechanical involvement of fluids in faulting." Journal of Geophysical Research: Solid Earth 100.B7 (1995): 12831-12840.

Hogan, John P., and M. Charles Gilbert. "The Southern Oklahoma aulacogen: A Cambrian analog for Mid-Proterozoic AMCG (anorthosite-mangerite-charnockite-granite) complexes?." In Basement tectonics 12, pp. 39-78. Springer, Dordrecht, 1998.

Horton, Steve. "Disposal of hydrofracking waste fluid by injection into subsurface aquifers triggers earthquake swarm in central Arkansas with potential for damaging earthquake." Seismological Research Letters 83.2 (2012): 250-260.

International Society for Rock Mechanics. The complete ISRM suggested methods for rock characterization, testing and monitoring: 1974-2006. International Soc. for Rock Mechanics, Commission on Testing Methods, (2007).

Johnson, Kenneth S. "Geologic history of Oklahoma." Earth sciences and mineral resources of Oklahoma: Oklahoma Geological Survey Educational Publication 9 (2008): 3-5.

Johnson, Kenneth S. Geology of the southern Midcontinent. Oklahoma Geological Survey, 1989.

Katz, O., M. C. Gilbert, Z. Reches, and J. C. Roegiers. "Mechanical properties of Mount Scott granite, Wichita Mountains, Oklahoma." Oklahoma Geology Notes 61, no. 2 (2001): 28-34.

Katz, Oded, and Ze'ev Reches. "Microfracturing, damage, and failure of brittle granites." Journal of Geophysical Research: Solid Earth 109.B1 (2004).

Keranen, Katie M., Matthew Weingarten, Geoffrey A. Abers, Barbara A. Bekins, and Shemin Ge. "Sharp increase in central Oklahoma seismicity since 2008 induced by massive wastewater injection." Science 345, no. 6195 (2014): 448-451.

Kern, H. "The effect of high temperature and high confining pressure on compressional wave velocities in quartz-bearing and quartz-free igneous and metamorphic rocks." Tectonophysics 44, no. 1-4 (1978): 185-203.

Kibikas, W. M., B. M. Carpenter, and A. Ghassemi. "The petrophysical and mechanical properties of Oklahoma's crystalline basement." In 53rd US Rock Mechanics/Geomechanics Symposium. American Rock Mechanics Association, 2019.

Kolawole, F., C. S. Johnston, C. B. Morgan, J. C. Chang, K. J. Marfurt, D. A. Lockner, Z. Reches, and B. M. Carpenter. "The susceptibility of Oklahoma's basement to seismic reactivation." Nature Geoscience 12, no. 10 (2019): 839-844.

Labuz, J. F., and Luigi Biolzi. "Experiments with rock: remarks on strength and stability issues." International Journal of Rock Mechanics and Mining Sciences 44, no. 4 (2007): 525-537.

Lajtai, E. Z., R. H. Schmidtke, and L. P. Bielus. "The effect of water on the time-dependent deformation and fracture of a granite." In International Journal of Rock

Mechanics and Mining Sciences & Geomechanics Abstracts, vol. 24, no. 4, pp. 247-255. Pergamon, 1987.

Langer, Sebastian, Yaron Finzi, and Louise Marie Olsen-Kettle. "Dynamic triggering of earthquakes is promoted by crustal heterogeneities and bimaterial faults." Physics of the Earth and Planetary Interiors 238 (2015): 34-41.

Laubach, Stephen E., Jon E. Olson, and Michael R. Gross. "Mechanical and fracture stratigraphy." AAPG bulletin 93, no. 11 (2009): 1413-1426.

Lidiak, Edward G., and Rodger E. Denison. "Geology of the Blue River Gneiss, eastern Arbuckle Mountains, Oklahoma." In Basement Tectonics 13, pp. 139-153. Springer, Dordrecht, 1999.

Lidiak, Edward G., Rodger E. Denison, and Robert J. Stern. "Cambrian (?) mill creek diabase dike swarm, Eastern arbuckles: A glimpse of Cambrian rifting in the southern Oklahoma aulacogen." Oklahoma Geological Survey, Guidebook 38 (2014): 105-122.

Liner, Kevin Matthew. "An investigation of 3D seismic deep basement events in Osage County, Oklahoma." (2015).

Lockner, David A., and Nicholas M. Beeler. "Rock failure and earthquakes." International Geophysics Series 81, no. A (2002): 505-538.

Logan, John M., and L. W. Teufel. "The effect of normal stress on the real area of contact during frictional sliding in rocks." Pure and Applied Geophysics 124, no. 3 (1986): 471-485.

Martin, C. Derek. "Seventeenth Canadian geotechnical colloquium: the effect of cohesion loss and stress path on brittle rock strength." Canadian Geotechnical Journal 34, no. 5 (1997): 698-725.

Masuda, Koji. "Effects of water on rock strength in a brittle regime." Journal of Structural Geology 23, no. 11 (2001): 1653-1657.

Mattaboni, Paul, and Edward Schreiber. "Method of pulse transmission measurements for determining sound velocities." Journal of Geophysical Research 72, no. 20 (1967): 5160-5163.

Mavko, Gary, Tapan Mukerji, and Jack Dvorkin. The rock physics handbook. Cambridge university press, 2020.

McGarr, Arthur. "Maximum magnitude earthquakes induced by fluid injection." Journal of Geophysical Research: solid earth 119, no. 2 (2014): 1008-1019.

Nicksiar, Mohsen, and C. D. Martin. "Factors affecting crack initiation in low porosity crystalline rocks." Rock mechanics and rock engineering 47, no. 4 (2014): 1165-1181.

Northcutt, Robert A., and Jock A. Campbell. "Geologic provinces of Oklahoma." In Basement Tectonics 12, pp. 29-37. Springer, Dordrecht, 1998.

Paterson, Mervyn S., and Teng-fong Wong. Experimental rock deformation-the brittle field. Springer Science & Business Media, 2005.

Peng, S., and A. M. Johnson. "Crack growth and faulting in cylindrical specimens of Chelmsford granite." In International Journal of Rock Mechanics and Mining Sciences & Geomechanics Abstracts, vol. 9, no. 1, pp. 37-86. Pergamon, 1972.

Schön, Jürgen H. Physical properties of rocks: Fundamentals and principles of petrophysics. Elsevier, 2015.

Segall, Paul, and S. Lu. "Injection-induced seismicity: Poroelastic and earthquake nucleation effects." Journal of Geophysical Research: Solid Earth 120, no. 7 (2015): 5082-5103.

Shadoan, Tanner. "Seismic Radiation During Slip Along Bi-material Faults: An Experimental Investigation." (2019).

Shah, Anjana K., and G. Randy Keller. "Geologic influence on induced seismicity: Constraints from potential field data in Oklahoma." Geophysical Research Letters 44, no. 1 (2017): 152-161.

Simmons, Gene, and William F. Brace. "Comparison of static and dynamic measurements of compressibility of rocks." Journal of Geophysical Research 70, no. 22 (1965): 5649-5656.

Simpson, Dale R., and John H. Fergus Jr. "The effect of water on the compressive strength of diabase." Journal of Geophysical Research 73, no. 20 (1968): 6591-6594.

Skoumal, Robert J., Michael R. Brudzinski, and Brian S. Currie. "Proximity of Precambrian basement affects the likelihood of induced seismicity in the Appalachian, Illinois, and Williston Basins, central and eastern United States." Geosphere 14, no. 3 (2018): 1365-1379.

Thomas, William A., and Christine A. Powell. "Necessary conditions for intraplate seismic zones in North America." Tectonics 36, no. 12 (2017): 2903-2917.

Van Schmus, W. R., M. E. Bickford, P. K. Sims, R. R. Anderson, C. K. Shearer, and S. B. Treves. "Proterozoic geology of the western midcontinent basement." Precambrian: Conterminous USA Geological Society of America, Boulder, Colo., Geology of North America 2 (1993): 239-258.

Walsh III, F. Rall, and Mark D. Zoback. "Probabilistic assessment of potential fault slip related to injection-induced earthquakes: Application to north-central Oklahoma, USA." Geology 44, no. 12 (2016): 991-994.

Walsh, J. B., and M. A. Grosenbaugh. "A new model for analyzing the effect of fractures on compressibility." Journal of Geophysical Research: Solid Earth 84, no. B7 (1979): 3532-3536.

Wawersik, W. R., and W. F. Brace. "Post-failure behavior of a granite and diabase." Rock mechanics 3, no. 2 (1971): 61-85.

Wong, Louis Ngai Yuen, Varun Maruvanchery, and Gang Liu. "Water effects on rock strength and stiffness degradation." Acta Geotechnica 11, no. 4 (2016): 713-737.

Wyllie, Malcolm Robert Jesse, Alvin Ray Gregory, and Louis Wright Gardner. "Elastic wave velocities in heterogeneous and porous media." Geophysics 21, no. 1 (1956): 41-70.

Yu, Weiqi. "Laboratory Geomechanical Characterization of the Arbuckle Group and Crystalline Basement Rocks in Oklahoma." (2017).

Yun, Tae Sup, Franco Matias Francisca, J. Carlos Santamarina, and Carola Ruppel. "Compressional and shear wave velocities in uncemented sediment containing gas hydrate." Geophysical Research Letters 32, no. 10 (2005).

CHAPTER II FIGURES

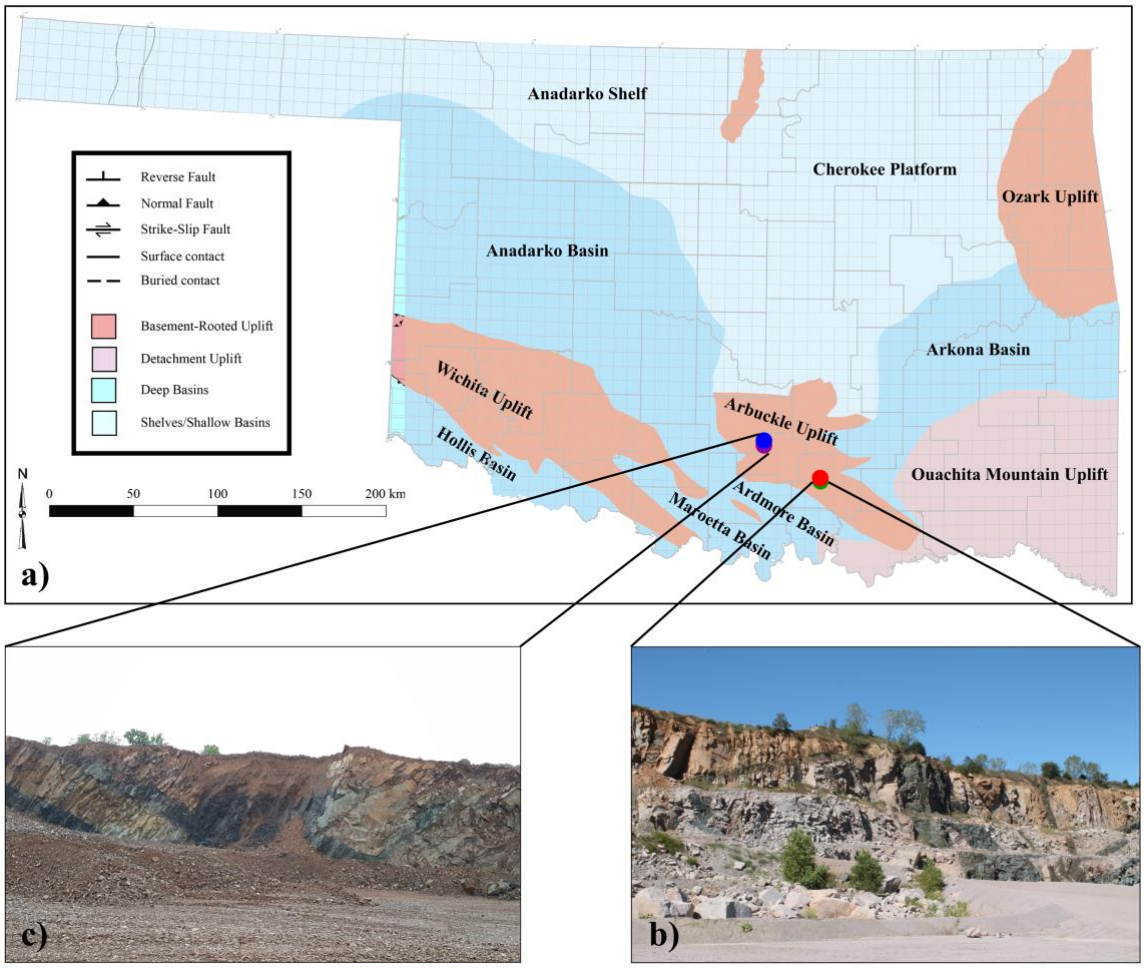

Figure 2.1: Lithologic map of surface geology in Oklahoma (a) (adapted from Northcutt and Campbell, 1998), with locations of Mill Creek Quarry (b) and Davis Quarry (c) where samples were procured.

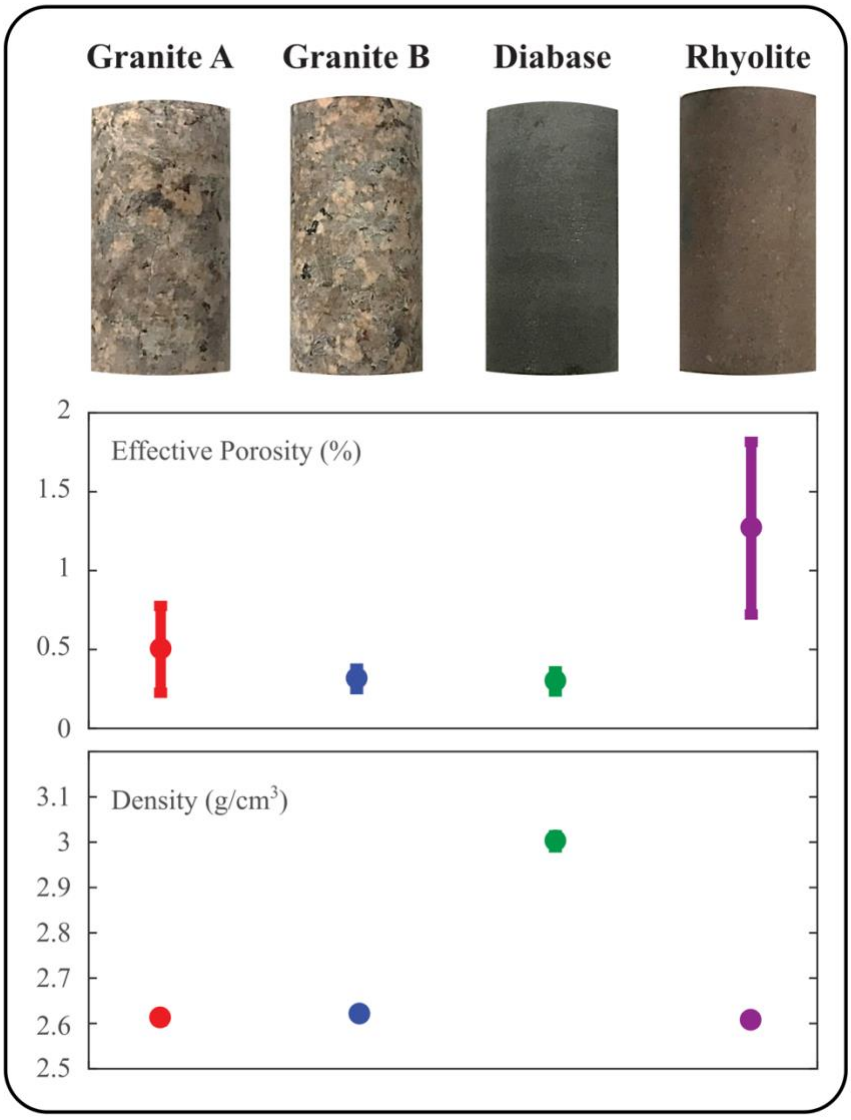

Figure 2.2: Representative basement samples (top) and measured bulk characteristics (bottom). Effective porosity (measured through saturation method (ISRM 2007)) and bulk dry density of rock types are displayed beneath each rock sample.

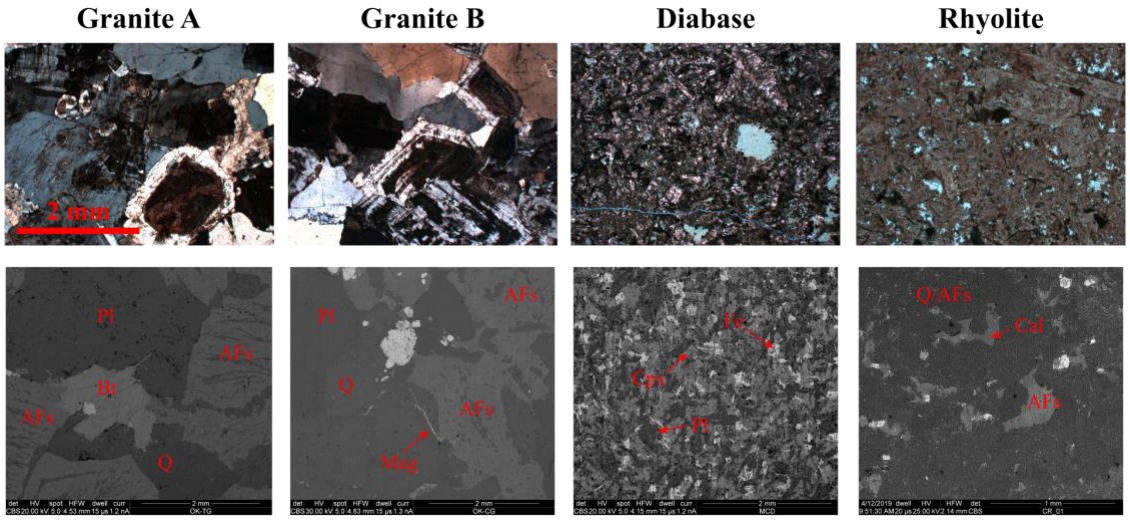

Figure 2.3: Photomicrographs and SEM images of basement rocks tested here. Q = quartz; AFs = alkali feldspar; Pl = plagioclase; Bt = biotite; Mag = magnetite; Cpx = clinopyroxene; Fe = iron oxide; Cal = calcite.

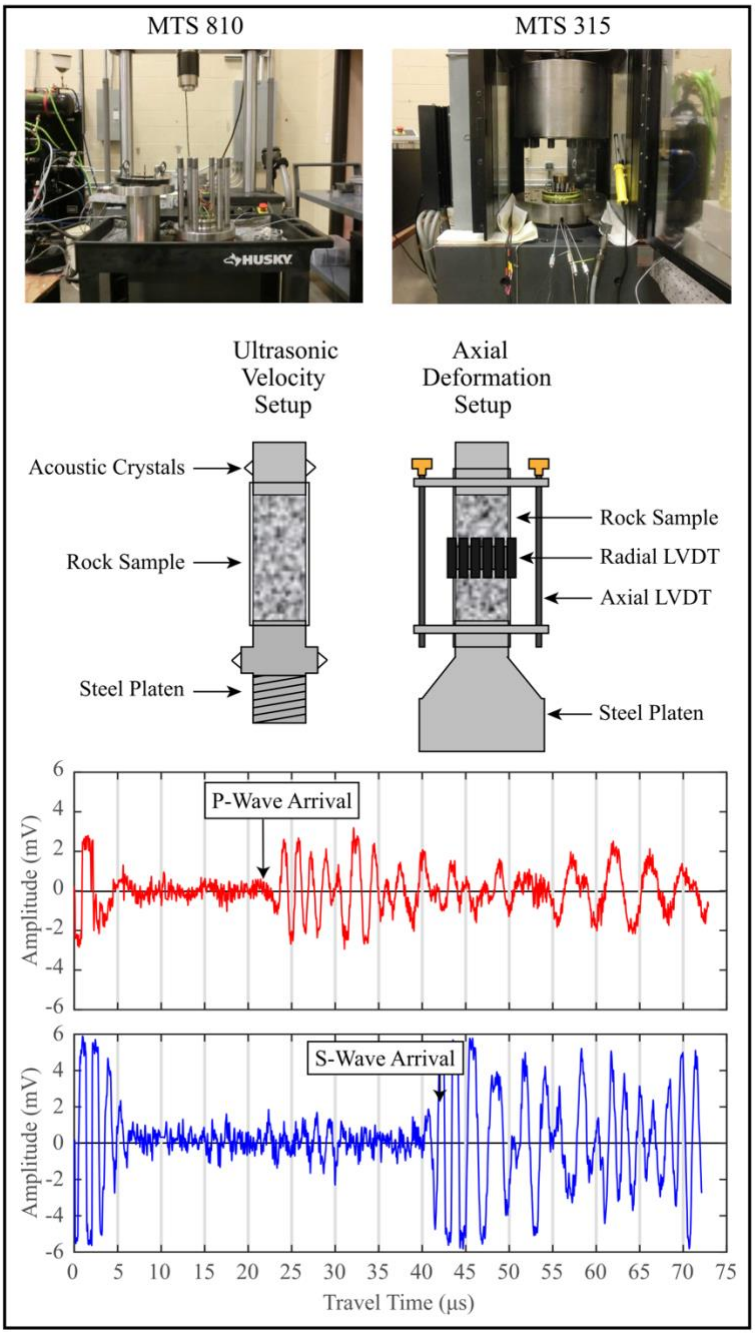

Figure 2.4: MTS frames used and setup schematic for ultrasonic velocity and axial deformation tests. Examples of P- and S-waveforms generated in red and blue, respectively.

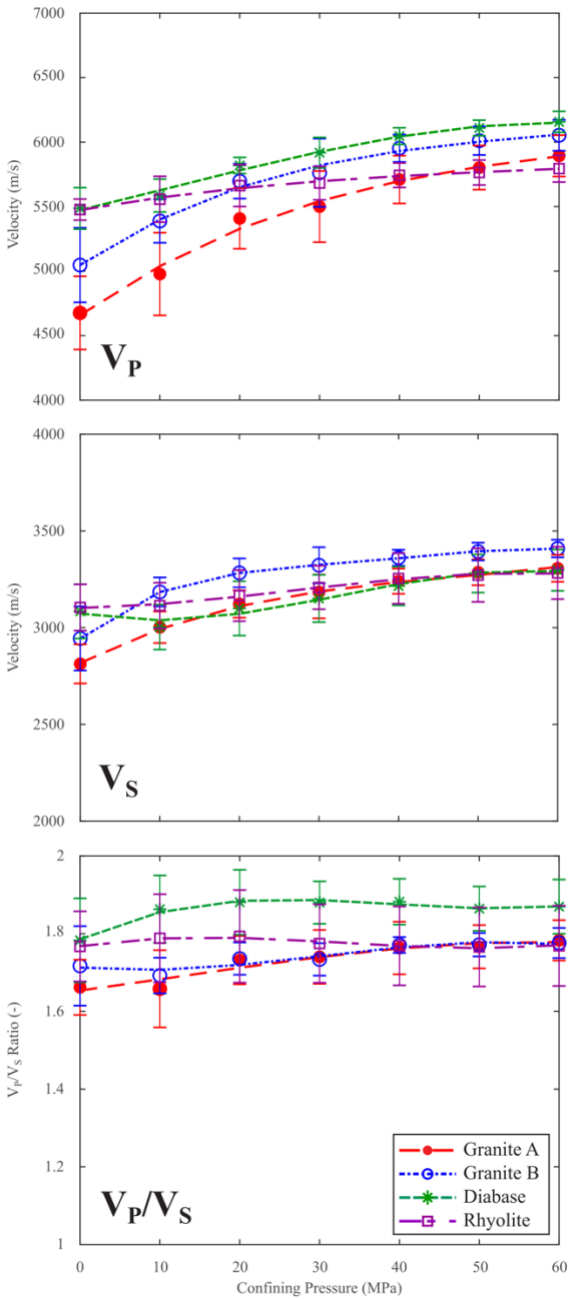

Figure 2.5: Variation in compressional (V_P) and shear wave (V_S) velocities loaded hydrostatically from 0 to 60 MPa. Points indicate average velocity measured at each condition. Curves are polynomial fits of average V_P and V_S for each rock type. Error bars show ± 1 standard deviation of the average velocity.

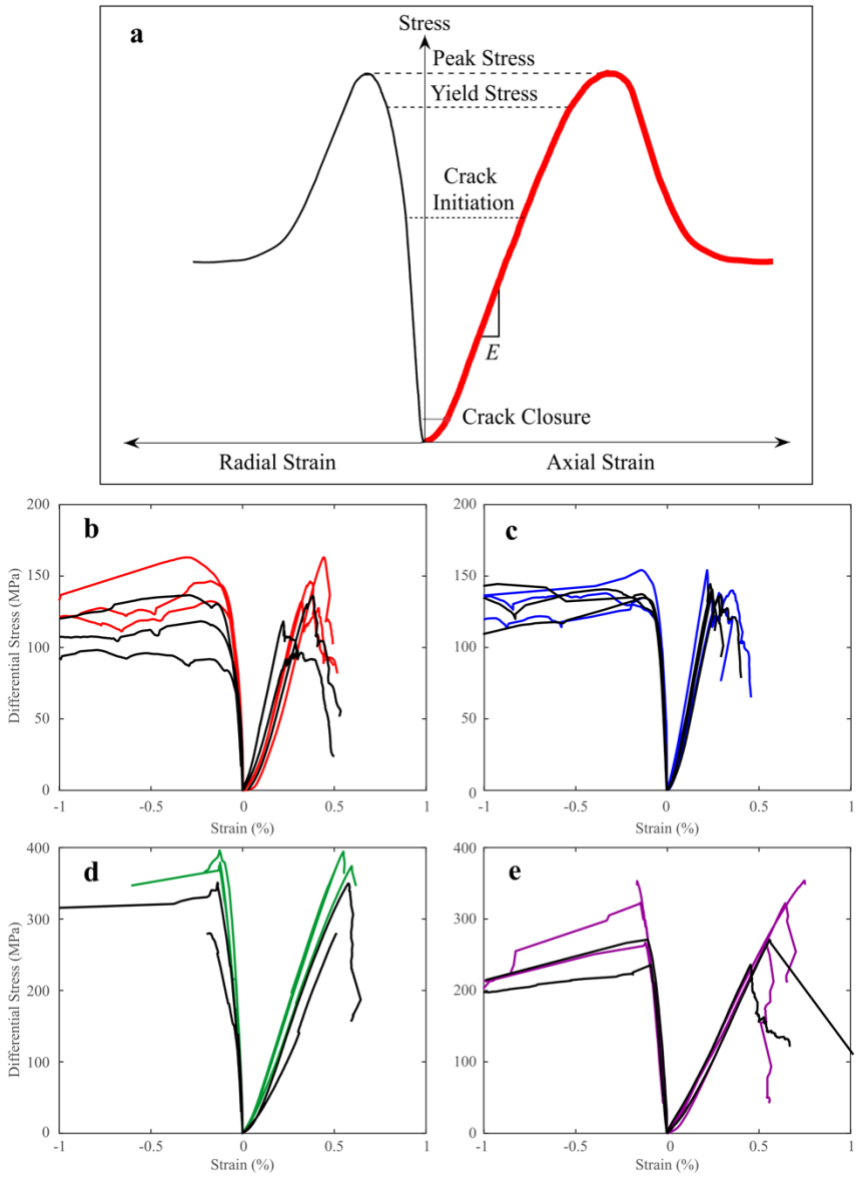

Figure 2.6: a) Schematic of axial and radial strain with data indicating key deformation characteristics such as the crack closure, initiation, yield and failure stresses, as well as the Young's modulus *E* (see Martin (1997) for more detail). Deformation data for uniaxial compressive tests of b) Granite A, c) Granite B, d) diabase, and e) rhyolite are displayed below. Colored lines represent tests under room dry conditions, while black lines represent tests of water-saturated samples.

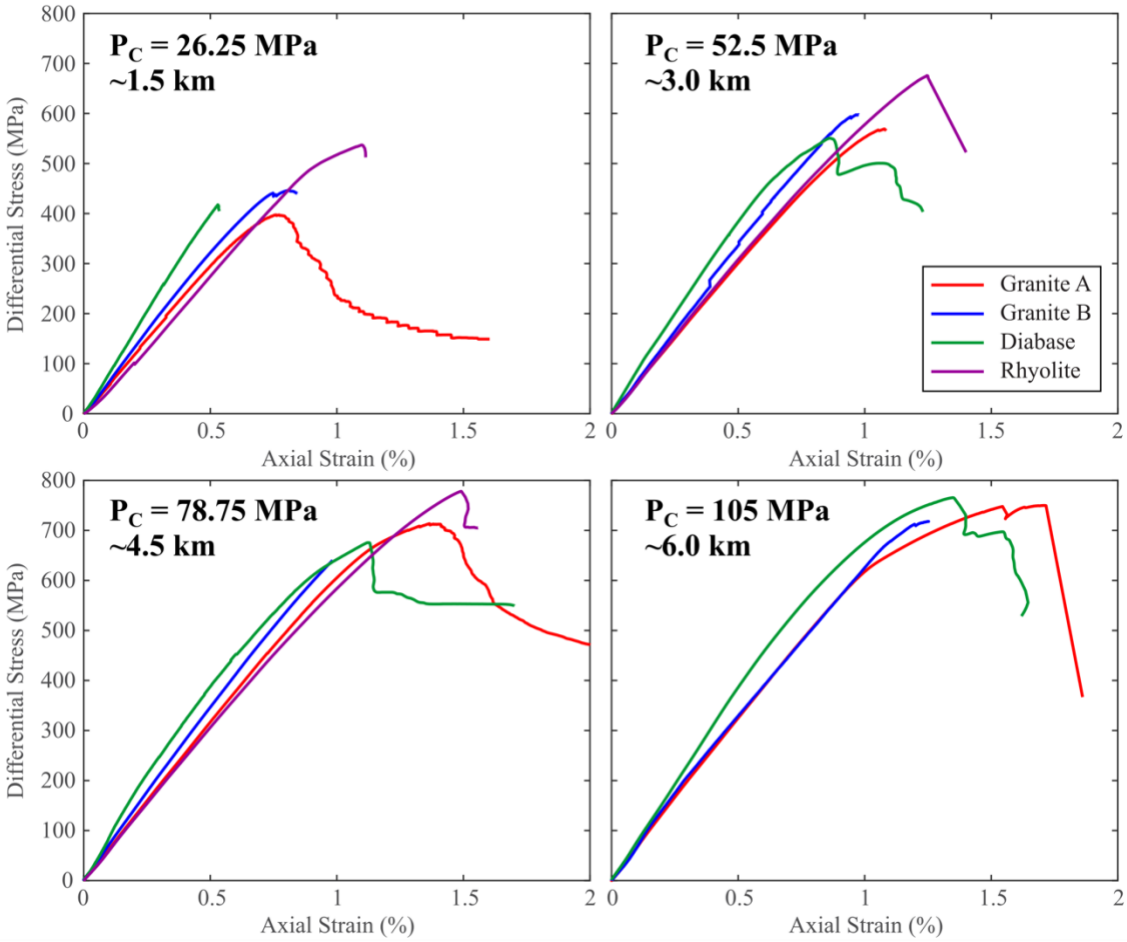

Figure 2.7: Axial strain data for basement samples deformed under confined conditions. Deformation tests were conducted until steady state stress was reached or complete sample failure occurred.

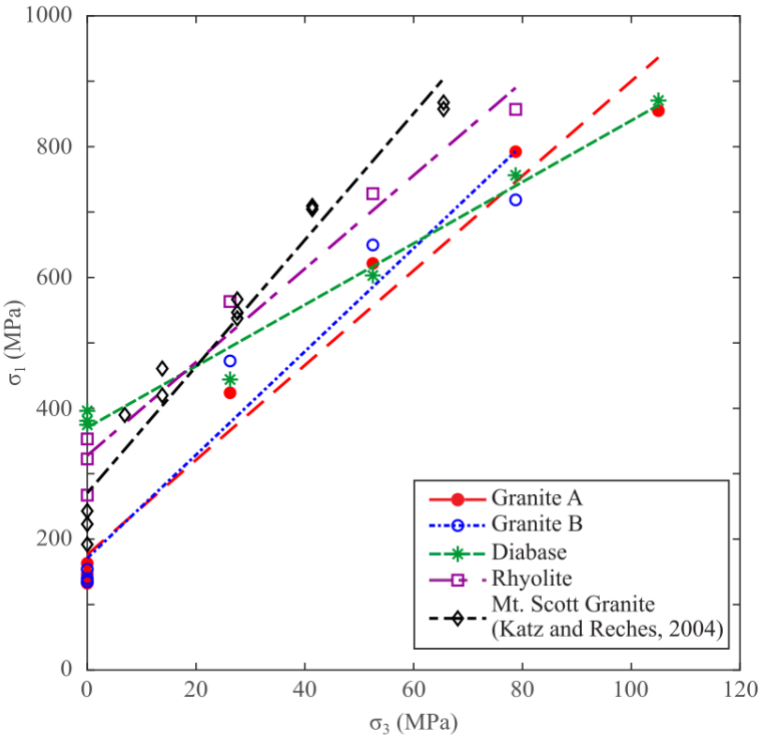

Figure 2.8: Maximum and minimum stresses of basement rocks during failure. Linear regression of strength data shows the evolution of basement strength with increasing confining pressure.

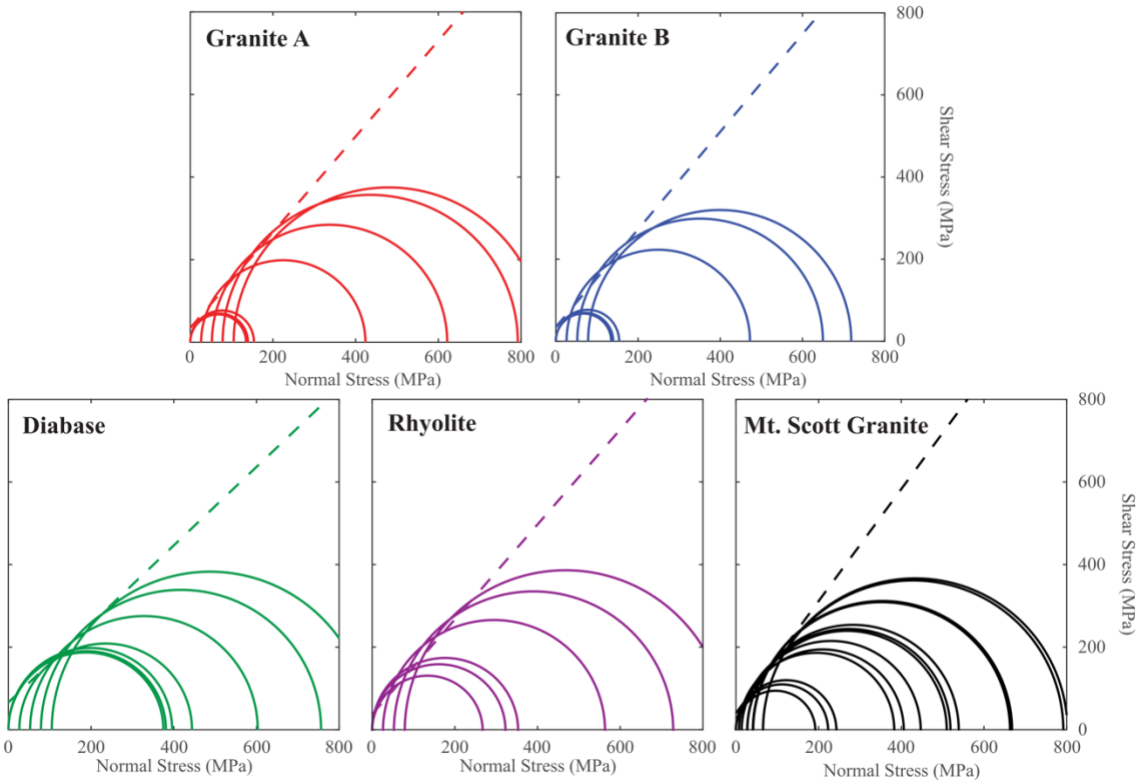

Figure 2.9: Mohr-Coulomb failure envelopes extrapolated from maximum and minimum compressive stresses at failure in Figure 2.8. Envelopes derived from Equation (1) are plotted in each with dashed lines. Granitic samples have higher friction angles but lower cohesion than the finer-grained diabase or rhyolite.

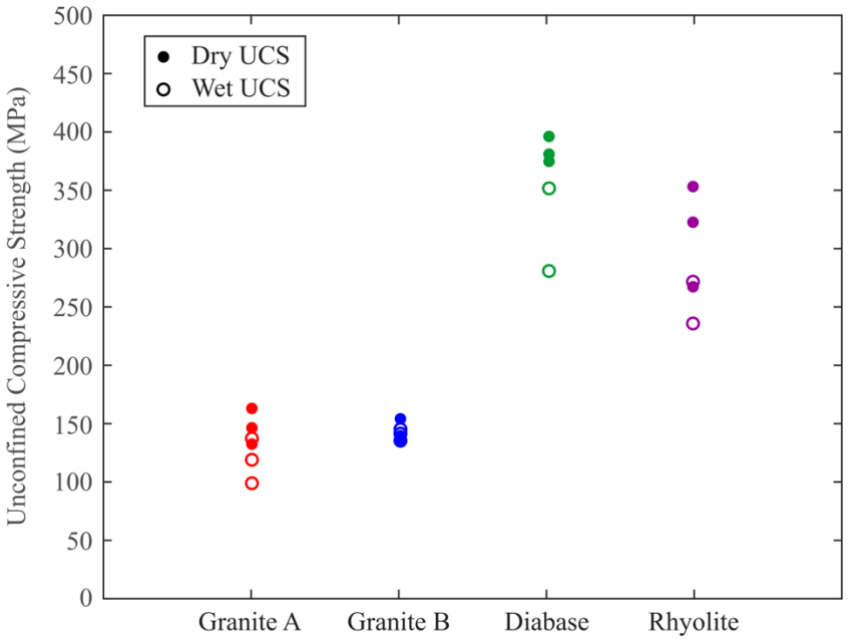

Figure 2.10: UCS values for basement samples deformed in both dry and wet conditions.

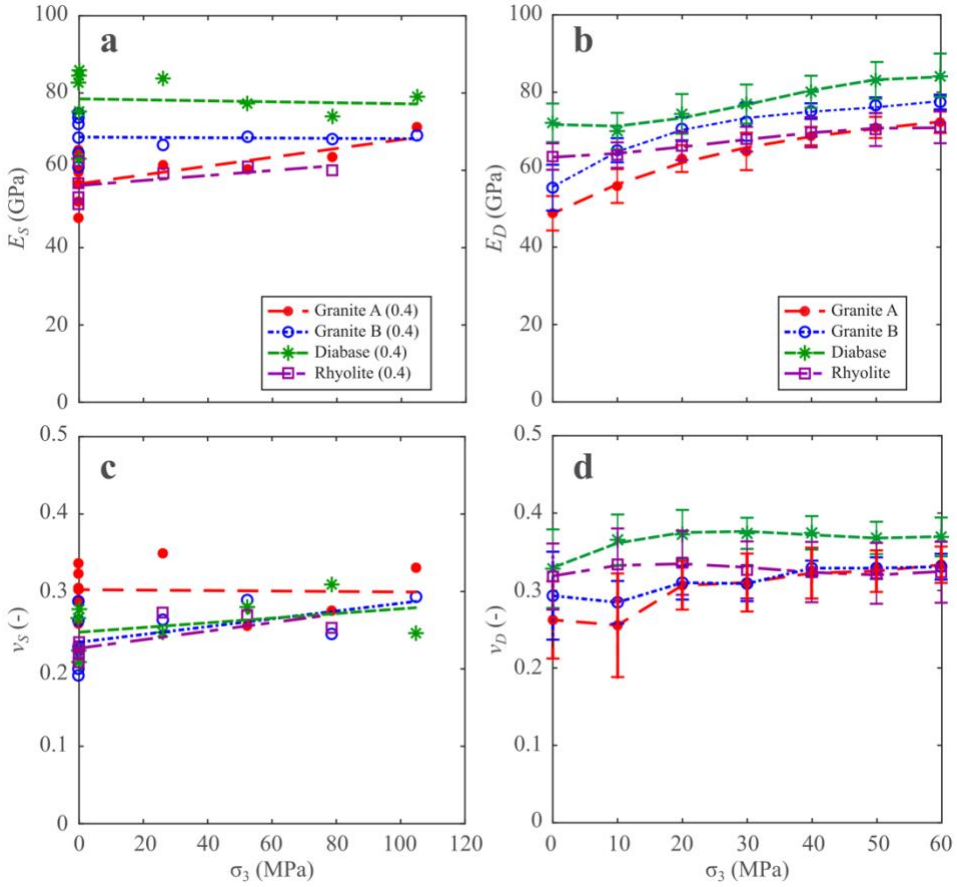

Figure 2.11: Data for static Young's modulus (a), dynamic Young's modulus (b), static Poisson's ratio (c), and dynamic Poisson's ratio (d) against least principal stress (P_c). Only static moduli values measured at 0.4 of failure stress are plotted against dynamic measurements.

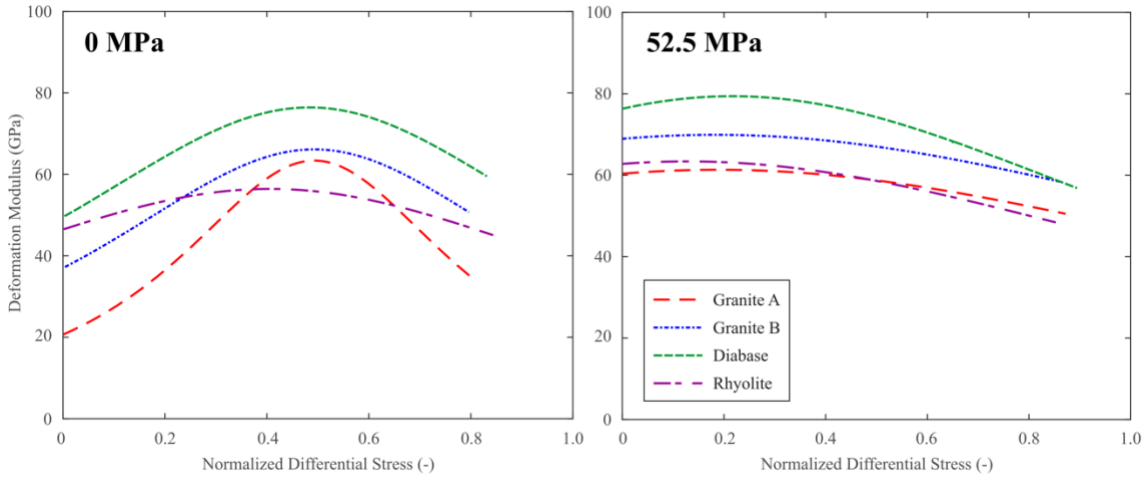

Figure 2.12: Deformation modulus of samples deformed uniaxially (left) and at 52.5 MPa confining pressure (right). Degradation of elastic moduli with increasing differential stress can give an approximation of the relative proportions of elastic and inelastic damage in each rock mass.

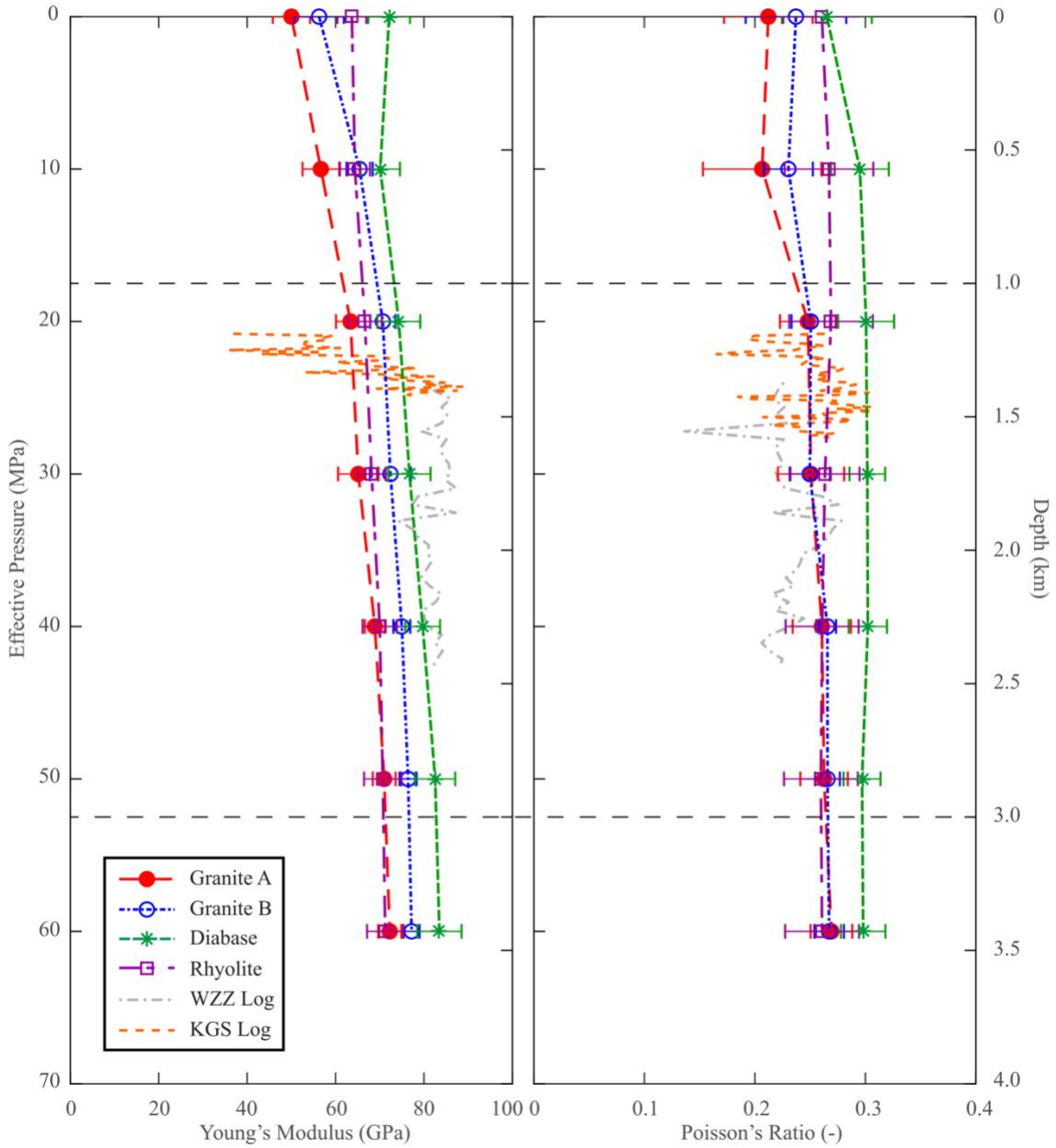

Figure 2.13: Dynamic Young's modulus and Poisson's ratio calculated from laboratory tests and sonic log data from Wah Zha Zhi and Wellington wells. Effective pressure and depth are approximated based on the assumed lithostatic and hydrostatic gradients of 27.5 and 10 MPa/km. Log data for Wah Zha Zhi and Wellington wells made available by Spyglass Energy Group LLC and the Kansas Geological Survey, respectively.

CHAPTER II TABLES

Rock Type	Bulk Density (g/cm^3)	Effective Porosity (%)	Location
Granite A	2.604 ± 0.006	0.506 ± 0.278	Mill Creek, Oklahoma
Granite B	2.620 ± 0.005	0.301 ± 0.065	Davis, Oklahoma
Diabase	3.001 ± 0.013	0.317 ± 0.064	Mill Creek, Oklahoma
Rhyolite	2.621 ± 0.005	1.288 ± 0.529	Davis, Oklahoma

Table 2.1: Bulk rock information for basement specimens evaluated in this study. All values are reported with ± 1 standard deviation.

	Sample	Condition	P_c (MPa)	σ_f (MPa)	$E_{0.2}$ (GPa)	$E_{0.4}$ (GPa)	$\nu_{0.2}$ (-)	$\nu_{0.4}$ (-)
Granite A	TG_01	Dry	0	163.06	34.89	56.23	0.14	0.32
	TG_07	Dry	0	146.40	36.87	59.37	0.12	0.26
	TG_24	Dry	0	132.51	35.20	59.77	0.09	0.29
	TG_04	Wet	0	118.31	49.80	65.07	0.08	0.34
	TG_27	Wet	0	136.61	36.52	51.75	0.18	0.30
	TG_28	Wet	0	98.21	34.68	47.52	0.03	0.30
	TG_15	Dry	26.25	397.41	61.52	61.16	0.29	0.35
	TG_17	Dry	52.50	569.00	61.34	60.09	0.21	0.25
	TG_18	Dry	78.75	713.55	64.07	63.29	0.24	0.27
	TG_19[a]	Dry	105.00	749.94	65.23	71.02	0.26	0.33
Granite B	CG_01	Dry	0	154.13	63.50	74.63	0.08	0.26
	CG_17	Dry	0	134.89	50.91	60.69	0.11	0.19
	CG_21	Dry	0	139.64	51.34	64.30	0.14	0.20
	CG_03	Wet	0	144.49	51.98	71.82	0.18	0.29
	CG_20	Wet	0	134.68	44.44	68.29	0.12	0.23
	CG_22	Wet	0	140.69	57.84	73.45	0.18	0.22
	CG_15	Dry	26.25	446.16	68.04	66.40	0.22	0.26
	CG_11	Dry	52.50	597.26	69.91	68.52	0.22	0.29
	CG_12	Dry	78.75	639.91	70.33	67.91	0.21	0.24
	CG_16[b]	Dry	105.00	752.00	71.60	68.89	0.26	0.29
Diabase	MCD_08	Dry	0	374.76	64.51	75.27	0.15	0.22
	MCD_14	Dry	0	396.08	76.00	84.25	0.16	0.21
	MCD_11	Dry	0	380.93	74.74	84.64	0.18	0.25
	MCD_04	Wet	0	280.07	46.00	62.96	0.13	0.28
	MCD_12	Wet	0	350.91	64.21	82.47	0.15	0.27
	MCD_05	Dry	26.25	417.80	82.18	83.70	0.22	0.25
	MCD_06	Dry	52.50	550.61	79.38	77.11	0.27	0.28
	MCD_09	Dry	78.75	677.56	83.85	73.83	0.28	0.31
	MCD_10	Dry	105.00	765.53	78.61	78.89	0.24	0.25
Rhyolite	CR_03	Dry	0	353.17	53.52	56.42	0.19	0.23
	CR_07	Dry	0	322.63	50.37	62.21	0.21	0.23
	CR_09	Dry	0	267.28	46.25	51.07	0.16	0.23
	CR_11	Wet	0	270.89	45.24	56.59	0.13	0.22
	CR_12	Wet	0	235.10	47.73	52.82	0.19	0.21
	CR_04	Dry	26.25	537.03	55.73	59.09	0.16	0.27
	CR_05	Dry	52.5	675.68	63.19	60.72	0.26	0.27
	CR_06	Dry	78.75	778.20	62.11	59.91	0.22	0.25

Table 2.2: Strength and deformation properties of Granite A (TG), Granite B (CG), diabase (MCD) and rhyolite (CR). P_c and σ_f are the confining pressure and maximum differential stress during sample deformation. $E_{0.2}$, $E_{0.4}$, $\nu_{0.2}$, $\nu_{0.4}$ are the Young's moduli and Poisson's ratio measured at 0.2 and 0.4 of the failure stress. a – during TG_19 test, radial LVDT data above ~600 MPa was not valid as strain data experienced anomalous dilation behavior. b – value is the maximum strength recorded during deformation of CG_16, but higher differential stresses were not recorded, so value is not the peak strength.

Rock Type	C (MPa)	φ (degrees)
Granite A	32.8	49.2
Granite B	30.4	50.8
Diabase	85.5	40.4
Rhyolite	61.3	49.0

Table 2.3: Numerically derived strength parameters for basement rock tests from Equations (4) and (5).

CHAPTER III: DEVELOPING A 1D VELOCITY MODEL OF THE CONTINENTAL BASEMENT UTILIZING ULTRASONIC VELOCITY MEASUREMENTS

3.1 Introduction

Seismic exploration is a crucial tool for understanding the subsurface, which is largely inaccessible to direct observation and characterization. An essential component of this is the construction of an appropriate velocity model. Such models are often used for seismic applications such as stacking, time migration, depth migration, and lithological property identification (Schultz, 1998). 1D velocity models are commonly utilized to identify the source characteristics of earthquakes, including their hypocenters and origin times, and are useful for developing more complex 2D and 3D velocity models (Kisslinger et al., 1994). Ideally, a velocity model would be constructed with direct velocity measurements such as from sonic log data (Maxwell, 2014). Due to data scarcity, velocity models are more commonly constructed through indirect observation of the reflection/refraction of seismic waves in the subsurface.

Given the importance of such models, numerous techniques, including full-waveform inversion (Brossier et al., 2015), migration velocity analysis (Al-Yahya, 1989), and seismic tomography (Asnaashari et al., 2013), have been developed to produce velocity models that may characterize the subsurface. Each method for velocity model building is limited by the criterion for assessing each model and the assumptions made about subsurface structure (Duveneck, 2004). However, a key factor in a model's accuracy is the incorporation of plausible geophysical or geological features (Asnaashari, 2013). Such

"prior information" can help to constrain seismic velocity data and converge on the optimal velocity model (Schultz, 1998).

In the last decade, a dramatic surge in seismicity occurred in the intraplate regions of Oklahoma and Kansas. Geophysical analyses have revealed that the overwhelming majority of seismic events were concentrated in the crystalline basement of these regions rather than the overlying sedimentary strata. Consequently, this surge in seismicity has brought renewed interest in improving the geophysical characterization of the deep crystalline basement in the central US. Unfortunately, there exists little direct characterization of velocity in the crystalline basement (Kibikas et al., 2020; Kolawole et al., 2020), so the majority of 1D and 3D velocity models utilized for the earthquake location in the region have primarily relied on velocity models that require significant assumptions and simplifications of basement physical properties and geometry (Keranen et al., 2014; Darold et al., 2015; Chen, 2016; Marsh, 2018; Walter et al., 2020). This is problematic for a number of reasons: 1) the top basement topography has been shown to be remarkably heterogeneous throughout the region (e.g., Crain and Chang, 2018); 2) the basement has been shown to display significant lateral heterogeneity both in structure and lithology (e.g Toth, 2014; Boak et al., 2016; Shah and Keller, 2017); 3) the models are inherently biased towards the basement structure in the north-central Oklahoma and south-central Kansas regions where seismicity has been predominant and may not reflect the true broader regional velocity structure, with the possible exception of the model discussed by Toth, 2014.

This work provides new insight into the velocity structure within the crystalline basement of Oklahoma and Kansas. Laboratory experimental methods were used to

measure the ultrasonic velocities of vertically-oriented basement rocks from outcrops and boreholes. These datasets, along with existing ultrasonic velocity measurements and sonic log data for the region, were used compared with existing 1D and 3D velocity models developed from seismic wave propagation across the region. The work has two main purposes: providing new information for the vertically-oriented velocity in the upper crust for calibrating seismic models and illustrating the lateral heterogeneity of the basement in the central US.

3.2 Methods

3.2.1 Basement Rocks

Basement rocks in this study were obtained from both surface outcrops and basement penetrating wells in Oklahoma and Kansas. Though the basement top is rarely exposed at the surface, there are a few relatively small outcrops in south-central, southwest, northeast Oklahoma. We obtained the Mill Creek cores from the large outcrop in the Arbuckle Mountains region (Kolawole et al., 2019), while we obtained the Spavinaw cores from a small outcrop in northeastern Oklahoma (Benson, 2014). Cores were also provided from basement penetrating wells included the KGS 1-32 Wellington well in southern Kansas, the Jones-46 well in northeastern Oklahoma, and the Frisco Railroad well in southern Oklahoma (Figure 3.1b).

The KGS samples are coarse-grained granite composed of plagioclase and quartz, with relatively lower alkali feldspar. Macro- and microfractures are well cemented with calcite. Pervasive titanite, pyrite, and iron-oxide content, along with calcite cementation, suggest extensive alteration by fluid infiltration. The Jones-46 material is a very fine-grained rhyolite with extensive and heterogeneous phenocrysts. The matrix is dominantly

quartz and alkali feldspar, with minor plagioclase, calcite, biotite, chlorite, apatite content. Phenocryst size is highly variable throughout the rhyolite cores; they are mainly quartz or alkali feldspar that often displays perthitic texture. The Frisco Railroad core is a very coarse-grained granite (>2 mm) with a typical quartz and feldspar content. Trace minerals include biotite, barite, titanite, and chlorite. Although fractures are sparse throughout the granite, alteration of biotite to chlorite and epidote suggest the rock has experienced periodic fluid infiltration. The Mill Creek material is a very coarse and highly fractured granite. Though dominantly composed of quartz and alkali feldspar, biotite content is extensive and displays frequent alteration to chlorite and iron-oxide. The rock has been extensively fractured and weathered due to surface exposure at the outcrop. The Spavinaw material is a fine-to-medium grained granite, with a micrographic texture of quartz, alkali and potassium feldspar. The main accessory minerals are magnetite and biotite, but the rock has been heavily altered to produce chlorite, titanite, rutile and iron-oxide. Fractures are sparse but dominantly sealed by chlorite.

For the velocity tests, samples were cored parallel to the vertical direction from both the outcrop and borehole materials. Cylindrical specimens with 25.4 and 38.1 mm diameters were ground at the top and bottom to parallel (<.01 mm). 38.1 mm samples were further polished into octagonal prisms for the experimental setup (Figure 3.2). Sample dimensions were measured and recorded in Table 3.1.

3.2.2 Vertical Velocity Testing

All specimens were dried at ~50 ºC for >24 hours prior to testing. Two types of setups were used for measuring the vertical velocities in the basement rocks. All rocks were tested under a hydrostatic stress state (i.e., $\sigma_1 = \sigma_2 = \sigma_3$). In the first setup, ultrasonic

velocities were measured from ambient conditions (~0 MPa) to 60 MPa using the pulse transmission technique. Samples were placed between steel two endcaps with mounted P- and S-wave piezoelectric crystals (resonant frequency 250 kHz). To measure velocity, a pulse (with a frequency of 500 kHz) was passed through each sample parallel to the long axis. The received waveforms were recorded with an external oscilloscope (Keysight Technologies 33500B Series Waveform Generator). At ambient conditions, velocities were recorded with the use of a benchtop vice. After being recorded, samples were jacketed and placed into a pressure vessel (MTS 810, see Kibikas et al., 2020). Pressure was then increased hydrostatically in increments of 10 MPa, recording the P- and S-wave velocities (V_P and V_S) at each increment, then unloaded after reaching 60 MPa. Because S-wave crystals are aligned parallel to one another, each sample was then rotated 90º from its previous orientation with the steel endcaps. Velocities were again measured for each sample from 0 to 60 MPa to observe the change in vertical velocity depending upon orientation (Figure 3.3).

For the second setup, the octagonal samples were coated with honey as a coupling medium. Each sample was then loaded into a Three-Dimensional Ultrasonic Velocity Test System (see Lee et al., 2019 for further details). Ten rams, one for each sample face, are placed against the sample faces and pressurized via a series of external syringe pumps to apply stress to each face. Pressure was increased hydrostatically in increments of 10 MPa up to 60 MPa. Three piezoelectric crystals, one P-wave and a pair of orthogonally oriented S-wave crystals, were mounted on each ram for measuring the velocities in each orientation of the sample. To measure the ultrasonic velocity, an electric signal generated at pulse (with a frequency ~1 MHz) each source face that traveled through the sample and was received

at the opposite sample face. The corresponding P- and S-wave signals were recorded with an external oscilloscope. Although the velocities were measured along the horizontal specimen faces, that data is beyond the scope of this work and will be reported in a future work (Figure 3.3).

Ultrasonic velocities were used here to derive the dynamic moduli of the various rocks with pressure. In particular the dynamic Young's modulus (E_d) and Poisson's ratio (v_d) were found with the equations:

$$E_d = \frac{\rho V_S^2 (3V_P^2 - 4V_S^2)}{(V_P^2 - V_S^2)} \quad (1)$$

$$v_d = \frac{V_P^2 - 2V_S^2}{2(V_P^2 - V_S^2)} \quad (2)$$

where V_P, V_S and ρ are the P-wave velocity, S-wave velocity, and bulk density, respectively.

3.3 Experimental Results

The measured P- and S-wave velocities as a function of confining pressure in the vertically-oriented basement rocks are shown in Figure 3.4. For comparison with other basement rocks in the region, the P- and S-wave velocities from Kibikas et al. (2020) and Yu (2017) are shown as well (Figure 3.4c). The KGS sample consistently has higher P- and S-wave velocities than any of the basement rocks from Oklahoma, though the S-wave velocities are anomalously low in the cylindrical test. In contrast, Mill Creek granites have by far the lowest velocities measured, which might be due to the extensive fracturing and weathering in the outcrop samples. This fits with the observation that the Mill Creek granites also display the greatest change in velocity with pressure of any basement rock. The Jones-46 rhyolite samples display the least change in velocity as pressure increases in

both the cylindrical and octagonal tests, something that is similarly seen in the rhyolites from Kibikas et al. (2020).

It can be seen in Figure 3.4 that velocity increases with each increment of confining pressure, which can be explained by the closure of compliant cracks with pressurization (Blake and Faulkner, 2016). The velocity gradient in the stress domain ($\partial V/\partial \sigma$) is higher for all cylindrical basement rocks than for the octagonal basement rock tests. Generally, the cylindrical tests at low pressure have lower velocities than what was observed in the octagonal tests, though this difference diminishes at higher pressures (see Table 3.2 for velocities and 60 MPa). This is easily demonstrated by plotting the P- and S-wave velocities normalized by the value at 60 MPa as seen in Figure 3.5. For example, V_P and V_S of the octagonal Jones-46 sample from 10 to 60 MPa change only by 0.90 and 0.43 %, respectively, while V_P and V_S of the cylindrical Jones-46 sample change as much 14.89 and 8.16 % over the same interval, respectively. All granitic rocks exhibit greater changes in velocity compare to the rhyolites over the course of tests, similar to what was observed in the data from Kibikas et al. (2020) (Figure 3.5). The greatest change in both P- and S-wave velocity is observed in the Mill Creek samples, which also have the closest normalized velocities between the octagonal and cylindrical tests. That the least dense and most fractured basement rock demonstrates the greatest change in velocity underscores the relationship between both fracture content and velocity.

Experimentally determined dynamic Young's moduli (E_d) and Poisson's ratio (ν_d) are summarized in Figure 3.6 for all the vertically-oriented basement rocks. It can be seen that both E_d and ν_d in basement rocks increase with pressure, but that their relationships are not identical. The general trend in the E_d-pressure curves is consistent with the velocity-

pressure curves in Figure 3.4. Increasing confining pressure is also expected to increase rock density as cracks and pore spaces are closed. As can be seen from Equation 1, E_d depends upon the magnitude of the velocities and the bulk rock density. It follows then that the degree to which Young's moduli changes with pressure reflects the relative fracture content in the material. By contrast, ν_d can be said to depend upon the V_P/V_S ratio alone, meaning that higher Poisson's ratios reflect a higher V_P/V_S ratio as well. From Figure 3.6, both types of basement rock tests indicate a higher Poisson's ratio and V_P/V_S ratio should be observed in the KGS samples than for any rocks from Oklahoma.

3.4 Discussion

3.4.1 Comparing Laboratory and Field Data

Extrapolating laboratory data to field conditions is a common issue in experimental rock mechanics. In this case, we rely on a few assumptions to extend our results over the region of study. First, because the top basement depth varies across the region from outcropping in a few locations to being as deep as 12 km in the Anadarko Basin (Crain and Chang, 2018), we assumed the basement top was predominantly 1-3 km in depth as the majority of seismic activity has occurred where the top basement is shallower (Alt and Zoback, 2017). Second, for calculating the equivalent depth of our ultrasonic velocity tests, we assumed constant lithostatic and hydrostatic gradients of 27.5 and 10 MPa/km, respectively (Kibikas et al., 2020). Therefore, we assume an effective pressure gradient of 17.5 MPa/km for our models. Third, because the majority of seismicity in the region has occurred at depths of only 3-8 km (Johann et al., 2018; Kolawole et al. 2019), and the depth of the Mohorovičić Discontinuity (Moho) varies from 36 to 47 km across the region (Tave, 2013), our results were only extrapolated to a depth of 30 km.

The 1D velocity models derived here are shown in Figures 3.7 and 3.8. The average V_P and V_S at pressure were used to derive theoretical 1D velocity curves of the data assuming a logarithmic fit. Data reported here, Kibikas et al. (2020), and Yu (2017) are shown in the three leftmost panels, while extrapolated velocity models (e.g., Keranen et al., 2014; Chen, 2016, Ratre and Behm, 2019), utilizing a variety of different assumptions for the models, are shown in fourth panel. Examples of existing sonic log data are shown in the rightmost panels. Sonic log data for the Millsap #1 penetrated only the sedimentary basement rocks in Osage County (derived from Banerjee et al. (1999)), while KGS 1-32 and Wah Zha Zhi #1 wells show sonic logs for granitic basement rocks in north-central Oklahoma and south Kansas (Figures 3.7e and 3.8e).

All ultrasonic velocities reported here are well fitted by a logarithmic function which is extended to a depth of 30 km (equivalent to an effective pressure of 525 MPa). The gradient for both the cylindrical velocity tests of the basement rocks is steeper for both V_P and V_S than for the octagonal velocity tests of the same rock types. This would be expected from the observations in Figure 3.5. On the other hand, the logarithmic fit to the velocity models developed by Keranen et al. (2014) are somewhat poorer by comparison. However, it is worth acknowledging that the model fits for V_P and V_S from the cylindrical measurements are fairly similar to those developed through seismic techniques. The octagonal tests generally predict lower velocities than are inferred at a depth of 30 km from the other methodologies.

The high V_S with depth predicted by the synthetic models (Figure 3.8d) is a result of the V_P/V_S ratio being assumed as a constant value of 1.73 (Keranen et al., 2014). A constant V_P/V_S ratio has been utilized in the development of numerous velocity models in

this region and elsewhere (Darold et al., 2015; Chen, 2016; Schoenball et al., 2017). As pointed out by Nicholson and Simpson (1985), this assumption is flawed for a number of reasons. Firstly, it has been shown that velocity ratios in the continental crust decreases with depth and pressure (Christensen and Mooney, 1995). Secondly, the velocity ratio varies depending upon the rock type and mineral content. For example, quartz has a low V_P/V_S and Poisson's ratio of 1.48 and 0.08, respectively (Birch, 1961). Correspondingly, silica-poor crystalline rocks (i.e., mafic rocks) will have higher V_P/V_S than silica-rich rocks like granite or rhyolite. Thus, the velocity ratio will vary in Oklahoma both laterally and with depth (as silica-content will decrease in the lower crust). To demonstrate this, the models of V_P and V_S shown in Figures 3.7 and 3.8 were used to derive the corresponding V_P/V_S and plotted against pressure and depth in Figure 3.9.

Based on the ultrasonic data reported here, as well as in Kibikas et al. (2020) and Yu (2017), we find that the velocity ratios are not constant. Rather they experience a strong initial increase at shallower depths (i.e., <5 km) then gradually approach a constant value with depth. This trend is most common in granitic basement rocks; the Jones-46 rhyolite and Colbert rhyolite from Kibikas et al. (2020) show minor or even decreasing trends in V_P/V_S with increasing pressure or depth. Interestingly, the mafic diabase (Figure 3.9c) also displays the highest V_P/V_S ratio over most of the tested intervals, with very little change predicted by the models with depth. The sonic data also supports the inference that the V_P/V_S value in the basement is not constant. For the Wah Zha Zhi #1 and KGS 1-32 Wellington wells, we found they possessed mean V_P/V_S ratios of 1.69 and 1.75, respectively. The higher ratio in the KGS well supports the observation that the ultrasonic tests with KGS samples generally have higher V_P/V_S ratios than any of the other basement

rocks (Figure 3.9). Other authors have the choice of V_P/V_S ratio for many velocity models does not agree with existing well log data in the Oklahoma-Kansas region, calling into question the precision of some of the velocity models (Schoenball and Ellsworth, 2017).

3.4.2 Synthesizing a Cumulative 1D Model

Assuming the crystalline basement in the central US is isotropic and homogenous is liable to introduce errors in velocity models developed and consequently impact the accuracy of earthquake relocation (Nicholson and Simpson, 1985). A separate velocity structure for V_P and V_S, and correspondingly a variable V_P/V_S ratio, is desirable for any velocity model, particularly where there is a paucity of corroborating direct laboratory or field data such as in our region (Mauer and Kradolfer, 1996; Magistrale et al., 2000; Kim et al., 2011). Ultrasonic velocities and sonic logs show the velocity structure of the crystalline basement will vary depending upon the location and corresponding rock type. Any velocity model should take into account changes in lithology, as characteristics such as mineralogy and fracture/porosity content affect relationship between V_P and V_S especially at lower pressures and depths (Lee, 2003). For the Oklahoma-Kansas region, 1D velocity models should reflect a decreasing vertical V_P/V_S ratio from north-to-south (Figure 3.9). The change in velocity structure across the region may be better understood with further research into the vertical and horizonal velocity anisotropy of the crystalline basement rocks, something to be covered in a future work.

3.5 Conclusions

A set of vertically-oriented basement rocks from Oklahoma and Kansas were prepared. Two types of ultrasonic velocity tests were used to measure the P- and S-wave velocities at hydrostatic conditions. The results were used to derive information about the

elastic moduli of the crystalline basement. The experimental results were then used to derive theoretical 1D velocity models with pressure and depth in the region, which were compared to the results of existing sonic logs and seismic models. We found that ultrasonic velocities in the basement are considerably more variable than is assumed in many theoretical models for the region. While P-wave velocities are somewhat similar in structure, S-wave velocities rarely match seismically derived models because of the assumption of a constant V_P/V_S in many such models. For improved accuracy of understanding basement structure and seismicity, we recommend P- and S-wave velocities be independently derived for future velocity models in the region, which may be verified with consideration of the 1D ultrasonic velocity models developed here.

Acknowledgements

This material is based upon work supported by the Department of Energy under Award Number DE-FE0031687."

herein do not necessarily state or reflect those of the United States Government or any agency thereof.

References

Al-Yahya, Kamal. "Velocity analysis by iterative profile migration." Geophysics 54, no. 6 (1989): 718-729.

Alt, Richard C., and Mark D. Zoback. "In situ stress and active faulting in Oklahoma." Bulletin of the Seismological Society of America 107, no. 1 (2017): 216-228.

Asnaashari, Amir, Romain Brossier, Stéphane Garambois, François Audebert, Pierre Thore, and Jean Virieux. "Regularized seismic full waveform inversion with prior model information." Geophysics 78, no. 2 (2013): R25-R36.

Banerjee, S., D. Djikine, G. Guo, T. K. Reeves, B. Sharma, L. Volk, and S. George. An Exploration 3D Seismic Field Test Program in Osage County, Oklahoma. No. DOE/PC/91008-0376. National Petroleum Technology Office, Tulsa, OK (US), 1999.

Benson, William Alan. "The Spavinaw granite (proterozoic), Mayes County, Oklahoma." (2014): 258-264.

Birch, Francis. "The velocity of compressional waves in rocks to 10 kilobars: 1." Journal of Geophysical Research 65, no. 4 (1960): 1083-1102.

Blake, O. O., and D. R. Faulkner. "The effect of fracture density and stress state on the static and dynamic bulk moduli of Westerly granite." Journal of Geophysical Research: Solid Earth 121, no. 4 (2016): 2382-2399.

Boak, Jeremy, Jefferson Chang, Chen Chen, Kevin Crain, Amberlee Darold, Deepak Devegowda, Ahmad Ghassemi, and Stephen Marsh. "4D Integrated Study Using

Geology, Geophysics, Reservoir Modeling & Rock Mechanics to Develop Assessment Models for Potential Induced Seismicity Risk Project 12122-91."

Brossier, Romain, Stéphane Operto, and Jean Virieux. "Velocity model building from seismic reflection data by full-waveform inversion." Geophysical Prospecting 63, no. 2 (2015): 354-367.

Chen, Chen. "Comprehensive analysis of Oklahoma earthquakes: From earthquake monitoring to 3D tomography and relocation." (2016).

Christensen, Nikolas I., and Walter D. Mooney. "Seismic velocity structure and composition of the continental crust: A global view." Journal of Geophysical Research: Solid Earth 100, no. B6 (1995): 9761-9788.

Darold, Amberlee P., Austin A. Holland, Jennifer K. Morris, and Amie R. Gibson. "Oklahoma earthquake summary report 2014." Okla. Geol. Surv. Open-File Rept. OF1-2015 (2015): 1-46.

Duveneck, Eric. "Velocity model estimation with data-derived wavefront attributes." Geophysics 69, no. 1 (2004): 265-274.

Johann, Lisa, Serge A. Shapiro, and Carsten Dinske. "The surge of earthquakes in Central Oklahoma has features of reservoir-induced seismicity." Scientific reports 8, no. 1 (2018): 1-14.

Keranen, Katie M., Matthew Weingarten, Geoffrey A. Abers, Barbara A. Bekins, and Shemin Ge. "Sharp increase in central Oklahoma seismicity since 2008 induced by massive wastewater injection." Science 345, no. 6195 (2014): 448-451.

Kibikas, William M., Brett M. Carpenter, and Ahmad Ghassemi. "Mechanical strength and physical properties of Oklahoma's igneous basement." Tectonophysics 777 (2020): 228336.

Kim, Seongryong, Junkee Rhie, and Geunyoung Kim. "Forward waveform modelling procedure for 1-D crustal velocity structure and its application to the southern Korean Peninsula." Geophysical Journal International 185, no. 1 (2011): 453-468.

Kissling, Edi, W. L. Ellsworth, D. Eberhart-Phillips, and Urs Kradolfer. "Initial reference models in local earthquake tomography." Journal of Geophysical Research: Solid Earth 99, no. B10 (1994): 19635-19646.

Kolawole, F., C. S. Johnston, C. B. Morgan, J. C. Chang, K. J. Marfurt, D. A. Lockner, Z. Reches, and B. M. Carpenter. "The susceptibility of Oklahoma's basement to seismic reactivation." Nature Geoscience 12, no. 10 (2019): 839-844.

Kolawole, Folarin, Molly Simpson Turko, and Brett M. Carpenter. "Basement-controlled deformation of sedimentary sequences, Anadarko Shelf, Oklahoma." Basin Research 32, no. 6 (2020): 1365-1387.

Lee, Myung W. Velocity ratio and its application to predicting velocities. US Department of the Interior, US Geological Survey, 2003.

Lee, Ji Soo, John Brumley, Evan Morgan, and Lance Despain. "Three-dimensional ultrasonic wave velocity test system." U.S. Patent 10,345,269, issued July 9, 2019.

Magistrale, Harold, Steven Day, Robert W. Clayton, and Robert Graves. "The SCEC southern California reference three-dimensional seismic velocity model version 2." Bulletin of the Seismological Society of America 90, no. 6B (2000): S65-S76.

Marsh, Stephen. "Development of a state-wide velocity profile in Oklahoma using ambient noise seismic tomography." (2018).

Maurer, Hansruedi, and Urs Kradolfer. "Hypocentral parameters and velocity estimation in the western Swiss Alps by simultaneous inversion of P-and S-wave data." Bulletin of the Seismological Society of America 86, no. 1A (1996): 32-42.

Maxwell, Shawn. Microseismic imaging of hydraulic fracturing: Improved engineering of unconventional shale reservoirs. Society of Exploration Geophysicists, 2014.

Nicholson, Craig, and David W. Simpson. "Changes in Vp/Vs with depth: Implications for appropriate velocity models, improved earthquake locations, and material properties of the upper crust." Bulletin of the Seismological Society of America 75, no. 4 (1985): 1105-1123.

Ratre, Pranshu, and Michael Behm. "A comprehensive seismic 3D model of the central Oklahoma crust from local earthquake waveforms: implications for the mid-continent rift (MCR)." In AGU Fall Meeting Abstracts, vol. 2019, pp. T21F-0388. 2019.

Schoenball, Martin, and William L. Ellsworth. "Waveform-relocated earthquake catalog for Oklahoma and southern Kansas illuminates the regional fault network." Seismological Research Letters 88, no. 5 (2017): 1252-1258.

Schultz, Phil. The seismic velocity model as an interpretation asset. Society of Exploration Geophysicists, 1998.

Selves, Tyler. "Factors influencing seismicity in south-central Kansas and northern Oklahoma." PhD diss., Wichita State University, 2017.

Shah, Anjana K., and G. Randy Keller. "Geologic influence on induced seismicity: Constraints from potential field data in Oklahoma." Geophysical Research Letters 44, no. 1 (2017): 152-161.

Tave, Matthew A. "Imaging of the crust and Moho beneath Oklahoma using receiver functions and Pn tomography; with emphasis on the Southern Oklahoma Aulacogen." PhD diss., 2013.

Toth, Christopher Robert. "Separation of the Earthquake Tomography Inverse Problem to Refine Hypocenter Locations and Tomographic Models: A Case Study from Central Oklahoma." PhD diss., University of Oklahoma, 2014.

Walter, Jacob I., Paul Ogwari, Andrew Thiel, Fernando Ferrer, Isaac Woelfel, Jefferson C. Chang, Amberlee P. Darold, and Austin A. Holland. "The Oklahoma Geological Survey Statewide Seismic Network." Seismological Research Letters 91, no. 2A (2020): 611-621.

Yu, Weiqi. "Laboratory Geomechanical Characterization of the Arbuckle Group and Crystalline Basement Rocks in Oklahoma." (2017).

CHAPTER III FIGURES

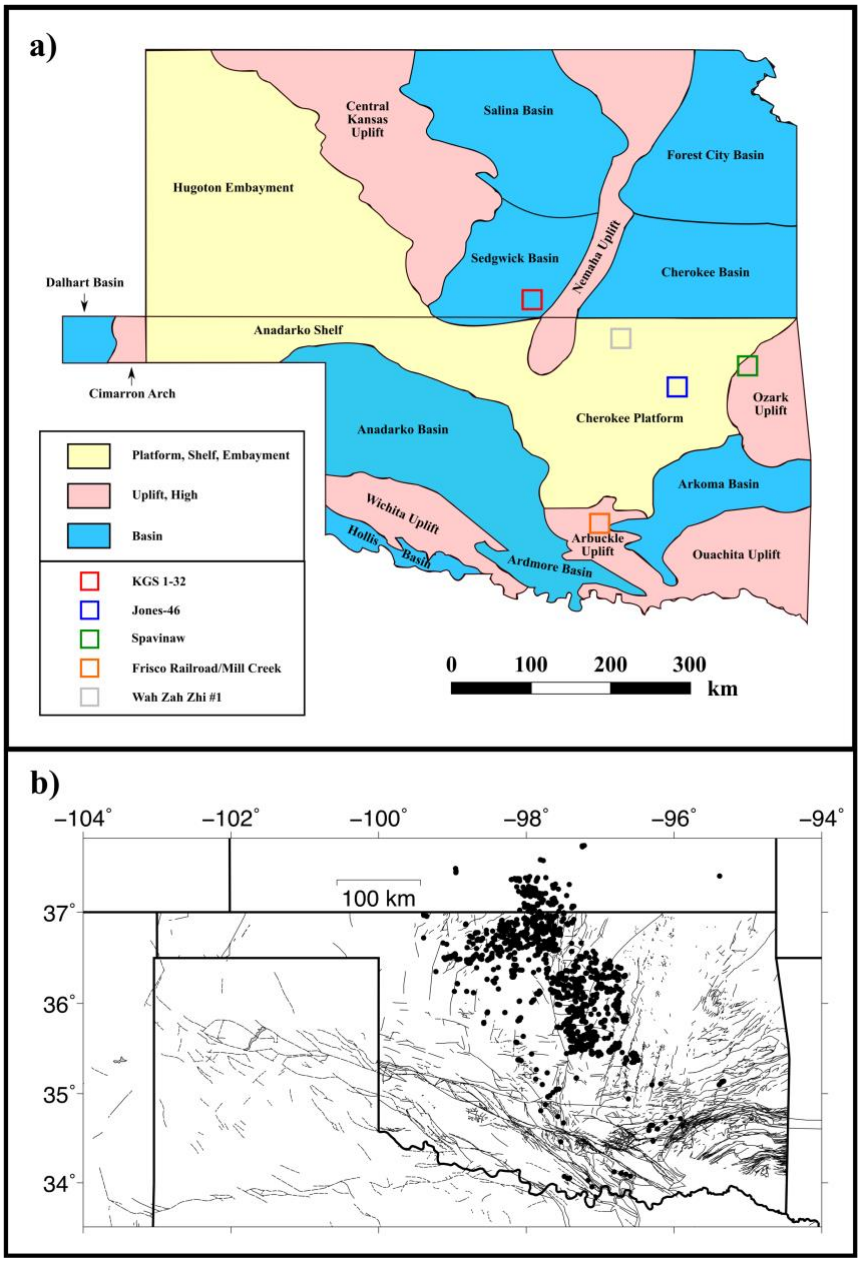

Figure 3.1: a) Regional tectonic provinces of Oklahoma and Kansas with the sampling and well locations marked by boxes (adapted from Selves (2017)) and b) regional schematic showing recent seismic activity (M3.0+) from the OGS catalogue.

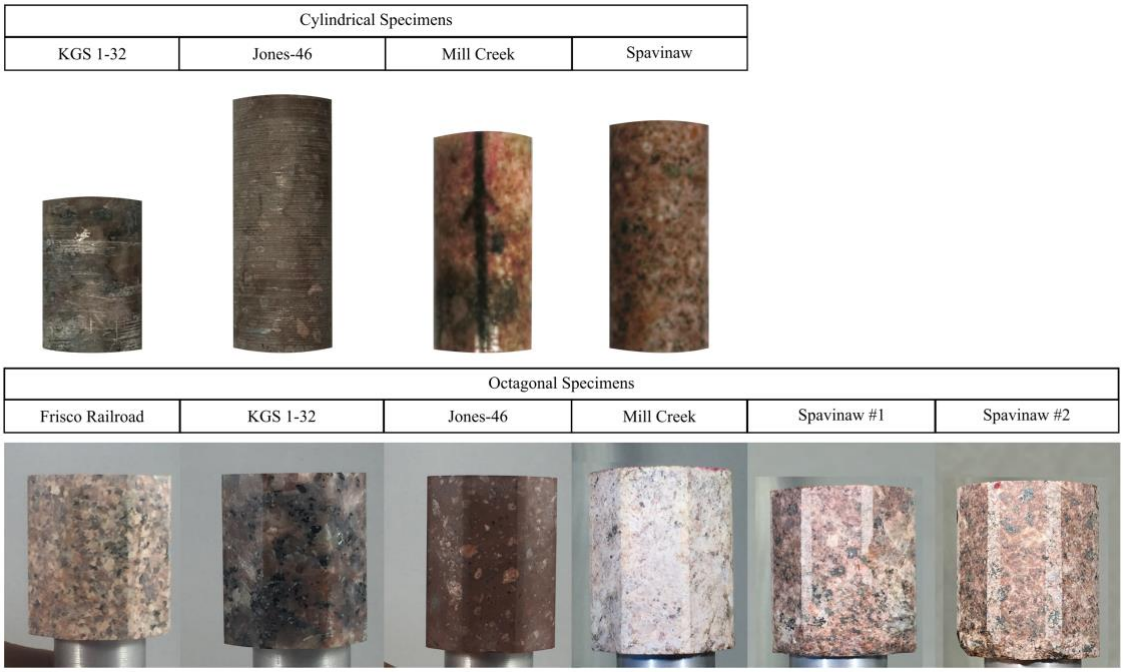

Figure 3.2: Images of tested cylindrical (top row) and octagonal (bottom row) samples.

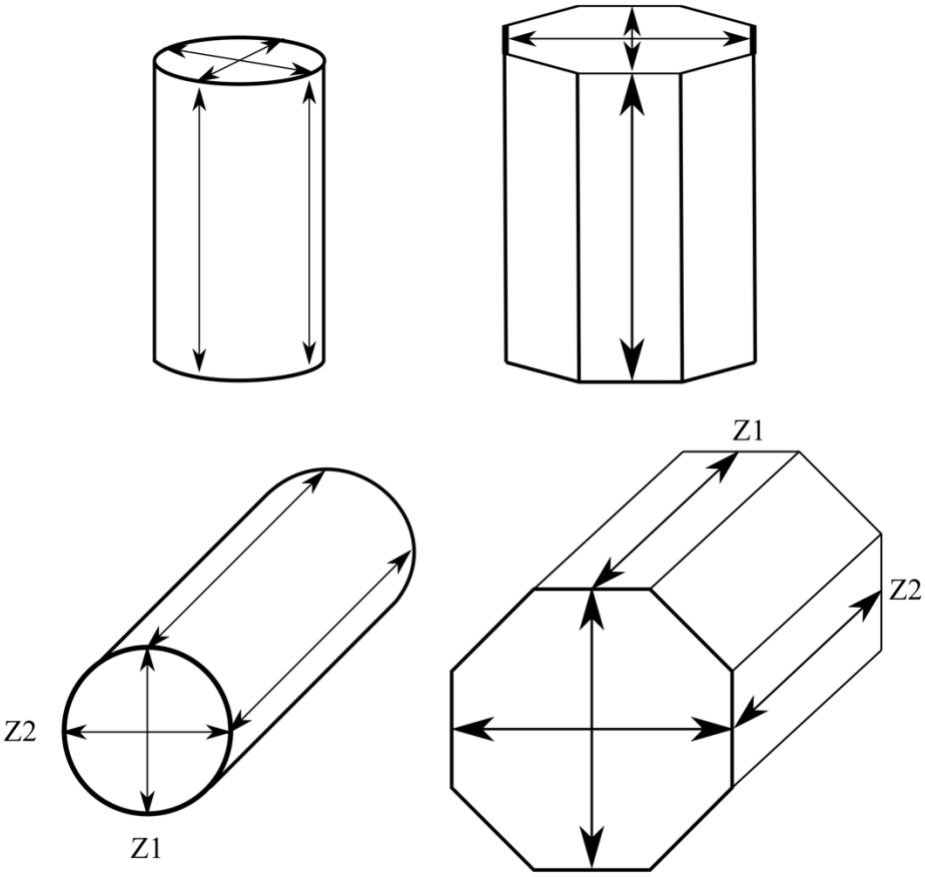

Figure 3.3: Schematic of samples and orientation of velocity measurements relative to sample axes. Z1 and Z2 of the cylindrical tests mark the plane parallel to the S-wave piezoelectric crystal on the platens during the first and second loading of the cylindrical samples. Z1 and Z2 of the octagonal tests mark the P- and S-waves propagating vertically down and vertically up, respectively.

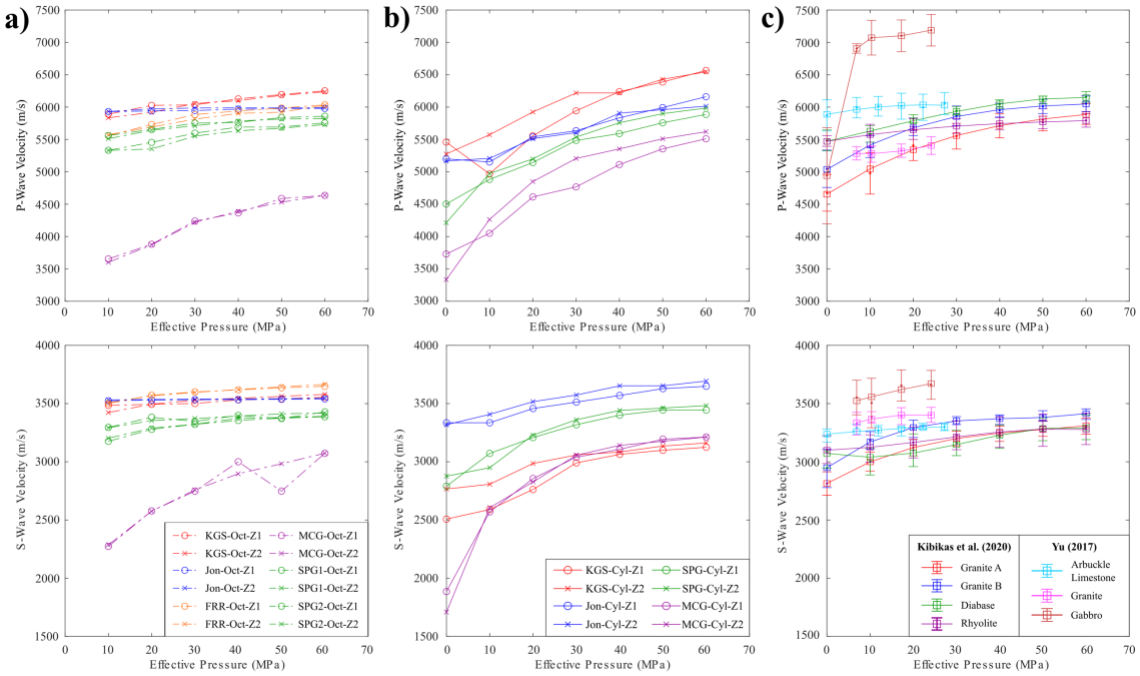

Figure 3.4: P- and S-wave velocities from a) octagonal basement rock tests, b) cylindrical basement rock tests, and c) basement rocks tested in Kibikas et al. (2020) and Yu (2017). Circles represent the first orientation utilized for velocity tests; X represents the second orientation used for velocity tests.

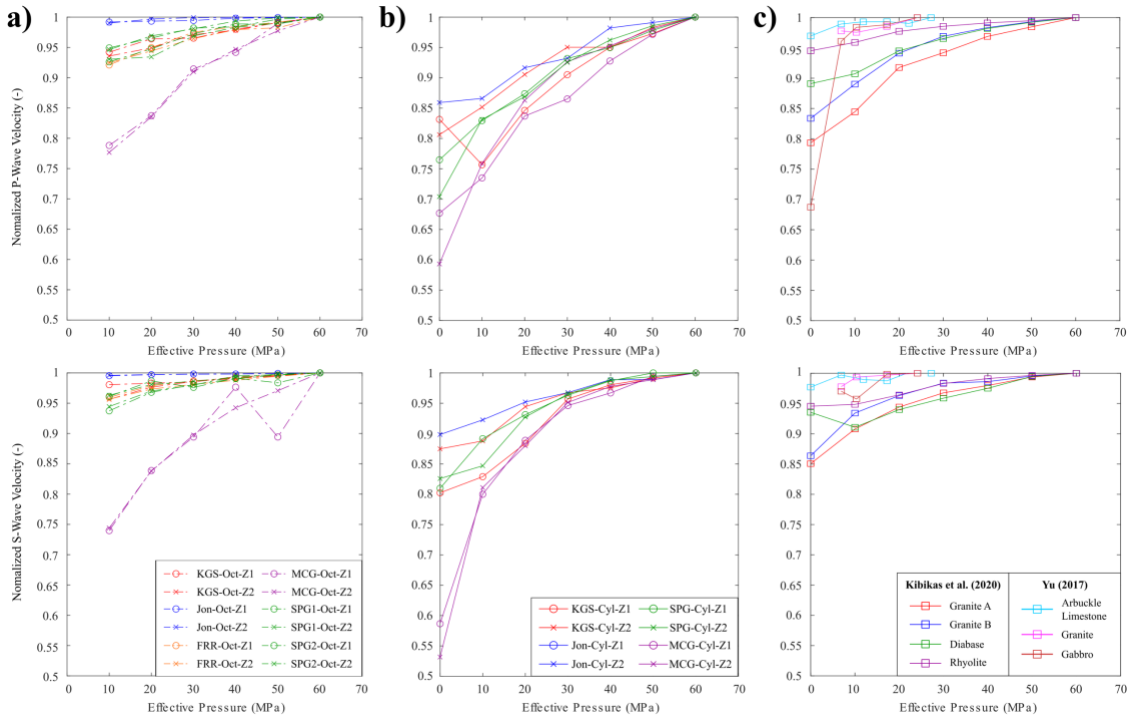

Figure 3.5: P- and S-wave velocities normalized by the values at 60 MPa for a) octagonal basement rock tests, b) cylindrical basement rock tests, and c) basement rocks tested in Kibikas et al. (2020) and Yu (2017). Circles represent the first orientation utilized for velocity tests; X represents the second orientation used for velocity tests.

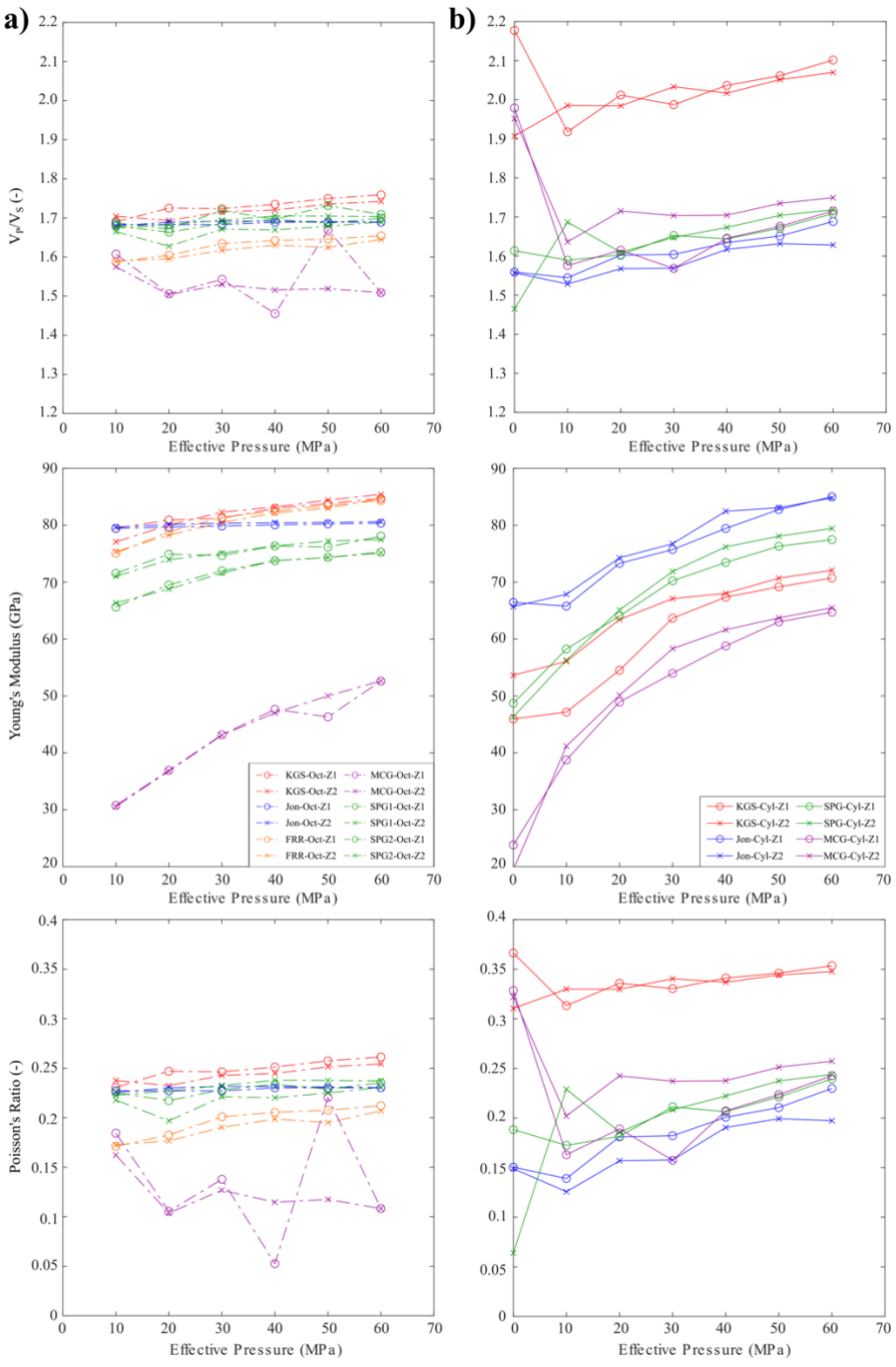

Figure 3.6: V_P/V_S ratio, dynamic Young's moduli (E_d) and dynamic Poisson's ratios (ν_d) for a) the octagonal basement rock tests and b) the cylindrical specimen tests. Circles represent the first orientation (Z1) utilized for velocity tests; X represent the second orientation (Z2) used for velocity tests.

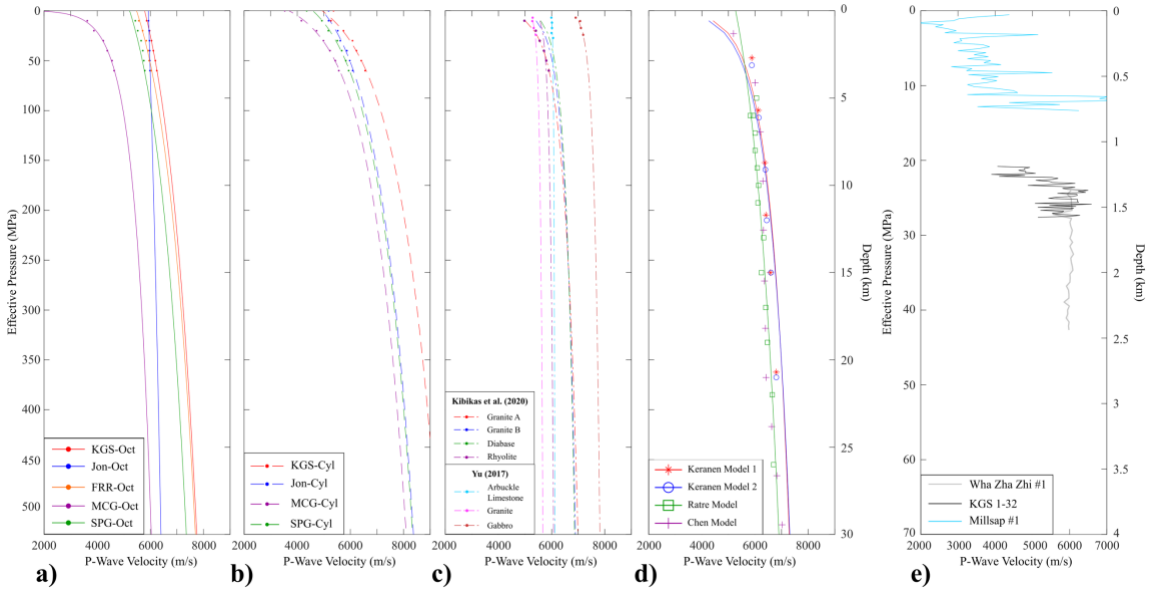

Figure 3.7: 1D models for P-wave velocity with depth and pressure extrapolated from ultrasonic velocity data, seismic inversions, and well logs. Velocity models listed are from a) the octagonal tests, b) the cylindrical tests, c) data from Kibikas et al. (2020) and Yu (2017), and d) seismic models developed by other researchers, while e) displays sonic log data from Oklahoma and Kansas.

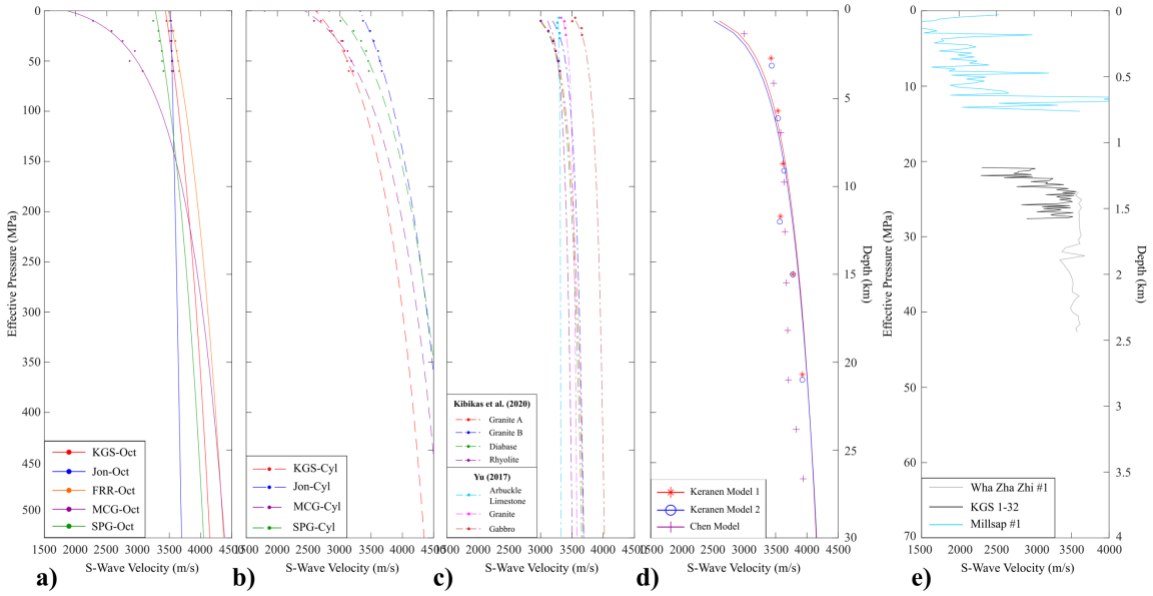

Figure 3.8: 1D models for S-wave velocity with depth and pressure extrapolated from ultrasonic velocity data, seismic inversions, and well logs. Velocity models listed are from a) the octagonal tests, b) the cylindrical tests, c) data from Kibikas et al. (2020) and Yu (2017), and d) seismic models developed by other researchers, while e) displays sonic log data from Oklahoma and Kansas.

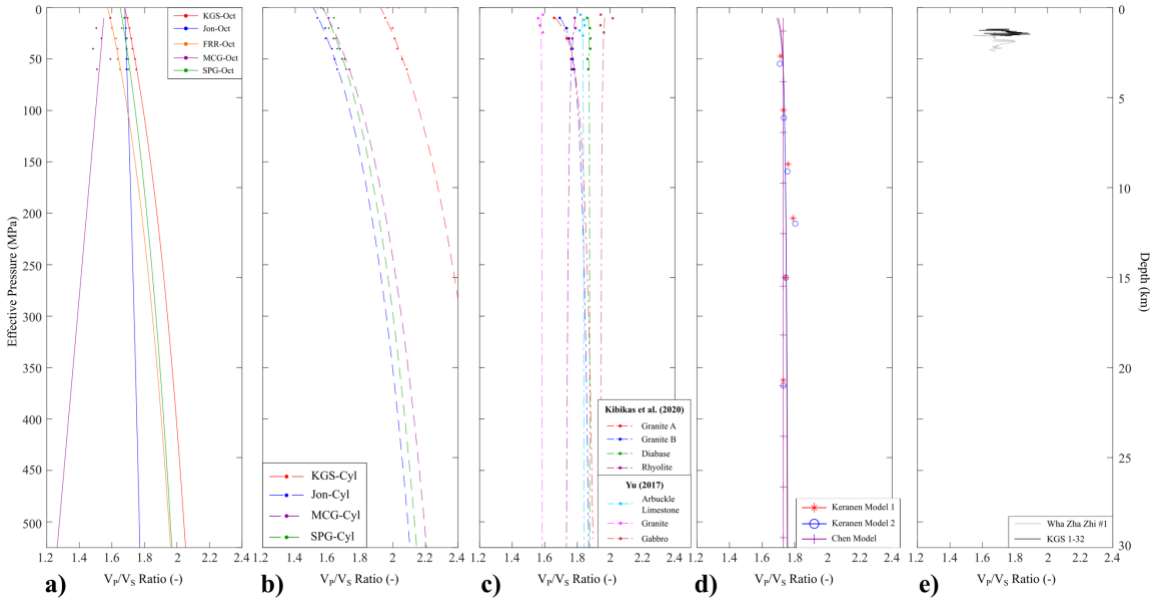

Figure 3.9: 1D models for velocity ratios with depth and pressure extrapolated from ultrasonic velocity data, seismic inversions, and well logs. Velocity models listed are from a) the octagonal tests, b) the cylindrical tests, c) data from Kibikas et al. (2020) and Yu (2017), and d) seismic models developed by other researchers, while e) displays sonic log data from Oklahoma and Kansas.

CHAPTER III TABLES

		Jones-46	Frisco Railroad	KGS 1-32	Mill Creek	Spavinaw 1	Spavinaw 2
Cylindrical	Length (mm)	66.04	-	37.56	56.54	57.81	-
	Diameter (mm)	25.42	-	24.83	25.37	25.42	-
	Density (g/cm^3)	2.634	-	2.676	2.525	2.634	-
Octagonal	Length (mm)	47.12	42.88	41.80	44.25	43.78	43.61
	Average Diameter (mm)	38.49	35.84	35.90	36.2	36.00	36.68
	Density (g/cm^3)	2.606	2.614	2.658	2.514	2.680	2.656

Table 3.1: List of sample dimensions for all rocks evaluated in this work.

	V_P Octagonal (m/s)	V_S Octagonal (m/s)	V_P Cylindrical (m/s)	V_S Cylindrical (m/s)
KGS 1-32	6252.11	3554.31	6566.43	3124.79
	6235.68	3579.50	6543.55	3161.62
Jones-46	5980.00	3540.38	6160.45	3648.62
	5990.87	3545.69	6014.57	3693.51
Frisco Railroad	6035.43	3648.21	-	-
	6028.09	3665.03	-	-
Mill Creek	4635.92	3072.62	5510.72	3212.50
	4637.06	3073.48	5620.28	3212.50
Spavinaw 1	5858.53	3428.28	5886.97	3445.17
	5823.72	3418.65	5984.47	3482.53
Spavinaw 2	5757.08	3387.24	-	-
	5730.10	3390.66	-	-

Table 3.2: List of V_P and V_S values recorded at the maximum confining pressure 60 MPa in each test.

CHAPTER IV: ULTRASONIC VELOCITY ANISOTROPY IN THE CRYSTALLINE BASEMENT OF THE MIDCONTINENT

4.1 Introduction

Quantifying the in-situ state of stress, defined by the principal stress orientations and magnitudes, remains a significant priority in the study of the in various fields of research (Heidbach et al., 2016). Knowledge of the state of in-situ stresses is critical for many areas of resource exploration and production (Reiter and Heidbach, 2014; Kingdon et al., 2016), as well as geotechnical applications such as CO_2 sequestration (carbon capture storage) and nuclear waste repositories (Williams et al., 2016; Jo et al., 2019). Additionally, the in-situ stress state is a key factor to understanding the effects such applications may induce in the subsurface (induced seismicity, subsurface subsidence, etc.) and how to avoid or mitigate them (Fredrich et al., 2000; Gambolati and Teatini, 2015; Snee and Zoback, 2016).

Numerous techniques have thus been developed to characterize the state of stress in the subsurface. Direct methods for estimating stress state include, but are not limited to, overcoring, hydraulic fracturing, strain relief methods, and borehole breakouts (Ljunggren et al., 2003). These methods are economically inefficient in most cases, so often indirect techniques are employed that rely on secondary observation of the subsurface, such as through the use of earthquake focal mechanism inversions (Hardebeck and Hauksson, 2001). One such techniques is through the measurement of velocity anisotropy and shear-wave splitting. Seismic velocities in crustal rocks are generally sensitive to the stress state. First discovered in the lab by Simmons and Nur (1969), in an anisotropic stress field (e.g., $\sigma_1 \neq \sigma_2 \neq \sigma_3$) the differences in applied stress will result in anisotropic velocities in rocks

dependent upon the seismic wave and stress field orientations. Since then, large-scale observations of shear-wave splitting in the subsurface (i.e., propagating shear waves splitting into two distinct polarizations with different velocities) has led to the broad acceptance of velocity anisotropy as a means of determining the principal stress orientations (Crampin, 1985; Boness and Zoback, 2004; Gao et al., 2011; Tsuji et al., 2011).

However, there exist issues with relating seismic anisotropy in the crust with the in-situ stress orientations. The relation between seismic anisotropy and stress state is dependent upon the anisotropy being induced by stress rather than any other intrinsic factors (Barton, 2006). Velocity anisotropy in the crust can be attributed to several possible mechanisms (Crampin and Lovell, 1991; Boness and Zoback, 2004): 1) an anisotropic stress field in-situ causing the preferential closure of fractures creating generating a fast polarization parallel to S_{Hmax} (e.g., the greatest horizontal stress); 2) dilation of stress-aligned fluid-filled cracks that produce a fast polarization parallel to S_{Hmax}; 3) direct-stress induced anisotropy due to inherent properties of the rock; 4) alignment of fractures or structural features regardless of stress orientations; 5) aligned minerals or grains. Anisotropy due to lithologic or structural characteristics is often assumed for sedimentary rocks and some metamorphic rocks (Wang, 2002). Conversely, crystalline igneous and metamorphic rocks are often assumed to be isotropic, and thus velocity anisotropy observed is attributed to the stress field or local fault orientations (Mavko et al., 1995).

In the past decade, the Oklahoma-Kansas region saw a dramatic surge in seismicity in the previously stable region (Ellsworth et al., 2015). This seismic activity, although linked to wastewater disposal in sedimentary formations, has been traced almost entirely

to the underlying crystalline basement rocks (Chang and Segall, 2016; Hincks et al., 2018). This seismicity has generated a renewed interest in characterizing the geophysical and geomechanical properties of the intraplate basement. One aspect of this is characterizing the in-situ stress state, particularly the basement stress orientations which control the likelihood of unstable fault slip occurring (Alt and Zoback, 2017; Qin et al., 2019; Kolawole et al., 2019). However, due to the depth of the basement, the relative lack of basement surface outcrops in the region, and the lack of significant prior interest, there exists very few options to directly characterize the basement stress state. Thus, indirect methods such as velocity anisotropy and shear-wave splitting will need to be employed to determine the basement stress state (i.e., Alt and Zoback, 2017).

There are several issues with utilizing velocity anisotropy to determine stress orientations in the Oklahoma-Kansas region. First, although it is often assumed that crystalline rocks (ex., granite) are largely isotropic and any seismic anisotropy is stress-induced, in practice all rocks exhibit anisotropic behavior; even crystalline rocks such as granite exhibit intrinsic anisotropy due to pre-existing cracks with preferred orientations (Douglass and Voight, 1969; Takemura et al., 2003). Indeed, Sano et al. (1992) showed that granites can exhibit velocity anisotropy under confining pressure up to 100 MPa. Second, wells penetrating basement rock have previously shown that the anisotropic polarization of elastic waves does not always correlate with stresses determined through other methods (Boness et al., 2004; Goswami et al., 2019). Highly fractured areas such as shear zones are known to produce anomalous velocity anisotropies. Third, direct characterization of basement velocities across the region is sparse (Yu, 2017; Kibikas et al., 2020), with practically no existing measurement of intrinsic anisotropy for these

basement rocks, meaning that measures of seismic anisotropy in the basement will heavily rely upon numerous material assumptions. This is particularly important, as anisotropy can also be a useful tool for discriminating between different rock types in the crust (Rabbel and Mooney, 1996). Fourth, recent research characterizing the local and regional velocity anisotropy in Oklahoma/Kansas has shown velocities in the basement are heterogenous and affected by both the stress orientations and structural features, producing several fast polarization directions (Cochran et al., 2019; Ortega Romo, 2020).

This work seeks to provide new insight into the inherent anisotropy of the crystalline basement of the Oklahoma-Kansas region. Experimental methods were utilized to measure the elastic wave velocities of five basement rock types oriented vertically and horizontally to the surface at hydrostatic conditions to eliminate the effect of stress-induced anisotropy. Basement rocks tested were also analyzed through stereologic techniques to correlate microstructural observations with elastic wave velocities measured. Finally, we compared our experimental observations with existing well log sonic data to characterize the material dependency of velocity anisotropy and how it may affect the determination of stress orientations.

4.2 Materials and Methodology

4.2.1 Basement Rocks

Given the scarcity of material available to sample, we obtained basement rocks from both surface outcrops and basement-penetrating wells. Though the basement top is rarely exposed at the surface, there are a few relatively small outcrops in south-central, southwest, northeast Oklahoma (Figure 4.1). The Mill Creek cores were obtained from the large outcrop in the Arbuckle Mountains region (Kolawole et al., 2019), while the

Spavinaw cores were obtained from a minor outcrop in northeastern Oklahoma (Benson, 2014). Samples were obtained from basement-penetrating wells that include the KGS 1-32 Wellington well in southern Kansas (Holubnyak et al., 2018), the Jones-46 well in northeastern Oklahoma (Denison et al., 1987), and the Frisco Railroad well in southern Oklahoma (Figure 4.1).

XRD analysis, along with transmission and scanning electron microscope observations (Figure 4.2), were used to characterize the lithology of each basement rock studied (Table 4.1). The KGS samples are coarse-grained granites composed of plagioclase and quartz, with relatively lower alkali feldspar (Table 4.1). Moderate fracturing is exhibited with prominent calcite sealing (Figure 4.2b). Pervasive titanite, pyrite, and iron-oxide content, along with calcite cementation, suggest extensive alteration induced by fluid infiltration. The Jones-46 samples are from the Washington Volcanic Group (Denison et al., 1987). They are very fine-grained rhyolites with extensive and heterogeneous phenocrysts. Their matrix is dominantly an intergrowth of fine quartz and K-feldspar, with moderate plagioclase, calcite, biotite, chlorite, apatite content (Figure 4.2c). Phenocryst size is highly variable throughout the rhyolite cores; they are mainly quartz or K-feldspar that often displays perthitic texture. The Frisco Railroad cores are very coarse-grained granites (>2 mm) composed of mostly feldspars with a minor quartz content. Trace minerals identified in these cores include biotite, barite, titanite, and chlorite (Figure 4.2a). Although fractures are sparse throughout the granite, alteration of biotite to chlorite and epidote suggests the rock has experienced periodic fluid infiltration. The Mill Creek cores are very coarse and highly fractured granites (Figure 4.2d). Though dominantly composed of quartz, plagioclase, and K-feldspar, biotite content is extensive and displays frequent

alteration to chlorite and iron-oxide. The Spavinaw cores are fine-to-medium grained granites, with micrographic textures of quartz, alkali and potassium feldspar. The main accessory minerals are magnetite (with grains visible to the naked eye) and biotite, but the rock has been heavily altered to produce chlorite, titanite, rutile and iron-oxide. Fractures are sparse but dominantly sealed by chlorite. The granite also displays significant myrmekitic texture, or an intergrowth between quartz and plagioclase, further indicating significant hydrothermal alteration (Figure 4.2e).

Basement samples were cored relative to the orientation of the vertical and horizontal directions from borehole and outcrop material. Each rock was cored into cylinders with 25.4 and 38.1 mm diameters, then ground into flat surfaces at the top and bottom to parallel (<.01 mm). Three 25.4 mm samples were cored of each basement rock (except Frisco Railroad due to material shortage). Each 25.4 mm cylinder was cored at an orthogonal orientation to one-another, with one sample parallel to the vertical axis and two parallel to the horizontal axis (see Figure 4.4c). Each 38.1 mm sample was cored parallel to the vertical axis. These were further polished into octagonal prisms for the experimental setup (Figure 4.3, bottom row) with average diameters of ~1.4-1.5 mm between parallel faces. Samples were oven-dried for a period of 24-48 hours prior to testing to measure the dry density of each sample. Sample dimensions were measured and recorded in Table 4.2.

4.2.2 Velocity Tests

Two types of setups were used for measuring the vertical velocities in the basement rocks. All rocks were tested at hydrostatic pressures (i.e., $\sigma_1 = \sigma_2 = \sigma_3$). In the first setup, ultrasonic velocities were measured from ambient conditions (~0 MPa) to 60 MPa using the pulse transmission technique. Samples were placed between steel two endcaps with

mounted P- and S-wave piezoelectric crystals with a frequency of 250 kHz (Figure 4.4b). To measure velocity, a pulse (with a frequency of 500 kHz) was passed through each sample parallel to the long axis. The received waveforms were recorded through an external oscilloscope (Keysight Technologies 33500B Series Waveform Generator). At ambient conditions, velocities were recorded with the use of a benchtop vice to apply a minute pressure. After being recorded, samples were jacketed and placed into a pressure vessel (MTS 810, see Kibikas et al., 2020). Confining pressure was then increased in increments of 10 MPa then unloaded after 60 MPa. At each 10 MPa increment the P- and S-wave velocities (V_P and V_S) were recorded. Because S-wave crystals are aligned parallel to one another in our setup, once the test was over, each sample was removed from the vessel and rotated 90º from its previous orientation relative to the polarization direction of the S-wave crystals. The rocks were again pressurized in a similar manner, recording the velocities from 0 to 60 MPa to observe the change P- and S-wave velocity at an orthogonal polarization. Each sample was delineated as X, Y, or Z, with X and Y being parallel to the horizontal axis and Z being parallel to the vertical axis. The first measurements were marked with as X1/Y1/Z2 and the second as X2/Y2/Z2 (Figure 4.4c).

For the second setup, the octagonal samples were first coated with honey as a coupling medium. Each sample was then loaded into a Three-Dimensional Ultrasonic Velocity Test System (see Lee et al., 2019 for further details). Ten rams, one for each sample face, are placed against the sample faces and pressurized via a series of external syringe pumps to apply stress to each face (Figure 4.5a). Pressure was increased hydrostatically in increments of 10 MPa up to 60 MPa. Three piezoelectric crystals, one P-wave and a pair of orthogonally-oriented S-wave crystals, were mounted on each ram for

measuring the velocities in each orientation of the sample (Figure 4.5b and 4.5c). An electric signal generated at pulse (with a frequency ~1 MHz) across each source face that traveled through the sample to be received at the opposite sample face. The corresponding P- and S-wave signals were recorded with an external oscilloscope and used to determine P-, S1-, and S2-wave orientations. The horizontal faces were delineated by their orientation from 0-360º (Figure 4.5c), while the vertical faces were delineated as Front (top) and Back (bottom) (Figure 4.5b).

The orientation of the samples relative to the cardinal directions (i.e., North-South-East-West) was not known for all samples. While all samples were oriented either vertically and horizontally, only the directions for the Mill Creek and Spavinaw samples were known. For these rocks, the Y-oriented cylindrical samples and 0-180º faces on the octagonal sample were oriented to measure velocities parallel to North-South, while the X-oriented and 90-270º faces on the octagonal sample were oriented to measure velocities parallel to East-West.

Ultrasonic velocities were used here to derive the dynamic moduli of the various rocks with pressure. In particular the dynamic Young's modulus (E_d) and Poisson's ratio (v_d) were found with the equations:

$$E_d = \frac{\rho V_S^2 (3V_P^2 - 4V_S^2)}{(V_P^2 - V_S^2)} \quad (1)$$

$$v_d = \frac{V_P^2 - 2V_S^2}{2(V_P^2 - V_S^2)} \quad (2)$$

where V_P, V_S and ρ are the P-wave velocity, S-wave velocity, and bulk density, respectively.

4.2.3 Microstructural Characterization

Elastic anisotropy may be significantly influenced by the presence of fractures in the samples. For our rock samples, which lack an obvious textural component to the naked eye, it is necessary to characterize the microfracture densities in order to better understand the role basement lithology plays in velocity anisotropy observed. To characterize these features, 10 polished thin-sections were prepared from five of the octagonal samples tested. 2 thin-sections were prepared from each sample: one thin-section was cut parallel to the vertical axis and along 0-180º directions (YZ-plane) and one section was cut parallel to the horizontal axes, with the thin-section long axis parallel to 0-180º direction and short axis parallel to the 90-270º direction (XY-plane). Using transmitted light photomicrography, fracture densities in each thin-section were quantified using stereologic techniques (Underwood, 1970). A grid with an area of 11x11 mm^2 was constructed in each thin-section, with 2 sets of 21 lines (spaced at 0.5 mm intervals) oriented orthogonally to one another (Figure 4.6). In each thin-section, the lines were aligned with one of the directions of velocity measurement. Lines in the YZ-plane thin-section were parallel to the Front-Back directions and 0-180º directions, while lines in the XY-plane thin-section the lines were parallel to the 0-180º directions and 90-270º directions. In the XY-plane thin-sections, images were also rotated so another set of lines would be parallel to the 45-225º and 135-315º directions, corresponding to the sample orientations shown in Figure 4.5c. The number of fractures that intersected the orthogonal lines was counted, allowing the crack surface area per unit volume (Underwood, 1970) to be calculated:

$$S_V = \left(\frac{\pi}{2P_I}\right) + \left(2 - \frac{\pi}{2}\right) P_{II} \qquad (3)$$

where S_V is the crack surface area per unit volume (mm^2/mm^3), P_I is the number of cracks intersected by horizontal lines, and P_{II} is the number of cracks intersected by vertical lines. Anisotropy of crack distribution (Underwood, 1970) was also characterized through:

$$\Omega_{23} = \frac{P_I - P_{II}}{P_I + \left(\frac{4}{\pi} - 1\right)P_{II}} \quad (4)$$

where Ω_{23} is a dimensionless number. Since crack distribution was measured in four different horizontal directions, S_V and Ω_{23} were calculated using the P_{II} values for each horizontal orientation.

4.3 Experimental Results

4.3.1 Velocity Measurements

The calculated ultrasonic velocities from both sets of experiments are shown in Figures 4.7 and 4.8. Due to issues with apparatus in the octagonal setup, we were unable to record V_{S1} for the vertical axis (i.e., Front-Back) for the Mill Creek, Spavinaw #1, and Spavinaw #2 samples.

The cylindrical tests demonstrate different basement rocks exhibit significant variation in both P- and S-wave velocities (Figure 4.7). KGS 1-32 samples display the highest P-wave velocities in all orientations, while the Jones-46 samples generally have the highest S-wave velocities. By contrast, the Mill Creek samples demonstrate much lower velocities on average compared to the other basement rocks at all confining pressures, though with increased pressure the difference diminishes (Figure 4.7). The gradient of velocity with pressure ($\delta V/\delta\sigma$) is also noteworthy, as it differs with sample orientation and rock type. As a rule, the Jones-46 samples exhibit very shallow velocity gradients while the Mill Creek samples exhibit the highest velocity gradients. Velocity gradients in the

Spavinaw samples are generally low but are highly variable between the KGS 1-32 samples (Figure 4.7). The Jones-46 samples exhibit very little P- or S-wave anisotropy between orientations compared to the other granitic basement rocks.

Velocity measurements in the octagonal samples are both similar and different to measurements recorded during the cylindrical tests (Figure 4.8). P-, S1-, and S2- velocities follow similar trends of non-linear velocity change with increasing pressure. The KGS 1-32 sample generally has the highest or near-highest P-wave velocities in both horizontal and vertical orientations. The Mill Creek sample has significantly lower P- and S-wave velocities than the other rocks for all orientations, but simultaneously demonstrates the greatest increase in velocity from 10 to 60 MPa confining pressures. Both the Spavinaw #1 and #2 samples generally have lower velocities than all but the Mill Creek samples.

However, there are notable differences between octagonal test results. First, the Frisco Railroad sample has high P- and S-wave velocities, though they are generally lower than the Jones-46 or KGS 1-32 measurements. While there is some variability, the Frisco Railroad measurements are more uniform than the Mill Creek sample, despite the similar sampling location (Figure 4.1). As a rule, the octagonal samples exhibit much shallower velocity gradients than any of the cylindrical samples do. To show this, the change in velocity from 10 to 60 MPa was shown for all samples in Figure 4.9. The change in velocity with confining pressure is greater for all cylindrical samples compared to the octagonal samples. The reason for this difference is unknown but can possibly be attributed the effect of different sample sizes (i.e., better sampling of fractures and damage), differences in the experimental setups, or the different frequencies used for the velocity tests (i.e., higher frequencies will have smaller wavelengths and better sample rock microstructures).

4.3.2 Dynamic Elastic Moduli

The average dynamic Young's modulus (E_d) and Poisson's ratio (υ_d) in both the horizontal and vertical orientations are shown in Figure 4.10. Average moduli were calculated from the sum of both vertical and horizontal measurements using both the S1 and S2 measurements to show how rock elasticity varies in the basement depending both upon the direction of propagation and the shear-wave polarization. E_d tends to increase with pressure for all the samples, with the Jones-46 samples displaying the least change with pressure and the Mill Creek samples displaying the greatest. In contrast, υ_d tends to exhibit minor to no change with pressure. Both the octagonal and cylindrical tests seem to exhibit trends of either static Poisson's ratio with pressure or a slight increase with pressure. Given the known relationship between Poisson's ratio and the V_P/V_S ratio (Christensen, 1996), this suggests an increasing V_P/V_S ratio with pressure and depth should be expected in the crystalline basement for Oklahoma and Kansas.

4.3.3 Microstructural Observations

Linear density of vertically-oriented (P_I) and horizontally-oriented (P_{II}) fractures is shown in Table 4.3 along with crack area per rock volume (S_V) and crack anisotropy (Ω_{23}) and for each orientation. S_V and Ω_{23} were calculated for the four different horizontal directions of each sample, in order to show how the calculations varied depending upon the orientation of the samples.

From the fracture data it is clear that crack distribution in all the samples is heterogenous and varies with the individual lithologies in the basement. The S_V parameter across the samples shows the total area of fractures per volume is greatest in the Mill Creek samples, as even after hydrostatic compression the fracture densities are more than twice

that of any other rock type. This is significant when compared to the Frisco Railroad borehole sample from the same area. The high S_V shows that in the near surface fracture content will be heavily enhanced, even compared to samples from a few hundred meters depth. The lowest fracture content observed was in the Jones-46 sample, both in the vertical and horizontal orientations.

To demonstrate fracture anisotropy within the basement samples, Figure 4.11 shows the linear fracture density measured in both vertical (YZ-Plane) and horizontal (XY-Plane) thin-sections. The degree of anisotropy is reflected in the Ω_{23} values, with positive values indicating vertically dominant fracture orientations and negative values indicating horizontally dominant fracture orientations (Table 4.3). For the Frisco Railroad and Mill Creek samples, the horizontal fracture density is greater than all the vertical fracture density measurements. In the case of the Jones-46 sample, horizontally oriented fractures are slightly preferred, though the difference is relatively small. Similarly, in the Spavinaw #1 sample the average fracture anisotropy is 0 across the sample, despite nearly twice the fracture density of the Jones-46 sample. In the KGS 1-32 sample, although the difference is small, the vertically oriented fractures predominate over the horizontally oriented fractures. It is interesting to note that these observations are perhaps indicative of a trend across the region of study in the basement (Figure 4.1). The samples from southern Oklahoma display distinct horizontally oriented fracturing, while in northern Oklahoma the samples display limited-to-negligible fracture anisotropy between the vertical and horizontal orientations, and in Kansas we see that fractures are more vertically dominant in orientation.

From Figure 4.11, we can also see that the linear fracture density is horizontally anisotropic. Although the degree varies from sample to sample, this is noteworthy because it suggests anisotropic velocity behavior would be observed in for all samples some degree, regardless of the imposed stress field.

4.4 Analysis and Discussion

4.4.1 Inherent Velocity Anisotropy

All geologic materials are to a greater or lesser extent anisotropic, the degree to which is thought to depend primarily upon lithologic and microstructural characteristics in a given material. In crystalline rocks, spatial variations of seismic velocities are primarily attributed to fracture densities and the preferential opening/closing of cracks relative to the principal stresses. Our results demonstrate that basement rocks from Oklahoma and Kansas exhibit both velocity and microstructural anisotropy regardless of the imposed stress field. This suggests the inherent characteristics of the basement lithologies will influence seismic anisotropy.

When considering the anisotropy of a given medium, three common models for describing anisotropic structure in the subsurface are vertically transverse isotropy (VTI), horizontally transverse isotropy (HTI), and orthorhombic symmetry (ORT). Each model describes how velocity changes rotation relative to an axis of symmetry aligned with the minimum velocity measured. VTI and HTI are primarily used to describe anisotropy for sedimentary rocks and materials with vertically aligned fractures, respectively, with ORT being a combination of the two for materials with both vertical and horizontal anisotropy (e.g., vertically fractured sedimentary rocks).

To show the vertical and horizontal variations in velocity, we plotted the ratios of horizontal and vertical velocities for all horizontal measurements with the octagonal samples (i.e., $V_{Horzontal}/V_{Vertical}$) in Figure 4.12. Ratio values of 1 indicate negligible velocity anisotropy in the vertical plane, while higher or lower values indicate the degree of anisotropy in the vertical orientations. For most of the basement rocks tested, V_P ratios show very small degrees of anisotropy in the vertical plane, with a slight preference for higher vertical velocities than horizontal overall. V_S ratios show much greater anisotropy in the vertical plane by comparison across all orientations, an expected occurrence given the greater prevalence of shear-wave splitting in the crust. In contrast to the V_P ratios, lower V_S ratios indicate shear wave velocities are more often greater horizontally than vertically.

Of all the samples, the Mill Creek sample shows the largest degree of anisotropy between all orientations, both in the vertical and horizontal planes. While the ratio values for most of the basement rocks tend to approach 1 as confining pressure increases, the Mill Creek samples remain highly anisotropic at higher pressures, even increasing for the case of the V_P ratios. The horizontal anisotropy can be seen by comparing between the ratios for different horizontal orientations (Figure 4.12). Anisotropy in the horizontal plane, between the different horizontal measurements, is more prominent than within the vertical plane. Even the most isotropic basement rock, the Jones-46 sample, shows distinct maximum and minimum V_S about the horizontal plane, with large ratios in the 0-180º directions and low ratios in the 45-225º directions.

From the velocity ratios it is clear that the different basement rocks are both vertically and horizontally anisotropic, and may be more accurately characterized with an orthorhombic or even orthotropic symmetry, as suggested by Sano et al. (1992) for granitic

rocks. The question then becomes to what degree are the basement rocks anisotropic in both the horizontal and vertical planes. Seismic anisotropy is often characterized in terms of Thomsen's parameters, which are a simple method for expressing the magnitude of anisotropy in a transverse isotropic medium (Thomsen, 1986; Thomsen, 1988). Using these parameters, the P- and S-wave velocity anisotropy can be shown as a function of velocity orientation. In particular, the P-wave anisotropy (ε) and S-wave anisotropy (γ) parameters are given by:

$$\varepsilon = \frac{C_{11} - C_{33}}{2C_{33}} = \frac{\rho V_{PH}^2 - \rho V_{PV}^2}{2\rho V_{PV}^2} \quad (4)$$

$$\gamma = \frac{C_{66} - C_{44}}{2C_{44}} = \frac{\rho V_{SH}^2 - \rho V_{SV}^2}{2\rho V_{SV}^2} \quad (5)$$

where V_{PH} and V_{PV} are the horizontal and vertical P-wave velocities, V_{SH} and V_{SV} are the horizontal and vertical S-wave velocities, and ρ is the bulk density, respectively. As the axis of symmetry seems to vary between the crystalline rocks (i.e., lacks a uniform symmetry plane between materials), we calculated the parameters assuming VTI for each horizontal orientation measured (Figure 4.13). Since the S1 and S2 velocities were not always collected or clear for some test orientations, shear waves were averaged for the calculation of γ.

The trends in Figure 4.13 are similar to those observed in Figure 4.12. For both anisotropy parameters, positive values indicate a maximum horizontal velocity while negative values indicate a maximum vertical velocity. P-wave anisotropy parameters are small overall, with only the Mill Creek and Spavinaw samples exhibiting large positive or negative values. Between samples, a slightly positive P-wave anisotropy seems to be favored in the vertical planes. By contrast, S-wave anisotropy is much more variable and

larger than P-wave anisotropy. Negative γ values are preferred over positive values, and parameters tend to remain flat or rather than approach 0 as pressure increases. Of interest is the observation that unlike most of the P-wave anisotropy parameters measured, S-wave anisotropy does not approach 0 with increasing pressure in most cases. This may indicate that the response of rocks in the basement to a uniform pressure is not necessarily uniform.

Our results indicate that horizontal anisotropy is significant in most of the basement rocks, and that this varies with the different lithologies. Considering the role anisotropy plays in determining the stress orientations, the magnitude of this intrinsic anisotropy should be understood. The horizontal velocity anisotropy can be quantified as a function of the maximum and minimum velocities (Birch, 1961; Ji et al., 2007), as in:

$$An = 100 * \frac{V_{Max} - V_{Min}}{V_{Mean}} \quad (6)$$

where V_{Max}, V_{Min}, and V_{Mean} are the maximum, minimum and mean horizontal velocities measured for each sample. The calculated horizontal velocity anisotropy is plotted as both a function of pressure and depth for all the experimentally tested rocks in Figure 4.14. Depths were calculated by assuming lithostatic and hydrostatic gradients equal to 27.5 and 10 MPa/km for the Oklahoma and Kansas region (Walsh and Zoback, 2016; Kolawole et al., 2019; Kibikas et al. 2020).

From Figure 4.14 we can see that different the anisotropic behavior with increasing pressure varies between stresses. Three patterns were observed in particular. Pattern 1: With increasing pressure the anisotropy will rapidly decrease in a quasi-exponential manner (e.g., Mill Creek cylindrical samples). This pattern has been observed by others, including Kern and Wenk (1990), Wang (2002), and Ji et al. (2007), and is primarily attributed to the closure of the aligned microcracks which reinforce any anisotropy induced

by mineral or fabric preferred orientation in the samples. Pattern 2: velocity anisotropy initially increases with pressure then begin to decrease or approach a steady-state value at higher pressures (Figure 4.14c, Frisco Railroad sample). This may possibly be attributed to heterogeneous closure of microcracks at low pressure, potentially opposing some other mechanism of generating anisotropy. Pattern 3: Anisotropy remains fairly constant when pressurization occurs, changing very little except perhaps at the lowest pressures (Figure 4.14b, Jones-46 samples). This pattern indicates an overall lack of anisotropic features such as microcracks, and that the anisotropy may be attributed more to factors such as grain alignment which are unchanged by such low pressures (Ji et al., 2007).

4.4.2 Microstructural Controls of Anisotropy

A few inferences may be made from the velocity anisotropy trends. First, the horizontal anisotropy is largest in the Mill Creek samples, followed by the Spavinaw and KGS 1-32 samples (Figure 4.14). The Frisco Railroad and Jones-46 samples exhibit the lowest anisotropy, as well as the smallest change in anisotropy with pressure/depth. These observations comport with the initial sample characterization and fracture measurements; the Mill Creek samples are the least dense (Table 4.2) and this can be attributed to the large fracture densities in Table 4.3. While the KGS 1-32 and Spavinaw samples are denser overall than the Mill Creek rocks, both XRD and thin-section analysis show that these rocks have undergone heavy hydrothermal alteration compared to the other rocks (Table 4.1). Furthermore, SEM analysis of the KGS 1-32 and Spavinaw samples shows that much of the fracture content has been sealed by calcite and chlorite, respectively, and may easily affect the inherent anisotropy measured (Figures 4.13 and 4.14). These observations

indicate fractures in the basement do control velocity anisotropy to a greater or lesser degree.

Second, comparing the horizontal anisotropy in the Mill Creek and Frisco Railroad octagonal samples (Figure 4.14), the effect of depth and weathering processes can be demonstrated for a given lithology. Though the rocks come from the same area, the Mill Creek sample is from an outcrop while the Frisco Railroad sample is from a borehole (depth ~55 m). At the surface, the basement rock is highly fractured and highly anisotropic, while a few dozen meters depth produces a much lower anisotropy and fracturing. Despite the effect of depth though, both samples appear to preserve a horizontally dominant fracture anisotropy (i.e., negative S_V values, Table 4.3). By contrast, rocks from northern Oklahoma and southern Kansas all retain near 0 or positive S_V values, both from outcrop and core samples, meaning this is likely a feature of the rocks and not depth itself. It appears that with depth and pressure, rocks of the same lithology may preserve the dominant trends in fracture anisotropy, and possibly velocity anisotropy as result.

To show the effect of inherent fracture density and fracture aperture orientations on velocity, we plotted the horizontal velocities at 60 MPa and fracture densities in Figure 4.15. Upon stress relaxation after the pressurization cycle, it is expected that the underlying fabric of the fractures should remain unchanged and thus comparable (Plumb et al., 1984). In the horizontal plane, P-wave anisotropy is lowest in the Jones-46, Frisco Railroad, and to a lesser extent KGS 1-32 samples. The fracture anisotropy is similarly low for these samples as well, though we note for the Frisco Railroad sample a higher preference for fracturing in the 0-180º while velocity is greatest in the 45-225º directions. Considering the relative magnitude of fractures and the low P-wave anisotropy, it is entirely feasible such

small variance is as much controlled by other textural features such as grain orientations. This is supported by the fact that the Jones-46 sample shows a preferred fracture orientation parallel to 0-180º but exhibits a peak velocity in the 45-225º and 90-270º directions (Figure 4.15b). While the anisotropy may be controlled by the fracture orientations when an anisotropic stress field is imposed, this is not always guaranteed. Others have noted that highly fractured rocks, such as in shear zones or near faults, will exhibit anisotropy that does not correlate with the fracture orientations observed (Boness and Zoback, 2004; Goswami et al., 2019). This is especially important for the Mill Creek, and possibly Spavinaw #1, samples which show anomalous velocity anisotropy in the horizontal planes.

An additional point of note is the horizontal measurements of the two oriented samples (Figures 4.15d and 4.15e). In these samples, both the velocity and fracture orientations correspond to the cardinal directions, with 0-90-180-270 corresponding to N-E-S-W for each sample. For the Mill Creek sample, the anisotropy can be largely dismissed for correlating stress orientations as the high degree of fracturing is likely to generate anomalous stress field calculations. For the Spavinaw #1 sample there are two interesting points of note. First, the two peak velocities observed occur in the 45-225º and 135-315º directions, roughly equivalent to the NE-SW and NW-SE directions. These correlate well with the principal fracture orientations noted by Kolawole et al. (2019) for basement rocks in Oklahoma. Additionally, the Spavinaw #2 sample also has maximum P- and S-wave velocities in the same orientations. Secondly, the primary fracture direction in the Spavinaw #1 sample is 45-225º or roughly NE-SW in the region. This agrees both with larger fracture and fault data for the region but also with the purported stress orientations determined from shear-wave splitting in the state (Alt and Zoback, 2017).

4.4.3 Comparing Laboratory and Field Data

Velocity anisotropy and the polarization of shear-waves is a potentially useful tool for geophysical determination of either the stress or fault orientations in the crystalline basement, as both can affect the polarization of seismic velocities. Ortega Romo (2020) showed that shear-wave splitting in the basement produced two fast polarization directions across north Oklahoma and south Kansas. The author showed that in most areas the fast polarizations of shear waves corresponded to either S_{HMax} or mapped basement faults (Qin et al., 2019). They also noted several discrepancies: 1) the local and regional observations differ for the primary polarization direction (attributed to S_{HMax}) in several areas; 2) where S_{HMax} and fault orientations are shown to both match the fast polarization direction, the cause of the source of the second polarization is unknown and may be attributed to several factors (stress rotations near fault, fault related fabrics, etc.); 3) the dominant factor influencing each shear-wave polarization differs across the Oklahoma/Kansas. These results suggest that at a regional level, the directions of velocity polarization often correspond to the principal stress directions, especially where seismogenic and sedimentary faults are shown to be parallel to S_{HMax}. However, locally the regional stress orientations sometimes differ from the fast polarization directions, which is attributed to faults or even unknown structural and lithologic features (Cochran et al., 2020).

At the experimental level, it is clear that intrinsic anisotropy exists in many basement rocks across the region. This poses an issue when velocity anisotropy, particularly shear-wave splitting, is used as a tool to measure the stress orientations. For example, Alt and Zoback (2017) used the velocity anisotropy determined from well logs in Oklahoma to determine the horizontal stress directions, with the only criterion being that

the measured anisotropy be greater than 2%. From the data in Figure 4.14, it is clear that shear-wave anisotropy is near or greater than 2% in most of the rocks unrelated to the stress orientations. While anisotropy often decreases with depth and pressure (e.g., Birch, 1961; Kern and Wenk, 1990), our observations suggest it may not be a reliable tool to use without a prior understanding of the local geology.

As an example of this disparity between the measured anisotropy and the inherent rock properties, we determined the anisotropy from the KGS 1-32 well log within the basement using Eq. 6 and compared it with our experimental measurements of the same rock in Figure 4.16. KGS 1-32 was a CO2-EOR well drilled in the Wellington Field in Kansas, penetrating a significant amount of basement rock and was able to record the maximum and minimum velocities in the crystallin rock (Schwab et al., 2017). P- and S-wave anisotropy in the well log measurements on average ranged from 2-10%, with high anisotropy (nearing ~25%) being observed at ~1.4 km depth (Figure 4.16c).

The mean anisotropy measurements for the KGS 1-32 well are shown in Table 4.4. The mean well log anisotropies are weighted higher slightly due to the anomalously high values around ~1.4 km, possibly due to the presence of anomalous fracturing or faulting (Goswami et al. 2019). The average P-wave anisotropy between the octagonal and cylindrical ultrasonic measurements is around 4.59%, nearly equal to the average anisotropy in measured in the well log. The mean shear-wave anisotropies are more variable, but the S2 anisotropy is fairly close between the experimental and well log measurements. It is feasible that a greater anisotropy was detected in our samples due to damage during sample preparation and the higher frequencies used to measure sample velocities (Chapman, 2003; Barton, 2006; Liu et al., 2006). Nevertheless, since our results

utilized an isotropic stress field, it seems unlikely that anisotropy in the well log measurements is solely due to the stress field.

While the orientations of the principal horizontal stresses are not known for our samples or the well log, a few observations are worthy of note. Schwab et al. (2017) reported that a majority of the faults in the Wellington field area were primarily strike-slip and nearly vertical, striking predominantly NNE (~i.e., 10-40º). Tensile fractures and borehole breakouts corroborated the observed dominant fracture trend (Schwab et al., 2017). They postulated that this direction was parallel S_{HMax} for the region. In our fracture measurements with the KGS sample, we noted the dominant fracture orientation was vertical, with two orthogonal fracture orientations in the horizontal plane being higher than the others (Table 4.3, $P_{II}^{45\text{-}225}$ and $P_{II}^{135\text{-}315}$), with the greatest in the 45-225º orientation. The existence of two dominant, mostly orthogonal fracture orientations in the basement had been previously hypothesized by others (e.g., Kolawole et al., 2019) and agrees with our observations here. We also find that the maximum horizontal P- and S2-wave anisotropy exists between the 45-225º and 135-315º directions, and that with pressure the anisotropy between the two orientations increases even as velocity anisotropy decreases between the 0-180º and 90-270º directions. In other words, as confining pressure increases crack closure leads to a maximum velocity anisotropy orientation becoming more pronounced. A not insubstantial amount of this anisotropy can be attributed to the pre-existing microcrack orientations (and possibly grain alignment). However, this anisotropy will not necessarily reflect the stress field and should be pared with 1) other methods for determining the in-situ stress orientations and 2) a more complete understanding of the regional lithology.

4.5 Conclusions

Using a suite of experimental ultrasonic velocity tests, we were able to directly characterize the velocity anisotropy in the crystalline basement of Oklahoma and Kansas in an isotropic stress field. Ultrasonic velocities in the horizontal and vertical directions were measured for five basement rock types from outcrop and borehole samples. Our observations were paired with thin-section characterization of fractures in the vertical and horizontal planes to demonstrate the effect of intrinsic anisotropy on basement rocks. Our results show there is a not inconsiderable degree of velocity anisotropy present in basement rocks at the experimental level, both in the vertical and horizontal directions. The basement rocks are shown to exhibit both pressure- and orientation-dependent velocity anisotropy regardless of the stress directions. Microstructural observations indicate crack anisotropy varies in the basement with depth, location, and rock type. Velocity and fracture measurements were related to attempts measure the stress orientations in the field. We determined that, within certain basement lithologies, sufficient intrinsic anisotropy exists due to microcrack orientations to affect in-situ stresses determined by well log and geophysical measurements of velocity. The impact of intrinsic velocity anisotropy may be mitigated though with sufficient understanding of the regional basement lithology and comparison with other stress field determination methods.

Acknowledgements

This material is based upon work supported by the Department of Energy under Award Number DE-FE0031687."

Disclaimer: This report was prepared as an account of work sponsored by an agency of the United States Government. Neither the United States Government nor any agency

thereof, nor any of their employees, makes any warranty, express or implied, or assumes any legal liability or responsibility for the accuracy, completeness, or usefulness of any information, apparatus, product, or process disclosed, or represents that its use would not infringe privately owned rights. Reference herein to any specific commercial product, process, or service by trade name, trademark, manufacturer, or otherwise does not necessarily constitute or imply its endorsement, recommendation, or favoring by the United States Government or any agency thereof. The views and opinions of the author expressed herein do not necessarily state or reflect those of the United States Government or any agency thereof.

References

Alt, Richard C., and Mark D. Zoback. "In situ stress and active faulting in Oklahoma." Bulletin of the Seismological Society of America 107, no. 1 (2017): 216-228.

Barton, Nick. Rock quality, seismic velocity, attenuation and anisotropy. CRC press, 2006.

Benson, William Alan. "The Spavinaw granite (proterozoic), Mayes County, Oklahoma." (2014): 258-264.

Birch, Francis. "The velocity of compressional waves in rocks to 10 kilobars: 2." Journal of Geophysical Research 66.7 (1961): 2199-2224.

Boness, Naomi L., and Mark D. Zoback. "Stress-induced seismic velocity anisotropy and physical properties in the SAFOD Pilot Hole in Parkfield, CA." Geophysical Research Letters 31, no. 15 (2004).

Chang, Kyung Won, and Paul Segall. "Injection-induced seismicity on basement faults including poroelastic stressing." Journal of Geophysical Research: Solid Earth 121, no. 4 (2016): 2708-2726.

Chapman, Mark. "Frequency-dependent anisotropy due to meso-scale fractures in the presence of equant porosity." Geophysical prospecting 51, no. 5 (2003): 369-379.

Christensen, Nikolas I. "Poisson's ratio and crustal seismology." Journal of Geophysical Research: Solid Earth 101, no. B2 (1996): 3139-3156.

Cochran, Elizabeth S., Robert J. Skoumal, Devin McPhillips, Zachary E. Ross, and Katie M. Keranen. "Activation of optimally and unfavourably oriented faults in a uniform local stress field during the 2011 Prague, Oklahoma, sequence." Geophysical Journal International 222, no. 1 (2020): 153-168.

Crampin, Stuart. "Evaluation of anisotropy by shear-wave splitting." Geophysics 50, no. 1 (1985): 142-152.

Crampin, Stuart, and John H. Lovell. "A decade of shear-wave splitting in the Earth's crust: what does it mean? what use can we make of it? and what should we do next?." Geophysical Journal International 107, no. 3 (1991): 387-407.

Denison, Rodger E., M. E. Bickford, Edward G. Lidiak, and Eva B. Kisvarsanyi. "Geology and geochronology of Precambrian rocks in the central interior region of the United States." (1987): 12-14.

Douglass, Peter Mack, and Barry Voight. "Anisotropy of granites: a reflection of microscopic fabric." Geotechnique 19, no. 3 (1969): 376-398.

Ellsworth, William L., Andrea L. Llenos, Arthur F. McGarr, Andrew J. Michael, Justin L. Rubinstein, Charles S. Mueller, Mark D. Petersen, and Eric Calais. "Increasing

seismicity in the US midcontinent: Implications for earthquake hazard." The Leading Edge 34, no. 6 (2015): 618-626.

Fredrich, J. T., G. L. Deitrick, J. Arguello, G. Jose, and E. Derouffigenac. Geomechanical modeling of reservoir compaction, surface subsidence, and casing damage at the Belridge diatomite field. No. SAND2000-1127J. Sandia National Labs., Albuquerque, NM (US); Sandia National Labs., Livermore, CA (US), 2000.

Gambolati, Giuseppe, and Pietro Teatini. "Geomechanics of subsurface water withdrawal and injection." Water Resources Research 51, no. 6 (2015): 3922-3955.

Gao, Yuan, Jing Wu, Yoshio Fukao, Yutao Shi, and Ailan Zhu. "Shear wave splitting in the crust in North China: stress, faults and tectonic implications." Geophysical Journal International 187, no. 2 (2011): 642-654.

Goswami, Deepjyoti, Sukanta Roy, and Vyasulu V. Akkiraju. "Delineation of damage zones from 3 km downhole geophysical logs in the Koyna seismogenic zone, western India." Journal of Geophysical Research: Solid Earth 124, no. 6 (2019): 6101-6120.

Hardebeck, Jeanne L., and Egill Hauksson. "Crustal stress field in southern California and its implications for fault mechanics." Journal of Geophysical Research: Solid Earth 106, no. B10 (2001): 21859-21882.

Hincks, Thea, Willy Aspinall, Roger Cooke, and Thomas Gernon. "Oklahoma's induced seismicity strongly linked to wastewater injection depth." Science 359, no. 6381 (2018): 1251-1255.

Holubnyak, Yevhen, Willard Watney, Jennifer Hollenbach, Jason Rush, Mina Fazelalavi, Tandis Bidgoli, and Dana Wreath. "Pilot Scale CO 2 EOR at Wellington Filed in

South Central Kansas." In SPE Improved Oil Recovery Conference. Society of Petroleum Engineers, 2018.

Ji, Shaocheng, Qian Wang, Denis Marcotte, Matthew H. Salisbury, and Zhiqin Xu. "P wave velocities, anisotropy and hysteresis in ultrahigh-pressure metamorphic rocks as a function of confining pressure." Journal of Geophysical Research: Solid Earth 112, no. B9 (2007).

Jo, Yeonguk, Chandong Chang, Sung-Hoon Ji, and Kyung-Woo Park. "In situ stress states at KURT, an underground research laboratory in South Korea for the study of high-level radioactive waste disposal." Engineering Geology 259 (2019): 105198.

Kern, Hartmut, and H-R. Wenk. "Fabric-related velocity anisotropy and shear wave splitting in rocks from the Santa Rosa Mylonite Zone, California." Journal of Geophysical Research: Solid Earth 95, no. B7 (1990): 11213-11223.

Kibikas, William M., Brett M. Carpenter, and Ahmad Ghassemi. "Mechanical strength and physical properties of Oklahoma's igneous basement." Tectonophysics 777 (2020): 228336.

Kingdon, Andrew, Mark W. Fellgett, and John DO Williams. "Use of borehole imaging to improve understanding of the in-situ stress orientation of Central and Northern England and its implications for unconventional hydrocarbon resources." Marine and Petroleum Geology 73 (2016): 1-20.

Kolawole, F., C. S. Johnston, C. B. Morgan, J. C. Chang, K. J. Marfurt, D. A. Lockner, Z. Reches, and B. M. Carpenter. "The susceptibility of Oklahoma’s basement to seismic reactivation." Nature Geoscience 12, no. 10 (2019): 839-844.

Lee, Ji Soo, John Brumley, Evan Morgan, and Lance Despain. "Three-dimensional ultrasonic wave velocity test system." U.S. Patent 10,345,269, issued July 9, 2019.

Liu, Enru, Mark Chapman, Zhongjie Zhang, and John H. Queen. "Frequency-dependent anisotropy: Effects of multiple fracture sets on shear-wave polarizations." Wave Motion 44, no. 1 (2006): 44-57.

Ljunggren, C., Yanting Chang, T. Janson, and R. Christiansson. "An overview of rock stress measurement methods." International Journal of Rock Mechanics and Mining Sciences 40, no. 7-8 (2003): 975-989.

Mavko, Gary, Tapan Mukerji, and Nicola Godfrey. "Predicting stress-induced velocity anisotropy in rocks." Geophysics 60, no. 4 (1995): 1081-1087.

Nur, Amos, and Gene Simmons. "Stress-induced velocity anisotropy in rock: An experimental study." Journal of Geophysical Research 74, no. 27 (1969): 6667-6674.

Ortega Romo, Angie. "Aspects of Seismicity Clustering, Subsurface Structure, and Stress Orientations." (2020).

Plumb, Richard, Terry Engelder, and David Yale. "Near-surface in situ stress: 3. Correlation with microcrack fabric within the New Hampshire Granites." Journal of Geophysical Research: Solid Earth 89, no. B11 (1984): 9350-9364.

Qin, Yan, Xiaowei Chen, Jacob I. Walter, Jackson Haffener, Daniel T. Trugman, Brett M. Carpenter, Matthew Weingarten, and Folarin Kolawole. "Deciphering the stress state of seismogenic faults in Oklahoma and southern Kansas based on an

improved stress map." Journal of Geophysical Research: Solid Earth 124, no. 12 (2019): 12920-12934.

Rabbel, Wolfgang, and Walter D. Mooney. "Seismic anisotropy of the crystalline crust: what does it tell us?." Terra Nova 8, no. 1 (1996): 16-21.

Reiter, Karsten, and Oliver Heidbach. "3-D geomechanical–numerical model of the contemporary crustal stress state in the Alberta Basin (Canada)." Solid Earth 5, no. 2 (2014): 1123-1149.

Sano, Osam, Yozo Kudo, and Yoshiaki Mizuta. "Experimental determination of elastic constants of Oshima granite, Barre granite, and Chelmsford granite." Journal of Geophysical Research: Solid Earth 97, no. B3 (1992): 3367-3379.

Schwab, Drew R., Tandis S. Bidgoli, and Michael H. Taylor. "Characterizing the potential for injection-induced fault reactivation through subsurface structural mapping and stress field analysis, Wellington field, Sumner county, Kansas." Journal of Geophysical Research: Solid Earth 122, no. 12 (2017): 10-132.

Selves, Tyler. "Factors influencing seismicity in south-central Kansas and northern Oklahoma." PhD diss., Wichita State University, 2017.

Snee, Jens-Erik Lund, and Mark D. Zoback. "State of stress in Texas: Implications for induced seismicity." Geophysical Research Letters 43, no. 19 (2016): 10-208.

Takemura, Takato, Aliakbar Golshani, Masanobu Oda, and Kenichiro Suzuki. "Preferred orientations of open microcracks in granite and their relation with anisotropic elasticity." International Journal of Rock Mechanics and Mining Sciences 40, no. 4 (2003): 443-454.

Thomsen, Leon. "Weak elastic anisotropy." Geophysics 51, no. 10 (1986): 1954-1966.

Thomsen, Leon. "Reflection seismology over azimuthally anisotropic media." Geophysics 53, no. 3 (1988): 304-313.

Tsuji, Takeshi, Jack Dvorkin, Gary Mavko, Norimitsu Nakata, Toshifumi Matsuoka, Ayako Nakanishi, Shuichi Kodaira, and Osamu Nishizawa. "Vp/Vs ratio and shear-wave splitting in the Nankai Trough seismogenic zone: insights into effective stress, pore pressure, and sediment consolidation." Geophysics 76, no. 3 (2011): WA71-WA82.

Underwood, Ervin E. "Quantitative stereology." ADDISON-WESLEY PUBLISHING CO, READING, MASS. 1970, 274 P (1970).

Walsh III, F. Rall, and Mark D. Zoback. "Probabilistic assessment of potential fault slip related to injection-induced earthquakes: Application to north-central Oklahoma, USA." Geology 44, no. 12 (2016): 991-994.

Wang, Zhijing. "Seismic anisotropy in sedimentary rocks, part 2: Laboratory data." Geophysics 67, no. 5 (2002): 1423-1440.

Williams, John DO, Mark W. Fellgett, and Martyn F. Quinn. "Carbon dioxide storage in the Captain Sandstone aquifer: determination of in situ stresses and fault-stability analysis." Petroleum Geoscience 22, no. 3 (2016): 211-222.

Yu, Weiqi. "Laboratory Geomechanical Characterization of the Arbuckle Group and Crystalline Basement Rocks in Oklahoma." (2017).

CHAPTER IV FIGURES

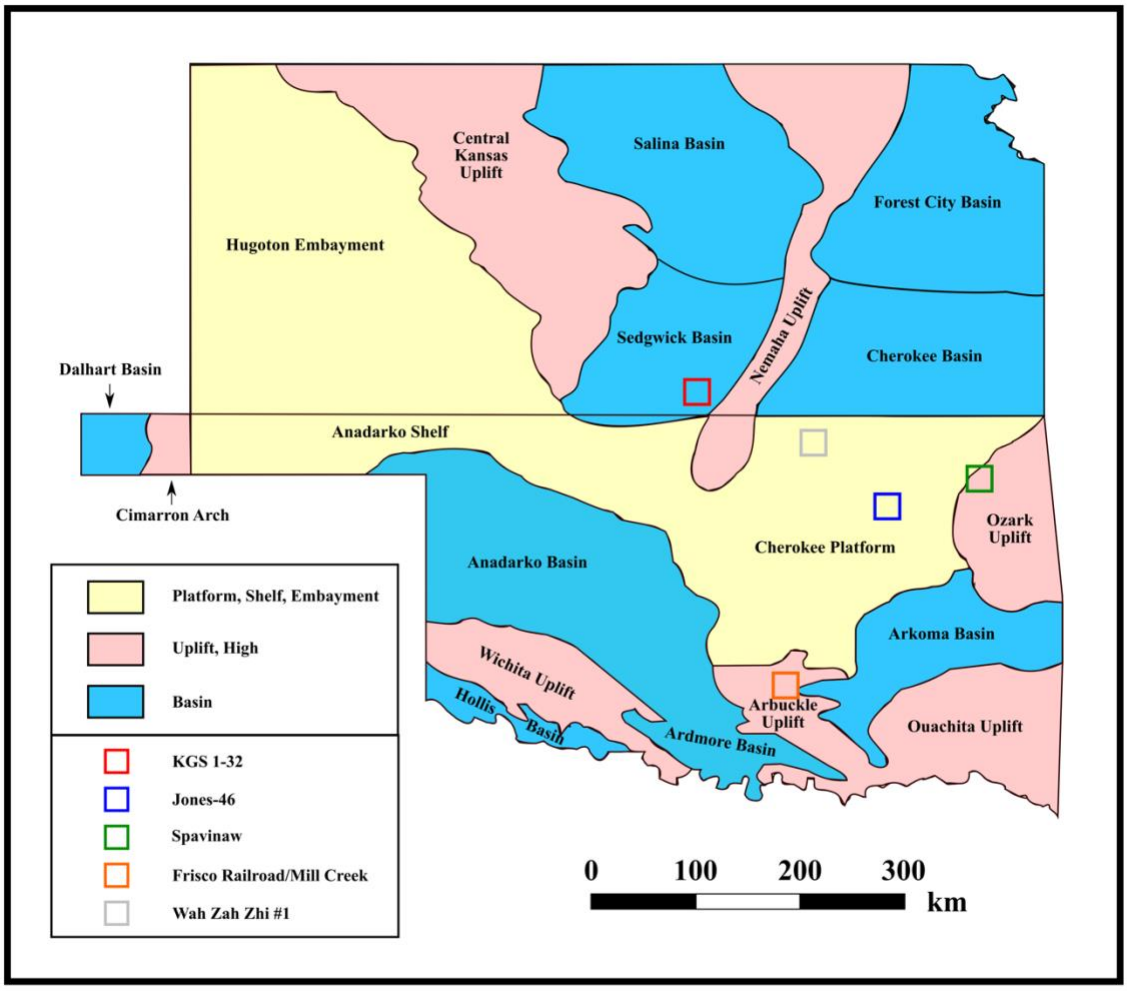

Figure 4.1: Regional tectonic provinces of Oklahoma and Kansas with the rock sampling and well locations marked by boxes. Modified from Selves (2017).

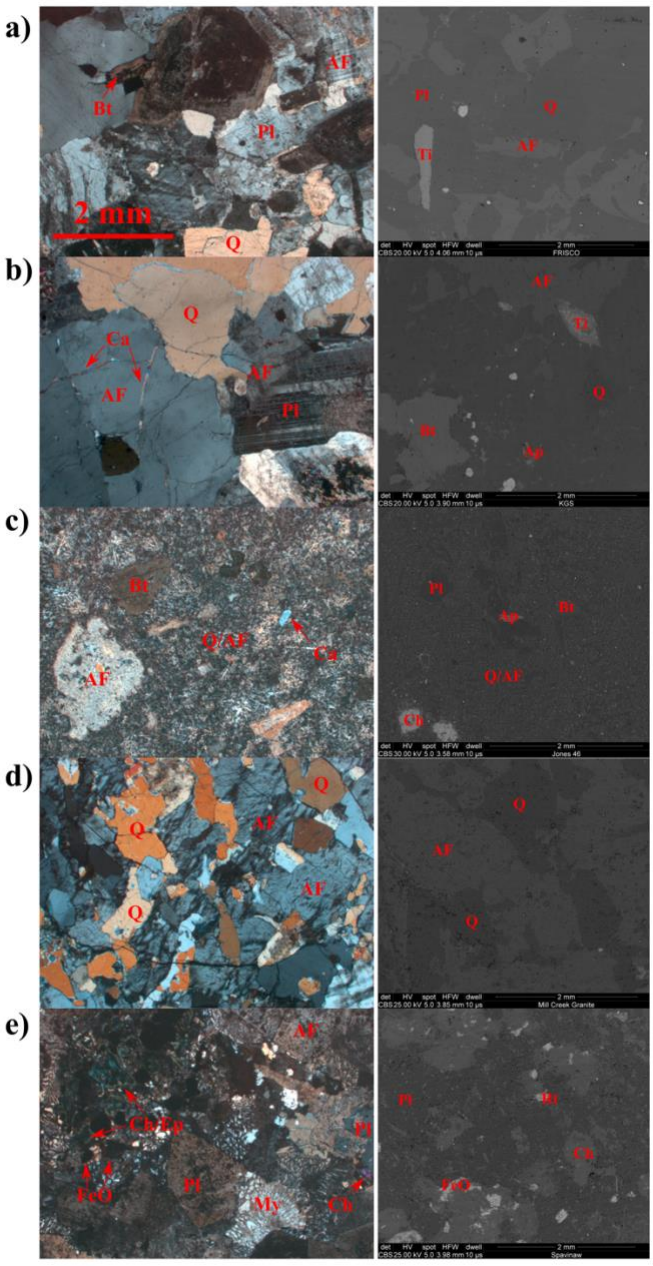

Figure 4.2: Photomicrographs (left) and SEM images (right) of five basement rock samples: a) Frisco Railroad; b) KGS 1-32; c) Jones-46; d) Mill Creek; e) Spavinaw. The symbols used indicate: Q = quartz; AF = K-feldspar; Pl = plagioclase; Bt = biotite; Ca = calcite; Ti = titanite; Ap = apatite; Ch = chlorite; Rt = rutile; Ep = epidote; FeO = iron-oxide; My = myrmekite texture.

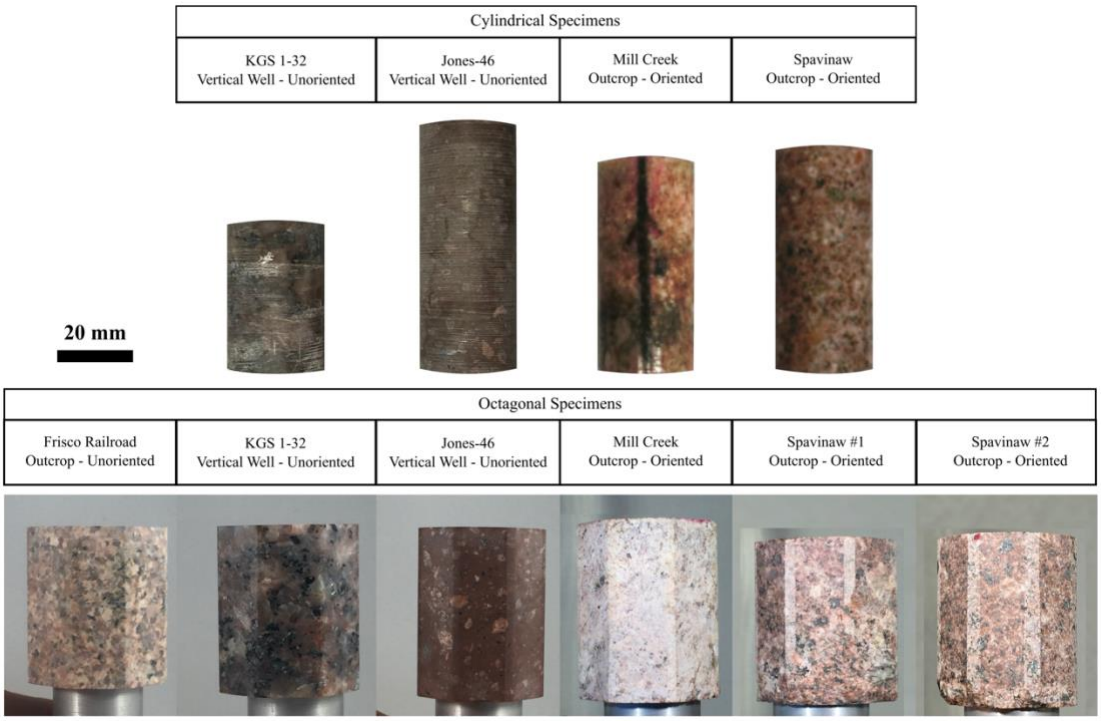

Figure 4.3: Images of tested cylindrical (top row) and octagonal (bottom row) samples.

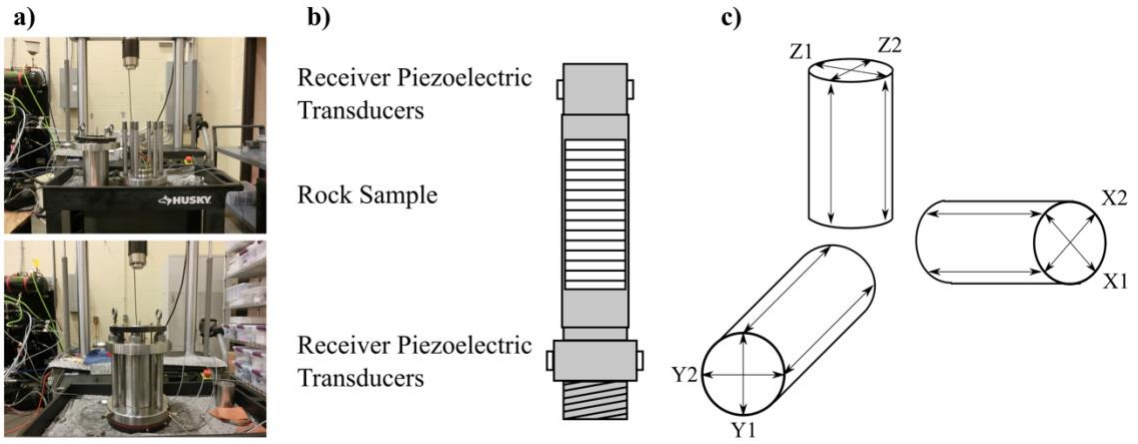

Figure 4.4: Schematic of the velocity setup for the cylindrical sample tests. a) Photos of the MTS 810 apparatus used in this study; b) general setup of each sample before loading into apparatus for testing; c) general orientation of the samples and velocity measurements for the first (X1/Y1/Z1) and second (X2/Y2/Z2) measurements.

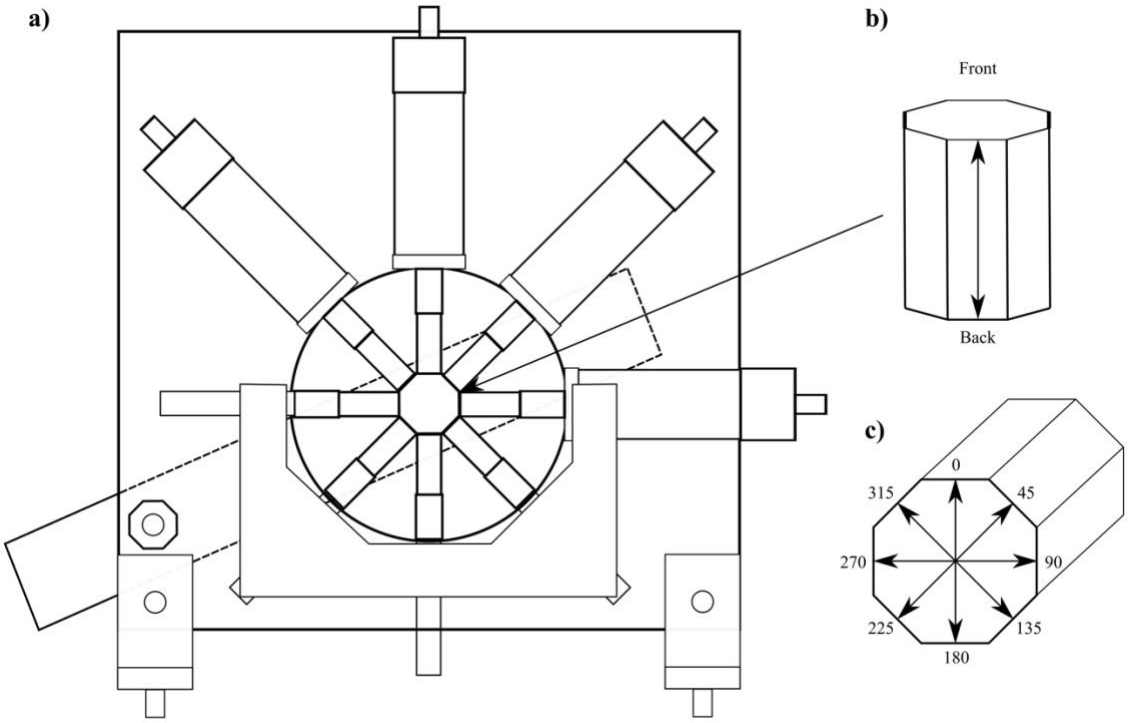

Figure 4.5: a) Schematic of apparatus used for octagonal velocity tests and b) orientation of velocity measurements in octagonal samples, with 0-360º being horizontal orientations and Front-Back being velocities measured being velocities traveling vertically up (Front) and down (Back).

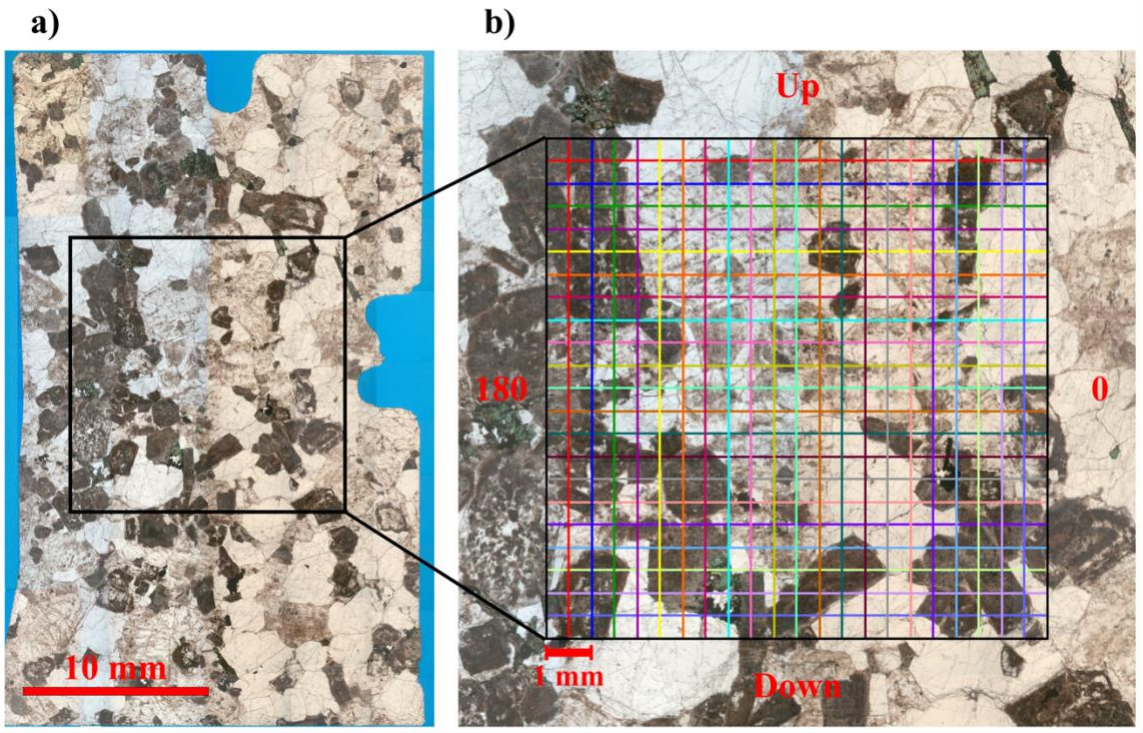

Figure 4.6: a) Composite image of photomicrographs for vertically oriented thin-section and b) example of gridlines for calculating fracture density over sample, each set of lines parallel to one of the primary directions for each thin-section.

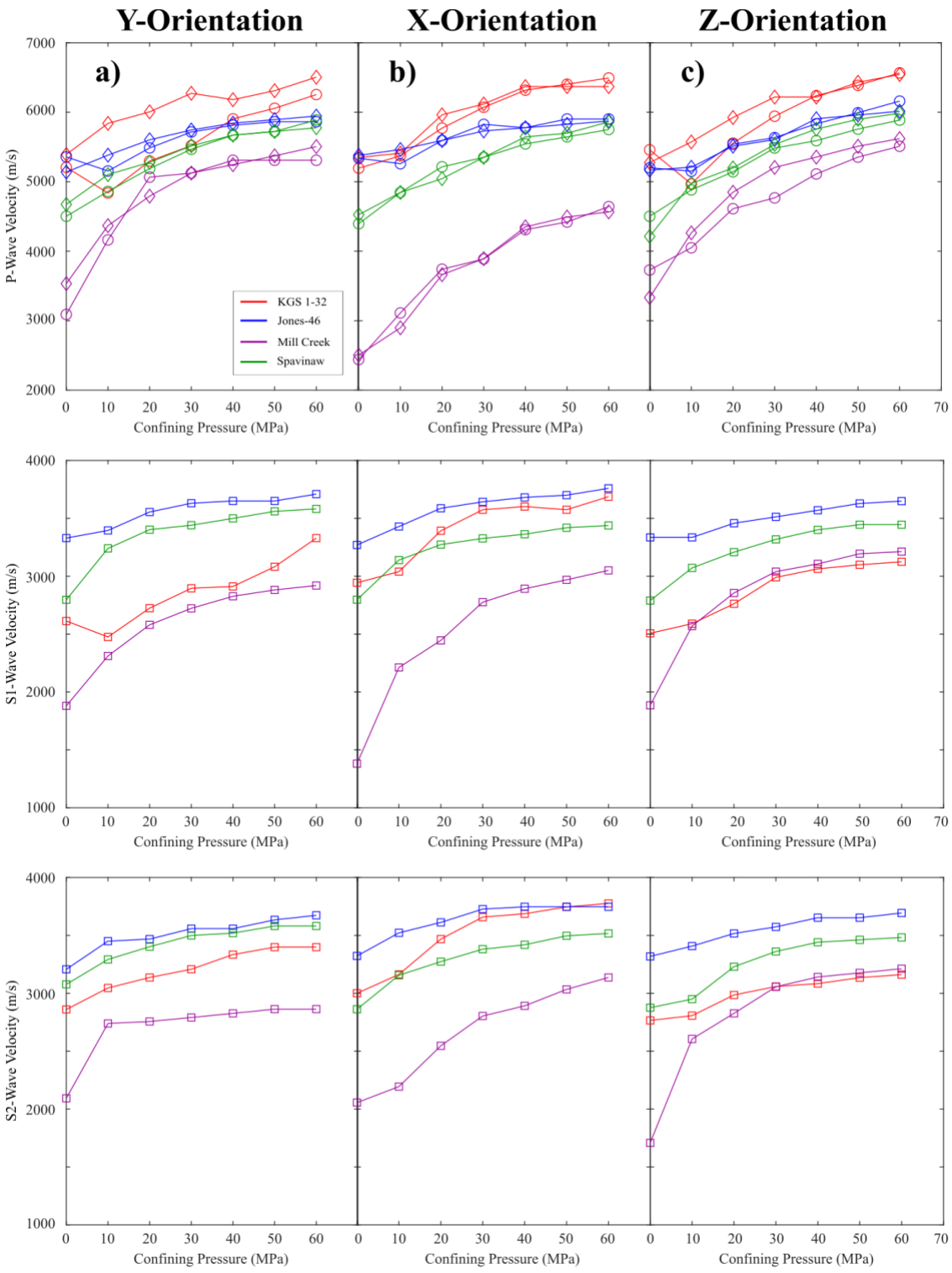

Figure 4.7: Velocity measured for cylindrical samples as a function of confining pressure. P-, S1-, and S2-wave velocities are given for the a) Y-orientation, b) X-orientation, and c) Z-orientations in each column.

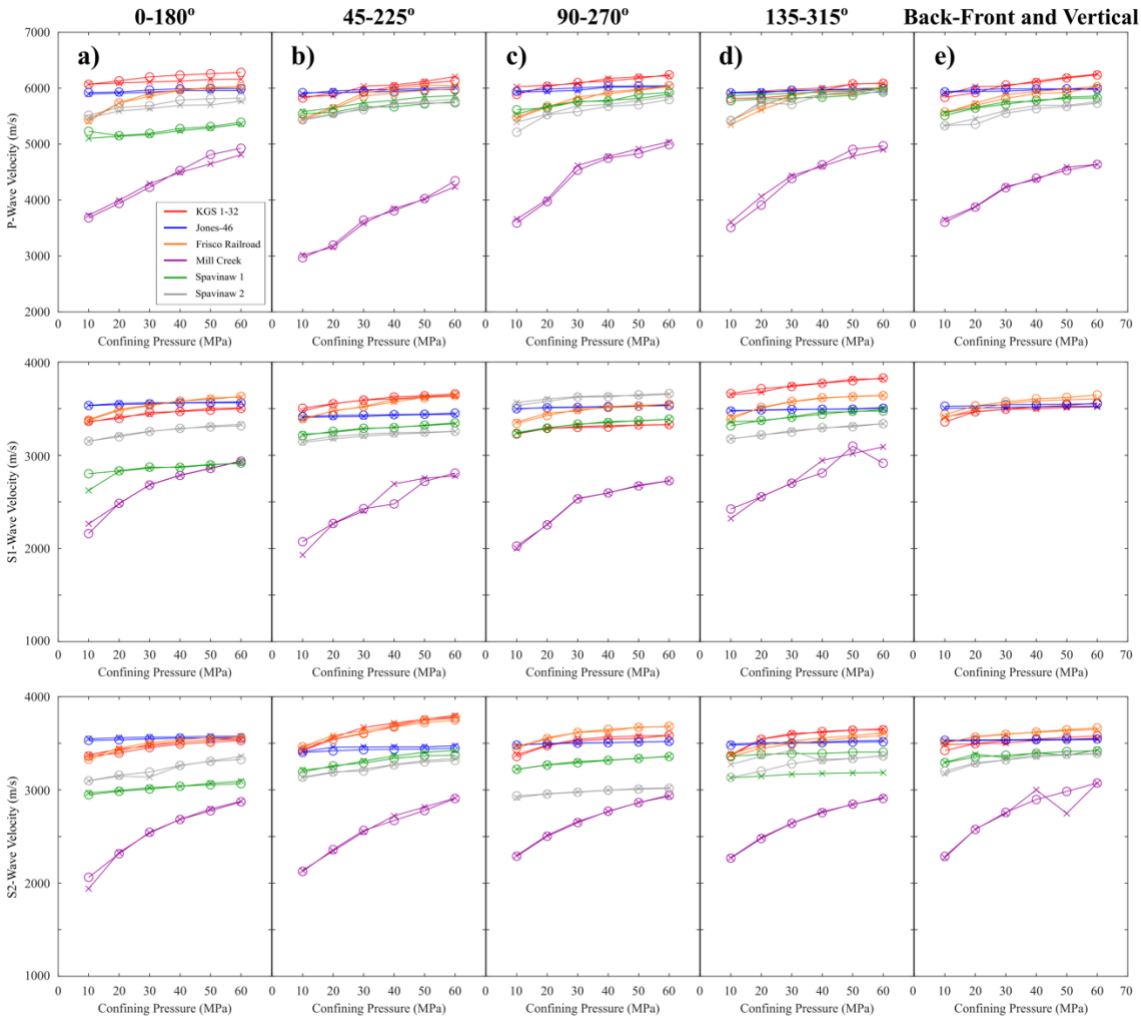

Figure 4.8: Velocity of P-, S1-, and S2-waves for octagonal samples measured in horizontal and vertical directions. P-, S1-, and S2-wave velocities are shown for the horizontal orientations a) 0-180, b) 45-225, c) 90-270, and d) 135-315, as well as the vertical orientation e) Front-Back. X indicate the 0/45/90/135/Back measurements while circles indicate 180/225/270/315/Front measurements.

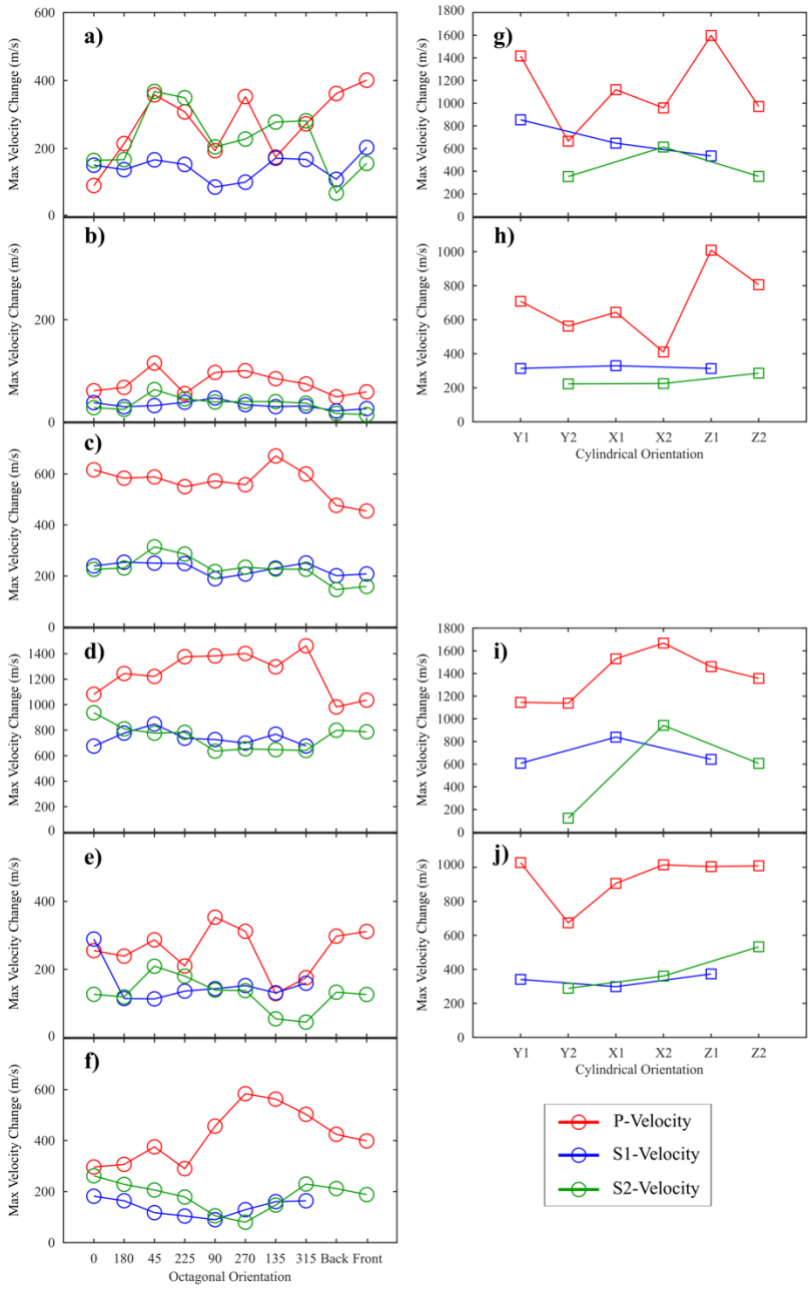

Figure 4.9: Maximum velocity change in octagonal (a-f) and cylindrical (g-j) sample tests from 10 to 60 MPa. Left column shows the maximum change in the horizontal plane in each orientation and the vertical plane for a) KGS 1-32, b) Jones-46, c) Frisco Railroad, d) Mill Creek, e) Spavinaw 1, and f) Spavinaw 2 octagonal samples. Right column shows the maximum change in the horizontal plane in each orientation and the vertical plane for g) KGS 1-32, h) Jones-46, i) Mill Creek, and j) Spavinaw cylindrical samples.

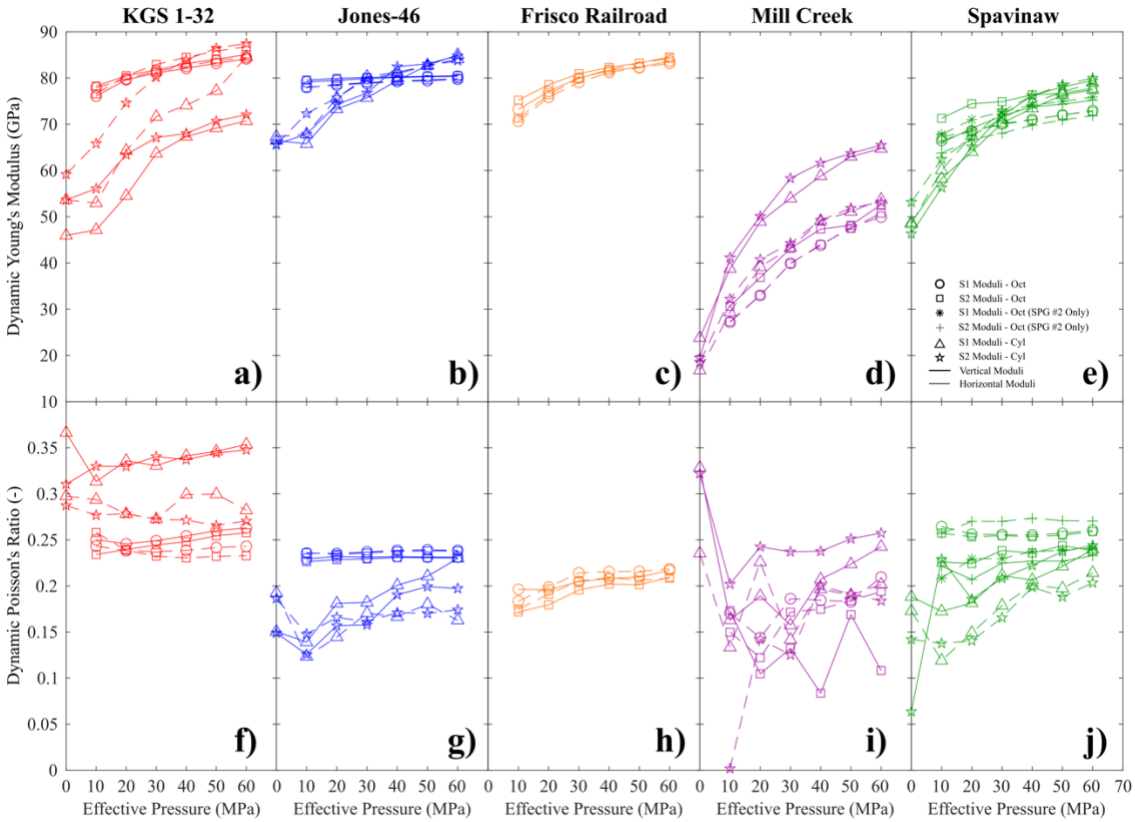

Figure 4.10: The relationship of the dynamic Young's moduli (a-e) and Poisson's ratio (f-j) with pressure is shown for both octagonal and cylindrical tests. Elastic moduli were calculated for samples KGS 1-32 (a and f), Jones-46 (b and g), Frisco Railroad (c and h), Mill Creek (d and i), and Spavinaw (e and j). Moduli were calculated for both the S1 and S2 velocity measurements from both the vertical measurements (solid lines) and horizontal measurements (dashed lines).

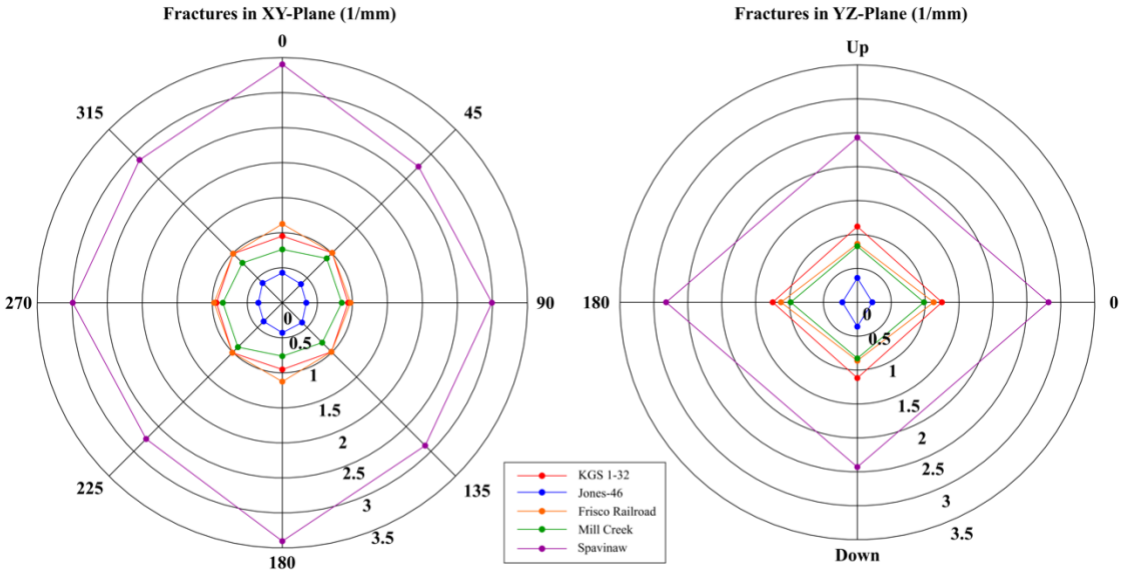

Figure 4.11: Linear fracture density measured in vertical and horizontal thin sections.

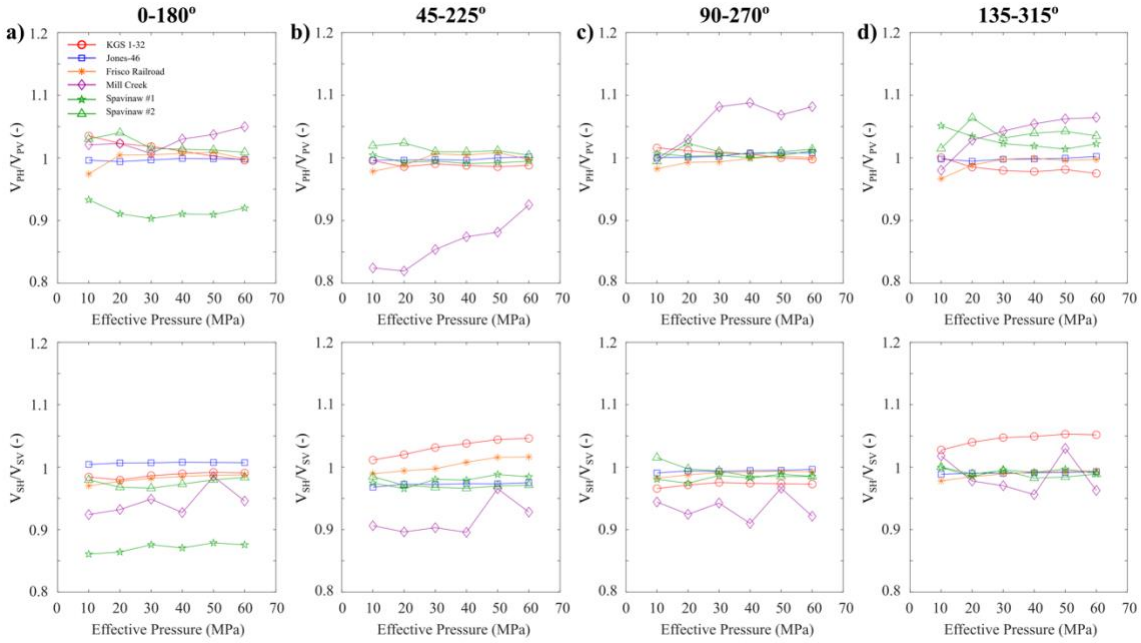

Figure 4.12: Ratios of V_P (top row) and V_S (bottom row) corresponding to the velocities measured in the horizontal directions (V_{PH} and V_{SH}) and vertical direction (V_{PV} and V_{SV}) as a function of confining pressure.

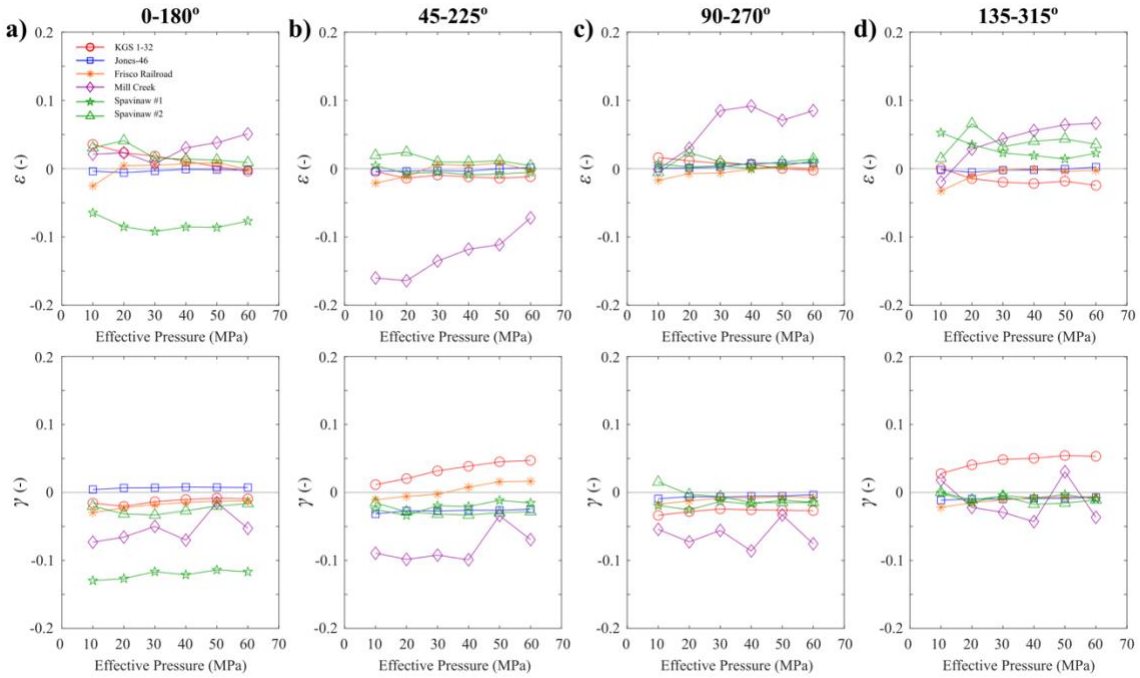

Figure 4.13: Velocity anisotropy parameters (ε and γ) as a function of confining pressure. Parameters are calculated assuming a transverse isotropic medium using the vertical and horizontal measurements for a) 0-180º, b) 45-225º, c) 90-270º, and d) 135-315º.

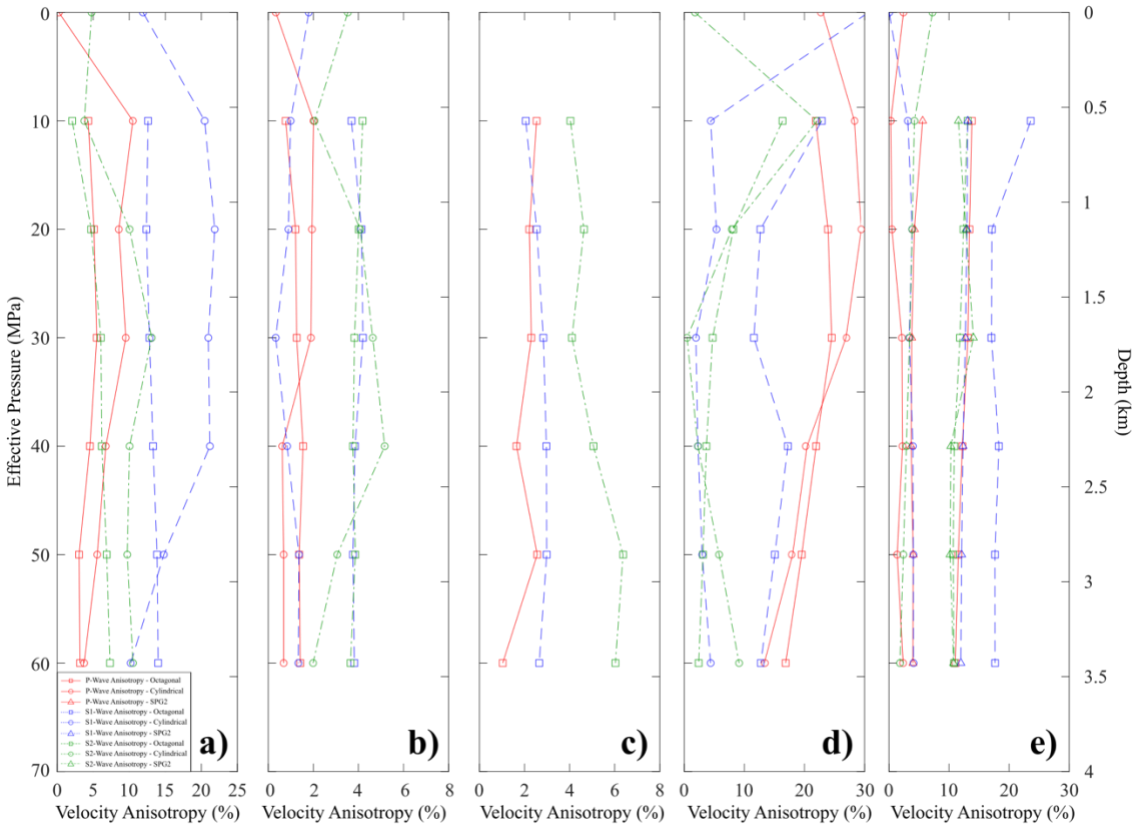

Figure 4.14: Horizontal velocity anisotropy (*An*) calculated for all basement samples as a function of both effective pressure and depth. Anisotropy of P-, S1-, and S2-waves is displayed for each basement rock. Values are reported for: a) KGS 1-32; b) Jones-46; c) Frisco Railroad; d) Mill Creek; e) Spavinaw (for both octagonal samples).

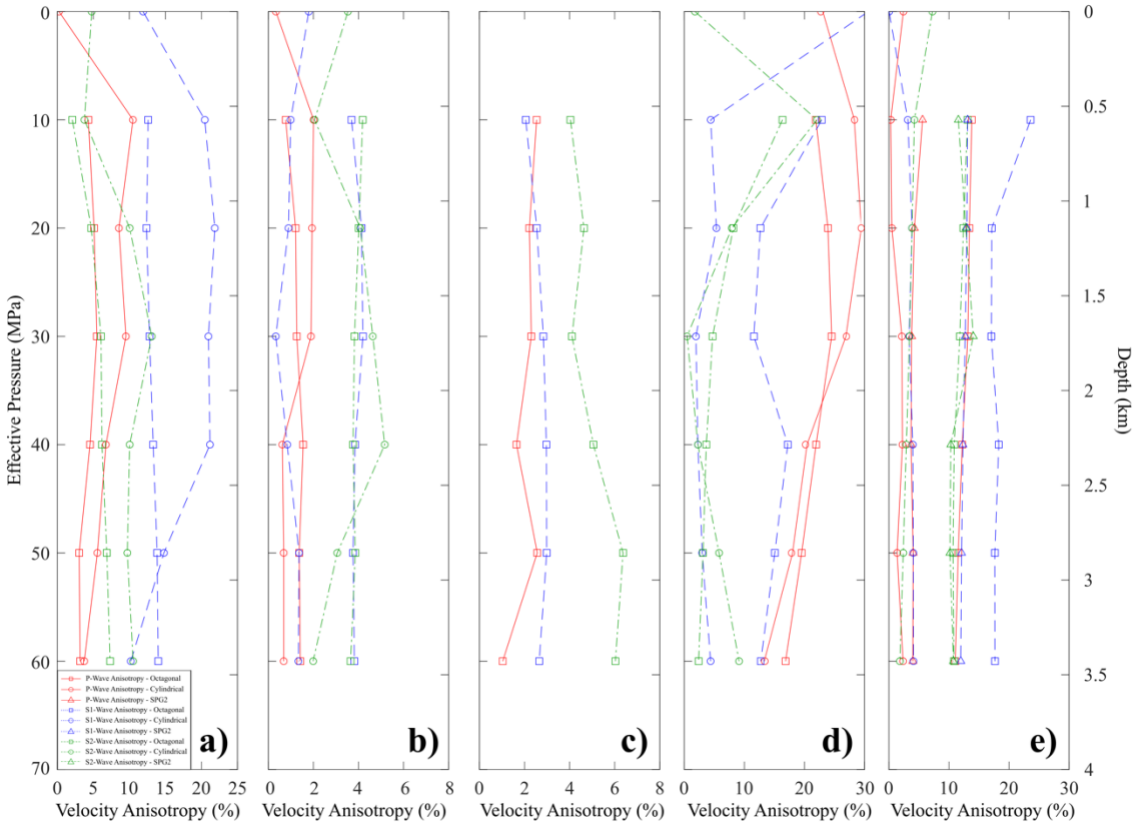

Figure 4.15: Circle diagrams showing the horizontal P-wave velocity measured at 60 MPa (left column) and linear fracture densities measured in the horizontal plane (right column). Measurements included are for: a) KGS 1-32; b) Jones-46; c) Frisco Railroad; d) Spavinaw #1; e) Mill Creek. Data for the Spavinaw #2 core is not shown since no thin section was prepared from the sample.

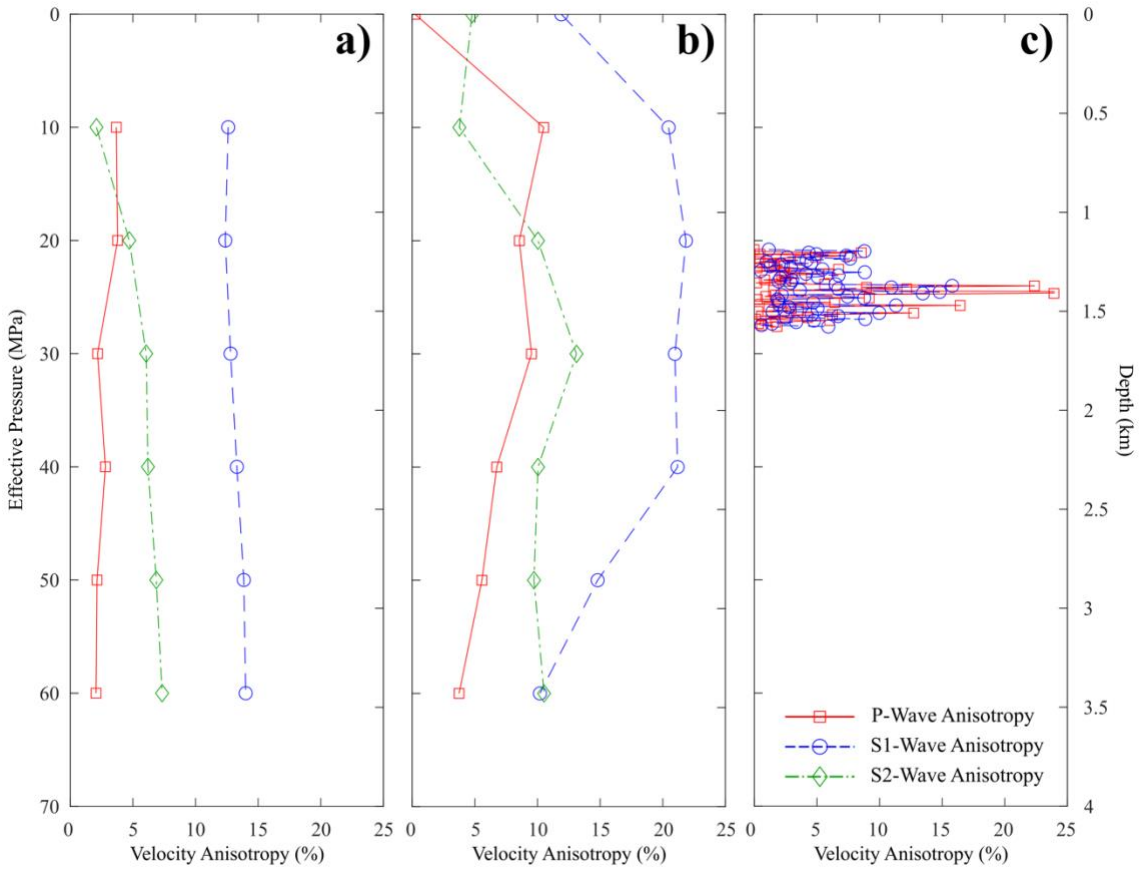

Figure 4.16: Measurements of the horizontal velocity anisotropy (*An*) exhibited in the KGS 1-32 well are shown for a) the octagonal velocity tests, b) the cylindrical velocity tests, and c) well log measurements.

CHAPTER IV TABLES

	KGS 1-32	Jones-46	Frisco Railroad	Mill Creek	Spavinaw
Albite-($AlSi_3$)NaO_8	24.4	32.8	50.7	29.9	9.5
Albite-($Na_{0.6}Ca_{0.4}$)$Al_{1.4}Si_{2.6}O_8$	28.6				33.4
K-Feldspar	18.8	32.7	30	37.3	27.1
Quartz	26.8	31.4	17.8	32.8	20.8
Biotite	1.4				
Pyrite		1.1			1.5
Chlorite*		2	1.5		7.7
Total	100	100	100	100	100

Table 4.1: XRD analysis of basement rocks examined in this study. *Chlorite group identified is Fe-Mg rich and most closely matches chamosite composition.

Cylindrical Specimens				
	Orientation	Length (mm)	Diameter (mm)	Density (g/cm^3)
KGS 1-32	X	46.75	24.92	2.68
	Y	42.28	24.94	2.68
	Z	37.56	24.83	2.68
Jones-46	X	70.37	25.44	2.59
	Y	68.25	25.27	2.60
	Z	66.04	25.31	2.60
Spavinaw	X	61.54	25.42	2.62
	Y	61.24	25.41	2.66
	Z	57.81	25.42	2.63
Mill Creek	X	55.52	25.11	2.51
	Y	44.38	24.91	2.52
	Z	56.54	25.37	2.52
Octagonal Specimens				
	Orientation	Length (mm)	Average Diameter (mm)	Density (g/cm^3)
KGS 1-32	Z	41.80	35.90	2.66
Jones-46	Z	47.12	35.84	2.61
Frisco Railroad	Z	42.88	38.49	2.61
Spavinaw #1	Z	43.78	36.00	2.68
Spavinaw #2	Z	43.61	36.68	2.66
Mill Creek	Z	44.25	36.20	2.51

Table 4.2: List of sample dimensions for all cylindrical and octagonal samples evaluated in this work. Orientations indicate the primary axis the sample was cored parallel to, with X/Y being horizontal and Z being vertical. The average diameter of the octagonal samples is the average of the four diameters between parallel horizontal faces.

	KGS 1-32	Jones-46	Frisco Railroad	Mill Creek	Spavinaw #1
P_I^V	1.12	0.36	0.86	2.43	0.83
$P_I^{0\text{-}180}$	1.25	0.22	1.13	2.82	0.98
$P_{II}^{0\text{-}180}$	0.95	0.43	1.13	3.4	0.76
$P_{II}^{45\text{-}225}$	1.01	0.38	1.01	2.75	0.9
$P_{II}^{90\text{-}270}$	0.94	0.34	0.97	2.99	0.85
$P_{II}^{135\text{-}315}$	0.99	0.4	0.99	2.88	0.81
$S_V^{0\text{-}180}$	2.16	0.75	1.84	5.28	1.63
$S_V^{45\text{-}225}$	2.19	0.73	1.79	4.99	1.68
$S_V^{90\text{-}180}$	2.16	0.71	1.77	5.1	1.66
$S_V^{135\text{-}315}$	2.18	0.74	1.78	5.05	1.64
$\Omega_{23}^{0\text{-}180}$	0.12	-0.15	-0.23	-0.29	0.06
$\Omega_{23}^{45\text{-}225}$	0.08	-0.04	-0.13	-0.1	-0.06
$\Omega_{23}^{90\text{-}180}$	0.13	0.04	-0.1	-0.17	-0.02
$\Omega_{23}^{35\text{-}315}$	0.09	-0.08	-0.11	-0.14	0.02

Table 4.3: Linear fracture density measured in the vertically oriented thin-sections ($P_{I/II}$) and horizontally oriented thin-sections (P_{II}) of five octagonal samples. Superscripts of V, 0-180º, 45-225º, 90-270º, and 135-315º were used to indicate the primary orientation of the measured fractures. S_V and Ω_{23} calculations are reported for the four different horizontal orientations and are labeled with the horizontal orientation utilized in each calculation.

	P-Anisotropy (%)	S1-Anisotropy (%)	S2-Anisotropy (%)	E_d (GPa)	v_d (-)
Octagonal	2.77	13.16	5.54	82.25 ± 3.11	0.24 ± 0.01
Cylindrical	6.41	17.34	8.86	72.58 ± 11.80	0.28 ± 0.01
Well Log	4.63	-	5.11*	66.16 ± 13.77	0.25 ± 0.03

Table 4.4: Mean horizontal anisotropy and dynamic moduli recorded with different observation methods for the KGS 1-32 Wellington well. *Only the horizontally polarized S-waves were reported for the KGS well log, and so were compared with S2-anisotropy measurements.

CHAPTER V: ANALYSIS OF MECHANICAL PROPERTIES OF CAPROCKS FROM THE NORTHEAST SICHUAN BASIN: IMPLICATIONS FOR SEALING EFFICIENCY OF LITHOLOGIES

5.1 Background

The accumulation of hydrocarbons in economically viable quantities requires specific lithologic, structural and petrophysical conditions be in place. These are collectively referred to as petroleum systems (e.g., Magoon and Dow, 1994). Accurately identifying potential petroleum systems for production requires that the relevant properties of each component be relatively constrained and understood. One essential element in a petroleum system is a trap or seal, which acts as a barrier to fluid migration in some direction. Often, this seal takes the form of a lithologic unit referred to as a caprock (Downey, 1994). In conventional resource plays, caprocks act as impermeable barriers to the upward migration of fluids in a reservoir, creating a stable fluid column in the underlying reservoir (Gluyas and Swarbrick, 2013). Typical caprocks are composed of mud- to silt-sized grains, possess minuscule pore throat diameters and high capillary entry pressures (Ingram et al., 1997). Ideally, caprocks suited for hydrocarbon accumulation are thick, laterally extensive and behave in a ductile manner (Grunau, 1987; Downey, 1994). Caprocks span a range of different lithologies – from shales to tight limestone (Downey, 1994; Schlömer and Kroos, 1997). However, caprock potential is likely linked to lithology beyond the general petrophysical characteristics related to fluid flow. Statistical evaluation of 341 carbonate fields in 27 sedimentary basins worldwide reveals that shales, carbonates and evaporites serve as 46%, 28% and 23% of the major caprocks, respectively (Jin, 2012).

While shales act as the seals for 80% of these fields though, carbonates and evaporites seal 23% and 55% of the total petroleum reserves worldwide, respectively (Jin, 2012).

The integrity of a caprock can be defined as the absence of flaws that increase the transmissivity of the formation (Petrie et al., 2014; Trujillo, 2018). Integrity is affected by the various mechanical, chemical and thermal forces acting on a caprock before, during and after exploration and production. While fluid-rock interaction may affect caprock integrity over large time scales, mechanical damage in the form of fracture/faulting is of greater importance (Hangx et al., 2010a; Petrie et al., 2014). The nucleation, propagation, mode and orientation of fractures in the subsurface is controlled by the in-situ stress state as well as the intrinsic geomechanical properties of the deforming rock (Ferrill and Morris, 2003; Peacock and Mann, 2005). This means that long-term caprock integrity is a function of lithology, regional stresses, and induced changes to in-situ conditions from hydrocarbon exploration and production.

Since geomechanical properties are indicative of caprock brittleness (i.e., likelihood of fracturing at a given condition), identifying properties that correlate with high caprock potential is critical to hydrocarbon exploration (Hao et al., 2000). Moreover, production often generates significant perturbations of the mechanical, chemical and thermal forces applied to a caprock-reservoir system (Hillis, 2001; Zoback and Zinke, 2002), which can, in turn, facilitate or re-initiate fracturing in the caprock, creating pathways for fluid leakage (Morris et al., 2011; Rutqvist, 2012). Understanding the variability of caprock mechanical behavior and the conditions that reduce caprock integrity is important for many geo-engineering projects (Hawkes et al., 2005). In this work we present the results of a set of petrophysical and geomechanical tests with several evaporite

and carbonate caprocks cored from wells in the northeastern Sichuan Basin. This work focuses on 1) identifying the geomechanical and petrophysical properties of each caprock, 2) understanding how these properties vary at different orientations, stress states and temperatures, and 3) developing an understanding of the characteristics associated with high caprock potential.

5.2 Geologic Setting

The Sichuan Basin is one of the most prolific oil and gas basins in China (Figure 5.1b). It is a large foreland-type basin comprised of 6-12 km of sedimentary succession overlying the Proterozoic basement. While a few oil-bearing structures have been identified in the basin, mostly in the north-central region, major discoveries have primarily been gas-bearing structures situated in the northwestern and southeastern provinces (Ma et al., 2007; Ma et al., 2008).

Based on its tectonic characteristics, the basin may be subdivided into an eastern high-steep faulted fold belt, a southern low-flat structural belt, a southwest low-steep structural belt, a west low-steep structural belt and a central low-flat belt (Figure 5.1a) (Lyu et al., 2017). The basin has evolved in a rather complex manner due to the numerous tectonic events that have shaped its current structure. Basin structures are strongly controlled by the basement morphology (Wang et al., 2008). The Precambrian Jinning and Chengjiang tectonic movements saw the consolidation of the crystalline basement framework, creating depressions in the east and west overlying ductile basement lithologies and divided by a central region overlying brittle basement (Ma et al., 2007). Existing subsidence and uplift were further enhanced during the Caledonian orogeny of the Silurian, forming the northeast-trending central uplift which has since strongly controlled the

structural trend of the region (Ma et al., 2008). This period saw significant extensional fault depressions that eventually encompassed most of the basin, forming many of the modern oil- and gas-bearing structures. Uplift of the cratonic margins during the Cenozoic, due to compression from the Pacific and Tethys, allowed for the inundation of the marine sediment that make up most of the basin's modern fields. This period also saw the basin begin to assume its modern rhombohedral shape, even as marine influence diminished with subsequent regression. Tectonic movement during the Cretaceous heavily folded the western basin margin, solidifying the modern basin uplifted region surrounded by adjacent depressions in the northwest and southeast. Finally, the Himalayan orogeny formed the modern basin morphology, tectonic compression creating numerous high-relief structures as the basin was uplifted further (Ma et al., 2008). The major gas-bearing structural and stratigraphic traps in the northern Sichuan Basin are a result of this complex tectonic and diagenetic history. The caprocks tested are derived from the northern portions of the eastern (I) and central (V) structural provinces (Figure 5.1a). The petroleum geology of this region has been of particular interest since the discovery of several large gas fields in the last twenty years (Figure 5.2).

Seal lithologies are often classified according to their lateral continuity and areal extent as either regional or direct caprocks. Regional caprocks are generally continuous over large areas with few gaps due to sedimentation or structural changes. Though both caprock types may control hydrocarbon accumulation, regional caprocks are more significant as they dictate the hydrodynamic behavior of the underlying strata, thus controlling the regional migration and preservation of hydrocarbons. Direct caprocks, by contrast, are mainly effective locally, and generally necessitate the presence of an overlying

regional seal as well (Downey, 1994). Evaporites and shales make up the overwhelming majority of regional seals, while direct caprocks are more variable in lithology (Jin, 2012). In the northern Sichuan Basin, the thick evaporite beds of the Early-Middle Triassic act as the regional caprocks. These include the members Jialingjiang and Leikoupo Formations that overlay the main carbonate reservoir rocks of the Early Triassic (Cai et al., 2003). While these evaporites may also act as direct seals for underlying gas reservoirs, interbedded impermeable carbonate sequences beneath these regional caprocks may also act as local direct caprocks as well, potentially sealing considerable quantities of oil and gas as well.

5.3 Experimental Methodology

5.3.1 Caprock Lithology and Petrophysics

Evaporite, limestone, and dolostone caprocks were identified in the Feixianguan (T_1f), Jialingjiang (T_1j), and Leikoupo (T_2l) Formations of the Sichuan Basin (Figure 5.2). Prospective caprocks were identified in six different wells across the northern basin, at depths in the range of 4-7 km. Although shale/mudstone is the most common lithology that acts as a caprock worldwide, none were identified in the region and depth of study and are thus beyond the scope of this work. Caprock from the six recovered core sections were cut and ground into right cylinders, with ends of each sample polished to within 0.01 mm of each other (Figure 5.3). Samples were cored both parallel and perpendicular to sedimentary bedding to evaluate the effects of lamination and fabric on caprock mechanical behavior.

Specimens were oven-dried and weighed to find their bulk density (Table 5.2). X-ray powder diffraction (XPRD) was conducted on samples of each caprock to evaluate bulk caprock mineralogy (Table 5.2). In the case of LS2 samples, bulk mineralogy of two

sections was evaluated due to the high variability observed along the caprock formation (Table 5.1). Direct and XPRD measurements of density appear to compare favorably, though specimen variability increases with clay and evaporite content in the specimens. Porosity values (Table 5.2) were determined through the difference in mineral densities and bulk densities of each caprock analyzed through XPRD. Porosity values should be treated as approximations of the caprock porosity.

Thin-sections were created from specimens of each caprock to corroborate laboratory measurements of bulk mineralogy (Figure 5.3). EV1 specimens are almost pure anhydrite, with low fracture content observed in thin-section (Figure 5.3a). Fractures are mostly thin and generally sub-parallel to bedding in both thin-section and hand samples of EV1. Sample lamination is not nearly as prominent as in other caprocks, though the elongate anhydrite grains are generally sub-parallel to one another. LS1 samples are fine-grained limestones, displaying very little grain-size heterogeneity. Laminations are very fine, visible only in thin-section, and fractures are rarely observed. EV2 samples are dolomite-rich anhydrite rocks. Samples display prominent banding visible to the naked eye characteristic of laminated evaporites, though the laminations appear to be very heterogeneous and only weakly controlled by bedding orientation. Thin-sections display prominent segregation of evaporite and carbonate minerals create much of this texture. Fractures tend to nucleate at contacts between carbonate and evaporite minerals. LS2 specimens exhibit significant lithologic variation across the caprock formation (Table 5.1). Specimens range from muddy limestones to fine-grained limestones, with clay and mica content increasing at shallower depths (Table 5.1). LS2 samples are primarily composed of calcite, though dolomitization and other alteration products such as chlorite are fairly

common. Laminations are more tortuous than in the tight limestones of LS1. DS1 samples are fine-grained dolostones, with minor calcite content. Unlike the other carbonate caprocks tested here, DS1 specimens display large grain-size heterogeneity (Figure 5.3e). Larger grains are distinguishable even in hand samples, while in thin-section large calcite and dolomite clasts with prominent twinning are interspersed throughout. DS2 caprocks are fine-grained dolomites, similar to DS1 specimens, though with greater dolomitization of calcite and silicate mineral content. However, the texture of DS2 samples is more akin to LS1 specimens, with low grain-size variability. This is expected as both LS1 and DS2 samples are derived from the second member of the Feixianguan Formation, though DS2 samples are somewhat shallower than those of LS1 (Table 5.2).

5.3.2 Hardness Tests

An Equotip Bambino 2 hardness tester was used to measure the rebound hardness of caprock samples. Hardness, in this case the Leeb Hardness or HL_D, was measured by the indentation and rebound of a metal ball, recording the impact and rebound velocities. The ratio of velocities is multiplied by 1000 to determine the hardness values, as in the equation:

$$HL_D = \frac{V_r}{V_i} * 1000 \quad (1)$$

where V_r and V_i are the rebound and impact velocity, respectively. Ten hardness measurements per available sample were used to determine the mean hardness values. Measurements were conducted on the top and bottom of each cylinder - five measurements per each - which had been polished into flat surfaces. However, the lengths of our samples were variable, and sample size can lead to variations in hardness unrelated to rock properties (Çelik and Çobanoğlu, 2019). To analyze the effect of size on caprock hardness,

mean hardness values were cross-plotted against sample lengths to clarify the difference in hardness of the caprock lithologies regardless of sample size.

5.3.3 Ultrasonic Velocity Tests

Samples were oven-dried at 50 C^{o} for 24 hours, set between two steel platens, and sealed with polyolefin tubing. Mounted on each platen were piezoelectric transducers to record both P- and S-wave signals. Wave velocities were recorded by pulsing transducers along one platen and recording the response via oscilloscope at the other platen. By measuring the travel-time of a wave through the metal platens and subtracting this delay from the arrival time observed for each sample, the true arrival time for the rock can be determined. Using the determined sample travel-time and length, the ultrasonic velocity could be calculated for each caprock. 0 MPa tests were made through a benchtop method of moderate application of pressure with a vice, after which samples were placed in a triaxial pressure vessel (MTS 810, Figure 5.5) and loaded at hydrostatic conditions. Velocities were recorded every 10 MPa from 0-60 MPa to evaluate their pressure dependence. Caprock velocities were measured in bedding perpendicular ($\perp$) and parallel ($\parallel$) samples from each well except DS1, where only perpendicular core was available.

5.3.4 Deformation Tests

Each sample was vacuum-saturated in de-ionized water for over 48 hours. Samples were then placed between two steel platens and jacketed with heat-shrink tubing and steel tie-wires. Axial and radial LVDTs were affixed to specimens to record sample displacements during experiments (Figure 5.5). Samples were placed in a triaxial deformation apparatus (MTS 816, Figure 5.6), where each was deformed with confining pressures of 0, 32.5, and 55 MPa. 32.5 and 55 MPa tests were conducted with pore

pressures of 10 MPa such that their effective confining stresses were 22.5 and 45 MPa, respectively. Although vacuum-saturation of samples is expected to be near total, for the confined tests, initially a minor pore pressure (~5 MPa) and confining pressure (~7-8 MPa) was applied for a period in excess of 2 hours to ensure fluid pressure diffusion through each of the caprocks prior to loading to the set testing conditions. Samples tested at 50 C^{o} were held at a small confining pressure (~5 MPa) and pore pressure (~3 MPa) while the temperature was raised at ~1 C^{o}/min. Conditions were maintained for a period of 4 hours to allow temperatures to equilibrate before beginning experiment. Axial deformation was conducted at a strain rate of 10^{-5} s^{-1} and data was recorded with a frequency of 0.5 Hz.

Raw data for tests was processed to yield axial strain, radial strain, differential stress. Effective confining pressure was determined using the equation:

$$\sigma_e = \sigma_c - \sigma_p \tag{2}$$

where σ_e, σ_c, and σ_p are the effective confining pressure, confining pressure, and pore pressure, respectively. The mean effective stress (σ_m) is the average of the three principal stresses at a given point during testing. Peak differential stress (σ_f) was defined as the maximum differential stress supported by a sample, while yield stress (σ_y) was defined as the differential stress at which the axial strain curve significantly deviates from linearity. Tangent Young's moduli (*E*) and Poisson's ratio (*v*) were determined from the axial and radial stress-strain data at 50% of the peak differential stress following ISRM guidelines (Ulusay, 2014). Hardness moduli (*H*) was determined from the tangent slope of the stress-strain data between σ_f and σ_y. A basic schematic of for calculating these values

is shown in Appendix B (Figure B.1). The determined mechanical parameters are listed in Table 5.3.

5.4 Experimental Results

5.4.1 Hardness

Rebound hardness is an often utilized because it provides a practical and efficient way to broadly characterize the mechanical properties of different rocks. This is especially relevant for studies where there is a paucity of material available, such as from core sections or cuttings, where static or conventional indentation tests are often infeasible (Çelik and Çobanoğlu, 2019). Here, we provide the broad characterization of caprock hardness to show how variable their mechanical response of caprocks may be depending on lithology.

Mean hardness values (HL_D) for limestone, dolostone and evaporite caprocks are displayed in Figure 5.6. Though sample size does affect hardness measurements, the trends observed for the different lithologies remain relatively consistent. Hardness is consistently greatest in the dolostones and lowest in the evaporites, regardless of sample size. One interesting observation is that mean hardness for a given lithology is more consistent (i.e., higher R^2 value) when average values are greater. Caprocks with higher average hardness tend to be vary less from the linear trend (Figure 5.6), while caprocks with lower average hardness tend to be less predictable and exhibit a greater range of hardness values for a given sample size. For example, the hardness values in the dolostone caprocks correlate, indicating hardness is likely more consistent in the lithology than evaporites or limestones.

5.4.2 Ultrasonic Velocities

Distinguishing the elastic response of the caprocks at different orientations can clarify the role that mineralogy and texture play in their corresponding geomechanical and petrophysical behavior. Data from velocity tests of caprock samples is shown in Figure 5.7.

Both V_P and V_S are pressure-dependent in all caprocks tested, regardless of sample orientation, with V_P on average being more pressure-dependent than V_S. Pressure-dependency of velocity is primarily controlled by changes to intrinsic petrophysical properties such as the closure of microcracks and pore spaces. Velocities are generally greater in bedding parallel samples, though this variance diminishes with increased confining pressure (Figure 5.7). Dolostones tend to have greater V_P and V_S compared to the other caprocks, in spite of the lower overall density compared to evaporites (Table 5.2). The regional evaporite caprocks generally exhibit lower velocities than the carbonate-rich caprocks (see Appendix B). It is worth noting that velocity anisotropy observed (i.e., the difference between bedding parallel and perpendicular velocities at the same conditions) appears to be less pronounced in the evaporite caprocks than in the carbonate caprocks.

The trends in V_P and V_S with pressure is also notably distinct between lithologies. Within the trend of increasing velocity with pressure, velocity increases more in the evaporite caprocks EV1 and EV2 (Figure 5.7). As pressure increases from ambient conditions to 60 MPa, V_P and V_S of the regional caprocks increase from 12-24% and 11-17% respectively, while the V_P and V_S of the direct caprocks increase from 5-21% and 4-21%. The difference between the regional and direct caprocks can also be seen between parallel and perpendicular sample velocity changes. While the increase in P-wave velocity is always greatest in samples oriented perpendicular to bedding, this is not consistent for

S-wave velocities in carbonate rocks. In all of the carbonate caprock samples, the change in S-wave velocity with pressure is lower in bedding perpendicular samples than bedding parallel samples, a trend not observed in the regional caprocks.

V_P/V_S is often useful for evaluating certain petrophysical characteristics in the surface (fluid content, bulk composition, etc.). Examining the V_P/V_S for our data, the evaporite caprocks tend to have higher ratios than any of the direct caprocks. Dolostones appear to promote higher shear velocities at given conditions. Additionally, the ratio may be affected grain-size heterogeneity in the caprocks; the lowest V_P/V_S values were observed in DS1 samples, which were noted as possessing a high grain-size variability visible at both the micro- and macroscale (Figure 5.3e).

5.4.3 Deformation Tests

The mechanical behavior of rocks is the result of a complex interplay of their intrinsic properties. The holistic nature of deformation under hydrothermal conditions requires that mechanical behavior be evaluated against several different variables. Here, caprock behavior is considered against both variable effective stresses and temperatures.

5.4.3.1 Effect of Pressure

Room temperature tests conducted at effective confining pressures of 0, 22.5, and 45 MPa are displayed in Figure 5.9. Samples oriented parallel to bedding were deformed at effective confining pressures of 0 and 22.5 MPa, while samples oriented perpendicular to bedding were deformed at effective confining pressures of 22.5 and 45 MPa. Geomechanical properties and testing conditions are shown in Table 5.3. Due to the variable composition of LS2 samples, additional tests were conducted to compare the effect specific lithology had on their mechanical behavior (Table 5.3).

By examining the axial deformation and corresponding geomechanical properties, three different characteristic mechanical behaviors can be distinguished – dolostone caprocks (DS1, DS2), limestone caprocks (LS1, LS2), and evaporite caprocks (EV1, EV2). Failure strength tends to be greatest in the dolostones (Table 5.3). As mechanical loading increases until the maximum strength is reached, dolostones exhibit pronounced strain-softening behavior (i.e., rapid drop in stress after failure) and macroscopic shear fracturing. Such mechanical behavior is characteristic of brittle deformation (ex. high Young's and hardening moduli, large stress drop, high failure stress, etc.), and dolostones exhibit such behavior even at the largest effective confining pressures.

Limestone caprocks possess comparable behavior to the dolostones under uniaxial conditions, with equivalent or greater elastic parameters during testing (Table 5.2). At 22.5 MPa, the limestones continue to exhibit brittle behavior with strain-softening post-failure. However, their strength increase with effective pressure is far less than that of the dolostone caprocks. The distinction between the two carbonate rock types becomes even more pronounced at 45 MPa, as the limestones no longer exhibit significant strain-softening after failure, with gradual decreases in their corresponding mechanical properties. This semi-brittle behavior is more pronounced in samples of LS2 than in LS1, though whether this is due to the presence of clay minerals or fabric anisotropy in samples of LS2 is uncertain. Of note also is the effect of heterogenous lithology on the deformation of LS2 samples. Those that were cored at shallower depths tend to be less brittle (i.e., lower Young's modulus, higher Poisson's ratio, lower peak strength) and exhibit less strain-softening with failure and dilatancy.

By contrast, the evaporite caprocks deform in a semi-brittle or even ductile behavior at low effective pressures, as seen by the pronounced lack of strain-softening and nearly flat post-failure behavior (Figure 5.8). Deformed samples tend to display multiple shear fractures post-deformation, suggesting the evaporites deform more through cataclastic flow than localized fracture and shearing. In caprocks, this type of deformation is ideal for caprock efficiency, as distributed deformation is less likely to allow fluid flow through a pressure seal than localized brittle fracturing.

Interestingly enough, parallel and perpendicular oriented samples display large variations in behavior at 22.5 MPa effective confining pressures (Figure 5.8). While perpendicular samples exhibit nearly flat post-failure deformation behavior, parallel samples deform in a more brittle manner with pronounced strain-softening and higher peak strengths. Correspondingly, the geomechanical properties of parallel samples are greater than those measured in perpendicular samples, indicating caprock integrity and bedding orientation are interrelated.

Analysis of the samples post-deformation allows additional geomechanical properties to be characterized. Using the angle of fracturing in the triaxially deformed samples to determine the shear and normal stress at failure, the bulk angle of internal friction (φ_i) and the cohesive strength (C) were quantified for each caprock (Table 5.4). The angle of internal friction defines the increase in shear strength of a lithology with effective pressure and thus the failure envelope, making it a useful indicator of brittleness. The highest values of φ_i are in the dolostone samples (DS1, DS2), with lower values observed in the evaporite caprocks. The limestones are more variable, though it is worth noting that LS1 - the most homogenous limestone - has a comparable angle of internal

friction to the dolostones while the more heterogenous LS2 samples are closer to the values observed in the evaporites. Whether this variation in mechanical properties can be attributed to compositional heterogeneity or phyllosilicate content (Table 5.1) is uncertain.

5.4.3.2 Effect of Temperature

The effect of increasing temperature is often similar to that of increasing confining pressure, with higher temperatures promoting greater crystal plasticity and distributed deformation (e.g., Lockner, 1995). Perpendicular samples of the caprocks deformed at 23 C° and 50 C° are displayed in Figure 5.9. For the most part, the tests at 50 C° do not show a significant deviation from the mechanical behavior at room temperatures. Nevertheless, the deformation results do offer some indications that temperature increase does promote more semi-brittle behavior. First, all caprocks tested at 50 C° exhibit minor reductions to their Young's moduli and peak stress, the degree to which depending upon rock type (Table 5.3). Second, the caprocks experience more strain-hardening behavior after yielding at 50 C° compared to the room temperature tests. The major exception to the minor effect on deformation behavior is the EV1 tests. While tests at both temperature conditions displayed semi-brittle post-failure behavior, the test at 50 C° reveals a significant reduction in the peak strength and elastic moduli. Such a difference is noteworthy, as the EV1 caprocks have the highest anhydrite content of all the rocks tested here, whereas the other evaporite caprock EV2 is not significantly weakened by the thermal load at all.

5.5 Discussion

5.5.1 Linking Caprock Lithology and Geomechanical Properties

At a given condition, the likelihood of shear fracture and faulting can be characterized as rock brittleness (Hajiabdolmajid and Kaiser, 2003; Tasarov and Potvin,

2013; Rybacki et al., 2016). When a caprock deforms in a brittle manner (e.g., high brittleness), fractures nucleate and propagate such that seal bypass systems can form and compromise caprock integrity (Petrie et al., 2012). When a caprock deforms in a ductile manner (i.e.., low brittleness), fracture nucleation is suppressed, and damage tends not to affect, or may even reinforce, caprock integrity (Ingram et al., 1997; Ingram and Urai, 1999; Trujillo, 2018). Numerous methods have been developed to characterize rock brittleness, though the majority utilize the rock elastic (ex., Young's modulus, Poisson's ratio) and inelastic (ex., peak differential stress, coefficient of internal friction) geomechanical properties to determine the fracture tendency at a given condition (Rybacki et al., 2016; Li and Ghassemi, 2018).

To understand the geomechanical properties used to assess caprock brittleness and how they vary with lithology, a review of existing experimentally determined mechanical properties in caprocks (or analogue lithologies) was conducted. Ranges of example parameters are shown in Figure 5.10 and Table 5.5. A list of the literature assessed for this analysis is provided in Appendix B. Evaporites, argillaceous rocks, and tight carbonates are the primary lithologies that seal hydrocarbons in sedimentary basins (Ma, 2020). Evaporite caprocks (e.g., anhydrite, gypsum, salt rock) are characterized by relatively low hardness, compressive strength, Young's moduli and generally high Poisson's ratios, as transitioning from brittle-to-ductile behavior at low effective confining pressures (i.e., 20-40 MPa) (De Paolo et al., 2008; Smith et al., 2009; Hangx et al., 2010a; Osinga, 2013; Trippetta et al., 2013; Mehrgini et al., 2016b; Wang et al., 2019). Argillaceous rocks (e.g., shales, mudstones) are the most variable caprock lithology; while they are characterized by low compressive strength, Young's moduli and coefficient of internal friction, elastic

parameters such as Poisson's ratio are highly variable even within the same formation (Bereskin and McLellan, 2008; Dewhurst et al., 2008; Zhou et al., 2010; Raven et al., 2011; Rybacki et al., 2015; Trujillo, 2018). Shale and mudstone properties can range over two orders of magnitude, making interpretation of their effectiveness as seals difficult (Vilarassa et al., 2013). Such variability may explain the greater prevalence of evaporite regional seals compared to argillaceous regional seals, despite the greater prevalence of shales and mudstones in sedimentary basins. Tight carbonates (e.g., dolostones, limestones) generally exhibit higher compressive strength, hardness, and Young's moduli, with relatively low Poisson's ratios (Lam et al., 2007; Trippetta et al., 2013; Mehrgini et al., 2016a; Raziperchikolaee et al., 2018; Trujillo, 2018; Zhang et al., 2019). As can be seen in Figure 5.11, dolostone caprocks in particular tend to have greater elastic and inelastic properties than limestones, as strength tends to increase with dolomite content in carbonate rocks (Cleven, 2008; Raziperichikolaee et al., 2018). Tight carbonates generally transition from brittle-to-ductile behavior at relatively low effective pressures and temperatures (i.e., 50-150 MPa, 50-100 C^{o}), though the transition is lower for limestones than it is for dolostones (Heard, 1960; Baud et al., 2000).

Jin (2012) noted that while mechanical properties varied with caprock lithology, there existed a strong correlation with caprock efficiency and certain characteristics. Good seals tended to be characterized by low hardness, compressive strength, Young's modulus and high plastic coefficients, while poor quality seals tend to possess higher hardness, compressive strength, Young's moduli, and low plastic coefficients. In other words, poor seals can resist greater deformation stresses without damage. This also means their brittleness is such that they are likely to fracture and experience reduced seal efficiency

compared to better sealing lithologies (Downey, 1994). However, as noted by Yang et al. (2013), the brittleness determined through individual lithologic and geomechanical properties can vary considerably and lead to contradictory interpretations of caprock behavior. To predict the geomechanical-risk to caprock integrity in the northeast Sichuan Basin, a more holistic approach is utilized in Figure 5.11, showing the relation between different mechanical properties and the relative brittle/ductile nature of different lithologies.

These results are similar to those reported by other authors investigating caprock mechanical properties (Table 5.5). The evaporite caprocks (EV1 and EV2) are relatively soft, with low compressive strengths, Young's moduli, and hardness values relative to carbonate caprocks. The trend of the evaporite caprocks toward more ductile mechanical behavior is consistent with the characteristics attributed to high sealing efficiency, corroborating their effectiveness as regional seals in the northeast Sichuan Basin (Ma, 2020). Indeed, evaporitic seals are noted as often having high sealing efficiency even in tectonically active regions such as the Sichuan Basin (Schlömer and Krooss, 1997; Xiaofei et al., 2015; Ma, 2020).

By contrast, the mechanical properties of the limestone (LS1 and LS2) and dolostone (DS1 and DS2) caprocks trend more toward brittle behavior, with greater hardness, yield and peak stresses, Young's moduli and coefficients of internal friction (Figure 5.11). The mechanical data also emphasizes the observation that caprock brittleness tends to increase with increasing dolomite content, as the dolostones are generally more brittle than the limestones. While the brittleness of limestone is intermediate between that of dolostone and evaporite caprocks, certain elastic and inelastic parameters in the

limestone caprocks are at or near parity with that of the evaporites. This can be attributed to the high clay content in LS2 samples (Table 5.1). The proportion of clay in carbonate caprocks is known to both reduce the strength and hardness (i.e., reduce the brittleness) while reducing their effective permeability (Lü et al., 2017).

Comparing these results with that of other caprock research (Table 5.5), it is clear that individual mechanical properties are not sufficient indicators of caprock integrity. Rather, the mechanical properties are not linearly related to one another. For example, Poisson's ratio determined in caprock lithologies, both in this work and others, is less consistent between individual samples, and for argillaceous rocks its values may even contradict other mechanical parameters determined (Trippetta et al., 2013; Mehrgini et al., 2016; Rybacki et al., 2016; Trujillo, 2018). Another example would be the coefficient of internal friction (μ_i), which while generally increasing with rock brittleness, can be anomalously high even in rocks with a low brittle-ductile transition threshold (De Paolo et al., 2008). These observations support the value of a more unified approach to "mapping" caprock brittleness based on numerous characteristics, rather than relying on individual properties to assess risk to integrity. From the results reported here for different caprock lithologies, the relative brittleness of caprocks is best indicated by pre-failure stress and strain measurements such as the Young's moduli, yield stress and hardness.

5.5.2 Implications for Caprock Integrity

Regional stress data from the caprock localities shows that the mechanical load for each caprock is well below the required threshold for failure predicted from the deformation tests (see Appendix B for further discussion). Avoiding caprock failure is not the only concern in preventing integrity loss though; permeability evolves dynamically as

a rock deforms rather than remaining static until macroscopic shear failure occurs (Zhang et al., 1994; Mitchell and Faulkner, 2008; De Paolo et al., 2009; Hangx et al., 2010b). For example, a rock under mechanical loading experiences an initial period of linear-elastic behavior where only small changes to porosity occur. As deformation continues, permanent inelastic deformation begins to accumulate until a critical threshold is reached whereby a rock can no longer accommodate a greater mechanical load. The evolution of permeability is strongly linked to the bulk rock volume change during deformation, though this hydromechanical coupling is not a one-to-one relationship (Zhu and Wong, 1997; De Paolo et al., 2009). As such volumetric strain can be used as a proxy for the change in permeability of the different caprock lithologies during undergoing mechanical loading (Figure 5.12).

When low-porosity rocks deform elastically, only minor linear permeability changes usually occur as existing cracks and pores compact or dilate, depending on the confining conditions (Hangx et al., 2010b; Wu et al., 2021). As the mechanical load increases, approaching the yield stress (σ_y), permeability will begin to rapidly increase (De Paolo et al., 2008). Stiffer caprocks are more prone to dilation and thus require relatively lower stress to enhance permeability, while more compliant caprocks generally experience a bulk reduction in permeability before yielding occurs and permeability increases (Zhu and Wong, 1997). In other words, the permeability evolution reflects caprock integrity and is a function of rock brittleness at any given condition. More brittle lithologies will experience greater increases in permeability under loading than less brittle lithologies (Alkin et al., 2007). This explains the prevalence of evaporite and mudstone lithologies with high caprock potential, as the mechanical and thermal load required for ductile

behavior to occur is lower than for most other lithologies (Hangx et al., 2010a; Bourg et al., 2015; Wang et al., 2019). The geomechanical-risk of caprock failure in carbonates is correspondingly greater, due to their more brittle nature. However, the geomechanical properties measured in this research indicate that limestone caprocks are less brittle than dolostones and are thus more effective seals.

Lithologic factors beyond the mechanical load are also relevant to caprock integrity. Carbonates are more vulnerable to rock-fluid interaction processes than other lithologies due to their high solubility and kinetic rates, meaning chemical dissolution is likely to enhance caprock degradation over relatively short timescales (Chou et al., 1989; Pokrovsky et al., 2005). This is of particular importance during injection and recovery operations where disequilibrated fluid likely interacts at the reservoir-caprock contact where shear stresses are concentrated. Conversely, the rapid precipitation of carbonate minerals will lead to more rapid healing of open fractures than in other caprock lithologies (Richard et al., 2015; Bergsaker et al., 2016). These competing chemo-mechanical processes in carbonates lead to caprock integrity being much more complex in the long-term compared to other lithologies.

The orientation of planes of weakness also contributes to caprock integrity. The axial deformation tests conducted at effective pressures of 22.5 MPa exhibit markedly different mechanical behavior oriented parallel and perpendicular to bedding (Table 5.3, Figure 5.8). The mechanical behavior and corresponding properties measured are indicative that parallel samples are more brittle than samples deformed perpendicular to bedding. One explanation for this is that most pre-existing fractures in the caprocks are predominantly subparallel to bedding, meaning the bedding orientation strongly controls

the geomechanical properties at a given condition (McLamore and Gray; 1967; Baud et al., 2005; Rybacki et al., 2015). This inference is supported by the elastic wave anisotropy observed in Figure 5.7, with parallel samples displaying greater average velocities than perpendicular samples. While the anisotropy of mechanical behavior is present in all caprocks, it is interesting to note that LS1 shows less deviation in mechanical behavior than the evaporite caprocks or LS2, all of which contain more elongate or phyllosilicate minerals that exhibit significant mechanical anisotropy as well. Another possible explanation for this is the existence of permeability anisotropy in the caprock samples. Although permeability is initially negligible in all samples during testing, other researchers have noted permeability is often greatest parallel to bedding and lowest perpendicular to bedding (Kwon et al., 2004). It is plausible that this difference in behavior reflects how fluids are able to transmit through the dilating material during both elastic and inelastic deformation, as this may affect the stress conditions. This however is less likely than the first explanation since higher permeability has also been shown to lower pore pressure build up and more stable pressurization (Farquharson et al., 2016), meaning local pore pressure and infiltration are more dependent upon the boundary conditions.

Regardless of the cause, the orthotropic nature of caprocks will likely affect their integrity under the various mechanical, chemical, and thermal forces induced by fluid injection and recovery operations. The orientation of caprock bedding relative to the regional tectonic stresses is thus of great importance to predicting caprock mechanical behavior.

5.6 Summary and Conclusions

The mechanical behavior of caprocks is controlled by both the interplay of their geomechanical properties and the in-situ mechanical, chemical, and thermal forces applied. The corresponding risk of caprock failure and seal bypass thus depends upon the material properties of a particular lithology in a caprock-reservoir system. In the northeast Sichuan Basin, there exist strong correlations between V_P, V_S, yield and failure stress, Young's modulus, and the coefficient of internal friction in the prospective caprock lithologies. Larger values indicate greater likelihood of brittle behavior than lower values, and thus the degradation of caprock integrity is probable during operations. The brittleness of a caprock is also likely to be highly orthotropic for lithologies containing elongate minerals such as phyllosilicates. Although individual mechanical properties may lead to contradictory predictions of caprock brittleness, mapping numerous elastic and inelastic properties in different lithologies reveals characteristic trends that, when compared with lithologies with known caprock potential, allow for deductions to be made about ideal caprock geomechanical properties. Caprocks with low risk will exhibit lower geomechanical properties, with low pressure-temperature conditions required to initiate a transition from brittle-to-ductile mechanical behavior. In this regard, evaporite caprocks are the least at risk of failure during injection and recovery operations, while dolostone caprocks are the least effective of a potential caprock lithology.

References

Alkan, H., Y. Cinar, and G. Pusch. "Rock salt dilatancy boundary from combined acoustic emission and triaxial compression tests." International Journal of Rock Mechanics and Mining Sciences 44, no. 1 (2007): 108-119.

Baud, Patrick, Laurent Louis, Christian David, Geoffrey C. Rawling, and Teng-Fong Wong. "Effects of bedding and foliation on mechanical anisotropy, damage evolution and failure mode." Geological Society, London, Special Publications 245, no. 1 (2005): 223-249.

Baud, Patrick, Alexandre Schubnel, and Teng-fong Wong. "Dilatancy, compaction, and failure mode in Solnhofen limestone." Journal of Geophysical Research: Solid Earth 105, no. B8 (2000): 19289-19303.

Bereskin, S. Robert, and John McLennan. "Hydrocarbon Potential of Pennsylvanian Black Shale Reservoirs, Paradox Basin, Southeastern Utah (OFR-534)." (2008).

Bergsaker, Anne Schad, Anja Røyne, Audrey Ougier-Simonin, Jérôme Aubry, and François Renard. "The effect of fluid composition, salinity, and acidity on subcritical crack growth in calcite crystals." Journal of Geophysical Research: Solid Earth 121, no. 3 (2016): 1631-1651.

Bourg, Ian C. "Sealing shales versus brittle shales: a sharp threshold in the material properties and energy technology uses of fine-grained sedimentary rocks." Environmental Science & Technology Letters 2, no. 10 (2015): 255-259.

Cai, Chunfang, Richard H. Worden, Simon H. Bottrell, Lansheng Wang, and Chanchun Yang. "Thermochemical sulphate reduction and the generation of hydrogen sulphide and thiols (mercaptans) in Triassic carbonate reservoirs from the Sichuan Basin, China." Chemical Geology 202, no. 1-2 (2003): 39-57.

Carey, J. W., L. P. Frash, and T. Ickes. "Experimental Investigation of Shear Fracture Development and Fluid Flow in Dolomite." In 52nd US Rock

Mechanics/Geomechanics Symposium. American Rock Mechanics Association, 2018.

Çelik, Sefer Beran, and İbrahim Çobanoğlu. "Comparative investigation of Shore, Schmidt, and Leeb hardness tests in the characterization of rock materials." Environmental Earth Sciences 78, no. 18 (2019): 1-16.

Chou, L. E. I., Robert M. Garrels, and Roland Wollast. "Comparative study of the kinetics and mechanisms of dissolution of carbonate minerals." Chemical geology 78, no. 3-4 (1989): 269-282.

Cleven, Nathan R. "Role of Dolomite Content on the Mechanical Strength and Failure-Mechanisms in Dolomite-Limestone Composites." (2008).

De Paola, N., D. R. Faulkner, and C. Collettini. "Brittle versus ductile deformation as the main control on the transport properties of low-porosity anhydrite rocks." Journal of Geophysical Research: Solid Earth 114, no. B6 (2009).

Dewhurst, D. N., A. F. Siggins, U. Kuila, M. B. Clennell, M. D. Raven, and H. M. Nordgard-Bolas. "Elastic, geomechanical and petrophysical properties of shales." In The 42nd US Rock Mechanics Symposium (USRMS). American Rock Mechanics Association, 2008.

Downey, Marlan W. "Hydrocarbon Seal Rocks: Chapter 8: Part II. Essential Elements." (1994): 159-164.

Farquharson, Jamie I., Michael J. Heap, and Patrick Baud. "Strain-induced permeability increase in volcanic rock." Geophysical Research Letters 43, no. 22 (2016): 11-603.

Ferrill, David A., and Alan P. Morris. "Dilational normal faults." Journal of Structural Geology 25, no. 2 (2003): 183-196.

Gluyas, Jon G., and Richard E. Swarbrick. Petroleum geoscience. John Wiley & Sons, 2021.

Grunau, Hans R. "A worldwide look at the cap-rock problem." Journal of Petroleum Geology 10, no. 3 (1987): 245-265.

Hajiabdolmajid, Vahid, and Peter Kaiser. "Brittleness of rock and stability assessment in hard rock tunneling." Tunnelling and Underground Space Technology 18, no. 1 (2003): 35-48.

Hangx, Suzanne JT, Christopher J. Spiers, and Colin J. Peach. "Mechanical behavior of anhydrite caprock and implications for CO2 sealing capacity." Journal of Geophysical Research: Solid Earth 115, no. B7 (2010a).

Hangx, S. J. T., C. J. Spiers, and C. J. Peach. "The effect of deformation on permeability development in anhydrite and implications for caprock integrity during geological storage of CO2." Geofluids 10, no. 3 (2010): 369-387.

Hao, Fang, Tonglou Guo, Yangming Zhu, Xunyu Cai, Huayao Zou, and Pingping Li. "Evidence for multiple stages of oil cracking and thermochemical sulfate reduction in the Puguang gas field, Sichuan Basin, China." AAPG bulletin 92, no. 5 (2008): 611-637.

Hao, Shisheng, Zhilong Huang, Guangdi Liu, and Yuling Zheng. "Geophysical properties of cap rocks in Qiongdongnan Basin, South China Sea." Marine and petroleum geology 17, no. 4 (2000): 547-555.

Hawkes, C. D., P. J. McLellan, and S. Bachu. "Geomechanical factors affecting geological storage of CO2 in depleted oil and gas reservoirs." Journal of Canadian Petroleum Technology 44, no. 10 (2005).

Heard, H. C. "Chapter 7: Transition from brittle fracture to ductile flow in Solenhofen limestone as a function of temperature, confining pressure, and interstitial fluid pressure." Geological Society of America Memoirs 79 (1960): 193-226.

Hillis, Richard R. "Coupled changes in pore pressure and stress in oil fields and sedimentary basins." Petroleum Geoscience 7, no. 4 (2001): 419-425.

Ingram, Gary M., and Janos L. Urai. "Top-seal leakage through faults and fractures: the role of mudrock properties." Geological Society, London, Special Publications 158, no. 1 (1999): 125-135.

Ingram, G. M., J. L. Urai, and M. A. Naylor. "Sealing processes and top seal assessment." In Norwegian Petroleum Society Special Publications, vol. 7, pp. 165-174. Elsevier, 1997.

Jin, ZhiJun. "Formation and accumulation of oil and gas in marine carbonate sequences in Chinese sedimentary basins." Science China Earth Sciences 55, no. 3 (2012): 368-385.

Kwon, Ohmyoung, Andreas K. Kronenberg, Anthony F. Gangi, Brann Johnson, and Bruce E. Herbert. "Permeability of illite-bearing shale: 1. Anisotropy and effects of clay content and loading." Journal of Geophysical Research: Solid Earth 109, no. B10 (2004).

Lam, Tom, Derek Martin, and Dougal McCreath. "Characterising the geomechanics properties of the sedimentary rocks for the DGR excavations." In Canadian geotechnical conference, Ottawa. 2007.

Lockner, David A. "Rock failure." Rock physics and phase relations: A handbook of physical constants 3 (1995): 127-147.

Lü, Xiuxiang, Yafang Wang, Hongfeng Yu, and Zhongkai Bai. "Major factors affecting the closure of marine carbonate caprock and their quantitative evaluation: A case study of Ordovician rocks on the northern slope of the Tazhong uplift in the Tarim Basin, western China." Marine and Petroleum Geology 83 (2017): 231-245.

Lyu, Wenya, Lianbo Zeng, Benjiang Zhang, Fengbin Miao, Peng Lyu, and Shaoqun Dong. "Influence of natural fractures on gas accumulation in the Upper Triassic tight gas sandstones in the northwestern Sichuan Basin, China." Marine and Petroleum Geology 83 (2017): 60-72.

Ma, Yongsheng. "Regional Cap Rock and Hydrocarbon Preservation." In Marine Oil and Gas Exploration in China, pp. 129-158. Springer, Berlin, Heidelberg, 2020.

Ma, Yongsheng, Xusheng Guo, Tonglou Guo, Rui Huang, Xunyu Cai, and Guoxiong Li. "The Puguang gas field: New giant discovery in the mature Sichuan Basin, southwest China." Aapg Bulletin 91, no. 5 (2007): 627-643.

Ma, Yongsheng, Shuichang Zhang, Tonglou Guo, Guangyou Zhu, Xunyu Cai, and Maowen Li. "Petroleum geology of the Puguang sour gas field in the Sichuan Basin, SW China." Marine and Petroleum Geology 25, no. 4-5 (2008): 357-370.

Magoon, Leslie B., and Wallace G. Dow. "The petroleum system: chapter 1: Part I. Introduction." (1994): 3-24.

McLamore, R., and K. E. Gray. "The mechanical behavior of anisotropic sedimentary rocks." (1967): 62-73.

Mehrgini, Behzad, Hossein Memarian, Maurice B. Dusseault, Hassan Eshraghi, Bahman Goodarzi, Ali Ghavidel, Maryam Niknejad Qamsari, and Maryam Hassanzadeh. "Geomechanical characterization of a south Iran carbonate reservoir rock at ambient and reservoir temperatures." Journal of Natural Gas Science and Engineering 34 (2016): 269-279.

Mehrgini, Behzad, Hossein Memarian, Maurice B. Dusseault, Ali Ghavidel, and Mohammad Heydarizadeh. "Geomechanical characteristics of common reservoir caprock in Iran (Gachsaran Formation), experimental and statistical analysis." Journal of Natural Gas Science and Engineering 34 (2016): 898-907.

Mitchell, T. M., & Faulkner, D. R. (2008). Experimental measurements of permeability evolution during triaxial compression of initially intact crystalline rocks and implications for fluid flow in fault zones. Journal of Geophysical Research: Solid Earth, 113(B11).

Morris, Joseph P., Yue Hao, William Foxall, and Walt McNab. "A study of injection-induced mechanical deformation at the In Salah CO2 storage project." International Journal of Greenhouse Gas Control 5, no. 2 (2011): 270-280.

Osinga, Sander. "Storage of oil sand waste in sub-surface salt caverns: a feasibility analysis based on experimental rock mechanics and geological setting." Master's thesis, 2013.

Peacock, D. C. P., and A. Mann. "Evaluation of the controls on fracturing in reservoir rocks." Journal of Petroleum Geology 28, no. 4 (2005): 385-396.

Petrie, E. S., J. P. Evans, and S. J. Bauer. "Failure of cap-rock seals as determined from mechanical stratigraphy, stress history, and tensile-failure analysis of exhumed analogsStress History and Tensile Failure Analysis of Exhumed Caprock Seal Analogs." AAPG Bulletin 98, no. 11 (2014): 2365-2389.

Petrie, Elizabeth S., Tamara N. Jeppson, and James P. Evans. "Predicting rock strength variability across stratigraphic interfaces in caprock lithologies at depth: Correlation between outcrop and subsurface Predicting Rock Strength Variability Across Stratigraphic Interfaces." Environmental Geosciences 19, no. 4 (2012): 125-142.

Pokrovsky, Oleg S., Sergey V. Golubev, and Jacques Schott. "Dissolution kinetics of calcite, dolomite and magnesite at 25 C and 0 to 50 atm pCO2." Chemical geology 217, no. 3-4 (2005): 239-255.

Raven, K., D. McCreath, R. Jackson, I. Clark, D. Heagle, S. Sterling, and M. Melaney. "Descriptive Geosphere Site Model." Intera Engineering Ltd. and Nuclear Waste Management Organization, NWMO DGR-TR-2011 24 (2011).

Raziperchikolaee, Samin, Mark Kelley, and Neeraj Gupta. "Geomechanical characterization of a caprock-reservoir system in the Northern Appalachian Basin: Estimating spatial variation of in situ stress magnitude and orientation." Interpretation 6, no. 3 (2018): T759-T781.

Richard, Julie, Mai-Linh Doan, Jean-Pierre Gratier, and François Renard. "Microstructures induced in porous limestone by dynamic loading, and fracture

healing: An experimental approach." Pure and Applied Geophysics 172, no. 5 (2015): 1269-1290.

Rutqvist, Jonny. "The geomechanics of CO 2 storage in deep sedimentary formations." Geotechnical and Geological Engineering 30, no. 3 (2012): 525-551.

Rybacki, Erik, Andreas Reinicke, Tobias Meier, Masline Makasi, and Georg Dresen. "What controls the mechanical properties of shale rocks?–Part I: Strength and Young's modulus." Journal of Petroleum Science and Engineering 135 (2015): 702-722.

Rybacki, Erik, Tobias Meier, and Georg Dresen. "What controls the mechanical properties of shale rocks?–Part II: Brittleness." Journal of Petroleum Science and Engineering 144 (2016): 39-58.

Schlömer, S., and B. M. Krooss. "Experimental characterisation of the hydrocarbon sealing efficiency of cap rocks." Marine and Petroleum Geology 14, no. 5 (1997): 565-580.

Smith, Steven A., Pat McLellan, Chris Hawkes, Edward N. Steadman, and John A. Harju. "Geomechanical testing and modeling of reservoir and cap rock integrity in an acid gas EOR/sequestration project, Zama, Alberta, Canada." Energy Procedia 1, no. 1 (2009): 2169-2176.

Tarasov, B. G., and M. F. Randolph. "Superbrittleness of rocks and earthquake activity." International Journal of Rock Mechanics and Mining Sciences 48, no. 6 (2011): 888-898.

Trippetta, F., C. Collettini, P. G. Meredith, and S. Vinciguerra. "Evolution of the elastic moduli of seismogenic Triassic Evaporites subjected to cyclic stressing." Tectonophysics 592 (2013): 67-79.

Trujillo, Natasha Andrea. Influence of lithology and diagenesis on mechanical and sealing properties of the Thirteen Finger Limestone and Upper Morrow Shale, Farnsworth Unit, Ochiltree County, Texas. New Mexico Institute of Mining and Technology, 2018.

Ulusay, Reşat, ed. The ISRM suggested methods for rock characterization, testing and monitoring: 2007-2014. Springer, 2014.

Vilarrasa, Víctor, Jesús Carrera, and Sebastià Olivella. "Hydromechanical characterization of CO2 injection sites." International Journal of Greenhouse Gas Control 19 (2013): 665-677.

Wang, Haixue, Tong Wu, Xiaofei Fu, Bo Liu, Sheng Wang, Ru Jia, and Chao Zhang. "Quantitative determination of the brittle–ductile transition characteristics of caprocks and its geological significance in the Kuqa depression, Tarim Basin, western China." Journal of Petroleum Science and Engineering 173 (2019): 492-500.

Wang, Ze-cheng, Wen-zhi Zhao, Zong-yin Li, Xing-fu Jiang, and Li Jun. "Role of basement faults in gas accumulation of Xujiahe Formation, Sichuan Basin." Petroleum Exploration and Development 35, no. 5 (2008): 541-547.

Wu, Tong, Xiaofei Fu, Bo Liu, Haixue Wang, Zhaohan Xie, and Zhejun Pan. "Mechanical behavior and damage-induced permeability evolution of mudstone

and gypsum caprocks." Journal of Petroleum Science and Engineering 196 (2021): 108079.

Xiaofei, F. U., J. I. A. Ru, W. A. N. G. Haixue, W. U. Tong, Meng Lingdong, and Sun Yonghe. "Quantitative evaluation of fault-caprock sealing capacity: A case from Dabei-Kelasu structural belt in Kuqa Depression, Tarim Basin, NW China." Petroleum Exploration and Development 42, no. 3 (2015): 329-338.

Yang, Yi, Hiroki Sone, Amie Hows, and M. D. Zoback. "Comparison of brittleness indices in organic-rich shale formations." In 47th US rock mechanics/geomechanics symposium. American Rock Mechanics Association, 2013.

Yawei, Li, and Ahmad Ghassemi. "Rock Failure Behavior and Brittleness under the Confined Brazilian Test." In 52nd US Rock Mechanics/Geomechanics Symposium. American Rock Mechanics Association, 2018.

Yunlan, He, Fu Xiaoyue, Liu Bo, Zhou Minghui, Xuefeng ZHANG, G. A. O. Jixian, Yang Yunkun, and Shi Kaibo. "Control of oolitic beaches sedimentation and diagenesis on the reservoirs in Feixianguan Formation, northeastern Sichuan Basin." Petroleum Exploration and Development 39, no. 4 (2012): 466-475.

Zhang, Shuqing, Stephen F. Cox, and Mervyn S. Paterson. "The influence of room temperature deformation on porosity and permeability in calcite aggregates." Journal of Geophysical Research: Solid Earth 99, no. B8 (1994): 15761-15775.

Zhang, Qiangxing, Jianfeng Liu, Huining Xu, Yin Zeng, Chunping Wang, and Lu Wang. "Experimental Investigation on Permeability Evolution of Limestone Caprock

under Coupled THM Processes." KSCE Journal of Civil Engineering 23, no. 12 (2019): 5090-5097.

Zhou, Xuejun, Zhengwen Zeng, and Hong Liu. "Laboratory testing on Pierre shale for CO2 sequestration under clayey caprock." In 44th US Rock Mechanics Symposium and 5th US-Canada Rock Mechanics Symposium. American Rock Mechanics Association, 2010.

Zhu, Wenlu, and Teng-fong Wong. "The transition from brittle faulting to cataclastic flow: Permeability evolution." Journal of Geophysical Research: Solid Earth 102, no. B2 (1997): 3027-3041.

Zoback, Mark D., and Jens C. Zinke. "Production-induced normal faulting in the Valhall and Ekofisk oil fields." In The mechanism of induced seismicity, pp. 403-420. Birkhäuser, Basel, 2002.

CHAPTER V FIGURES

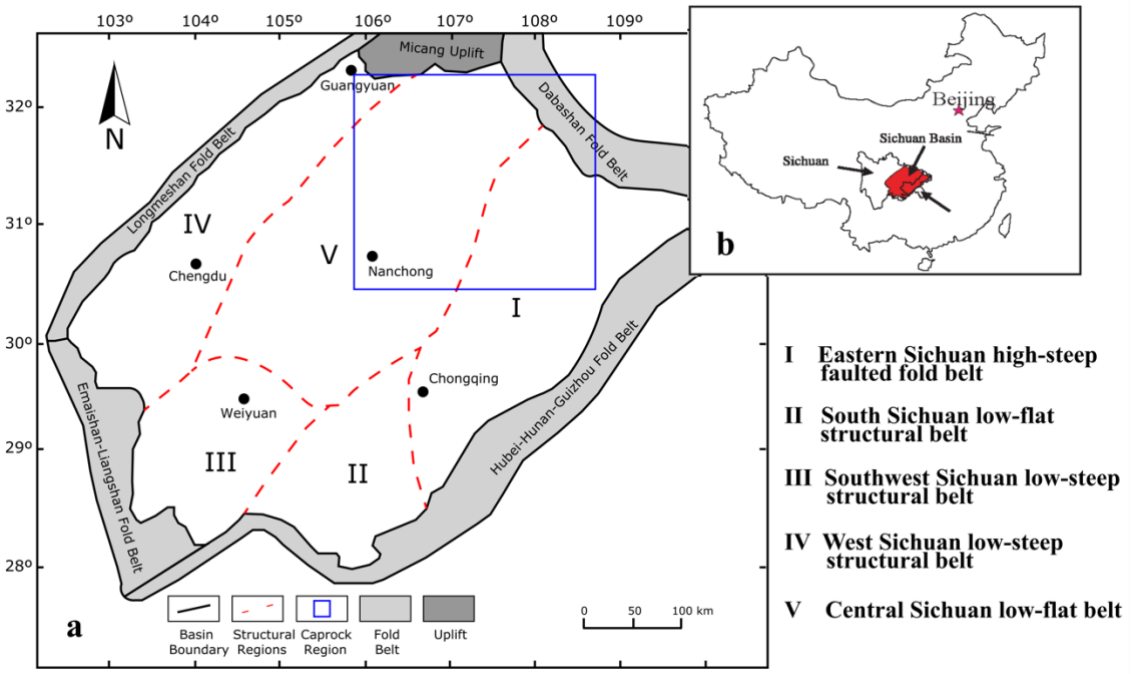

Figure 5.1: Overview map of the greater Sichuan Basin: a) general map showing major basin boundaries, structural provinces and region caprocks were retrieved (blue box) and b) map showing location of Sichuan Basin in China (adapted from Lyu et al., 2017).

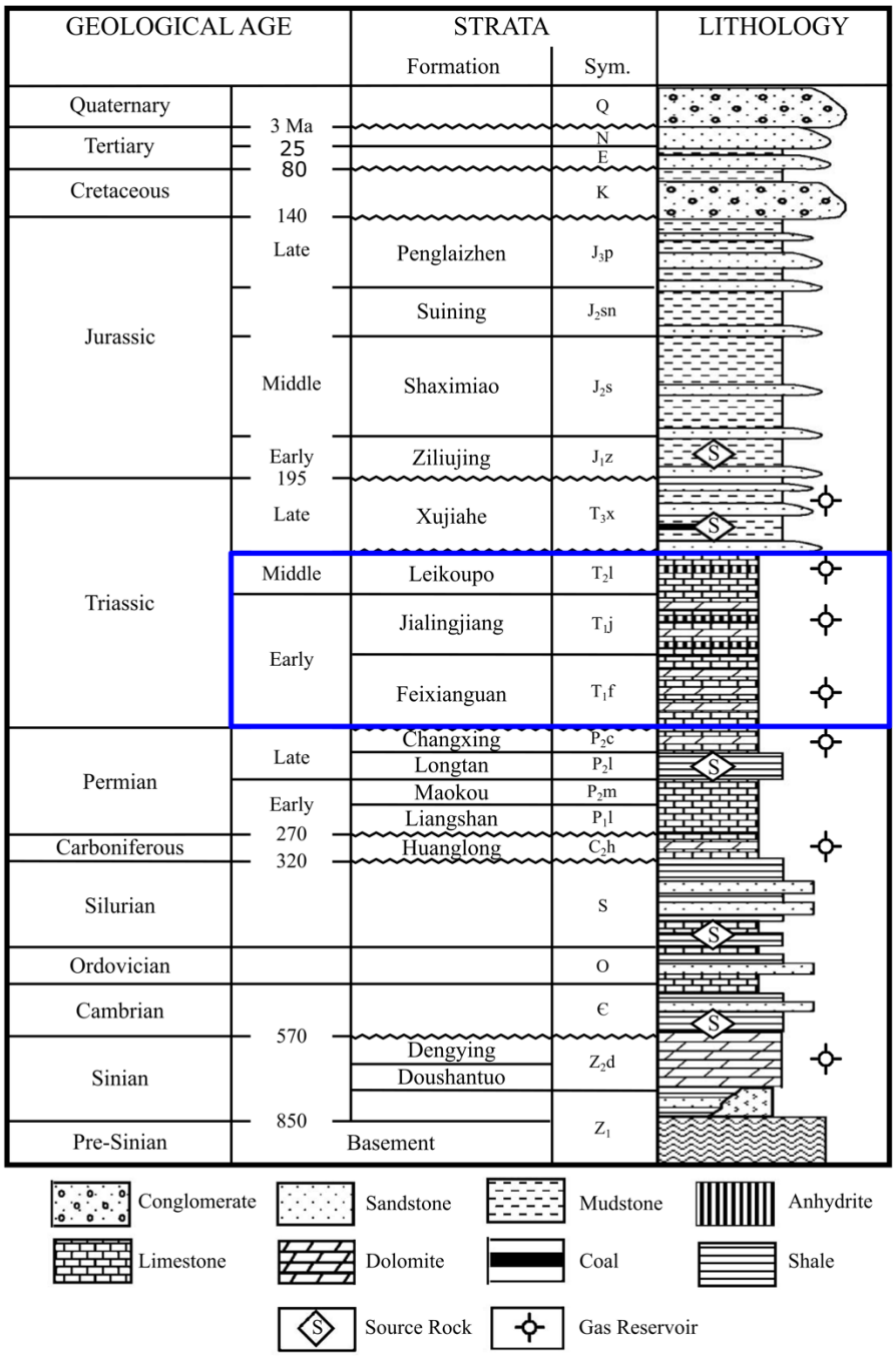

Figure 5.2: Generalized stratigraphic column of Sichuan Basin, modified from Hao et al. (2006). Stratigraphic location of caprock formations sampled for this study are indicated in the right-side column.

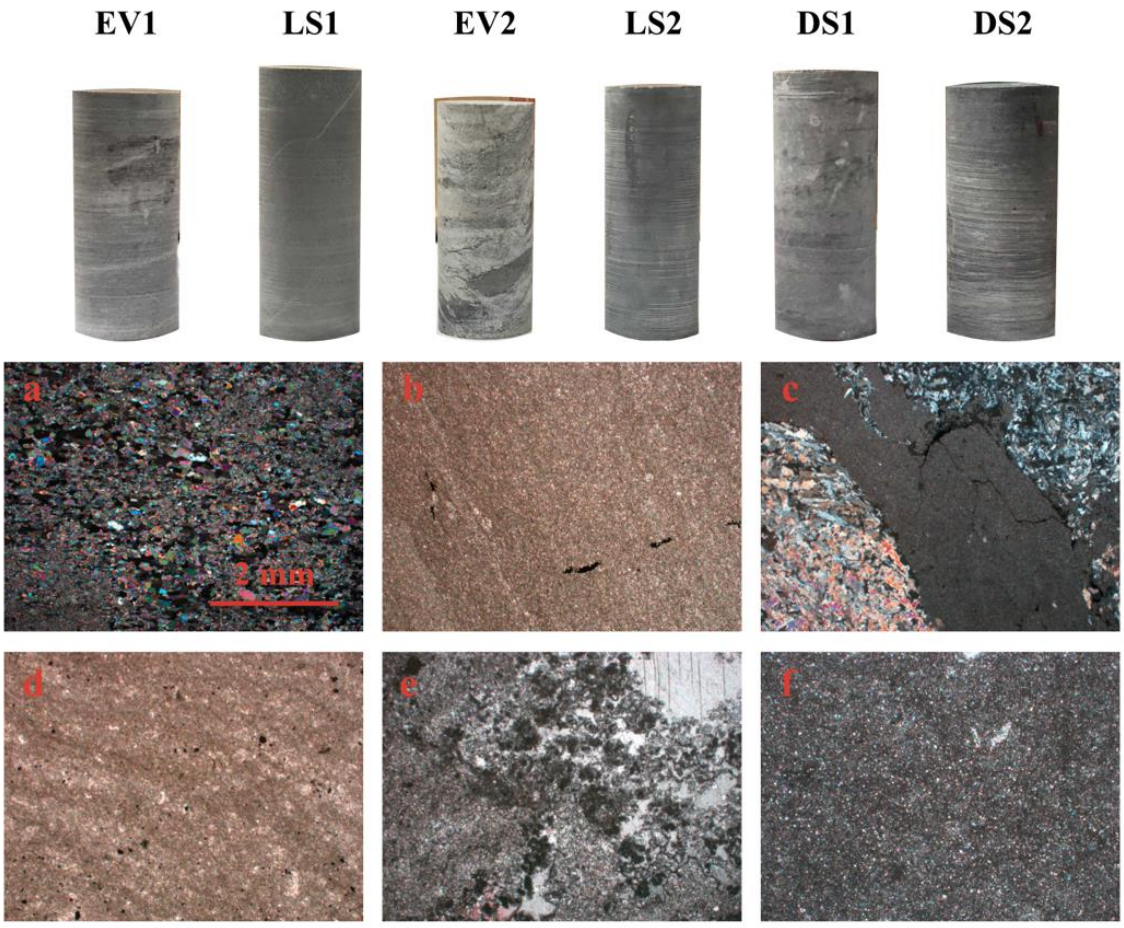

Figure 5.3: Cylindrical specimens of six caprocks cored perpendicular to bedding (top) and photomicrographs of thin-sections for corresponding caprocks (bottom). a) EV1 a fine-grained anhydrite rock with weak lamination; b) LS1 is a fine-grained homogeneous limestone; c) EV2 is a heterogenous rock composed primarily of anhydrite and dolomite distinct even in hand samples; d) LS2 is a muddy limestone that is highly heterogenous from sample to sample; e) DS1 is a dolostone with a large grain-size heterogeneity indicating multiple generations of dolomotization; f) DS2 is a fine-grained dolostone with a texture similar to that of LS1 indicative of early dolomitization.

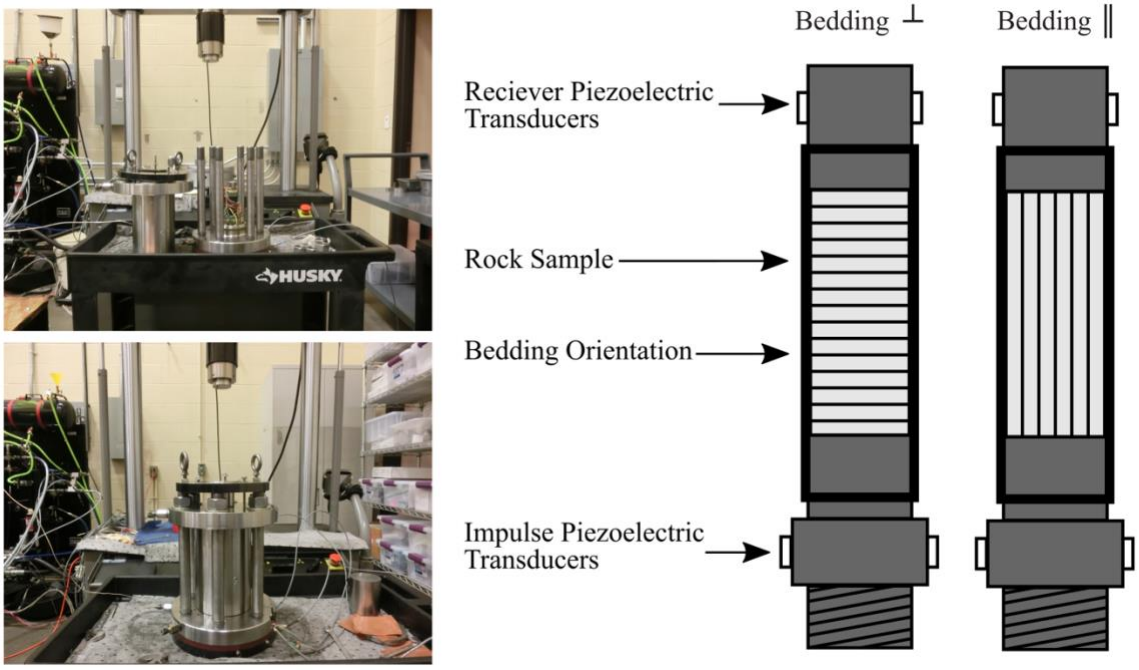

Figure 5.4: Photos of MTS 810 triaxial frame used for pressurizing samples (left) and setup of perpendicular (⊥) and parallel (∥) oriented samples for measuring elastic velocities (right).

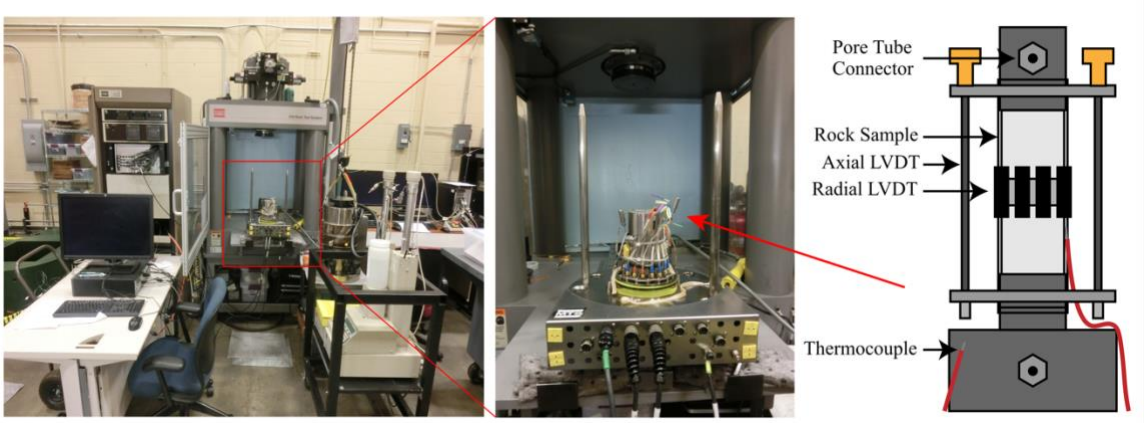

Figure 5.5: Axial deformation frame (MTS 816) used to conduct deformation tests and the general setup of samples for tests conducted (right). Thermocouples were attached during 50 C^{o} experiments to monitor temperature change in the pressure vessel and along the caprock specimen.

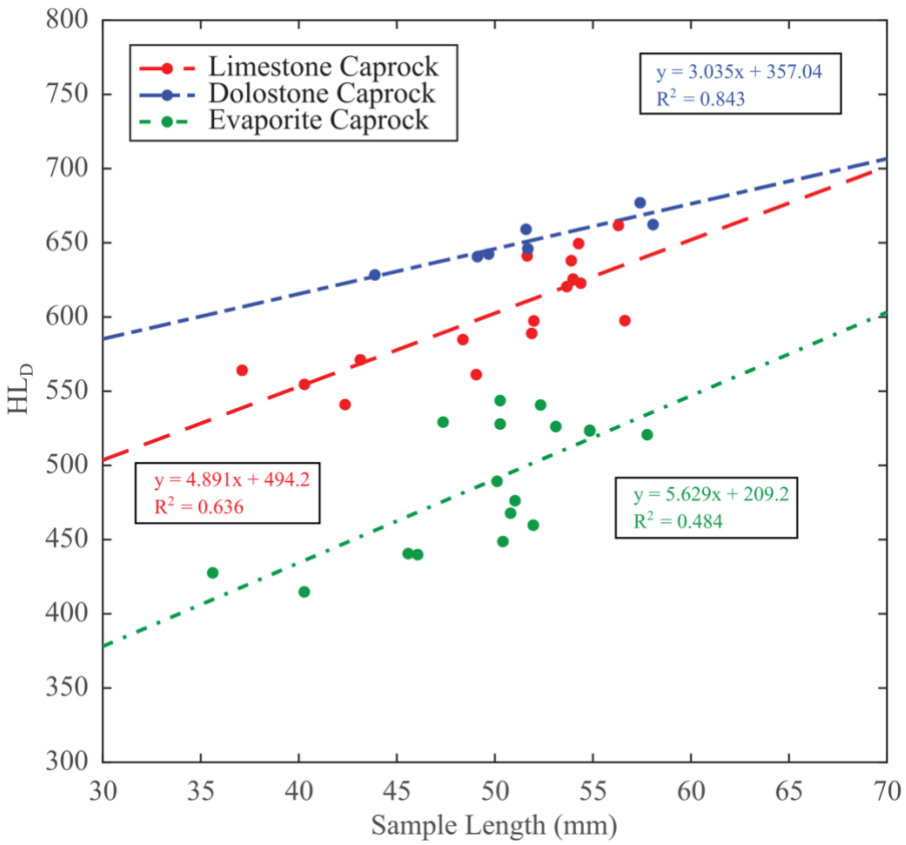

Figure 5.6: Cross-plot of hardness versus specimen length from the different caprock bulk lithologies. Lithology has a strong control on hardness measurements, as carbonate hardness values are greater and more consistent than those of evaporites. R = correlation coefficient.

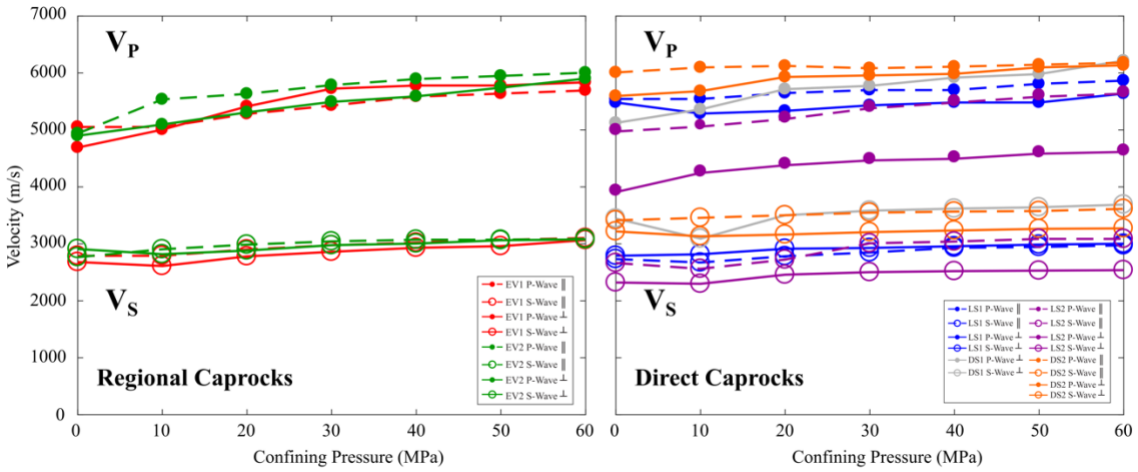

Figure 5.7: Velocity data for tests with direct and regional caprocks oriented parallel and perpendicular to bedding. Regional caprocks are primarily anhydrites, while the direct caprocks are limestones and dolostones.

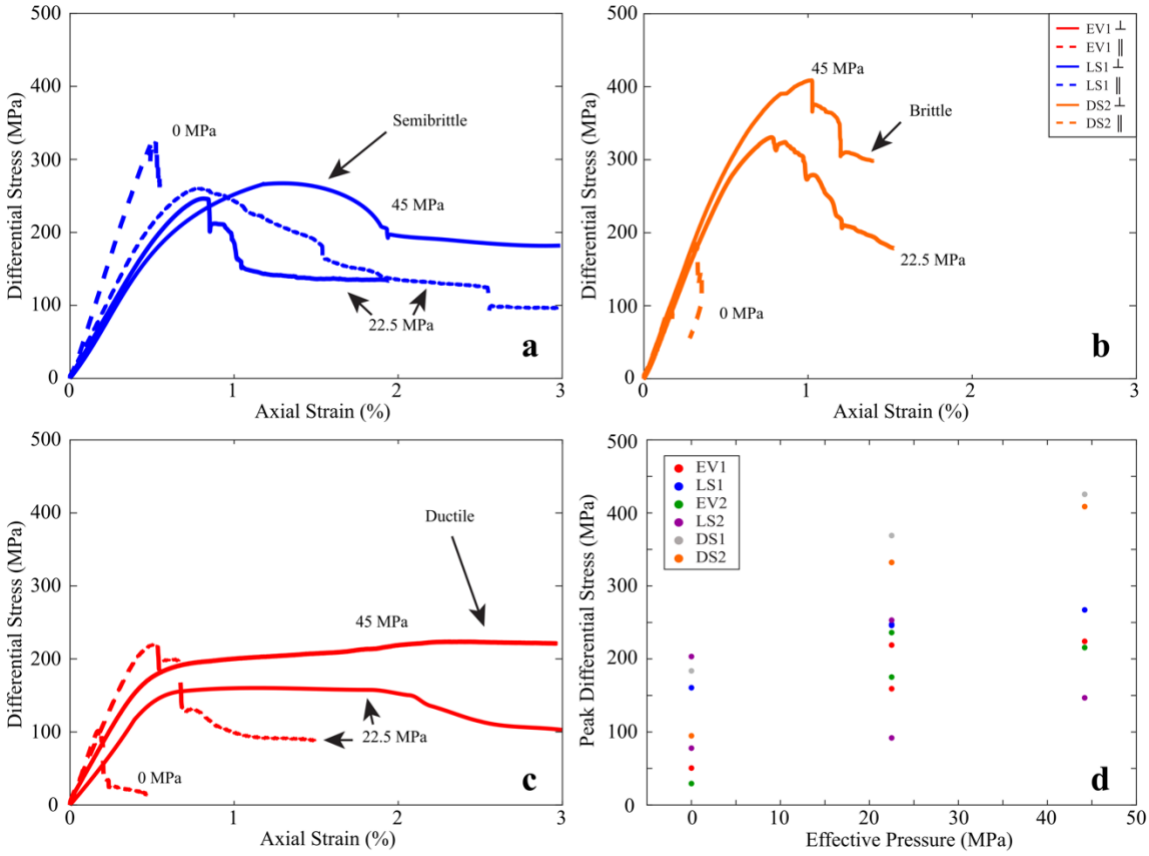

Figure 5.8: The influence of effective pressure on the representative stress-strain behavior of limestone (a), dolostone (b), and evaporite (c) caprocks and the change in caprock failure stress (σ_f) with effective pressure (d). Deformation tests for LS1 (limestone), DS2 (dolostone) and EV1 (evaporite) caprocks are plotted to distinguish the effect lithology can play on mechanical behavior with pressure. While the uniaxial tests all display characteristic brittle mechanical behavior, at effective confining pressures of 45 MPa the difference between the regional caprocks (EV1) and the direct caprocks (LS1, DS2) becomes more apparent.

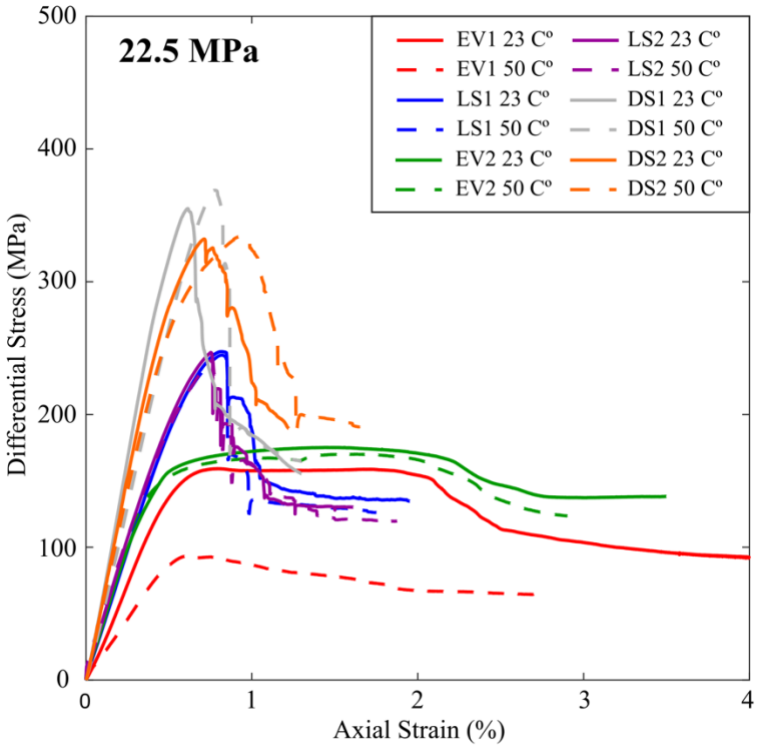

Figure 5.9: Axial strain data for deformation tests at 22.5 MPa effective confining pressures at temperatures of 23 C° (solid lines) and 50 C° (dashed lines). Increasing temperature tends to reduce the elastic properties (ex. Young's moduli or slope of strain curves) and strength properties (ex. peak differential stress experienced), with the degree varying by lithology. The effect is particularly prominent in the anhydrite-rich EV1, which experiences a large reduction in strength and elastic moduli compared to the other caprock lithologies.

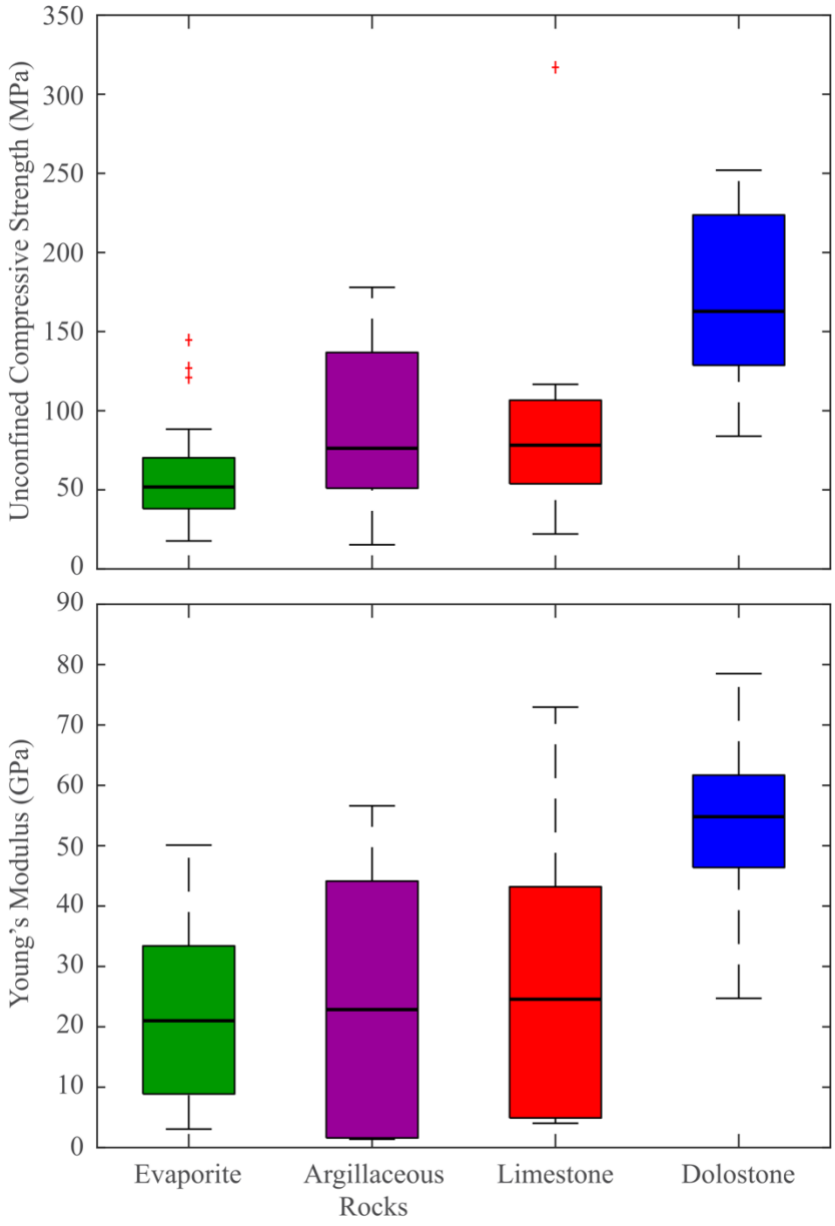

Figure 5.10: Summary of UCS (unconfined compressive strength) and Young's moduli data collected from literature. Means are plotted as horizontal black lines, bottom and top of each box are the 25th and 75th percentiles, whiskers extend to maximum and minimum values observed. Red crosses represent outlier values that are unrepresentative of data.

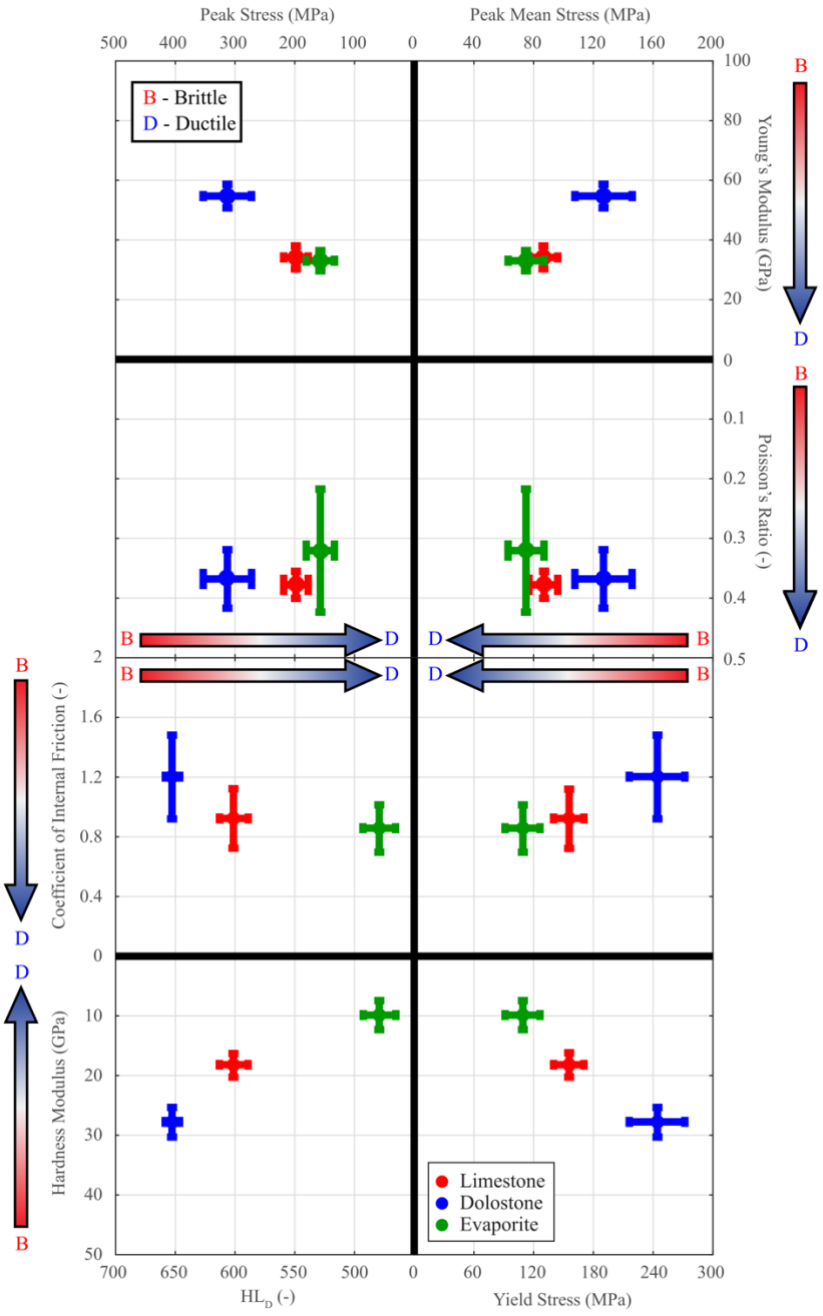

Figure 5.11: Plot of individual geomechanical properties measured in experiments. The central points represent mean value of geomechanical properties for each lithology where measured, while error bars indicate ±1 standard deviation. Gradients indicate the brittle/ductile nature of each property relative to each other.

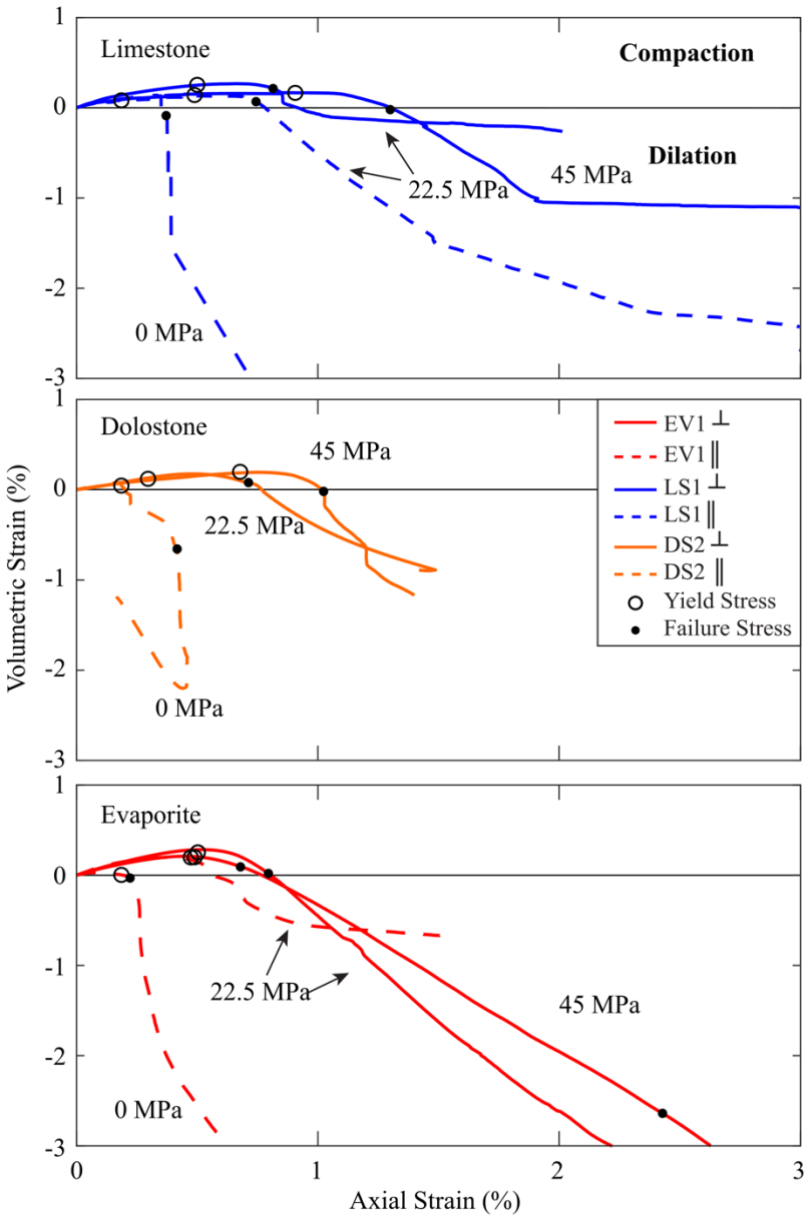

Figure 5.12: Representative data of caprock axial and volumetric strain in different lithologies are shown at each effective confining pressures. Yield and failure stresses are marked with circles and dots on each curve, respectively. Volumetric strain serves as a proxy for porosity change, as under the stress conditions tested the primary mechanisms for porosity change are pore closure and fracture nucleation. Rock permeability will evolve depending upon whether the confining pressure applied and whether the bulk volumetric change is compacting or dilating.

CHAPTER V TABLES

Well	Calcite	Dolomite	Mg-Calcite	Quartz	Anhydrite	Gypsum	Chlorite	Muscovite	Illite	Albite	Pyrite
EV1	-	-	-	1.9	98.1	-	-	-	-	-	-
LS1	94.2	-	-	5.8	-	-	-	-	-	-	-
EV2	-	30.2	-	3.6	62.4	3.8	-	-	-	-	-
LS2 (1)	39.2	31.8	-	4.1	-	-	15.4	4.8	3.3	1.4	-
LS2 (2)	70.3	10.5	-	6.2	-	-	11.6	-	-	-	1.4
DS1	32.5	65.1	-	2.4	-	-	-	-	-	-	-
DS2	5.1	65.5	9.4	9.3	-	-	-	8.1	-	-	2.6

Table 5.1: Quantified X-ray Powder Diffraction (XPRD) analyses. Values are reported in wt. %. Measurements of LS2 show the high variability of the caprock layer, with LS2 (1) being highly dolomitized with large mica and phyllosilicate content and LS2 (2) being more homogenous and no clay content.

Caprock	Depth (m)	Formation	Density[1] (g/cm^3)	Density[2] (g/cm^3)	Porosity[2] (%)
EV1	4705-4712	T_1j	2.878 ± 0.114	2.942	0.716
LS1	6704-6705	T_1f^2	2.709 ± 0.026	2.694	0.460
EV2	4891-4893	T_2l	2.893 ± 0.037	2.858	0.231
LS2	4142-4146	T_1f^4	2.767 ± 0.048	2.745	0.584
DS1	4826-4827	T_1f^3	2.792 ± 0.013	2.792	0.224
DS2	6001-6002	T_1f^2	2.792 ± 0.025	2.813	0.939

Table 5.2: Caprock petrophysical properties calculated from direct measurement of samples (1) and inference from XPRD data (2), noted by superscripts. Density and porosity values are reported in g/cm^3 and %, respectively.

Caprock	Sample Name	Orientation	σ_e (MPa)	T (C°)	σ_f (MPa)	σ_y (MPa)	*E* (GPa)	υ (-)	*H* (GPa)
EV1	1P	∥	0.00	23.00	50.59	44.29	33.33	0.51	22.96
	2P	∥	22.50	23.00	219.02	198.94	51.5	0.22	17.38
	1N	⊥	22.50	23.00	159.23	158.16	31.32	0.26	1.24
	3N	⊥	22.50	50.00	93.53	73.78	18.19	0.06	9.11
	2N	⊥	45.00	23.00	224.09	121.90	40.36	0.21	4.76
LS1	1P	∥	0.00	23.00	160.59	147.93	48.97	0.27	23.71
	2P	∥	22.50	23.00	245.88	186.63	44.55	0.38	19.26
	1N	⊥	22.50	23.00	247.39	194.95	38.89	0.29	18.29
	3N	⊥	22.50	50.00	244.74	196.76	37.29	0.38	16.93
	2N	⊥	45.00	23.00	267.15	157.07	36.22	0.37	13.00
EV2	1P	∥	0.00	23.00	29.33	21.39	16.42	0.74	8.31
	2P	∥	22.50	23.00	236.12	171.34	51.79	0.02	20.97
	1N	⊥	22.50	23.00	175.18	93.58	37.56	0.42	6.76
	3N	⊥	22.50	50.00	170.12	104.16	41.38	0.07	4.84
	2N	⊥	45.00	23.00	215.59	104.44	36.88	0.1	3.02
LS2	1P	∥	0.00	23.00	77.83	70.87	39.22	0.32	17.21
	3P	∥	0.00	23.00	203.32	195.73	48.56	0.23	31.17
	2P	∥	22.50	23.00	91.84	66.78	33.69	0.49	17.61
	1N	⊥	22.50	23.00	253.11	201.65	40.78	0.35	20.04
	3N	⊥	22.50	50.00	241.32	181.76	34.3	0.41	20.56
	2N	⊥	45.00	23.00	146.77	111.63	20.15	0.41	3.34
DS1	1N	⊥	0.00	23.00	183.66	176.24	40.39	0.22	23.22
	2N	⊥	22.50	23.00	355.09	278.37	70.56	0.55	39.44
	4N	⊥	22.50	50.00	369.01	303.13	54.64	0.33	33.21
	3N	⊥	45.00	23.00	425.47	294.77	60.42	0.56	34.38
DS2	1P	∥	0.00	23.00	94.76	83.70	33.9	0.22	25.38
	1N	⊥	22.50	23.00	332.19	263.45	56.34	0.31	26.69
	3N	⊥	22.50	50.00	334.67	234.87	50.92	0.21	19.69
	2N	⊥	45.00	23.00	408.64	320.27	58.03	0.37	21.11

Table 5.3: Key variables for all deformation tests conducted. σ_e = effective confining pressure; T = temperature; σ_f = failure stress; σ_y = yield stress; *E* = Young's modulus; υ = Poisson's ratio; *H* = hardening modulus.

Well	φ_I (º)	C (MPa)
EV1	36.1	21.2
LS1	41.4	41.4
EV2	22.0	52.5
LS2	32.5	26.0
DS1	43.5	43.9

Table 5.4: Angle of internal friction and cohesive strength derived from analysis of deformed samples post-deformation. Values were calculated using the fracture angle of each triaxially deformed caprock to find the shear and normal stresses, which were then linearized to find the overall angle of internal friction and cohesive strength.

	UCS (MPa)	E (GPa)	υ (-)
Evaporites	17 - 145/61.2	3 - 50/21.6	0.15 - 0.45/0.28
Argillaceous Rocks	15 - 178/90.3	1 - 56/23.9	0.24 - 3.00/0.67*
Limestones	22 - 317/89.0*	4 - 73/24.5	0.11 - 0.31/0.22
Dolostones	84 - 252/169.8	25 - 79/53.7	0.21 - 0.48/0.30

Table 5.5: Range and mean value of properties determined from mechanical tests of caprocks and analogous lithologies in the existing literature. UCS = Unconfined Compressive Strength; E = Young's modulus; υ = Poisson's ratio. *Anomalously high UCS and Poisson's ratio observed in limestones and mudstones tested by Trujillo (2018), respectively.

CHAPTER VI: CONCLUDING REMARKS

6.1 Summary of Chapters

This dissertation considered the properties of rocks in two regions where understanding and correctly modeling the subsurface is of critical importance.

The strength, sonic velocity, and elastic properties of several intact basement rock types from Oklahoma were measured using various experimental methods. It was shown that rock properties vary noticeably with different basement lithologies, even for compositionally similar granites from different localities such as Granite A and B. Experimental measurements showed that basement rock strength increases with pressure and depth but is reduced by the presence of fluids. Static and dynamic elastic moduli were shown to disagree significantly depending upon the basement rock type, with granites having the largest variation between the two. Characteristics like V_P/V_S and high elastic moduli were shown to be a good indicator of anomalous features like mafic dikes in the basement.

Data from experimental work was used to analyze and critique existing assumptions about velocities in the basement of Oklahoma and Kansas. Vertically oriented samples of basement rock from the region were used to find the trends in P- and S-waves with depth. Measurements were used to create 1D velocity profiles for the region that could be compared with existing models of the basement structure in the region. It was shown that existing models presume certain characteristics in the subsurface (e.g., constant V_S and V_P/V_S, regional homogeneity, etc.) that are contradicted by are contradicted by laboratory measurements. The inherent anisotropy of these basement rocks was also studied using both ultrasonic velocity and fracture measurements. It was shown that, within an isotropic

stress field, rocks in the basement exhibit non-negligible anisotropy. Observations of greater horizontal anisotropy than vertical anisotropy agree with regional observations, and sample fracture measurements of oriented samples show preferred fracture directions also agree with regional observations. Comparing the results with well log measurements showed that P- and S-wave anisotropy exists has been observed in the field but should not be assumed solely to be a function of the in-situ stresses. As 1D and 3D velocity models of the subsurface are a powerful tool for locating structures and seismicity in the basement, it is shown they must take into account the local geologic properties and variation to minimize errors.

The properties of evaporite and carbonate caprocks from the Sichuan Basin were determined to identify the characteristics of ideal caprocks and the behaviors expected of seals in the region. Experimental data showed caprock properties varied with pressure, temperature, and orientation. Deformation tests, when combined with regional stress measurements, were able to clarify the stresses required to initiate yield and failure in the caprocks that would compromise integrity. Experimental observations were compared with other laboratory caprock tests to show lithologic variability and identify global trends in ideal caprocks. By mapping the properties of different caprock lithologies, it was shown that information about the specific caprock lithology can be used to estimate its brittle-ductile character and subsequent stability in the subsurface. It was also inferred that carbonates may act as efficient caprocks in the region, but that they are more susceptible to brittle failure and thus require a better characterization than more ductile caprock lithologies.

6.2 Future Work

The properties derived for basement rocks in the Oklahoma/Kansas region provide a useful constraint of the subsurface behavior for the purposes of subsurface modeling and analysis. A next step in this work would involve quantifying these parameters at the hydro-chemo-mechanical conditions pertinent to the region, as these would enhance attempts at predicting the in-situ conditions required for induced seismicity. The basement strength and stability could also be further refined by utilizing failure criterion that incorporate information about the bulk rock quality and composition (e.g., Hoek-Brown). With the relative mechanical properties of the basement constrained, the data could be used to develop 1D or 3D geomechanical models of basement faults in the region. Geomechanical fault models where induced seismicity is known to have occurred could be used to simulate how the impact of different basement rock properties on fault re-activation. On a larger scale, the laboratory strength data could be utilized to determine the regional crustal strength in Oklahoma.

In chapters II, III, and IV I showed that velocities in the basement are affected by the lithological, spatial, and microstructural heterogeneity across the region. Geophysical measurements across Oklahoma/Kansas could be compared with the experimental measurements to potentially identify vertical and lateral changes in the basement rock composition. Identifying changes in the basement composition and structure could be useful in understanding deformation and structure of the overlying sediment as well. Since many regional velocity models treat V_P/V_S as constant, in the future a shear-wave model could be developed for the basement and compared with the models in Chapter III. Seismic velocity models, and particularly 1D velocity models, are an important component in the

re-locating faults where seismicity has occurred. With the experimental data and corresponding models, it would be useful to utilize each model to analyze and re-locate seismicity sources and see how the locations change depending upon the assumed basement composition. Further, the velocity anisotropy data in Chapter IV could also be compared with existing seismic velocities to identify how stress or fault orientations can produce different degrees of seismic anisotropy.

In Chapter V, the experimentally measured rock properties of several caprocks were compared with other experimental measurements and used to map the geomechanical properties of different caprocks lithologies. Locally, this work could be expanded by similar measurements of argillaceous or shale caprocks from the Sichuan Basin, as they act as prominent caprocks as well. This would offer further clarification on what characteristics are important for a caprock to maintain in the region. Globally, this work could be expanded by compiling field measurements of caprocks and correlating these properties with cases where caprock integrity was compromised in-situ. Additionally, lithology is seen as prominent factor in determining caprock quality and efficiency. The experimental data reported here shows that minor compositional changes such as clay content and dolomitization, even in small amounts, significantly alter caprock properties from the more homogenous rock types such as limestone and evaporite. A better understanding of compositional variations in caprocks, when combined with an understanding of the reservoir-caprock paleoenvironment, could allow for: 1) determining the caprock stability based on the predicted conditions of deposition and 2) identifying thresholds of composition that enhance or reduce caprock brittleness in-situ. Finally, caprock integrity in limestone, dolostone, and evaporite caprocks of the Sichuan Basin could be directly

shown by developing geomechanical models of the reservoir-caprock system using the measured properties for each caprock lithology. By simulating in-situ changes due to petroleum exploration and production, the relative impact of lithology on caprock stability could be demonstrated.

APPENDIX A: MECHANICAL RESPONSE OF CASTLEGATE SANDSTONE UNDER HYDROSTATIC CYCLIC LOADING

A.1 Motivation and Methods

Periodic fluctuations in the subsurface stresses are quite common over both large and short time scales. For example, stress changes are often induced in the near-wellbore environment of natural gas storage reservoirs, wastewater injection wells and geothermal projects (Heffer, 2002; Dusseault, 2010; Davidson et al., 2016; Martínez-Garzón et al., 2017; Ye et al., 2019). Such stress changes are expected to alter mechanical behavior of rocks in-situ from the predicted response of a static stress state (Rutqvist, 2008; Yoon et al., 2014). The current behavior reflects the stress- and time-dependency of rocks (i.e., stress path or stress history) and must be understood in order to predict the effect of future stress changes.

The effect of stress path and stress fluctuations, which can affect properties such as the elastic moduli (Shalev et al., 2014; Ingraham et al., 2017), elastic wave velocity (Holt et al., 1991; Ma and Zoback, 2018), and permeability (Zivar et al., 2019) of rocks, is often studied through cyclic loading experiments under various conditions (Bernabe, 1987; Warpinski and Teufel, 1992; Shalev et al., 2014). These are of particular importance to reservoir rocks, where cyclic stress states are commonly induced by the migration or injection of various fluids and lead to a variety of impacts (Nagel, 2001; Zang et al., 2019).

Sandstones for example are a prominent reservoir rock type with heavily investigated hydromechanical properties, but with less work on how stress cycling impacts sandstone porosity and permeability. Sandstone permeability and other petrophysical properties have been shown to evolve with stress cycling depending upon the effective

stress, fluid composition, clay content, cycle duration, pore or confining pressure cycling, and stress history (Dey, 1986; Bernabe, 1987; Keaney, 1996; Heap et al., 2009). Little attention has been given to how sandstone properties evolve with stress cycling at low effective pressures, or how properties relate to the loading rate, stress cycle amplitude and period, and total compaction. Here, the effects of cyclic loading were measured on a reservoir-analogue sandstone to observe the evolution of rock mechanical and petrophysical properties. Hydrostatic loading tests were conducted with various loading conditions, such as different cycling rates, effective stresses, and test durations. Stress, strain, and permeability were monitored in sandstones to observe the impact of stress history on rock behavior.

Tests were conducted with eight samples of Castlegate sandstone (CG). Composed primarily of quartz (~90 %), calcite cement, feldspars and Fe-rich clays, with a grain size averaging from 0.2 mm to 0.25 mm, and an average porosity of ~26 ± 0.3 and low pre-existing fracture content, the sandstone serves as a reasonable reservoir-analogue. Samples were cored perpendicular to bedding as right cylinders, with the dimensions listed in Table A.1. The various testing conditions are shown in Table A.2, and a general schematic of the test conditions is shown in Figure A.2. Confining pressure (P_c) was first increased at incrementally or at a constant rate, then pore pressure (P_p) was increased to the maximum value utilized in the test. Stress cycling was then initiated, with either confining pressure or pore pressure decreasing at constant rate until the minimum effective pressure (P_{eff}) was achieved before increasing pressure at the same rate. This stress cycling continued to the test end, whereby pressure was unloaded at a constant rate. The only exception to this was CG_009, which was kept at a constant effective stress of 10.34 MPa (i.e., creep test).

Although the average effective stress during the cycling tests was 1.5-2 MPa greater than the average effective stress in CG_009, the difference in pressure is small and thus the test conditions are still comparable. Axial (ε_{ax}) and radial (ε_{rad}) strains, reported as percent strain, were measured through a set of mounted LVDTs on each sample, and effective pressure was calculated from the difference between the confining pressure and pore pressure.

The only pauses in the stress cycling were to measure permeability, during which confining pressure and pore pressure were decreased. With a differential pore pressure between the sample ends, permeability was calculated using Darcy's Law:

$$k = \frac{QL\mu}{A\Delta p} \quad (1)$$

where k is the sample permeability, Q is the volumetric flow rate, μ is the dynamic viscosity, L and A are the sample length and area, and Δp is the pore pressure drop between the sample ends. Flow rate was kept constant for each test (~8×10^{-8} m^3/s). For CG_001 and CG_003, permeability was determined prior to and after the stress cycling portion of the tests occurred, while for the rest it was determined periodically during the stress cycling portions (Table A.2) for a maximum and minimum effective pressure (P_k).

A.2 Stress Cycling Induced Deformation and Permeability Changes

The axial and radial strains during testing are shown in Figure A.2. The strains illustrate the time-dependency of deformation in the samples. Axial deformation is universally greater than radial deformation, regardless of the differing conditions. Moreover, axial strain is more sensitive to fluctuations in stress induced by stress cycling. This anisotropy of deformation is likely an inherent characteristic of the specific lithology, given its ubiquity between samples, with the degree of anisotropy being attributable to

sample-to-sample variation. Typically for sandstones, during the initial hydrostatic loading, the stress-strain relationship of our samples is initially non-linear due to crack-closure and grain-rearrangement, then becomes linear above 5-10 MPa. Permanent non-recoverable damage accumulates as stress cycling occurs, such that when unloaded a degree of strain is retained (~0.2-0.8 %). The only exception to this is CG_009, the constant stress test, which exhibits a permanent strain upon unloading less than 0.1 %.

The axial and radial strains were used to calculate the volumetric strain (ε_v) of each sample during testing. To show the impact of stress cycling over time, we change in volumetric strain per unloading cycle shown in Figure A.3. The change in strain from the peak to the nadir of each cycle (see Figure A.1) increases initially in all samples during the early part of the test then changes more gradually over time. Volumetric strain per cycle increases as the stress cycle amplitude increases. CG_006 and CG_007 have the largest cycle amplitudes and similarly display the greatest strain change, followed by CG_010 and then CG_005, CG_004, and CG_003. CG_005 does not seemingly follow this trend, as cycle amplitude matches that of CG_006 and CG_007 but exhibits behavior more akin to CG_003 and CG_004. This may be an effect of the differing pressurization rates during cycling, as CG_003/4/5 were all tested with 8-hour cycle lengths instead of 4-hour cycle lengths for CG_006/7. Additionally, samples tested with 8-hour stress cycles exhibited an increasing strain change over time, samples with 4-hour stress cycles static or even decreasing strain changes per cycle over time, while the sample with a 2-hour cycle rate shows a marked decreasing trend in cycle strain change (Figure A.3). All of this further implies that loading rate during cycling impacts the long-term mechanical behavior of the sandstones.

The permeability over time is shown in Figure A.4 for the 8-hour cycles (Figure A.4a), 4- and 2-hour and constant stress tests (Figure A.4b). Over time the permeability decreases for all samples, with the largest reduction in the first few days before decreasing in a quasi-linear manner. Notably, permeability in CG_010 (with 2-hour cycle lengths) decreases less than the 4-hour cycle length tests, suggesting a possible impact again from the cycle loading rate. It is also noteworthy the similarity between CG_006/7, despite the former having pore pressure cycled and the latter having confining pressure cycled. This might indicate that the mechanism of the stress change is of negligible importance to the rock properties as long as the effective pressure is maintained. Figure A.4c shows that the effect of pressure on permeability for the initial incremental increase of pressure during loading of CG_005/6/7. During initial loading, permeability does not markedly increase or decrease as the pressure increases on each sample. The only exception to this is CG_005 where a large drop in permeability occurs above ~8 MPa. From the volumetric strain measured during testing, the sample experienced an anomalously large increase in strain between 7-8 MPa. From these observations, we infer that permeability at low pressures may be controlled more by the volumetric strain than the mechanical load applied.

A.3 Impact of Stress Path on Reservoir-Analogue Properties

In high porosity sandstones (> ~15%), initially deformation during hydrostatic pressurization occurs through the grain rearrangement and grain sliding, after which stress and strain have a quasi-linear relationship before the onset of grain crushing and fracturing (David et al., 1994). However, in our experiments the mean effective stress is relatively constant during each test. This indicates the corresponding changes to mechanical behavior in our tests should be attributed solely to their respective stress paths rather than the

absolute stresses. Such an observation is supported by the aforementioned difference in unloading strain between the stress cycling tests and the constant stress test (i.e., CG_009).

The effect of the different loading conditions can be seen in Figure A.5, where we showed the change in volumetric strain at the peak of every five cycles with both time and cycle number. CG_009/010 were plotted differently due to their test conditions, with CG_010 corrected due to stress cycles only beginning after five days of constant stress and CG_009 recording the change in strain for every 100^{th} measurement (Figure A.5d). The peak cycle strain change was approximately logarithmic for all samples. Initially peak strain increased markedly, before becoming increasing more gradually or remaining nearly constant over time. Samples with 8-hour cycle lengths (Figure A.5a/b) accumulated more strain than samples with shorter cycle lengths (Figure A.5c/d), but the increase in peak cycle strain over time for slower cycles becomes diminishes more quickly than the tests with faster cycles. More interesting is the difference between CG_009/010 and the other tests. These two exhibited much less strain change over time compared to the tests with 8- and 4-hour cycle lengths (Figure A.5d). Although both increase initially as the other tests do, their change in peak strain rapidly becomes near constant over time.

The effect of stress cycles was also investigated through the change in the bulk modulus (B) in our test. The bulk modulus is the stress per unit strain required to compress the bulk rock and was derived from the ratio of effective pressure change to volumetric strain change. A higher bulk modulus generally indicates a more rigid, less porous rock. The effect of each test on sample elastic and inelastic behavior can be seen by comparing the B measured during the hydrostatic loading and unloading at the start and end of each test, respectively (Table A.3). While the initial loading moduli ranged from 2-3 GPa, the

unloading moduli measured at the end were universally larger for our samples and tends to increase with the duration testing (with the exception of CG_007). These values though were lower than the dry and wet modulus values reported for the same rock (Ingraham, 2012; Ingraham et al., 2017). This may be due to the magnitude of stress at which B was measured, as the bulk moduli evolve non-linearly with pressure (Shalev et al., 2014). To describe the evolution in elasticity during testing, we also determined *B* for the unloading of each stress cycle and showed it in Figure A.6. The cycling *B* values always exceeded the values measured at the start and ending of the tests. Tests with 8-hour cycle lengths exhibited much larger but more scattered *B* values than the faster cycling tests, and a decreasing trend over time. For 4-hour cycle lengths, moduli are less variable and near-constant after the first few days of testing, while for 2-hour cycle lengths the moduli gradually increase over time (Figure A.6b).

These observations, along with the mechanical data, can clarify the effect cyclic stress conditions on the mechanical behavior of sandstone:

1. Hydrostatic cycling of confining pressure or pore pressure facilitate similar mechanical changes in our samples, so long as the effective pressure is maintained.
2. Hydrostatic stress cycling at such low effective pressures induces significantly more inelastic damage overall than hydrostatic creep does. CG_001 was tested for only 2 days and 5 hydrostatic cycles, and its permanent inelastic strain was more than seven times that of CG_009 despite the test length (Figure A.2, Table A.3).
3. Loading rate and duration exert a significant degree of control on the inelastic damage induced. The peak volumetric strain increases at a diminishing rate as cycling continues. Initially volumetric strain rapidly increases between cycles, after which peak

strain in the 8- and 4-hour cycle tests generally increases more gradually in a non-linear manner. With 2-hour cycles, the volumetric strain increases in a logarithmic manner after cycling begins (~4.8 day into test) and is more similar to the constant stress test than the others (Figure A.7d).

4. Greater compaction occurs over time with greater cycle amplitudes. For example, volumetric strain in CG_005 increases more over time than for the other 8-hour cycle tests, as it has a stress amplitude of 4.8 MPa compared to the 3.3 MPa of the other 8-hour cycle tests.

Porosity and permeability are expected to decrease as a function of pressure (French et al., 2016) and are often fitted with a power-law or exponential function (Rice, 1992, David et al., 1994). While an overall decrease in porosity and permeability was observed in our samples, this cannot be attributed solely to the magnitude of pressure, especially given the initial observations in Figure A.4c. Permeability appears more sensitive to volumetric strain (i.e., compaction) in the samples than the absolute effective pressure applied. This is especially true for our samples, as the fracture content, which often controls fluid flow, is low for our samples and is thus permeability is mainly a function of the intergranular porosity.

Permeability depends upon the stress history in our samples. In Figure A.7, the permeability and volumetric strain measured at high and low P_k conditions was compared between four different loading conditions. While permeability generally decreases over time at all conditions, the decrease in permeability is both greater and less scattered for the high P_k measurements. While the volumetric strain is more consistent and increases over time for all conditions, the high P_k tests shown a greater change in strain during the

permeability measurements. These results imply further that permeability will depend upon the amount of compaction induced by in the sandstone samples rather than the pressures exhibited.

Between the different tests, the loading rate seems to have the greatest impact on sample permeability. For example, CG_004 was cycled with a loading rate of 0.8625 MPa/hr in 8-hour cycles and exhibited the highest permeability values and the greatest scatter overall. Conversely, the lowest permeabilities were recorded in CG_006, which was loaded in 4-hour cycles at a rate of 2.415 MPa/hr, which along with CG_007 exhibited very consistent trends in permeability. The test duration also seems particularly important for permeability, as the earliest values recorded during a test (CG_004) were much greater and more variable than after a few days of stress cycles. Similar observations were seen in both CG_009/010, which both exhibited high initial permeabilities in the first few days before becoming more consistent over time. It is also noteworthy that between these two tests, the constant stress test (CG_009) exhibited near constant permeabilities after the first few days, while the test with 2-hour cycles (CG_010) decreased in permeability once stress cycles initiated.

A.4 Prescriptions for Cyclic Loading in Sandstone Reservoirs

From this analysis, the transport properties of an intact sandstone depend on the volumetric strain, and/or the rate of change in volumetric strain. After the initial loading period, permeability and strain decreases and increase, respectively, more over time for samples that undergo hydrostatic cycling. With faster cycling rates, permeability will be more consistent and volumetric strain will increase more quickly overall. As inelastic compaction via grain rearrangement is the primary deformation mechanism at low pressure

conditions, mechanical behavior and permeability at any given point will depend on the amount of volumetric strain change (e.g., porosity change) over a given interval.

Stress cycling in-situ is a common phenomenon generated through both natural and anthropogenic sources. However, stress perturbations induced by fluid injection and extraction projects occur on much more rapid timescales than under natural conditions. Several prescriptions from this work may therefore be suggested to mitigate unwanted degradation of reservoir characteristics during such projects. Initially, high porosity and permeability reductions should be expected at any condition. Cycling pressure with lower loading rates and amplitudes should lead to less reduction in porosity over time. A trade-off for porosity and permeability "stability" is that these conditions should also expect greater variability in their mechanical and petrophysical properties than with higher loading rates and cycle stress amplitudes. These prescriptions depend upon the magnitude of the mean effective stress during stress cycling, since higher effective pressures diminish the impact of the unloading-loading cycles (Dey, 1986; Shalev et al., 2014). If the goal is to minimize sandstone reservoir changes during injection or recovery projects on large timescales, then ideally one would induce less than 3 MPa of effective stress change and over large cycle durations.

These prescriptions come with two caveats. First, if the effective stresses are sufficient to induce fracturing in the reservoir, or the reservoir contains significant pre-existing damage, fracture porosity may dominate sandstone petrophysical and mechanical behavior during stress cycling rather than intergranular porosity. Second, a number of authors have suggested that amount of clay content will heavily influence any changes to sandstone porosity and permeability (Dey, 1986; Warpinski and Teufel, 1992; David et al.,

1994). In this rock, clay content is minor, thus its impact is expected to be small and localized. We therefore also suggest that understanding stress cycling and stress history impacts on a sandstone reservoir requires sufficient characterization of the reservoir rocks.

Acknowledgements

Sandia National Laboratories is a multimission laboratory managed and operated by National Technology and Engineering Solutions of Sandia, LLC., a wholly owned subsidiary of Honeywell International, Inc., for the U.S. Department of Energy's National Nuclear Security Administration under contract DE-NA-0003525. This work is registered with the Sandia internal designation SAND2021-3446 O.

This work has been previously published in the journal *Geofluids*, https://doi.org/10.1155/2021/8871103.

References

Bernabe, Yves. "The effective pressure law for permeability during pore pressure and confining pressure cycling of several crystalline rocks." Journal of Geophysical Research: Solid Earth 92, no. B1 (1987): 649-657.

David, Christian, Teng-Fong Wong, Wenlu Zhu, and Jiaxiang Zhang. "Laboratory measurement of compaction-induced permeability change in porous rocks: Implications for the generation and maintenance of pore pressure excess in the crust." Pure and Applied Geophysics 143, no. 1 (1994): 425-456.

Davison, J. M., I. Foo, F. Ellis, and A. Proughten. "The in-situ stress response of reservoirs to pressure reduction followed by pressure increase: depletion and rebound stress paths from two case studies." In 50th US Rock

Mechanics/Geomechanics Symposium. American Rock Mechanics Association, 2016.

Dey, Thomas N. "Permeability and electrical conductivity changes due to hydrostatic stress cycling of Berea and Muddy J sandstone." Journal of Geophysical Research: Solid Earth 91, no. B1 (1986): 763-766.

Dusseault, Maurice B. "Deep injection disposal: environmental and petroleum geomechanics." In ISRM International Symposium-6th Asian Rock Mechanics Symposium. International Society for Rock Mechanics and Rock Engineering, 2010.

French, M. E., F. M. Chester, J. S. Chester, and J. E. Wilson. "Stress-dependent transport properties of fractured arkosic sandstone." Geofluids 16, no. 3 (2016): 533-551.

Heap, M. J., P. Baud, P. G. Meredith, A. F. Bell, and I. G. Main. "Time-dependent brittle creep in Darley Dale sandstone." Journal of Geophysical Research: Solid Earth 114, no. B7 (2009).

Heffer, K. "Geomechanical influences in water injection projects: An overview." Oil & Gas Science and Technology 57, no. 5 (2002): 415-422.

Holt, R. M., E. Fjær, A. M. Raaen, and C. Ringstad. "Influence of stress state and stress history on acoustic wave propagation in sedimentary rocks." In Shear waves in marine sediments, pp. 167-174. Springer, Dordrecht, 1991.

Ingraham, Mathew Duffy. "Investigation of localization and failure behavior of Castlegate sandstone using true triaxial testing." Ph. D. Thesis (2012).

Ingraham, Mathew D., Stephen J. Bauer, Kathleen A. Issen, and Thomas A. Dewers. "Evolution of permeability and Biot coefficient at high mean stresses in high

porosity sandstone." International Journal of Rock Mechanics and Mining Sciences 96 (2017): 1-10.

Keaney, Gemma M., Phillip Meredith, Stanley Murrell, and John Barker. "Determination of the effective stress laws for permeability and specific storage in a low porosity sandstone." In Gulf Rocks 2004, the 6th North America Rock Mechanics Symposium (NARMS). American Rock Mechanics Association, 2004.

Ma, Xiaodong, and Mark D. Zoback. "Static and dynamic response of Bakken cores to cyclic hydrostatic loading." Rock Mechanics and Rock Engineering 51, no. 6 (2018): 1943-1953.

Martínez-Garzón, Patricia, Grzegorz Kwiatek, Marco Bohnhoff, and Georg Dresen. "Volumetric components in the earthquake source related to fluid injection and stress state." Geophysical Research Letters 44, no. 2 (2017): 800-809.

Nagel, N. B. "Compaction and subsidence issues within the petroleum industry: From Wilmington to Ekofisk and beyond." Physics and Chemistry of the Earth, Part A: Solid Earth and Geodesy 26, no. 1-2 (2001): 3-14.

Rice, James R. "Fault stress states, pore pressure distributions, and the weakness of the San Andreas fault." In International geophysics, vol. 51, pp. 475-503. Academic Press, 1992.

Rutqvist, Jonny, and C. M. Oldenburg. "Analysis of injection-induced micro-earthquakes in a geothermal steam reservoir, the Geysers Geothermal Field, California." In The 42nd US Rock Mechanics Symposium (USRMS). American Rock Mechanics Association, 2008.

Shalev, Eyal, Vladimir Lyakhovsky, Audrey Ougier-Simonin, Yariv Hamiel, and Wenlu Zhu. "Inelastic compaction, dilation and hysteresis of sandstones under hydrostatic conditions." Geophysical Journal International 197, no. 2 (2014): 920-925.

Warpinski, N. R., and L. W. Teufel. "Determination of the effective-stress law for permeability and deformation in low-permeability rocks." SPE formation evaluation 7, no. 02 (1992): 123-131.

Zhuang, Li, Kwang Yeom Kim, Sung Gyu Jung, Melvin Diaz, Ki-Bok Min, Arno Zang, Ove Stephansson, Günter Zimmermann, Jeoung-Seok Yoon, and Hannes Hofmann. "Cyclic hydraulic fracturing of pocheon granite cores and its impact on breakdown pressure, acoustic emission amplitudes and injectivity." International Journal of Rock Mechanics and Mining Sciences 122 (2019): 104065.

Zivar, Davood, Jalal Foroozesh, Peyman Pourafshary, and Soroush Salmanpour. "Stress dependency of permeability, porosity and flow channels in anhydrite and carbonate rocks." Journal of Natural Gas Science and Engineering 70 (2019): 102949.

APPENDIX A FIGURES

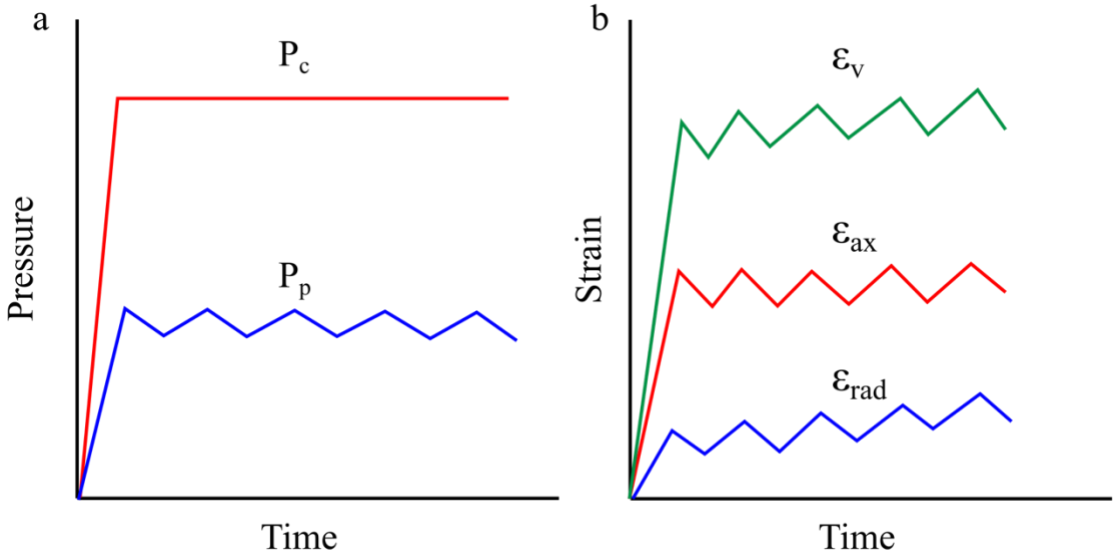

Figure A.1: Model of stress-strain evolution over time during cyclic loading tests. a) Plot of confining pressure (P_c) and pore pressure (P_p) over test duration; b) Plot of axial (ε_{ax}), radial (ε_{rad}) and volumetric strains (ε_v) over test duration.

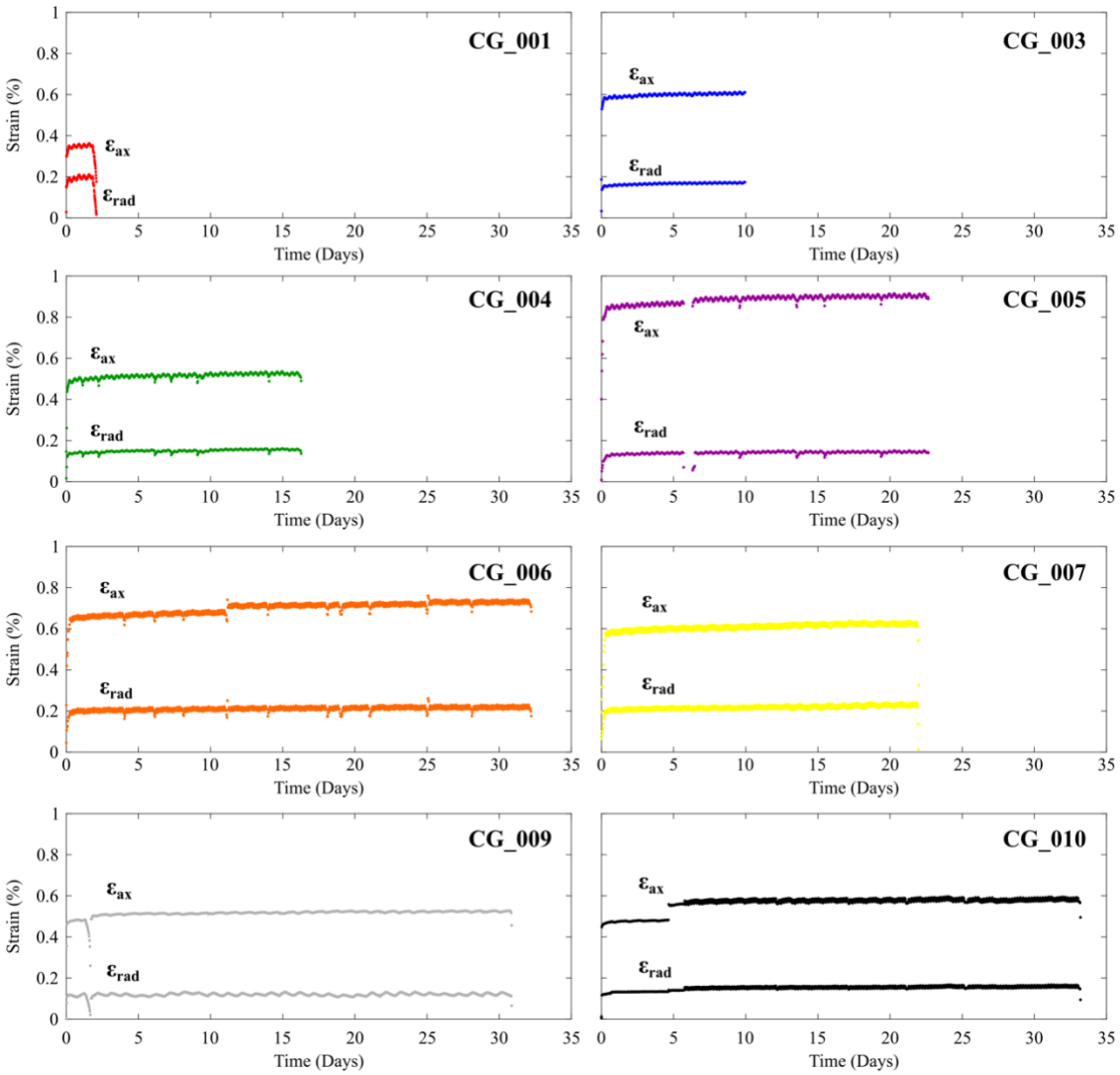

Figure A.2: Axial and radial strains for the duration of each test.

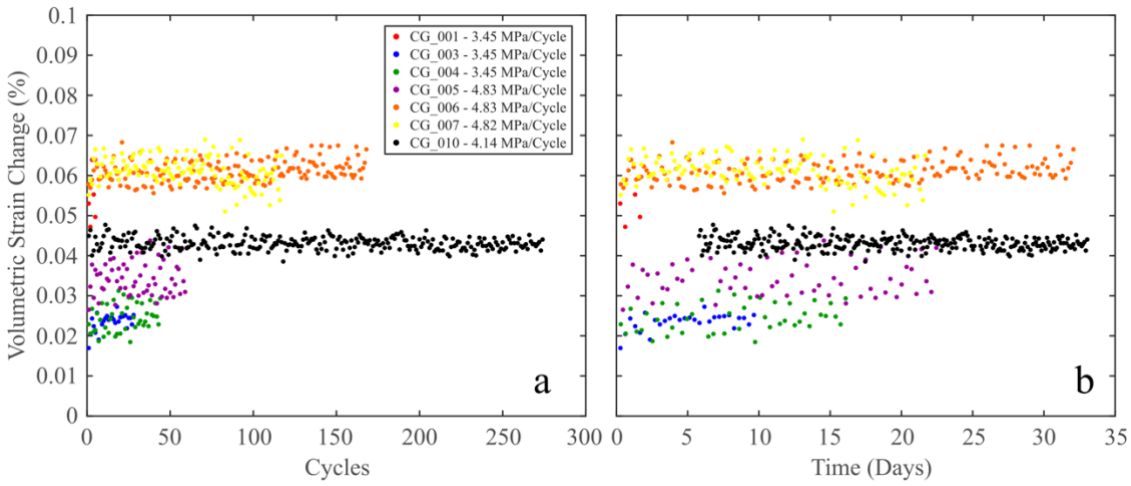

Figure A.3: Change in volumetric strain during unloading portion of each cycle plotted against number of cycles (a) and time elapsed (b). Volumetric strain change is calculated from the difference in the peak and valley of each cycle during the unloading portion.

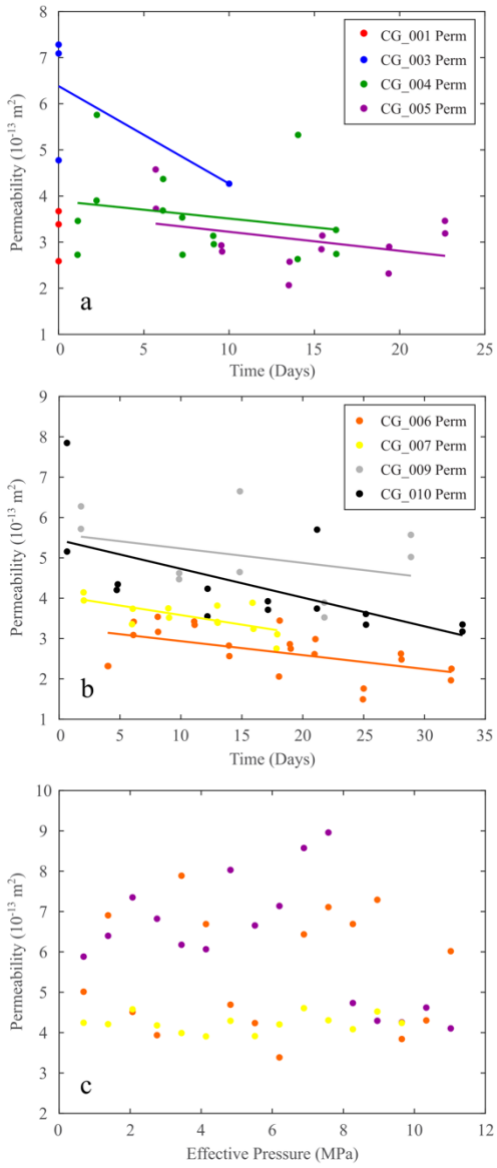

Figure A.4: Permeability determinations: a) Permeability as a function of time during for 8-hour cycle tests; b) Permeability as a function of time during for 4-hour cycle tests (CG_006, CG_007), 2-hour cycle tests (CG_010), and tests without stress cycling (CG_009); c) Permeability measured at intervals of 0.69 MPa during the initial confining pressure loading of CG_005, CG_006, and CG_007, prior to stress cycling initiation.

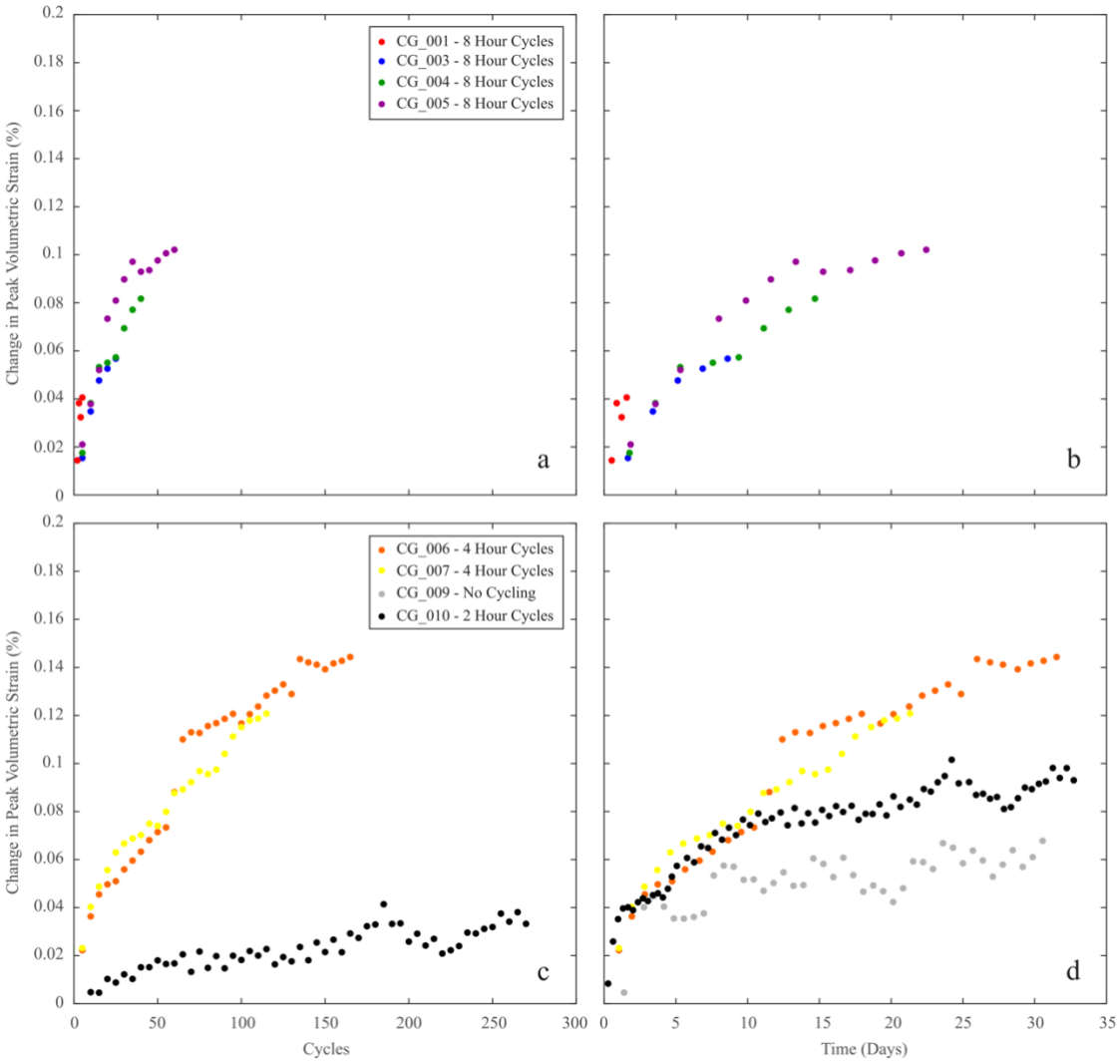

Figure A.5: Average peak volumetric strain of every five cycles during the tests; tests conducted with 8-hour cycle rates are plotted against cycle number (a) and time elapsed (b), while samples hydrostatically loaded with 4-hour cycle rates, 2-hour cycle rates and no stress cycling are plotted against cycle number (c) and time elapsed (d). CG_010 in (c) only shows the strain during cycling, while CG_010 in (d) shows both the initial static period (~5 days) followed by the initiation of stress cycling.

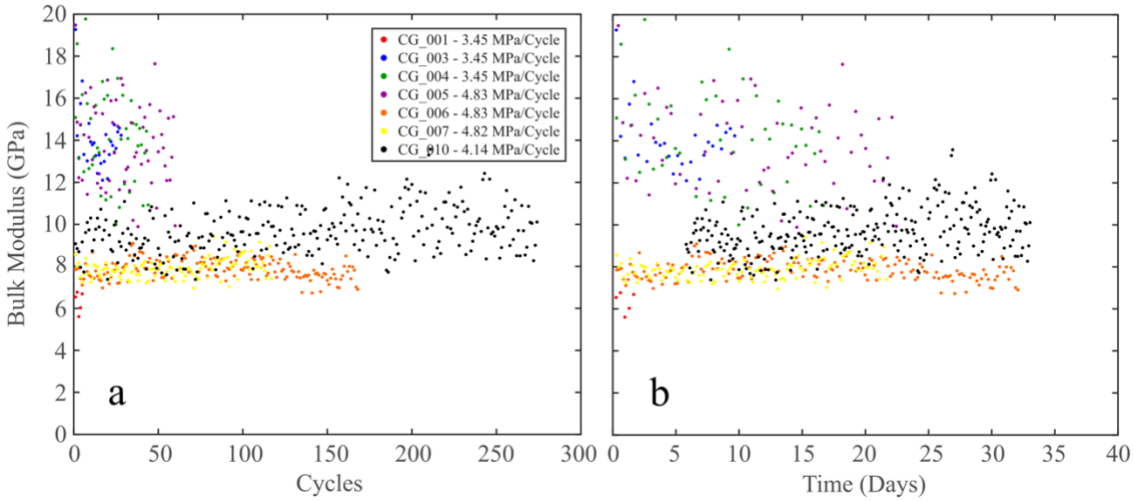

Figure A.6: Evolution of unloading bulk moduli during hydrostatic stress cycling. Bulk moduli values are compared with the number of cycles (a) and the time elapsed (b).

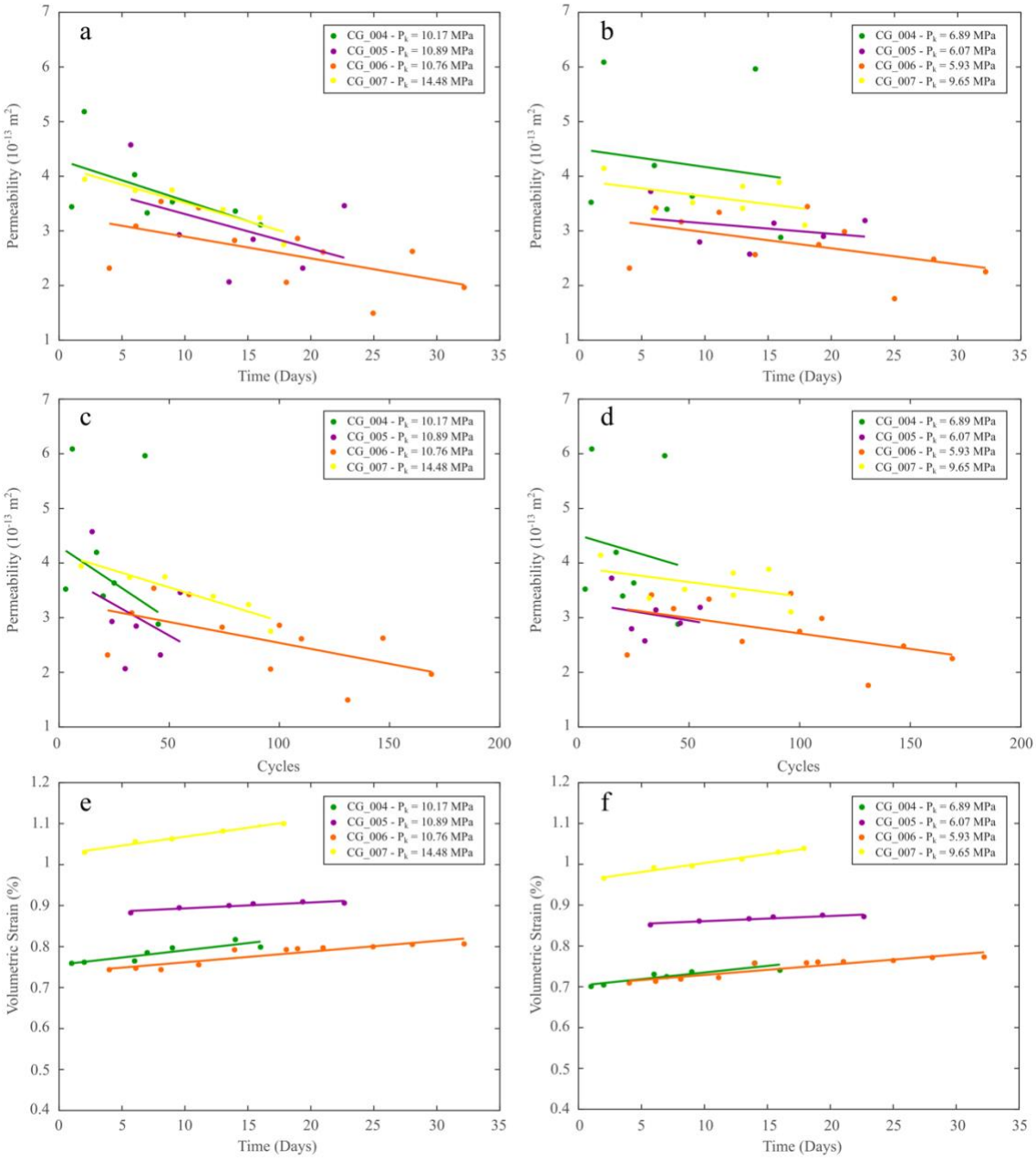

Figure A.7: Comparison of permeability and volumetric strain measured during each permeability test. High P_k permeability measurements are compared with time (a) and number of cycles (c) elapsed, while low P_k permeability measurements are compared with time (b) and number of cycles (d) elapsed. Volumetric strain recorded at high P_k (e) and low P_k (f) permeability measurements are compared with time elapsed.

APPENDIX A TABLES

Sample Number	Length (cm)	Diameter (cm)	Weight (g)	Density (g/cm^3)
CG_001	8.18	3.77	178.58	1.96
CG_003	8.15	3.78	178.31	1.95
CG_004	8.15	3.78	178.84	1.95
CG_005	8.22	3.77	179.17	1.96
CG_006	8.19	3.74	175.40	1.95
CG_007	8.24	3.74	178.08	1.96
CG_009	8.21	3.75	177.40	1.95
CG_010	8.23	3.76	178.90	1.96

Table A.1: Dimensions of Castlegate sandstone samples tested in this study.

Sample	P_c (MPa)	P_p (MPa)	P_{eff} (MPa)	P_k (MPa)	Cycle Time (Hours)	# of cycles	Duration (Days)
CG_001	20.68	10.34 & 6.89	10.34 & 13.79	0.55	8	5	2
CG_003	20.68	10.34 & 6.89	10.34 & 13.79	0.55	8	28	10
CG_004	20.68	10.34 & 6.89	10.34 & 13.79	10.17 & 6.72	8	44	16
CG_005	20.68	11.03 & 6.20	9.65 & 14.48	10.89 & 6.07	8	60	23
CG_006	20.68	11.03 & 6.20	9.65 & 14.48	10.76 & 5.93	4	168	32
CG_007	14.82 & 10	0.35	9.65 & 14.47	14.48 & 9.65	4	117	22
CG_009	20.68	10.34	10.34	10.27	-	-	31
CG_010	20.68	10.34 & 6.20	10.34 & 14.48	10.34	2	274	33

Table A.2: Testing conditions for each hydrostatic loading test. Tests with multiple pressure conditions indicate maximum and minimum pressure of each cycle. P_c = confining pressure; P_p = pore pressure; P_{eff} = effective pressure during cycles; P_k = effective pressure during permeability tests. When two values of P_c, P_p, P_{eff}, or P_k are listed, this represents the maximum and minimum pressure of each cycle.

Sample	Loading *B* (GPa)	Unloading *B* (GPa)	Cycle Loading Rate (MPa/Hr)	Unloading ε_v (%)
CG_001	2.38	3.18	0.8625	0.179
CG_003	2.88	4.50	0.8625	0.540
CG_004	2.61	5.24	0.8625	0.449
CG_005	2.14	5.03	1.2075	0.752
CG_006	2.27	4.40	2.415	0.652
CG_007	2.21	3.40	2.41	0.282
CG_009	2.64	5.52	-	0.025
CG_010	2.27	4.94	4.14	0.266

Table A.3: Values of the bulk modulus *B* measured during hydrostatic loading at test inception and unloading at test ending. Unloading ε_v is the volumetric strain calculated from a third-degree polynomial best-fit of the unloading curve. Test duration indicates the number of days each test lasted. Cycle loading rate represents the rate of effective stress change during cyclic loading.

APPENDIX B: CAPROCK SUPPLEMENTARY MATERIALS

This appendix details additional data, calculations and figures to support work in Chapter V.

Tables B.1 - B.6 show the parallel and perpendicular V_P and V_S measurements for each ultrasonic velocity test of the caprocks, along with the corresponding dynamic moduli calculations. The dynamic moduli provided are the Young's modulus (E), Poisson's ratio (ν), shear modulus (G), and bulk modulus (K) which were calculated with the equations:

$$E = \frac{\rho V_S^2 (3V_P^2 - 4V_S^2)}{(V_P^2 - V_S^2)} \quad (1)$$

$$\nu = \frac{V_P^2 - 2V_S^2}{2(V_P^2 - V_S^2)} \quad (2)$$

$$G = \rho V_S^2 \quad (3)$$

$$K = \rho(V_P^2 - \frac{4}{3}V_S^2) \quad (4)$$

where ρ, V_P, and V_S are the bulk density, compressional and shear wave velocities measured in the samples, respectively.

A schematic of the stress-strain diagrams for axial and radial strains is shown in Figure B.1 to clarify the determination of several relevant elastic and strength related properties in each test discussed in Chapter V. These parameters are reported in Table 5.3 and Figure 5.11.

The laboratory geomechanical parameters from literature review of caprock research is also elaborated on here. The specific sources and parameters available are listed in Table B.7. The experimentally measured failure stresses (σ_f) and Young's moduli for this work and from literature are displayed in Figure B.2 for comparison.

In the northeast Sichuan Basin, the stress regime is primarily extensional (i.e., $S_V > S_H > S_h$) with the maximum horizontal stress S_H trending N85E. Using stress data determined by Xie (2010) for the T_1f and T_2f members of the Puguang, Maoba and Dawan fields, as well as the pore pressure gradient from Yuanchun et al. (2008), the stress state for each caprock at depth could be approximated (Figure B.3).

Taking the minimum horizontal stress S_h as equivalent to the confining pressure at depth for each caprock, the differential stress in-situ could be approximated from the difference between S_h and the vertical stress S_V. Differential stress experienced by the regional caprocks EV1 and EV2 (evaporites) would be 69.1 and 71.7 MPa, respectively. Differential stress in-situ for caprocks LS1 and LS2 (limestones) is expected to be 98.2 and 60.8 MPa, respectively, while the differential stress in-situ for caprocks DS1 and DS2 (dolostone) is expected to be 70.8 and 87.9 MPa, respectively. Considering the effective minimum horizontal stress ($S_h - P_p$) is low, ranging from 6.29 MPa for the deepest caprock (LS2) to 9.88 MPa for the deepest caprock (LS1), it is reasonable to assume that brittle fracture and deformation is still predominant at in-situ conditions. Peak and effective confining stress data from the deformation tests were utilized to derive the differential stress required for brittle failure to occur in each caprock under in-situ conditions (Table 5.3). Failure stresses of caprocks at approximate effective confining pressures were: (1) EV1 and EV2 at 89.8 and 102.5 MPa, (2) LS1 and LS2 at 203.3 and 162.3 MPa, and (3) DS1 and DS2 at 251.3 and 197.6 MPa.

The maximum differential stresses experienced in-situ are below these thresholds. In-situ conditions for EV1 and EV2 are closest to the differential stresses required for failure, but these evaporite caprocks are more likely to behave in a ductile manner

compared to the other caprocks, especially with the additional effect of increased temperatures (Figure 5.9), and thus are low geomechanical risks. The carbonate caprocks, by contrast, are expected to deform brittlely under in-situ conditions. However, the difference between the predicted failure stresses and the current in-situ stress is greater than 100 MPa for each caprock. This means that caprock failure in the carbonates is unlikely to occur without (1) large changes in the stress state due to pore pressure drawdown or overpressure occurring during exploration and production or (2) the underlying reservoir or overburden being extremely compressible (Hawkes et al., 2005).

References

Hawkes, C. D., P. J. McLellan, and S. Bachu. "Geomechanical factors affecting geological storage of CO2 in depleted oil and gas reservoirs." Journal of Canadian Petroleum Technology 44, no. 10 (2005).

Xie, Furen, ed. Rock stress and earthquakes. CRC Press, 2010.

Yuanchun, Zhang, Zou Huayao, and Wang Cunwu. "Reserve and pressure change of paleo-oil reservoir in Puguang area." Si-chuan Basin 19, no. 6 (2008): 726-738.

APPENDIX B FIGURES

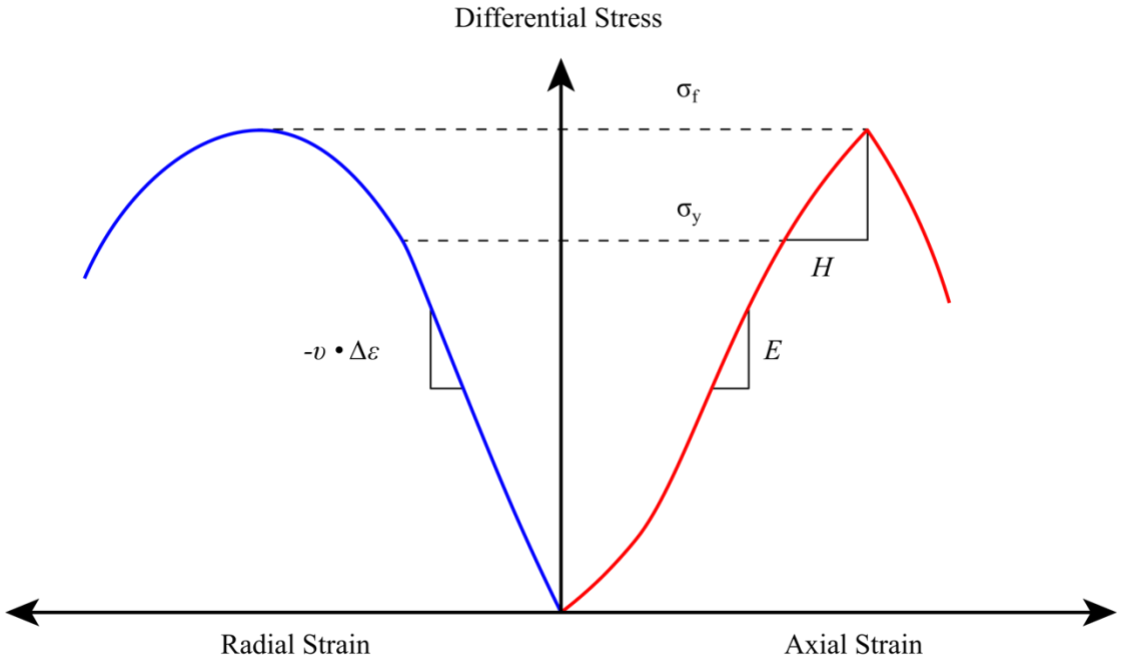

Figure B.1: Schematic of stress-strain curves and methodology for deriving elastic and inelastic properties from deformation test data.

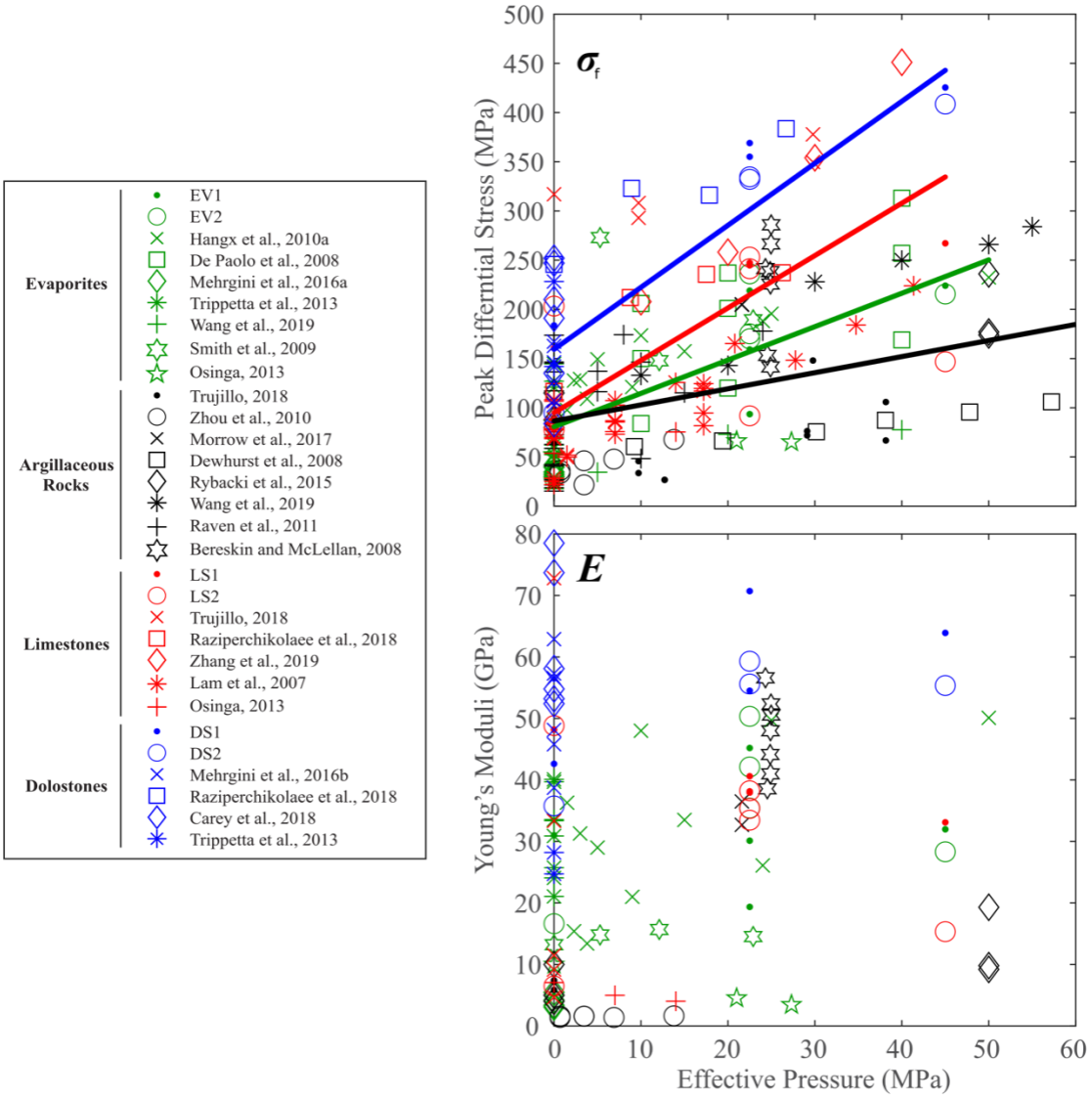

Figure B.2: Example of properties such as failure strength (σ_f) and Young's moduli (E) measured in this research and others with different caprock lithologies.

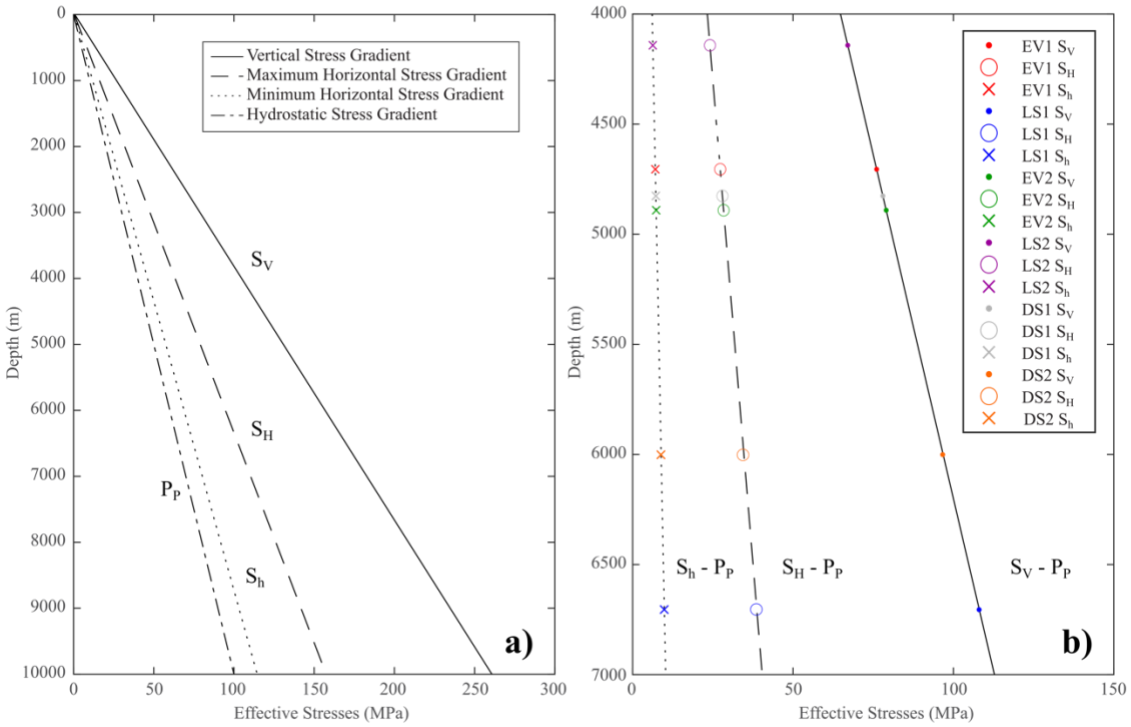

Figure B.3: The predicted stress gradients in the northeastern Sichuan Basin in our area of study (a) and the effective principal stresses for each caprock lithology at depth (b).

APPENDIX B TABLES

EV1 Parallel						
	V_P	V_S	E	ν	G	K
	m/s	m/s	GPa	-	GPa	GPa
0	5052.00	2790.54	57.15	0.28	43.39	22.32
10	5052.00	2790.54	57.15	0.28	43.39	22.32
20	5280.86	2901.68	61.96	0.28	47.75	24.13
30	5428.41	2975.75	65.23	0.29	50.62	25.38
40	5584.43	3022.03	67.68	0.29	54.48	26.17
50	5638.45	3069.78	69.64	0.29	55.10	27.01
60	5693.53	3102.46	71.11	0.29	56.12	27.59
EV1 Perpendicular						
	V_P	V_S	E	ν	G	K
	m/s	m/s	GPa	-	GPa	GPa
0	4690.87	2680.87	52.96	0.26	36.39	21.06
10	5005.24	2610.60	52.44	0.31	46.78	19.97
20	5413.36	2780.69	59.84	0.32	55.65	22.65
30	5724.55	2860.56	63.94	0.33	64.05	23.97
40	5779.93	2930.72	66.78	0.33	64.32	25.16
50	5779.93	2959.75	67.87	0.32	63.66	25.67
60	5836.39	3066.07	72.13	0.31	63.08	27.54

Table B.1: Dynamic properties measured in EV1 samples up to confining pressures of 60 MPa.

LS1 Parallel						
	V_P	V_S	E	ν	G	K
	m/s	m/s	GPa	-	GPa	GPa
0	5544.00	2732.96	54.06	0.34	56.13	20.18
10	5544.00	2672.73	52.05	0.35	57.31	19.30
20	5647.26	2783.13	56.07	0.34	58.26	20.93
30	5700.35	2848.50	58.47	0.33	58.56	21.92
40	5700.35	2931.12	61.29	0.32	56.84	23.21
50	5809.58	2945.36	62.20	0.33	59.93	23.44
60	5865.78	2974.25	63.43	0.33	61.09	23.90
LS1 Perpendicular						
	V_P	V_S	E	ν	G	K
	m/s	m/s	GPa	-	GPa	GPa
0	2790.96	55.67	0.33	53.04	21.01	2790.96
10	2817.43	55.73	0.30	46.84	21.41	2817.43
20	2914.16	58.96	0.29	46.20	22.90	2914.16
30	2928.53	59.91	0.30	48.73	23.13	2928.53
40	2957.69	61.09	0.29	49.59	23.59	2957.69
50	2987.43	62.04	0.29	48.96	24.07	2987.43
60	3002.53	63.31	0.30	53.31	24.31	3002.53

Table B.2: Dynamic properties measured in LS1 samples up to confining pressures of 60 MPa.

EV2 Parallel						
	V_P	V_S	E	ν	G	K
	m/s	m/s	GPa	-	GPa	GPa
0	4937.20	2766.65	57.62	0.27	41.96	22.67
10	5536.29	2905.06	65.48	0.31	57.44	24.99
20	5633.96	2986.56	68.91	0.30	58.78	26.41
30	5787.09	3043.48	71.80	0.31	62.60	27.43
40	5893.89	3072.76	73.44	0.31	65.59	27.96
50	5948.78	3072.76	73.70	0.32	67.51	27.96
60	6004.70	3087.61	74.54	0.32	69.13	28.23
EV2 Perpendicular						
	V_P	V_S	E	ν	G	K
	m/s	m/s	GPa	-	GPa	GPa
0	4898.55	2908.78	60.88	0.23	37.26	24.79
10	5095.48	2818.23	59.57	0.28	45.05	23.27
20	5308.90	2882.32	62.86	0.29	50.13	24.34
30	5492.96	2977.10	67.11	0.29	53.79	25.97
40	5589.86	3005.33	68.64	0.30	56.27	26.47
50	5741.79	3063.44	71.56	0.30	59.94	27.50
60	5902.21	3078.32	72.93	0.31	65.06	27.77

Table B.3: Dynamic properties measured in EV2 samples up to confining pressures of 60 MPa.

LS2 Parallel						
	V_P	V_S	E	ν	G	K
	m/s	m/s	GPa	-	GPa	GPa
0	4989.53	2648.69	50.48	0.30	42.89	19.36
10	5074.55	2546.77	47.67	0.33	47.20	17.90
20	5207.65	2708.93	53.24	0.31	47.84	20.25
30	5396.38	2994.97	63.24	0.28	47.36	24.75
40	5495.96	3025.40	64.79	0.28	49.67	25.26
50	5599.29	3072.21	66.92	0.28	51.79	26.05
60	5652.43	3072.21	67.22	0.29	53.44	26.05
LS2 Perpendicular						
	V_P	V_S	E	ν	G	K
	m/s	m/s	GPa	-	GPa	GPa
0	3925.30	2306.42	36.19	0.24	22.88	14.64
10	4261.67	2283.72	37.27	0.30	30.84	14.35
20	4396.21	2444.05	41.95	0.28	31.26	16.43
30	4481.09	2487.72	43.49	0.28	32.54	17.03
40	4510.12	2505.62	44.11	0.28	32.93	17.27
50	4599.50	2514.67	44.77	0.29	35.01	17.40
60	4630.09	2523.79	45.16	0.29	35.61	17.52

Table B.4: Dynamic properties measured in LS2 samples up to confining pressures of 60 MPa.

DS1 Perpendicular						
	V_P	V_S	E	ν	G	K
	m/s	m/s	GPa	-	GPa	GPa
0	5123.53	3443.64	72.34	0.09	29.27	33.25
10	5360.38	3091.40	67.03	0.25	44.83	26.79
20	5716.30	3503.08	82.52	0.20	45.74	34.40
30	5774.39	3582.60	85.43	0.19	45.50	35.98
40	5918.75	3619.11	88.23	0.20	49.25	36.72
50	5981.05	3642.31	89.65	0.21	50.70	37.19
60	6216.63	3689.61	93.74	0.23	57.46	38.16

Table B.5: Dynamic properties measured in DS1 samples up to confining pressures of 60 MPa.

DS2 Parallel						
	V_P	V_S	E	ν	G	K
	m/s	m/s	GPa	-	GPa	GPa
0	6008.91	3413.46	81.52	0.26	57.03	32.30
10	6097.18	3457.20	83.70	0.26	58.88	33.14
20	6124.86	3502.08	85.49	0.26	58.66	34.00
30	6083.43	3548.13	86.71	0.24	56.06	34.90
40	6110.99	3566.90	87.59	0.24	56.50	35.27
50	6145.79	3576.35	88.22	0.24	57.43	35.46
60	6180.99	3614.68	89.84	0.24	57.62	36.22
DS2 Perpendicular						
	V_P	V_S	E	ν	G	K
	m/s	m/s	GPa	-	GPa	GPa
0	5595.44	3218.74	73.44	0.25	49.50	29.31
10	5681.72	3132.74	71.17	0.28	54.31	27.77
20	5929.89	3163.48	73.68	0.30	61.73	28.31
30	5957.27	3206.74	75.41	0.30	61.62	29.09
40	5984.92	3234.89	76.60	0.29	61.87	29.61
50	6098.11	3263.54	78.30	0.30	65.03	30.13
60	6134.36	3271.82	78.82	0.30	66.08	30.29

Table B.6: Dynamic properties measured in DS2 samples up to confining pressures of 60 MPa.

	Peak Stress	Young's Modulus	Poisson's Ratio	Source
Evaporites	Yes	Yes	No	Hangx et al., 2010a
	Yes	No	No	De Paolo et al., 2008
	Yes	Yes	Yes	Mehrgini et al., 2016a
	Yes	Yes	Yes	Trippetta et al., 2013
	Yes	No	No	Wang et al., 2019
	Yes	Yes	Yes	McLellan et al., 2008
	Yes	Yes	Yes	Osinga, 2013
Argillaceous Rocks	Yes	Yes	Yes	Trujillo, 2018
	Yes	Yes	Yes	Zhou et al., 2010
	Yes	Yes	Yes	Morrow et al., 2017
	Yes	No	No	Dewhurst et al., 2008
	Yes	Yes	No	Rybacki et al., 2015
	Yes	No	No	Wang et al., 2019
	Yes	Yes	Yes	Bereskin and McLennan, 2008
	Yes	No	No	Raven et al., 2011
Limestones	Yes	Yes	Yes	Trujillo, 2018
	Yes	Yes	Yes	Raziperchikolaee et al., 2018
	Yes	No	No	Zhang et al., 2019
	Yes	No	No	Lam et al., 2007
	Yes	Yes	Yes	Osinga, 2013
Dolostones	Yes	Yes	Yes	Mehrgini et al., 2016b
	Yes	Yes	Yes	Raziperchikolaee et al., 2018
	Yes	Yes	Yes	Carey et al., 2018
	Yes	Yes	Yes	Trippeta et al., 2013

Table B.7: List of sources for mechanical properties measured through deformation tests with major caprock lithologies.